1987

Picosecond laser studies of V-T processes in gases and electronic excitation transport in disordered systems

John Francis Hedstrom
Iowa State University

Hedstrom, John Francis

PICOSECOND LASER STUDIES OF V-T PROCESSES IN GASES AND ELECTRONIC EXCITATION TRANSPORT IN DISORDERED SYSTEMS

Iowa State University PH.D. 1987

PLEASE NOTE:

In all cases this material has been filmed in the best possible way from the available copy. Problems encountered with this document have been identified here with a check mark __✓__.

1. Glossy photographs or pages _____
2. Colored illustrations, paper or print _____
3. Photographs with dark background _____
4. Illustrations are poor copy _____
5. Pages with black marks, not original copy _____
6. Print shows through as there is text on both sides of page _____
7. Indistinct, broken or small print on several pages ✓
8. Print exceeds margin requirements _____
9. Tightly bound copy with print lost in spine _____
10. Computer printout pages with indistinct print _____
11. Page(s) _____ lacking when material received, and not available from school or author.
12. Page(s) _____ seem to be missing in numbering only as text follows.
13. Two pages numbered _____. Text follows.
14. Curling and wrinkled pages _____
15. Dissertation contains pages with print at a slant, filmed as received _____
16. Other _____

_____

_____

Picosecond laser studies of V-T processes in gases and electronic excitation transport in disordered systems

by

John Francis Hedstrom

A Dissertation Submitted to the
Graduate Faculty in Partial Fulfillment of the
Requirements for the Degree of
DOCTOR OF PHILOSOPHY

Department: Chemistry
Major: Physical Chemistry

Approved:

Signature was redacted for privacy.

In Charge of Major Work

Signature was redacted for privacy.

For the Major Department

Signature was redacted for privacy.

For the Graduate College

Iowa State University
Ames, Iowa

1987

TABLE OF CONTENTS

LIST OF FIGURES

LIST OF TABLES

CHAPTER I. INTRODUCTION

The lure of inducing mode-specific, bimolecular reactivity through selective laser excitation has renewed interest in energy flow processes among vibrational, rotational, and translational degrees of freedom in excited species. Exoergic reactions frequently produce nonthermal product state distributions. On the basis of microscopic reversibility, the reverse reactions corresponding to preferred channels of the forward reaction should be accelerated when the products are excited into these states (1). Studies of infrared laser-induced chemical reactions have been based on analyses of product state distributions (2-5). When diatomic molecules are reacted with atoms, increased reactivity is sometimes observed when the diatomic molecule is vibrationally excited. The effect is known as vibrational enhancement, and it can be sizable in some instances. For the reaction

$$HCl + Br \longrightarrow HBr + Cl, \qquad (1.1)$$

rate constants for HCl in the vibrational states v = 0, v = 1, and v = 2 have been found to be 1×10^{-2}, 2×10^{4}, and 1×10^{9} liter/(mole sec), respectively (6). For the K + HCl(v = 1) reaction using a molecular beam apparatus, it was shown that the reaction cross-section for the HCl(v = 1) was approximately 100 times that for the HCl(v = 0) at the same mean collision energy (4). This latter experiment affirms that vibrational enhancement is the source of the increased reaction rates.

When polyatomic molecules are the reactants in laser-induced reac-

tions, careful evaluation of the relaxation processes must precede any interpretation of the reaction mechanism. Once absorbed, mode specific energy may become randomized throughout a number of vibrational modes in the molecule much more rapidly than the process which breaks the originally excited bond. For example, in a reaction between CH_3F and Cl_2 (5), CH_3F was excited into its C-F stretching mode, and yet the reaction products were found to be CH_2FCl and HCl. Clearly, an understanding of the processes controlling the rates and pathways for vibrational relaxation between various modes and degrees of freedom in polyatomic molecules is essential to an improvement in our knowledge of chemical reactivity.

Investigation into gas phase vibrational energy transfer of small nonreacting molecules in their ground electronic state has been reviewed (7-9). Processes involving a small change in the net vibrational energy ΔE and vibrational quantum number Δv were found to correspond to high energy transfer efficiencies. Consequently, the rate of energy transfer among excited vibrational levels should be rapid compared to vibrational to translational, rotational (V-T,R) relaxation rates, since there are usually accessible vibrational to vibrational (V-V) pathways with relatively small values for ΔE. An example of this effect can be observed in a pure sample of CH_3F. The V-T,R process

$$CH_3F(\nu_3) + CH_3F \longrightarrow CH_3F + CH_3F \quad (\Delta E = 1049\ cm^{-1},\ \Delta v = 1) \qquad (1.2)$$

requires 1.5×10^4 collisions (10), while the V-V transfer

$$CH_3F(\nu_3) + CH_3F(\nu_3) \rightarrow CH_3F(2\nu_3) + CH_3F \quad (\Delta E = 18\ cm^{-1},\ \Delta v = 0) \quad (1.3)$$

is extremely rapid, requiring only 4 collisions (11).

The collision numbers Z cited for equations 1.2 and 1.3 characterize the average number of collisions required to effect the respective transitions. In practice, several other terms are frequently employed for the discussion of energy transfer efficiencies, namely, a rate constant k, cross section σ, and transfer probability per collision P (12). The collision number and transition probability per collision are normalized to the hard sphere cross section $\sigma_{hs} = \pi d^2$ to yield

$$Z = P^{-1} = {}^{\sigma_{hs}}/_{\sigma}, \quad (1.4)$$

where d is one-half the sum of the hard sphere diameters of the colliding molecules.

Most theoretical results of collision-induced energy transfer are based on oversimplified models of the collision. Nevertheless, calculations based on these simplistic models agree at least qualitatively with experimental results for a number of systems (13-15), and, hence, provide useful models for discussion of the collision process. The Schwartz, Slawsky, and Herzfeld (SSH) theory (13), as modified by Tanczos (14), is the model used most frequently for the discussion of collision-induced energy transfer between two polyatomic molecules or between an atom and a polyatomic molecule in their ground electronic states.

Basic to the development of the SSH theory are the assumptions that molecules do not rotate during the interaction, and that they approach

each other along a straight path. Furthermore, the colliding molecules are presumed to interact with each other solely via two surface atoms--atom s on the first and atom s' on the second molecule. This interaction potential is written

$$V = V_o \exp [\alpha(-r + \sum_a A_{sa}Q_a + \sum_b A_{s'b}Q_b)], \tag{1.5}$$

where $A_{sa}Q_a$ is the displacement of the surface atom s due to the normal vibration Q_a, r is the equilibrium distance between centers of mass of the colliding molecules, α is the potential energy range parameter, and V_o is a preexponential constant. The sum over a is over all normal vibrations of the first molecule, and similarly the sum over b is over the normal vibrations of the second molecule. Since the form of the potential is an exponential, it can be written as

$$V = V_o \cdot V_r(r) \cdot V_1(Q_1) \cdot V_2(Q_2) \ldots V_n(Q_n), \tag{1.6}$$

where $V_r(r) = \exp(-\alpha r)$ and $V_n(Q_n) = \exp(\alpha A_{sn}Q_n)$.

The probability that during a collision vibrational mode Q_a in one molecule will change its quantum state from i to j, while a second mode Q_b in the same or in another molecule, simultaneously changes from state k to l is given by

$$P = P_o[V^{i\to j}(a)]^2 [V^{k\to l}(b)]^2 F(\Delta E,\varepsilon,T), \tag{1.7}$$

where P_o is a steric factor and $F(\Delta E,\varepsilon,T)$ is a translational factor which is a function of the net change in translational energy ΔE, the inter-

molecular Lennard-Jones potential well depth ε and the temperature T. The vibrational matrix element $[V^{i\to j}(a)]^2$ may be written as $|\langle\phi_i(a)|V_a(Q_a)|\phi_j(a)\rangle|^2$, where ϕ_i and ϕ_j are harmonic oscillator wavefunctions. Expanding the exponential $V_a(Q_a)$ in the matrix element leads to

$$[V^{i\to i}(a)]^2 = 1 \tag{1.8a}$$

$$[V^{i\to i\pm1}(a)]^2 = \frac{(i+\frac{1}{2}\pm\frac{1}{2})\alpha^2}{2\gamma_a N_s} \sum_s A_{sa}^2, \tag{1.8b}$$

$$[V^{i\to i\pm2}(a)]^2 = \frac{(i+1\pm1)(i\pm1)\alpha^4}{16\gamma_a^2 N_s} \sum_s A_{sa}^4, \tag{1.8c}$$

where γ_a is equal to $\frac{2\omega_a}{\hbar}$ and N_s is the number of surface atoms on the molecule. Since it is not possible to determine directly which surface atoms are involved in the collision, the vibrational matrix elements in equations 1.8b and 1.8c have been calculated by averaging the transition probabilities over all surface atoms.

The SSH "breathing sphere" model, although its approach is three-dimensional, formally reduces the collision dynamics of two polyatomic molecules to a collinear interaction between two diatomic molecules. The nominal vibrational coordinate χ_n of each "diatomic" molecule may be expressed as $\chi_n = \frac{1}{N_s} \sum_s A_{sn} Q_n$ for each normal mode of the correspondent polyatomic molecule. The reduction of the model to a collision between two diatomic molecules naturally obscures the symmetries and dynamic characteristics of the polyatomic vibrations (16). More recent models

include molecular rotation (17) and mode-matching (18) in their treatments of collision-induced energy transfer. In spite of its assumptions, SSH theory remains the most widely used theoretical tool for interpreting experimental results of collision-induced energy exchange of molecules in the ground electronic state.

It would appear on the surface that vibrational relaxation in an electronically excited state should be very similar to relaxation in the ground electronic state. Experimental results, however, suggest that relaxation in an electronically excited state may proceed through a different mechanism. In general, collision efficiencies for vibrational energy transfer are increased by orders of magnitude for molecules relaxing in the excited electronic state. In their study of vibrational relaxation in the $A^1\Pi$ state of CO, Fink and Comes (19) found that

$$CO(v=1) + He \rightarrow CO(v=0) + He \quad (\Delta E = 1481\ cm^{-1}) \tag{1.9}$$

requires only 77 collisions, compared to $\sim 10^8$ collisions for the ground state process ($\Delta E = 2143\ cm^{-1}$). Data for a number of other diatomic molecules (20-22) coincide with these findings. An anomaly to this trend in collisional relaxation efficiencies was reported by Marcoux et al. (23). They found that vibrational energy transfer from $CO(a^3\Pi, v'=1\text{-}3)$ requires at least 6×10^6 collisions with helium.

A similar pattern of vibrational relaxation has emerged from the handful of studies concerning polyatomic molecules in the excited electronic state. Two recent reviews (16,24) cite most of the results in this

area to date.

No completely plausible explanation has been given for the high efficiency of vibrational energy transfer in excited electronic states. The fact that cross sections frequently exceed gas kinetic values suggests that attractive interactions may play an important role in energy transfer rates in electronically excited molecules, because the range of attractive potentials is larger than hard sphere diameters. Rice (24) points out that molecules in the excited state have an open shell electron configuration, and a smaller ionization potential which would lead to stronger long-range attractive forces (relative to the ground state) between the excited molecule and a collision partner. Assuming that the attractive forces dominate the interaction for an excited state molecule, Lin et al. (25) developed a correlation between the relaxation efficiency and the intermolecular well depth. Parmenter and Tang (26) had limited success applying the correlation to collision induced-energy transfer data from $S_1(^1B_{2u})$ benzene. However, no correlation whatsoever was found for analogous ground state relaxation data.

The results of Parmenter and Tang (26) describing vibrational energy flow in S_1 benzene have given impetus for much of the ensuing research into energy transfer in electronically excited polyatomic molecules. The objective of their study was to follow mode-to-mode vibrational relaxation from the 6^1 level ($\nu_6' = 522\ cm^{-1}$) of S_1 benzene under single collision conditions.

Nine gases of varied complexity served as collision partners.

Although benzene has twenty vibrational levels lying within 500 cm^{-1} of the 6^1 level, over 70% of the depletion from this level could be accounted for by growth of population in just six vibrational levels, represented by four channels of energy transfer. The distribution of energy among the four channels is somewhat dependent on the vibrational structure of the collision partner. In every case, the addition of a quantum of the vibrational mode 16^1 to the initially pumped 6^1 level serves as an important precursor to vibrational equilibration.

Cross sections for vibrational energy transfer were near gas kinetic values for all collision partners. Helium was the least effective collision partner studied, yet overall relaxation from the 6^1 level of S_1 benzene required only 11 hard sphere collisions. The largest mode-to-mode cross sections were always to the $6^1 16^1$ level lying 237 cm^{-1} above the level of 6^1, even though the nearly resonant transfer to the level 11^1 (ΔE = 7 cm^{-1}) was available. For helium, 17 hard sphere collisions are required to add a quantum of 16^1 to the original level 6^1. Such high efficiencies for T-V transfer are not seen for energy flow within ground electronic states.

Later work by Atkinson, Parmenter and Tang (27) examined the role of vibrational resonance between S_1 benzene levels and polyatomic collision partners on mode-to-mode energy transfer efficiencies. OCS has a bending mode (ν_2'' = 520 cm^{-1}) nearly resonant with the 6^1 fundamental of S_1 benzene (ΔE = 2 cm^{-1}). V-V transfer to this mode is efficient, requiring only 10 collisions. However, T,R-V transfer from OCS adding a quantum of 16^1 to

benzene is even more efficient, requiring only 8 collisions.

Based on experimental data from S_1 benzene and SSH calculations for vibrational relaxation in ground states of small molecules (28-30), Parmenter and Tang formulated a set of general propensity rules to predict the flow pattern of vibrational energy in excited state molecules (24). The relative probability for a transition in which mode a changes its quantum number from i to j and mode b changes its quantum number from k to l is given by

$$P(i \to j | k \to l) \propto g_j \; g_l \; U_a^2 \; U_b^2 \; I \; (\Delta E_{VT}) \tag{1.10}$$

where g_j and g_l are the final-state degeneracies of modes a and b, respectively, U_a and U_b are the coupling matrix elements within the a and b manifolds, respectively, and $I(\Delta E_{VT})$ depends on the amount of energy switched between the V and T,R degrees of freedom. The U^2 factors are assigned a value of $10^{-|\Delta v|}$ for a change in quantum number Δv. Hence, each normal mode is assumed to have the same average projection onto the direction of impact. When the vibrational energy transfer is exothermic, $I(\Delta E_{VT})$ is set to 0.6 for $\Delta E_{VT} \leq 50$ cm^{-1} or $10^{-(\Delta E_{VT}/100)}$ for $\Delta E_{VT} \geq 50$ cm^{-1}. Either factor is multiplied by the Boltzmann factor exp $(-\Delta E_{VT}/kT)$ when the vibrational transfer is endothermic.

The propensity rules were found to give a good description of the pattern of energy flow as a result of collisions of S_1 benzene with a variety of partners. The factors composing the propensity rules oppose each other in a manner which accurately reproduces the mode selectivity

observed experimentally.

Studies by Chernoff and Rice (31) and Chernoff (32) on energy flow in $S_1(^1B_2)$ aniline and McDonald and Rice (33) on energy flow in $S_1(^1B_{3u})$ pyrazine corroborated certain features of the Parmenter-Tang propensity rules while being in discord with other facets of the rules. In each case, argon served as the sole collision partner probing the pathways of intramolecular vibrational energy transfer from a variety of S_1 levels. Plots of the energy transfer cross sections concur with the benzene data--that g, Δv, and ΔE_{VT} are the primary factors governing energy flow patterns. However, the dependence on ΔE_{VT} is somewhat steeper for aniline and pyrazine, and the restrictions on Δv are less strict than was found for benzene. Once again, V-T cross sections are large relative to those for ground state molecules, although V-T cross sections for S_1 pyrazine were generally an order of magnitude less than those found for S_1 benzene and aniline. The reduced cross sections for pyrazine have since been found to be the result of mixing of electronic states (34). An exothermic channel was a prominent first step toward equilibration among the vibrational levels for nearly every vibronic level pumped.

The most notable departure in the observed aniline and pyrazine vibrational relaxation cross sections from the qualitative pathways predicted by the propensity rules concerns the differentiation between mode types on the efficiencies of energy transfer. For example, the vibrational modes studies in S_1 aniline can be separated into two nearly noncommunicating groups of levels. Vibrational energy transfer is efficient

within a group of modes, and much less so for energy transfer between modes belonging to different groups. Mapping the energy flow from the 16^1 level of S_1 aniline following two successive collisions with argon (31) indicates that an unexpectedly large number of collisions will be required before a Boltzmann distribution among the vibrational levels in the S_1 electronic state is attained.

SSH theory alone thus cannot predict the observed selectivity for transfer of vibrational energy based on mode discrimination. The breathing sphere model makes the assumption that the molecules always approach each other in the most favorable orientation for all normal modes simultaneously. This is not a reasonable picture of intramolecular mode-to-mode transitions in polyatomic molecules. A trajectory most favorable for activation of one mode may be highly unfavorable for the deactivation of another mode. The absence of this "orientation factor" in the SSH theory permits mode mismatching in the transition probabilities predicted by the breathing sphere model. The Parmenter-Tang propensity rules, based on the breathing sphere model, are, therefore, subject to the same limitations in discerning between favorable and unfavorable molecular orientations for vibrational energy transfer.

McDonald and Rice (35) have formulated a correlation diagram model which explicitly includes the role of mode matching in the propensity rules. In its present form, the model is able to describe the intramolecular vibrational energy exchange in a polyatomic molecule as a result of a collision with an atom. Similar to the SSH theory and

Parmenter-Tang rules, the perturbation of a particular vibrational mode is proportional to the amplitude of the mode along the collision trajectory. However, the McDonald-Rice model does not assume that the molecule is in an optimal orientation for all normal modes concurrently. Instead, a set of representative collision trajectories γ is formulated, and the components of the collisional displacement χ_a^γ along the various normal coordinates are determined for each γ using group theory. After weighting each trajectory by an appropriate factor ω_γ, a collisional coupling term between vibrational states i and j can be written as

$$C_{ij} = \frac{1}{m} \sum_\gamma \omega_\gamma \prod_a (\chi_a^\gamma)^2, \tag{1.11}$$

where the product is over all vibrational modes, a, undergoing quantum number changes, and m is the mass of the atom which dominates the vibrational motion--for example, $C_{||}$ or $H_\perp$ (35). This coupling term replaces the $\frac{1}{N_s} \sum_s A_{sa}^2$ term in the vibrational matrix element (equation 1.8b) of the breathing sphere model.

The refined propensity rules of McDonald and Rice have been applied to S_1 systems of benzene, aniline, and pyrazine with atomic collision partners (35). When compared to observed values, the calculated rates agree quite well for nearly all vibrational energy transfer processes. Based on its agreement with observed rates and vibrational energy transfer pathways, this procedure marks a significant advance in describing energy flow.

Current research is directed toward the development of a more

thorough understanding of energy transfer processes in excited molecules by varying collision parameters. Lawrance and Knight (36,37) are presently accumulating data on vibrational relaxation from the $5_2 30_2$ level of S_0 p-difluorobenzene. These will be the first results for collision-induced vibrational energy transfer in a ground state aromatic molecule. Comparison of these data with the results of vibrational relaxation in S_1 p-difluorobenzene (34) should lend much insight into the relationship between vibrational energy transfer in excited and ground electronic state molecules. A preliminary report indicates that the rate coefficient for vibrational relaxation from the level $5_2 30_2$ is about 2 to 3 times the hard sphere value.

Studies on glyoxal reveal that the pattern of rapid collision induced energy flow observed in the aforementioned S_1 polyatomic molecules (benzene, aniline, pyrazine and p-difluorobenzene) is not exclusive to aromatic molecules (38-40). Strong propensity rules, V-T,R relaxation cross sections near gas kinetic values, and efficient endoergic energy transfer pathways were observed in relaxation from the 8^1 ($\nu_8' = 735$ cm^{-1}) level of $S_1(^1A_u)$ glyoxal for six collision partners, hinting that this behavior may be typical of all S_1 polyatomic molecules.

Tang and Parmenter (41) have extended investigation of S_1 benzene to levels where the density of states is greater than 10 per cm^{-1}. Their intent was to use propensity rules (equation 1.10) to model vibrational relaxation when several thousand levels lie within kT of the initial level. Comparison of experimental and calculated rate constants using

CO as a collision partner show that the upward trend in energy transfer rate constants with increasing energy of the prepared state is due primarily to the role of $\Delta v = 2$ and $\Delta v = 3$ transitions for a few additional channels available at high vibrational energy (41). Additionally, limits for V-T,R energy transfer $I(\Delta E)$ restrict transitions to states lying within about 250 cm^{-1} of the initial level. For the prepared state $6^2_1 1$ (ε_{vib} = 1967 cm^{-1}), 58 of the 2200 vibrational levels within ±250 cm^{-1} are seen to account for 66% of the total transfer probability. Rate constants calculated from the propensity rules correlate with experimental values for nine of the eleven prepared levels ranging in ε_{vib} from 0 to 2368 cm^{-1}, indicating that propensity rules may be useful for modeling vibrational relaxation involving many available channels for energy transfer.

Vandersall, Chernoff and Rice (42) have expanded the study of collision-induced energy transfer to include systems where the effects of long-range attractive forces between the collision pair must be considered. Vibrational energy transfer from the 0^0, $10b^1$, and I^1 levels of S_1 aniline were induced by single collisions with H_2O and CH_3F. It was expected that hydrogen bonding between H_2O and the amino group on the aniline would have a prominent effect on coupling between the inversion mode and other vibrational levels. CH_3F was included as a collision partner because it has a permanent dipole moment nearly equal to H_2O (1.85D), but it is unable to hydrogen bond. Thus, the effects of hydrogen bonding and dipole moment on energy transfer may be separated by comparison of the vibrational relaxation rates and pathways induced by these molecules. In both

H_2O and CH_3F, V-T,R energy transfer pathways are expected to predominate. The rates of depopulation induced by H_2O and CH_3F are both in excess of the hard sphere collision rate. The similarities between the two molecules as collision partners indicate that hydrogen bonding interactions are inconsequential in effecting vibrational energy transfer.

Comparison of H_2O and CH_3F to argon (31) as collision partners with S_1 aniline reveals some interesting features. When the inversion mode is inactive during a transition, mode-to-mode rate constants $k_4(i)$ are approximately five times larger for aniline collisions with H_2O and CH_3F than for collisions with argon. For transitions involving the inversion mode, the rates are further increased by a factor of five. A large dipole moment and rotational degrees of freedom are the basic properties which separate H_2O and CH_3F from argon (39). The dipole moments would account for the general increase in the rate constants $k_4(i)$ in a logical way since a permanent dipole is expected to increase the attractive component of the intermolecular force. It has been hypothesized that the rotational degrees of freedom can correlate with the inversion mode motion to account for the enhanced relaxation rates of inversion transitions with H_2O and CH_3F (42).

The realization that rotation of the collision partner can play an important role in vibrational energy transfer is not a recent consideration. Cottrell and Matheson (43) suggested that collision partners with small moments of inertia I are more likely to induce vibrational energy transfer through vibrational-rotational coupling than via a vibrational-

translational mechanism. Their observation accounted for the "anomalous" behavior of some collision pairs whose predicted energy transfer probabilities were calculated assuming vibrational-translational energy exchange (5,12,44).

Though the relative values compared well, calculated relaxation times using Cottrell and Matheson's formula were a factor of 30 faster than the observed times. Moore (44) proposed a theory similar to the SSH formalism which gives a much closer fit between calculated and experimental relaxation times. Figure 1-1 illustrates some of the basic concepts involved in the model. Atom A of a stationary, rotating diatomic molecule collides head on with atom B of a stationary vibrating molecule. The relative impact velocity is assumed to be dependent only on the rotational velocity ωd of atom A, where ω is the angular velocity, and d is the distance between atom A and the axis of rotation. This approximation is only valid when I/d^2 is much less than the molecular weight of the rotator. The interaction potential between atoms A and B is assumed to be

$$V = V_o \exp(-\alpha r)(1 + \alpha \Delta R), \tag{1.12}$$

where α is the potential energy range parameter, ΔR is the vibrational displacement from equilibrium, and r is the distance between the colliding atoms when $\Delta R = 0$. Substituting I/d^2 for the reduced mass of the rotator leads to an energy transfer probability given by

$$P_{1\to 0} = \left(\frac{17.1\, I^{13/6}\, \nu^{4/3}}{Z_o d^{13/3}\, T^{1/6}\, M\alpha^{7/3}}\right) \exp\left[-1.78\left(\frac{I\nu^2}{d^2\alpha^2 T}\right)^{1/3}\right] \exp\left(\frac{h\nu}{2kT}\right) \tag{1.13}$$

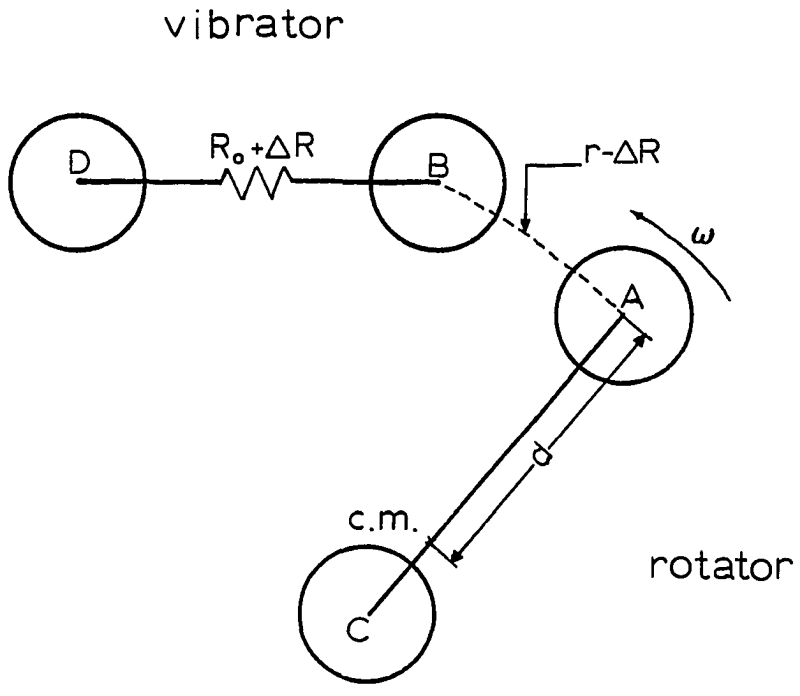

Figure 1-1. Model for vibrational-rotational energy transfer. Atom A of the rotator a distance d from the rotator center of mass collides head on with atom B of the vibrating molecule. Translational velocity is assumed to be negligible

for the transfer of one quantum of vibrational energy to rotational energy, where Z_0 is a steric factor, ν is the vibrational frequency, and M is the reduced mass of the vibrational normal coordinate.

Reports of collisional relaxation in electronically excited molecules have thus far separated the energy transfer mechanism into two classes, V-V and V-T,R. Of the latter relaxation process, the important role of V-T energy transfer has been ascertained through the use of atomic collision partners. The function of this thesis is to present data from the initial collision partner CO_2 in what will eventually be a complete study of V-R energy transfer in S_1 aniline.

Aniline has been shown to be a practical choice for the study of collision-induced energy transfer in the S_1 electronic state (32,45). This investigation will be restricted to the determination of vibrational energy transfer probabilities from the 0^0 level of S_1 aniline resulting from single collisions with CO_2. The lowest CO_2 vibration (ν_2 = 667 cm^{-1}) is in a range where intermolecular V-V transfer with aniline is not expected, and its rotational velocity is 2.6 times the average translational velocity, increasing the likelihood of V-R energy transfer.

Explanation of Dissertation Format

The study of collision induced energy transport in aniline represents but one part of the work to be presented in this dissertation. The remainder focuses on the development of time-resolved fluorescence ex-

periments, whose decay curves establish the degree to which current theories are able to accurately describe excitation transport in disordered two-dimensional and three-dimensional systems. The experimental conditions for these latter investigations are described in Chapter II as modifications of the synchronously mode-locked laser system used in the aniline study. An introduction to the subject of excitation transport in disordered systems is presented in Chapter V. Chapters VI and VII contain papers submitted to the Journal of Physical Chemistry describing excitation transport in disordered three-dimensional and two-dimensional systems, respectively.

CHAPTER II. EXPERIMENTAL

Introduction

The synchronously mode-locked (SML) dye laser has emerged as an ideal source of tunable, ultraviolet picosecond pulses for use in single vibronic level (SVL) fluorescence spectroscopy. In addition to exhibiting greater conversion efficiency, SML lasers permit tuning over a much wider section of the dye gain curve than their passively mode-locked counterparts (46). Using a three-plate birefringent filter as a tuning element, typical laser linewidths of $\sim$1 cm^{-1} are possible (47). This narrow bandwidth permits selective excitation to single excited state vibrational bands in many molecules.

The simplicity of the design of the SML system is one of its major advantages. Daily cavity adjustments required to optimize the mode-locking are minimal. The SML laser provides pulse stability for several hours, with infrequent tuning of the argon laser rear cavity mirror being the only further adjustment.

Several major changes were made to the SML system and its attendant detection equipment between their inceptive and final forms. Some theory has been included in this section to help clarify the choices made in equipment selection and modification.

Mode-Locked Argon Ion Laser

An argon ion laser (Model 553A, Control Laser Corp.) serves as a pump source for the SML dye laser. The oscillator cavity includes a water-cooled plasma tube and is bound at the ends by a highly reflective rear mirror and a partially transmitting output mirror.

Wavelength selection is provided by a Brewster angle prism inserted in the cavity near the rear mirror. To one of the triangular faces, a thin layer of piezoelectric material is deposited. Under proper conditions, the prism will act not only as a tuning element but also as an acoustic grating.

Although the cavity is biased to oscillate at 514.5 nm, inhomogeneous broadening in the plasma tube allows approximately 40 axial laser modes (48) to experience net gain while meeting the resonance frequency criterion $\omega_n = {}^{n\pi c}/L$, where L is the cavity length (158 cm) and n is an integer. When there is no mode-locking, each of these axial modes will have an uncertain time-dependent phase, resulting in a cavity light intensity which is simply the summed intensity of each of the oscillating modes (49).

A Harris Corp. acousto-optic modulator creates a time-dependent loss within the cavity. Under the proper conditions, this causes a specific phase relationship to develop among the circulating modes (Figure 2-1.). This phase relationship is created when an oscillating electric field, applied to a piezoelectric material, creates a stress in the material (50). From this initial stress, a longitudinal acoustic

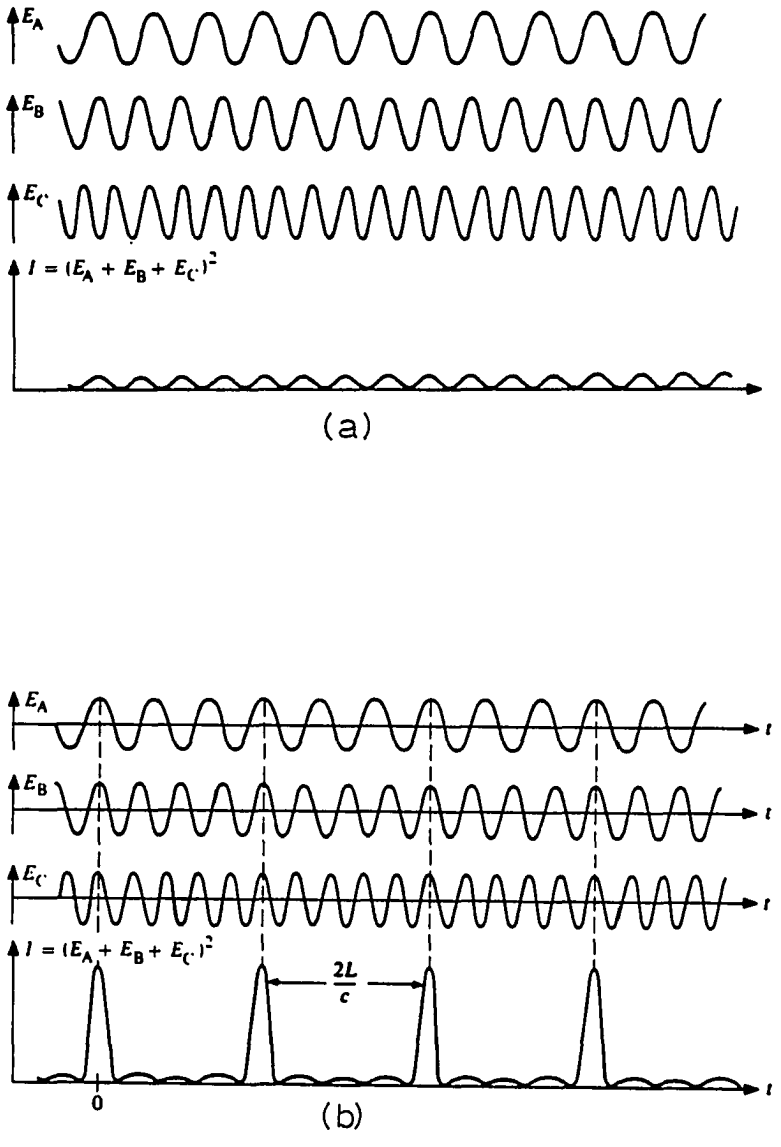

Figure 2-1. Comparison of outputs from nonmode-locked (a) and mode-locked (b) laser cavity oscillating in three longitudinal modes. From ref. (51)

wave is generated within the piezoelectric medium which propagates through the transducer into the prism. When the frequency of the acoustic wave matches a resonance frequency of the prism, a standing acoustic wave is established in the prism. The rarefaction and compression induced in the prism by the standing acoustic wave produces a periodic variation in its index of refraction (52). This pattern serves as a transmission grating for the argon beam. Intense diffraction occurs when the angle of incidence of light on the acoustic grating satisfies the Bragg condition

$$2\Lambda \sin\theta_B = \lambda, \tag{2.1}$$

where Λ is the acoustic wavelength and λ is the optical wavelength. The diffracted and incident beams will be separated by $2\theta_B$.

The fractional power diffracted by the grating P_d/P_o is

$$P_{d/P_o} = \pi^2 M_2 \frac{\ell^2}{2\lambda^2} \frac{P_a}{A}, \tag{2.2}$$

where ℓ is the length of the transducer parallel to the propagation direction of the optical beam and P_a/A is the acoustic power density. The acousto-optic figure of merit, M_2, associated with a material, gives a relative modulation effectiveness of a crystal. Although silica has a relatively low figure of merit, it is used in the intracavity modulator because of its high optical quality and transparency, which introduce a minimum of losses in the absence of modulation (50).

For practical purposes, the resonances of the prism/transducer system are the resonances of the silica prism, considered as a finite

elastic medium, whose extremities are free (50). Of these resonances, only those falling within one of the permitted acoustic frequency bands of the piezoelectric transducer vibrating independently are considered. In this approximation, the width of the silica resonances are on the order of 1 KHz, while those of the transducer are on the order of several MHz (50). Thus, there exist a series of narrow resonances $v_2/2e_2$ apart in frequency intervals centered around $(2n+1)v_1/2e_1$ (n = 0,1,2...) where v_1, e_1, and v_2,e_2 represent the velocity of sound and thickness in the piezoelectric medium and silica prism, respectively. There are three acoustic resonances within the frequency range of the currently used Harris mode-locker driver. These are at approximately 47.56, 47.96 and 48.36 MHz (see Figure 2-2). Generally, the length of the argon laser cavity is varied until the round trip frequency of the circulating laser light pulse, $c/2L$, equals twice the driving frequency of the modulator. Respective cavity lengths of 157.7, 156.4 and 155.1 cm are needed to synchronize the pulse frequencies with the 47.56, 47.96 and 48.36 MHz driving frequencies. Limits imposed by the Control Laser 553A argon laser mainframe result in a minimum cavity length of 157.2 cm. Consequently, we are constrained to mode-lock at an RF driving frequency near 47.56 MHz.

The modulator driver supplies RF power (0-1 watt) to the mode-locker through a directional coupler. Power which is not absorbed in the silica prism is reflected back towards the amplifier. A fraction of this power is fed to an RF detector, which converts the RF power to a positive

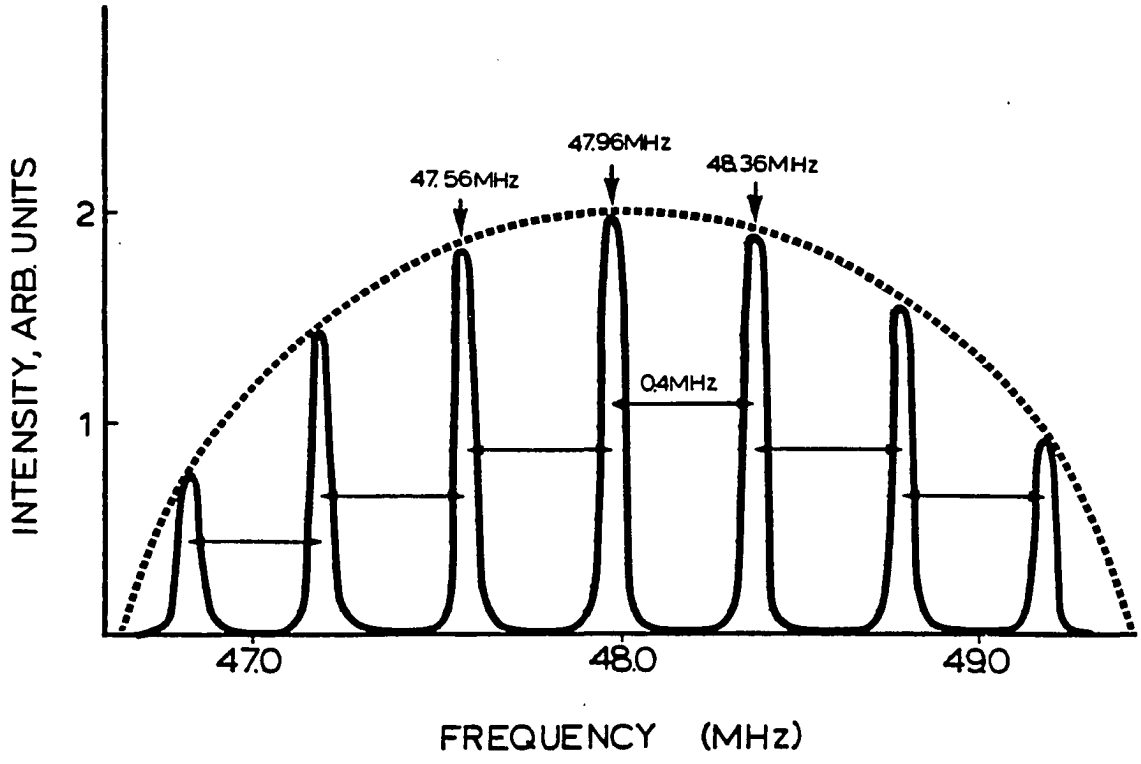

Figure 2-2. Light intensity diffracted out of laser cavity as a function of mode-locker frequency

DC voltage. By monitoring this DC level with a voltmeter while varying the RF frequency, the RF energy absorbed by the mode-locker can be determined. Figure 2-3 illustrates that at resonance the reflected voltage will be a minimum value.

With the reflected DC voltage initially set at 2 volts, at a frequency 150 KHz below the silica crystal resonance, the change in the reflected DC signal was monitored for varied RF frequency. The stability of the acoustic frequency was simultaneously monitored with a Hewlett Packard Model 524C frequency counter. The power reflected by the crystal decreased slowly as the RF frequency was raised. Beyond the resonance frequency, however, the reflected voltage increased rapidly. Within 10 KHz of resonance, an oscillatory behavior in the monitored DC voltage was noted, although the RF frequency was always stable within ±0.1 KHz. This behavior created problems when attempting to keep the RF frequency within 5 KHz of the crystal resonance, as recommended in the Harris Corp. User's Manual. It was subsequently found that the crystal resonance changes as the RF power supplied to the crystal is varied (Figure 2-4). Slight fluctuations in the power supplied to the crystal could, therefore, alter the resonance and significantly change the fraction of applied power reflected back to the RF detector when the frequency is within 10 KHz of crystal resonance. With an off-resonance voltage readout of 2 volts and the RF frequency set between 47.635 and 47.640 MHz, the mode-locking deteriorated rapidly. The region between 47.620 and 47.630 MHz provided the optimum pulse structure when the laser was mode-locked. In practice,

Figure 2-3. Plot of reflected voltage from the mode-locker vs. RF driving frequency. Similar plots were obtained for the other crystal resonances within the frequency range of the mode-locker driver

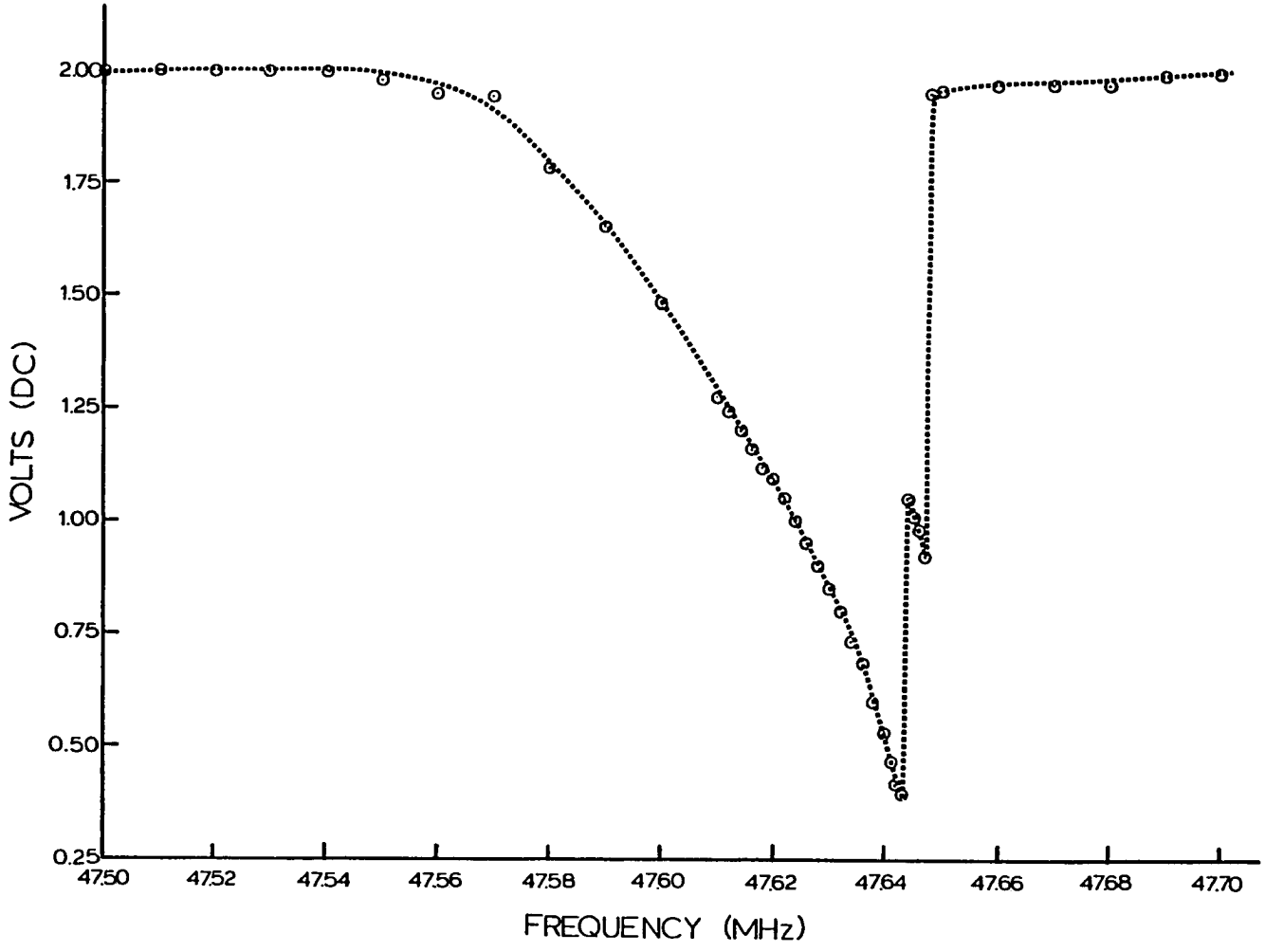
2.00
1.75
1.50
1.25
1.00
0.75
0.50
0.25
VOLTS (DC)
47.50
47.52
47.54
47.56
47.58
47.60
47.62
47.64
47.66
47.68
47.70
FREQUENCY (MHz)

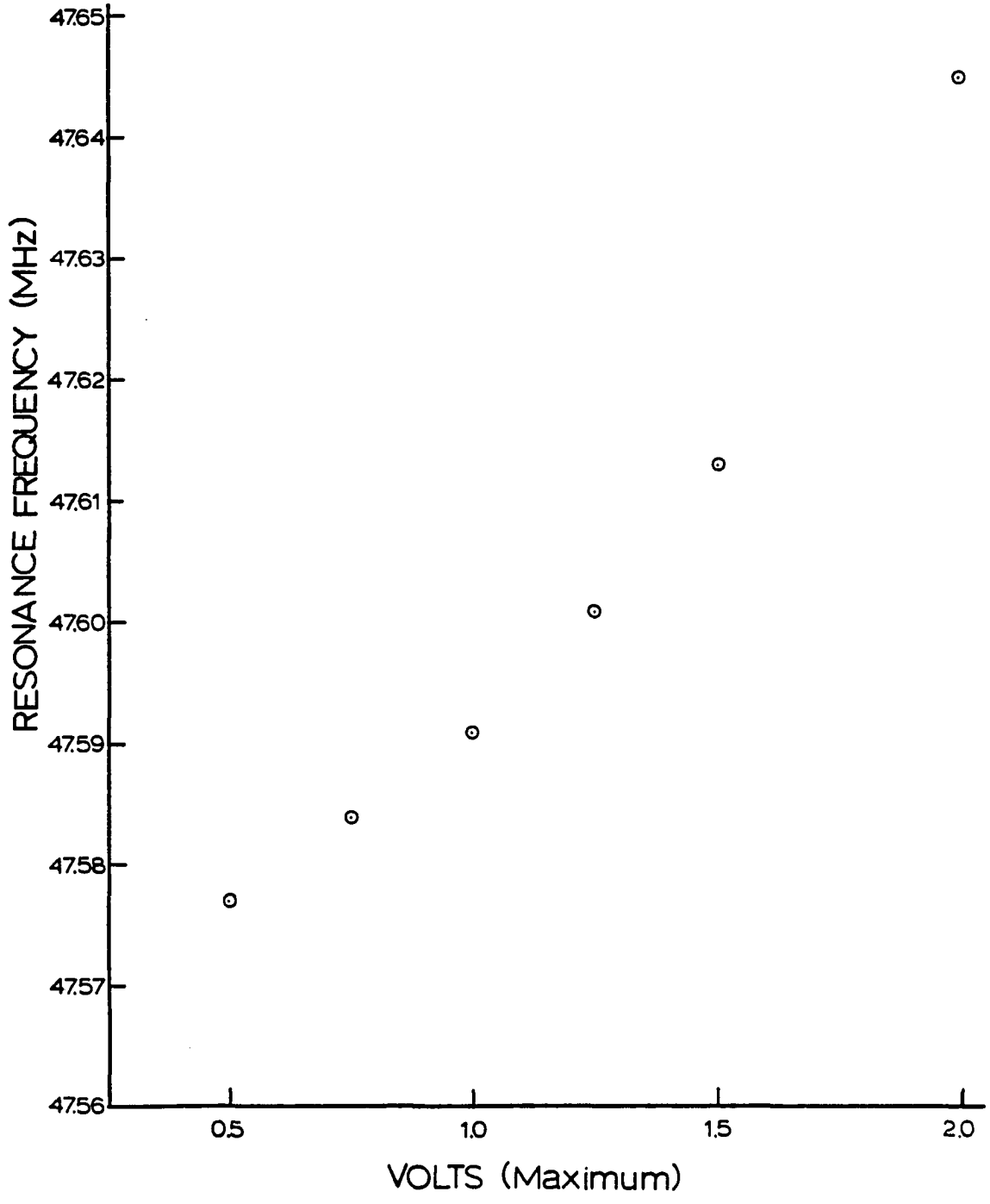
47.65
47.64
47.63
47.62
47.61
47.60
47.59
47.58
47.57
47.56
RESONANCE FREQUENCY (MHz)
0.5
1.0
1.5
2.0
VOLTS (Maximum)

the mode-locker frequency was left at 47.630 MHz, and the RF power was varied to attain the shortest pulse widths and maximum stability. Average mode-locked argon laser powers under these conditions were typically between 350 and 400 mW at 26A operating current.

Mode-locking causes the laser to generate pulses of high peak power and narrow pulse width. Typical peak pulse powers are between 20 and 30 times the average mode-locked power (48). Mode-locked pulses were monitored using an ITL fast photodiode (100 psec risetime) and Tektronix Model 549 Storage Oscilloscope with type 1S1 plug in sampling unit (350 psec risetime). Pulse width measurements from the oscilloscope trace including instrument response were typically ∿650 psec FWHM. From these data, argon laser pulse widths were estimated to be approximately 250 psec FWHM at 514.5 nm.

Only one modification to the commercially obtained mode-locking mount was needed to achieve mode-locked pulses stable within the tolerances required for synchronous mode-locking of a dye laser. A three-piece adjustable coupling flange supplied by Harris Corp., which attached the mode-locker to the argon laser rear end plate, was found to cause pulse to pulse instability in the argon laser output. The play between the threaded sections of the coupling rings made it impossible to make the cavity rigid. The flange was removed, and cavity length adjustment was controlled instead by mounting the mode-locker to a Line Tool Co. Model B translation stage anchored to the optical table.

Before the argon laser was modified, its front and rear cavity mirror

mounts had been spring loaded to three quartz resonator rods. Should temperature changes cause expansion or contraction of the laser components, the low thermal expansion index of quartz would help to retain the optical alignment and cavity length at their original settings. Mounting the mode-locker, which supersedes the rear cavity mirror, to the laser bench defeats the purpose of the quartz resonator rods. Some thermal stability is thus lost, but the overall stability is greatly enhanced in the resulting highly rigid mode-locked cavity, as evidenced through the mode-locked pulse stability seen with the sampling scope.

Dye Laser

A Coherent Inc. Model 590 dye laser, as received, was designed for use as a continuous wave laser. Based on the design of Kogelnik et al. (53), the folded three-mirror cavity was extremely stable. All of the optical components were secured in rigid mounts and attached to Invar rods for high thermal stability.

Figure 2-5 shows the arrangement of the experimental apparatus. Space limitations prevented collinear positioning of the dye laser with respect to the argon pump laser. Originally, two Oriel first surface aluminum coated mirrors were used to direct the argon pulses to the dye laser pump mirror. These mirrors provided ∿90% reflectivity at 514.5 nm and were burned easily by the argon beam. They were replaced by two Newport Research Corp. (NRC) dielectric multilayer coupling mirrors (98% reflectance at 514.5 nm) which have held up well to the argon beam.

Figure 2-5. Diagram of the excitation and detection apparatus used for this work

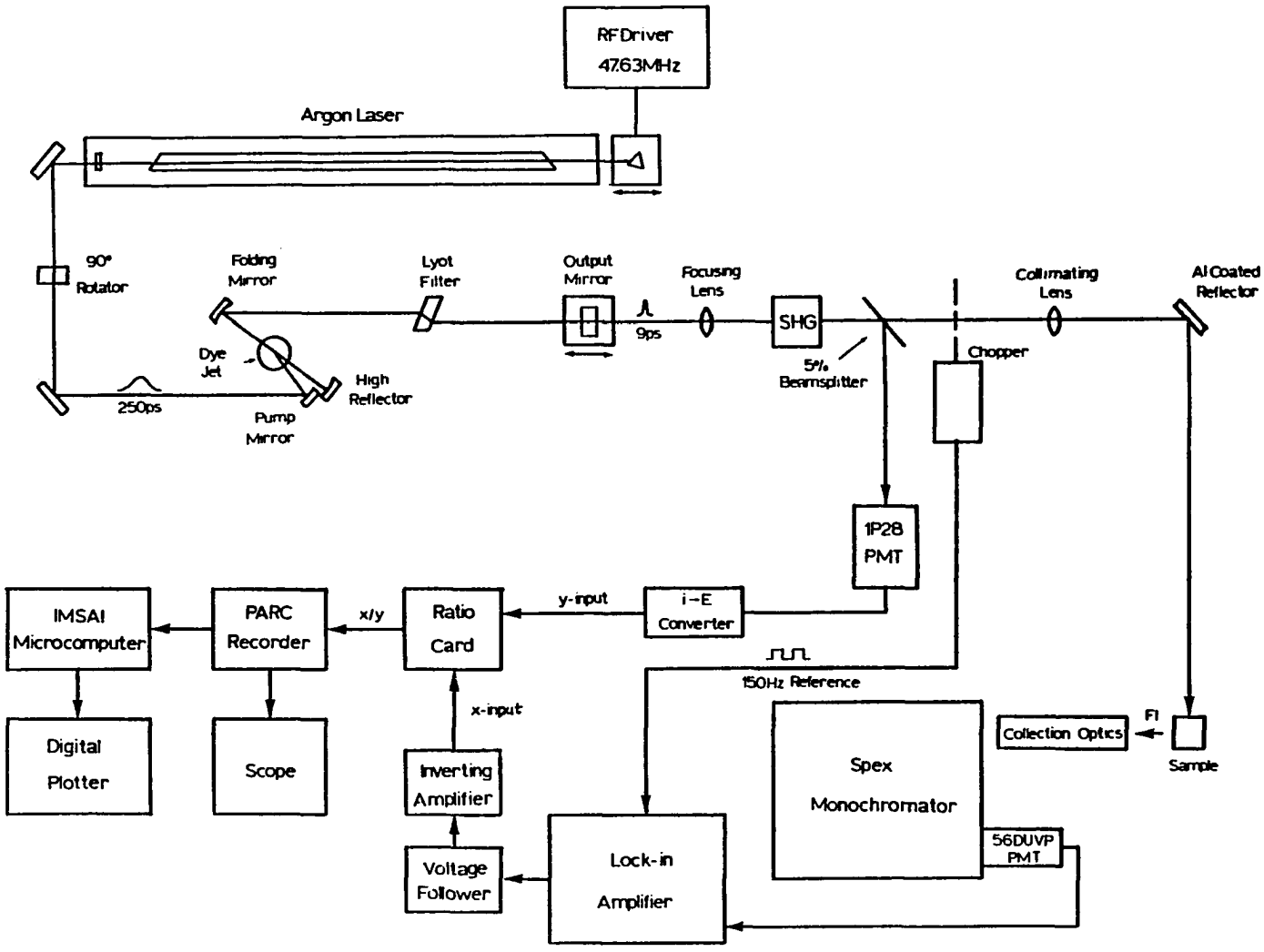
RF Driver
47.63MHz
Argon Laser
90°
Rotator
Folding
Mirror
Lyot
Filter
Output
Mirror
Focusing
Lens
SHG
Collimating
Lens
Al Coated
Reflector
Dye
Jet
High
Reflector
250ps
Pump
Mirror
9ps
5%
Beamsplitter
Chopper
1P28
PMT
IMSAI
Microcomputer
PARC
Recorder
x/y
Ratio
Card
y-input
i-E
Converter
150Hz Reference
Digital
Plotter
Scope
x-input
Inverting
Amplifier
Spex
Monochromator
Collection Optics
FI
Sample
Voltage
Follower
Lock-in
Amplifier
56DUVP
PMT

Cavity mirrors supplied by Coherent Inc. with the dye laser were a standard set for use with rhodamine 6G (rh6G) dye. The output mirror was replaced with a 5% transmitting flat mirror when using an extended cavity configuration. Cavity and pump mirrors were adjusted to focus the dye and argon pulses in the center of the dye jet. The focused dye and pump pulses intersect in the jet stream at $\sim$10° angle, creating a condition of high power densities and good overlap between the dye laser beam and argon pump beam in the active region of the dye.

The gain medium, a 0.25 mm thick stream of 3×10^{-3} M rh6G dye dissolved in ethylene glycol, flows through the jet at approximately 7 m/sec. Oriented at Brewster's angle with respect to the circulating dye pulse, the plane of the jet stream minimizes cavity losses for p-polarized pulses. Brewster windows in the argon laser cavity promote the generation of pump pulses s-polarized relative to the dye jet surface. Siegman et al. (54) have shown that fluorescent emission from rh6G is preferentially polarized in the direction of the pump pulse. Consequently, the s-polarized pulses of the argon laser will stimulate fluorescence experiencing high losses while passing through the 16 Brewster surfaces of one dye laser cavity round trip. To rectify this incompatibility between the two lasers, a 90° rotation plate, purchased from Continental Optics, was inserted into the argon laser beam path. The rotation plate, made of crystalline quartz with its optic axis in the direction of the propagating beam, does not exhibit birefringence, but it is optically active. The specific rotary power γ as a function of wavelength λ is

given by (55)

$$\gamma = (n_R - n_L)\pi/\lambda \ , \qquad (2.3)$$

where n_R and n_L denote the indices of refraction for right and left circularly polarized light, respectively. The absolute angle of rotation of the argon beam is dependent only on wavelength and quartz thickness. The Continental rotation plate was cut to rotate the 514.5 nm argon pulses by 90°, thereby generating dye laser pulses with minimal round trip cavity losses.

As mentioned previously, one of the attractive features of a dye laser is its broad tunability. In our case, rh6G will experience net gain from 565 to 635 nm, a spread much larger than the bandwidth limit of the dye pulse. Without a mechanism for tuning the output of the dye laser, however, it will tend to oscillate at the wavelength of the mode with the highest gain (49). To achieve lasing throughout the rh6G gain curve, the cavity must be biased to provide the highest gain at the wavelength desired.

The Coherent 590 dye laser utilizes a three-plate birefringent (Lyot) filter as its tuning element. The frequency which lases depends on the rh6G gain curve and the transmission characteristics of the Lyot filter. Tuning has been smooth and continuous over the entire lasing region. The cavity requires no realignment with changing frequency, and remains stable over long periods of time.

The concept and design of the Lyot filter are quite elegant. Each

plate of the filter is crystalline quartz with its optic axis in the plane of the crystal. All three optic axes are aligned with one another and the normal to these axes is at Brewster's angle θ relative to the cavity axis of the dye laser (Figure 2-6).

Quartz, a birefringent material, will have two values of refractive index for light at any angle of incidence. The phase difference δ between an e-ray and an o-ray is (48)

$$\delta = \frac{2\pi}{\lambda} d\ (n_o - n_e) \tag{2.4}$$

where d is the distance of penetration through the crystal, n_o is the ordinary index of refraction, and n_e is the extraordinary index of refraction. Wavelengths for which $\delta = 2n\pi$ will be unaffected by the filter. All other wavelengths will experience varying degrees of phase delay, causing the incident p-polarized light to emerge from the crystal as a combination of s- and p-polarized light. The s-polarized light will experience losses at subsequent Brewster surfaces. The thicknesses and orientations of the component plates are chosen so there will be only one frequency within the dye gain curve for which polarization will be unaffected (Figure 2-7) (47). Rotating the plates about an axis normal to the crystal surface ϕ changes n_e, and consequently the wavelength at which the phase difference equals a multiple of 2π.

Synchronous mode-locking requires that the round trip transit time of the circulating dye pulse match the interpulse spacing between argon pump pulses. The Coherent dye laser was modified to produce this synchrony by

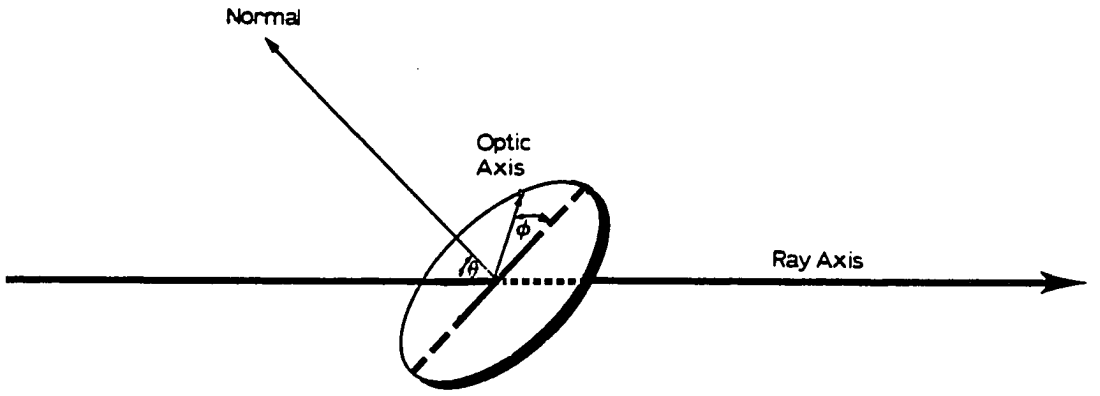

Figure 2-6. Quartz plate orientation for Lyot filter. The normal to the crystal plate is tilted to Brewster's angle Θ from the ray axis. Rotation of the optic axis about the normal is measured as Φ, the angle between the optic axis and the plane containing the ray axis and crystal normal

Figure 2-7. Qualitative transmission curves for the quartz plates comprising the Lyot filter: (a) thin plate, (b) intermediate plate, (c) thick plate, and (d) composite. Φ is set at 50° and θ is 32.8°

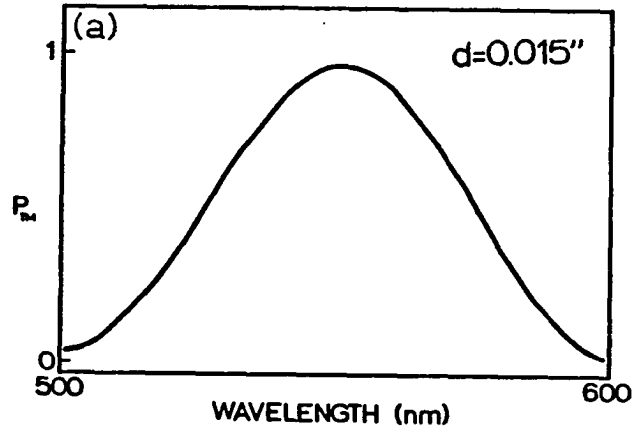
(a)
d=0.015"
1
0
500
600
WAVELENGTH (nm)

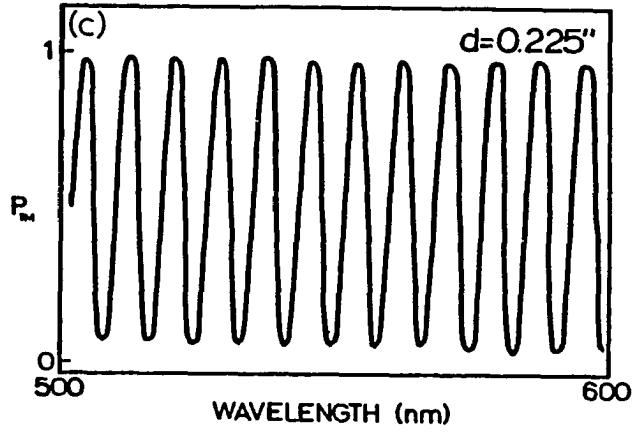
(c)
d=0.225"
1
0
500
600
WAVELENGTH (nm)

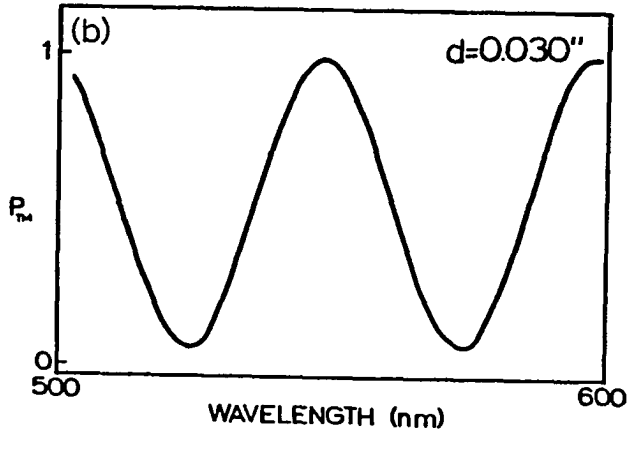
(b)
d=0.030"
1
0
500
600
WAVELENGTH (nm)

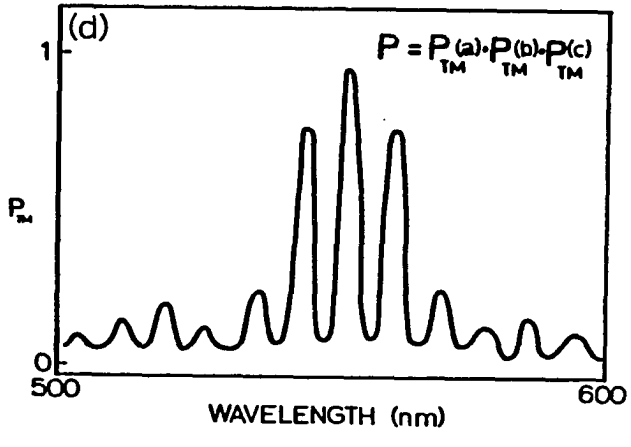
(d)
P = P(a)·P(b)·P(c)
1
0
500
600
WAVELENGTH (nm)

inserting the output mirror into an Oriel Model 1793 mount attached to a precision translation stage (Model M, Line Tool Co.). Adjustment of the translation stage provided the precision adjustment needed to cavity match the two lasers.

The rh6G jet stream acts as a temporal shutter in the dye laser, much as the mode-locking crystal does in the argon laser. Figure 2-8 shows that toward the end of the 250 psec argon pump pulse, the rh6G dye achieves net gain. At exact synchrony, the circulating dye pulse arrives at the jet when the gain crosses the threshold ($\Delta L = 0$). Together, the high stimulated emission cross section for rh6G (56) and the intensity of the incident dye pulse cause the gain to saturate and drop below threshold within a few picoseconds. The time-dependent inverted population of the dye molecules acts both to amplify the dye pulse and to set its temporal width.

McDonald et al. (57) have shown that the period between dye pulses emerging from the dye laser is equal to the interval between argon pulses, even when the round trip transit time of the dye is not equal to the 95.260 MHz pumping frequency:

$$\frac{c}{2L} \neq \nu_{pump}. \tag{2.5}$$

Figure 2-9 depicts qualitatively the results of Millar and Zewail (46) regarding the effect of cavity length mismatch on pulse properties. These properties are clearly asymmetric about $\Delta L = 0$ (47,58,59). The region of practical interest for our work concerns dye cavity lengths slightly

Figure 2-8. Synchronous pumping of the dye laser. In (a), the evolution in the gain of the rhodamine 6G dye is shown relative to the arrival of the argon pump pulse. The return of the dye pulse (b) depletes the dye gain within a few picoseconds after the dye gain crosses the threshold

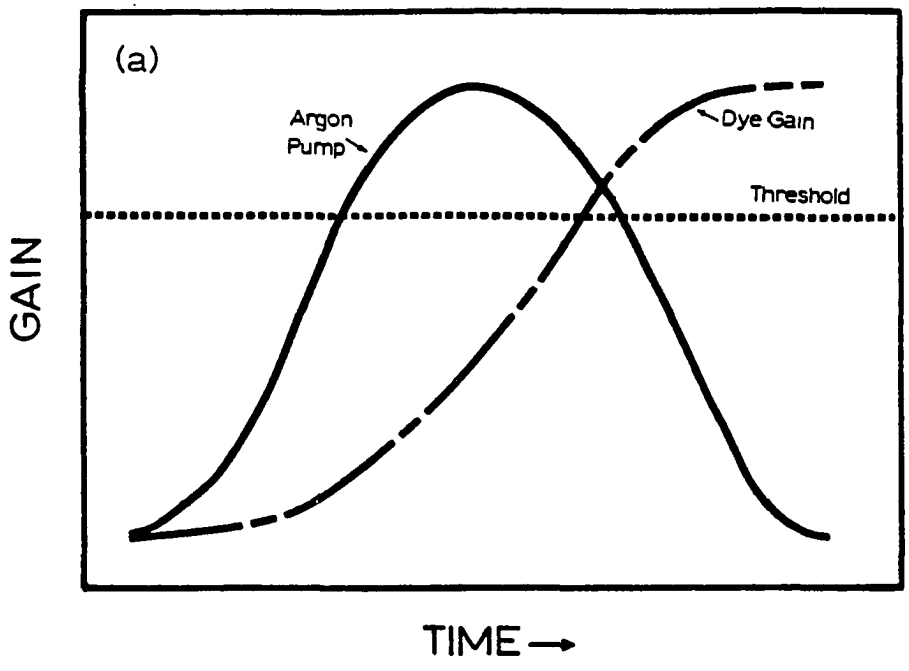
(a)
Argon
Pump
Dye Gain
Threshold
GAIN
TIME

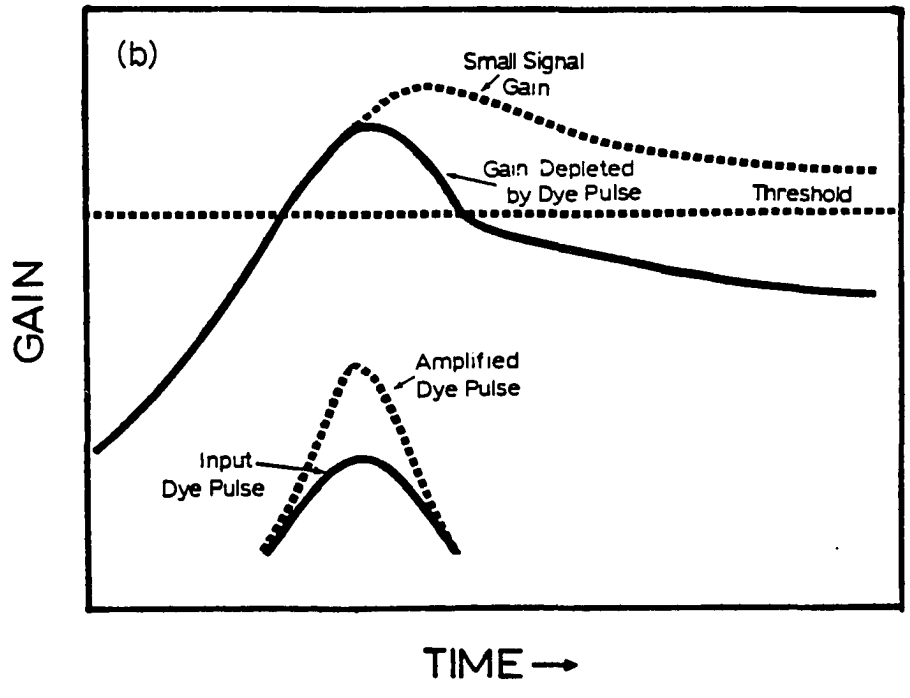
(b)
Small Signal
Gain
Gain Depleted
by Dye Pulse
Threshold
Amplified
Dye Pulse
Input
Dye Pulse
GAIN
TIME

Figure 2-9. Effect of cavity mismatch on dye pulse properties. The pulse energy and SHG power peak when the dye cavity is slightly longer than the argon cavity (a), whereas the pulse duration is shortest when the two cavities are matched (b)

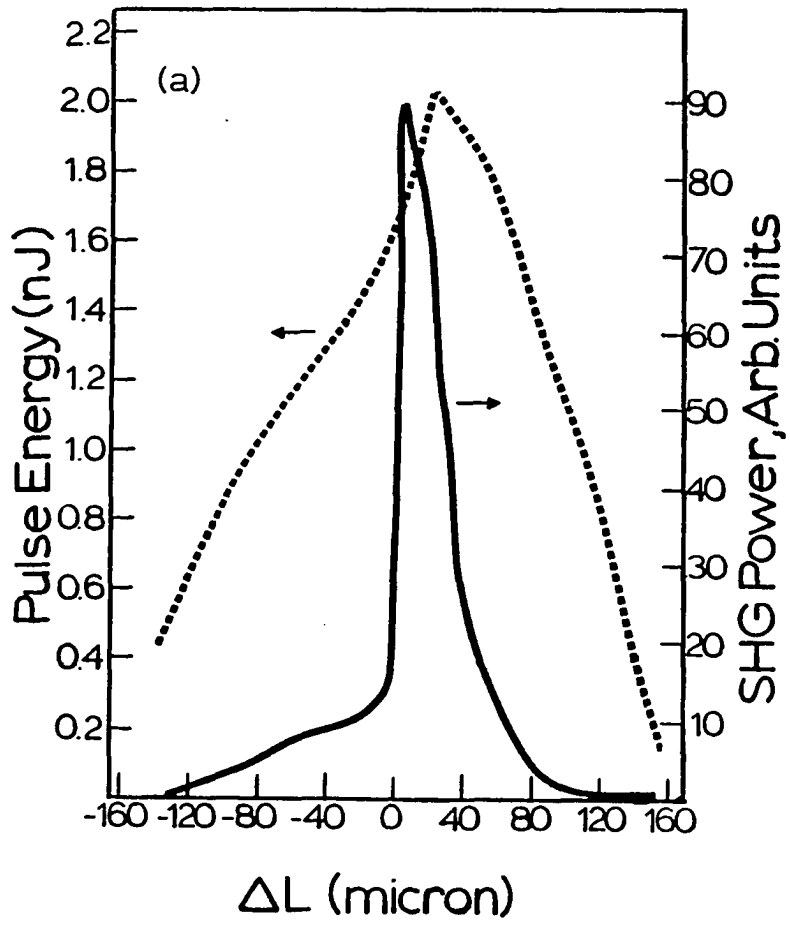
(a)
Pulse Energy (nJ)
SHG Power, Arb. Units
ΔL (micron)
2.2
2.0
1.8
1.6
1.4
1.2
1.0
0.8
0.6
0.4
0.2
90
80
70
60
50
40
30
20
10
-160 -120 -80 -40 0 40 80 120 160

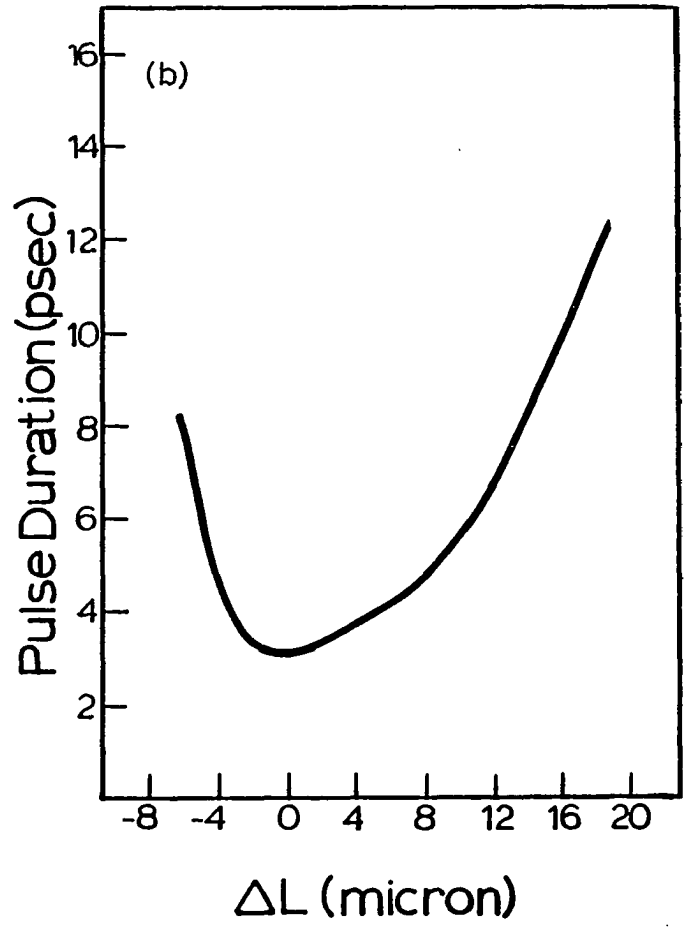
(b)
Pulse Duration (psec)
ΔL (micron)
16
14
12
10
8
6
4
2
-8 -4 0 4 8 12 16 20

longer than the pump laser. Although the pulse duration is shortest when the laser cavities are perfectly matched, the pulse energy peaks when the dye cavity is approximately 25 microns longer than optimum. Second harmonic power, being a function of both pulse energy and pulse duration, peaks at a cavity setting ~10 microns longer than the optimum length (46,57,58). Second harmonic power shows a much sharper dependence on cavity length than does pulse energy.

In this work, the dye laser output is frequency doubled and treated as a continuous wave source. Consequently, dye pulses only need to be temporally narrow to the limit where maximum SHG is produced. For experimental applications, all cavity parameters are adjusted to optimize the second harmonic power.

An autocorrelation trace of the dye laser output is presented in Figure 2-10. The dye cavity was adjusted to optimize the SHG intensity prior to performing the autocorrelation. An 8.75 psec, FWHM pulse width was measured for the dye laser fundamental. At this cavity setting, with the dye laser tuned to 590 nm, mode-locked conversion efficiencies of 21% were routinely observed. At 24A of argon laser tube current, this corresponds to average dye laser and argon laser powers of 48 and 232 mW, as measured by a Coherent Model 210 power meter.

Figure 2-10. Autocorrelation trace of the pulsed output from the synchronously mode-locked dye laser

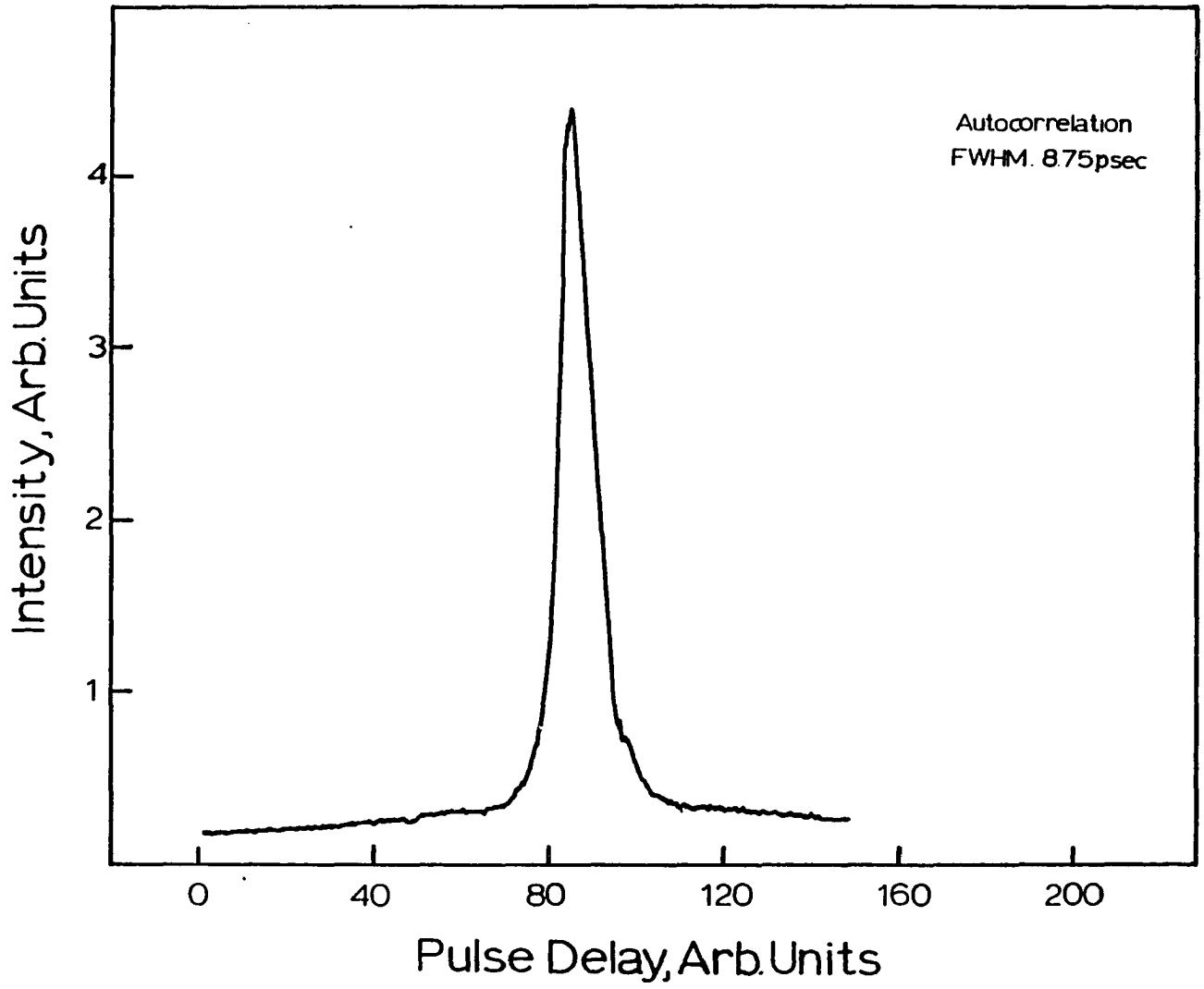
Autocorrelation
FWHM. 8.75psec
Intensity, Arb. Units
1
2
3
4
0
40
80
120
160
200
Pulse Delay, Arb. Units

Second Harmonic Generation

$S_1 \leftarrow S_0$ vibronic transitions from the ground state of aniline require pump wavelengths shorter than 294 nm. Tunability in this wavelength region is obtained by second harmonic generation (SHG) of the dye laser fundamental using an angle-tuned $LiIO_3$ crystal. The crystal, purchased from Cleveland Crystals Corp., is 8 x 8 x 2 mm and is cut for type I SHG.

A Lasermetrics Model S-2B KDP crystal was used for second harmonic generation prior to the acquisition of the $LiIO_3$ crystal. The KDP crystal, cut for type I SHG, measured 14 x 14 x 12.5 mm and was also angle-tuned. Although the $LiIO_3$ crystal was used in all experiments, the properties of both crystals will be compared and discussed whenever appropriate.

The nonlinear coefficient d_{ij} is related to the ability of an electric field to induce a polarization in a crystal by (60)

$$\underline{P}_{NL} = \underline{\underline{d}}\ \underline{E}\ \underline{E}\ , \tag{2.6}$$

where $\underline{P}_{NL}$ is the dielectric polarization, $\underline{\underline{d}}$ is the second order polarization tensor, and $\underline{E}$ represents the electric field vector of the laser beam in the crystal. For type I phase matching, the only nonzero components of the polarization tensor are d_{31} and d_{36} for $LiIO_3$ and KDP, respectively (61). Kleinman (60) has shown that SHG intensity is functionally dependent on $d_{ij}^2 \sin^2 \Theta_m$. The most attractive feature of $LiIO_3$ relative to KDP is its large nonlinear optical coefficient: $d_{31}(LiIO_3)=11.9\ d_{36}(KDP)$

(62). For type I SHG, the phase matching angle Θ_m is equal to (63)

$$\Theta_m = \arcsin [((n_o^{\omega})^{-2} - (n_o^{2\omega})^{-2})/((n_e^{2\omega})^{-2} - (n_o^{2\omega})^{-2})]^{\frac{1}{2}}, \qquad (2.7)$$

where

n_o^{ω} = ordinary refractive index of fundamental,

$n_o^{2\omega}$ = ordinary refractive index of second harmonic,

$n_e^{2\omega}$ = extraordinary refractive index of second harmonic.

For a fundamental wavelength of 600 nm, θ_m (KDP) is 60.46° and θ_m ($LiIO_3$) is 62.8°. Doubling crystals were placed in an Oriel Model 1450 adjustable mirror mount which permits fine tuning of the crystal orientation to the phase matching angle.

Other factors affecting the overall SHG intensity such as focusing effects, crystal thicknesses, and light absorption by the crystals, are considered in the Appendix. A final comparison of the doubling efficiencies for KDP and $LiIO_3$ in the appendix indicates that the $LiIO_3$ crystal will be approximately 10 times more effective than KDP for producing 300 nm frequency doubled light from a 600 nm laser fundamental.

Focusing the laser fundamental within the $LiIO_3$ crystal increases the energy density, which can improve SHG efficiency. The 588 nm input beam from the dye laser was focused with a 6 cm focal length biconvex glass lens, and the crystal was positioned to produce maximum SHG. A 15 cm focal length biconvex quartz lens was adjusted to recollimate the fundamental and second harmonic output.

A quartz beamsplitter reflected ∿5% of the doubling crystal output and directed it to a 1P28 photomultiplier tube. With the photomultiplier power supply (Model V303BEZ, Kepco) set at -500 V, and the reflected laser fundamental blocked by a Corning 754 filter, the second harmonic was observed with a Hewlett Packard (HP) Model 410C voltmeter. The signal gave a relative SHG power readout, which was used to optimize cavity parameters and to normalize the sample fluorescence to the pumping intensity.

Several precautions were taken to prolong the life of the $LiIO_3$ crystal. Since $LiIO_3$ absorbs strongly at 294 nm, there is a potential for damage to the crystal due to thermal effects. For this reason, the laser fundamental was blocked whenever data were not being recorded. Another source of potential crystal damage results from the hygroscopic nature of $LiIO_3$. To retard the deterioration of the crystal from atmospheric water vapor, it was stored in a desiccator when it was not being used. After seven months of regular use, there is no visible sign of damage to the crystal.

Sample Preparation

Aniline was obtained from the Aldrich Chemical Company with a stated purity of 99.9+%. Twice distilled, a small amount of this aniline was stored under vacuum at room temperature and kept in a dark environment. Prior to each sample preparation, the aniline was degassed using the freeze-pump-thaw technique. Coleman grade carbon dioxide, purchased from Matheson, with a stated purity of 99.99+%, was used as received.

The vacuum apparatus was comprised of three major components: the vacuum pumps, manifold, and pressure gauge. The pumping system consisted of an oil diffusion pump (Type PVMS-30, CVC Products) and a roughing pump which could be connected either in series or in parallel to the vacuum manifold. Two liquid nitrogen cooled traps, inserted in line between the manifold and pumps, condensed and collected gases diffusing into this region of the vacuum line. An MKS Baratron Type 220B pressure gauge with a 100 torr sensing head detected the pressure difference between the manifold and a 10^{-7} torr reference cavity. This difference was measured as a change in capacitance, and converted to a manifold pressure readout on a Keithley Model 177 microvoltmeter. Pressure readings should be accurate to within a few percent in the range 10^{-4}-30 torr. It was presumed that the oil diffusion pump drew a vacuum down to $\sim 10^{-6}$ torr, although no confirming measurements were possible with our apparatus, which lacked an ionization gauge. FETFE o-rings, purchased from Ace Glass, were used where any o-ring material was needed due to their inertness to aniline. A leak rate of 8.2 mtorr/hour was measured for the manifold. The small amount of impurities introduced into the manifold, however, have had no detectible effect in fluorescence experiments.

Teflon sleeves were used to provide an air tight seal between the fittings of the cold traps and the vacuum line. Unfortunately, these sleeves also served to permanently join the fittings together. The trap nearest to the diffusion pump was broken while it was being removed for

cleaning. It was replaced by a trap with a grease fitting to facilitate future removal. The remainder of the vacuum line was kept grease and mercury free. The second cold trap should prevent any grease vapors from entering into the manifold (64).

The fluorescence cell was composed of an Ace Glass high vacuum stopcock sealed to the glass to quartz graded seal tube on a Hellma cuvette. The walls of the cell were fused silica, and the internal pathlength was 1.0 cm. The stopcock contained a semi-needle valve teflon plug with FETFE o-rings, capable of holding a vacuum down to 10^{-7} torr. There were three fluorescence cells used in these experiments. One of these was evacuated and used as a background cell.

Sample preparation proceeded as follows. A fluorescence cell was attached to the manifold and evacuated overnight. The vacuum line was then flushed twice with CO_2 and the system evacuated once more. The manifold was isolated from the pumps, and degassed aniline was exposed to the vacuum chamber until a steady pressure reading of 0.42 torr was attained. Pressure readings may not be a completely accurate indicator of the quantity of aniline in the chamber due to aniline adsorption to the glass walls of the manifold. Aniline pressures recorded could be up to 20% low in some samples. Once the final aniline pressure was reached, the aniline reservoir was isolated from the manifold and CO_2 added to the chamber through a Nupro needle valve. The carbon dioxide was added slowly until the desired final pressure was reached. After allowing one hour for diffusive mixing of the gases, the stopcock on the fluorescence

cell was closed off. All gas samples were prepared the day they were to be used to insure that no contaminants had leaked into the cell with time.

Fluorescence Detection

The quartz lens which collimated the second harmonic output of the $LiIO_3$ crystal was moved to a position 29 cm from the crystal which was 14 cm beyond the focal length of the lens. This change resulted in a beam focus slightly beyond the fluorescence cell. The diameter of the converging beam in the cell was roughly 500 microns. When the beam was focused too tightly, pits developed on the walls of the cuvette. A one-inch diameter aluminum coated front surface mirror, purchased from NRC and set in an Oriel Model 1793 mirror mount, provided precise positioning of the UV pump beam into the sample cell.

Aniline fluorescence was collected and focused into the monochromator using a pair of biconvex fused silica lenses. The first, a collection lens, was 3.6 cm in diameter with a focal length of 5 cm. It was positioned 5 cm from the fluorescence origin to collimate the light. The focusing lens had a diameter of 5 cm and a 15 cm focal length (f/4.2). Placed 15 cm from the monochromator, this lens imaged the fluorescence line source onto the entrance slit of the monochromator. Both lenses were translated slightly to maximize the observed fluorescence signal. Using a f/4.2 focusing lens with an f/6.8 monochromator results in a spillover of $\sim$3.5 cm on each side of the first mirror inside the monochromator. Although there is some loss of detectable fluorescence

intensity, the signal strength is still more than adequate for this work.

A 0.75 meter, Czerny-Turner type monochromator (Model 1400-11, Spex) was used to spectrally resolve aniline fluorescence. The Spex is a double monochromator, which can be easily converted to a single monochromator when desired. The grating initially used was blazed for 1600 nm in first order. The ruled area of the grating was 102 x 102 mm and contained 600 grooves/mm. Scanning was controlled either by hand or through a variable speed dc motor geared to the grating sine drive.

A blazed grating is designed to concentrate spectral energy into one order. Figure 2-11 shows that a grating blazed at 1600 nm in first order will also be efficient for concentrating 267 nm and 320 nm light into 6th and 5th orders, respectively. At wavelengths intermediate to these two values, the light intensity will be partitioned among several orders (65,66), resulting in less selective diffraction and a smaller output signal. Fluorescence bands observed in this work lie between 290 and 302 nm, an inefficient diffraction region for the grating. Although fluorescence intensities measured in 6th order were stronger than those measured in 5th order, the output signal intensities were generally very weak. For this work, the use of a grating blazed at 1600 nm in 1st order is counterproductive to attainment of efficient fluorescence detection.

A single Spex diffraction grating, with λ_B = 300 nm in first order and n = 1200 grooves/mm, was obtained and utilized in the monochromator. Since only one such grating could be located, the Spex was utilized as a single monochromator. These modifications produced an increased diffrac-

Figure 2-11. Efficiency of grating blazed at 1600 nm in 1st order. At 267 nm (a), nearly all of the energy diffracted by the grating goes into the 6th order. Similarly for 320 nm (c), the energy is diffracted into the 5th order. Wavelengths between these two limits (b) will have energy diffracted into several orders depending on the position of the envelope curve

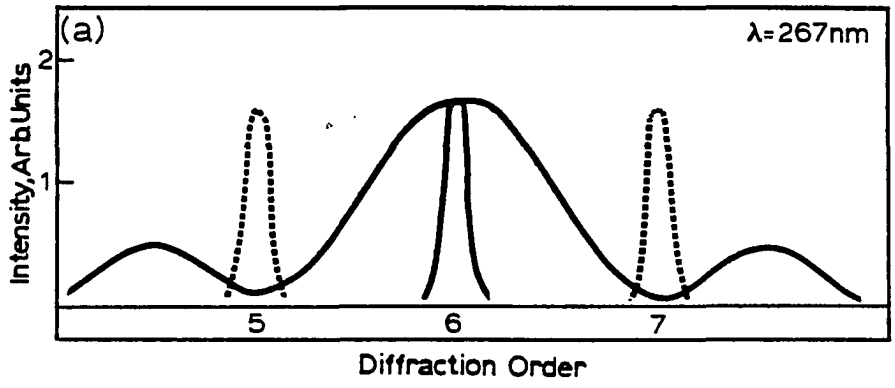
(a)
λ=267nm
Intensity,ArbUnits
2
1
5
6
7
Diffraction Order

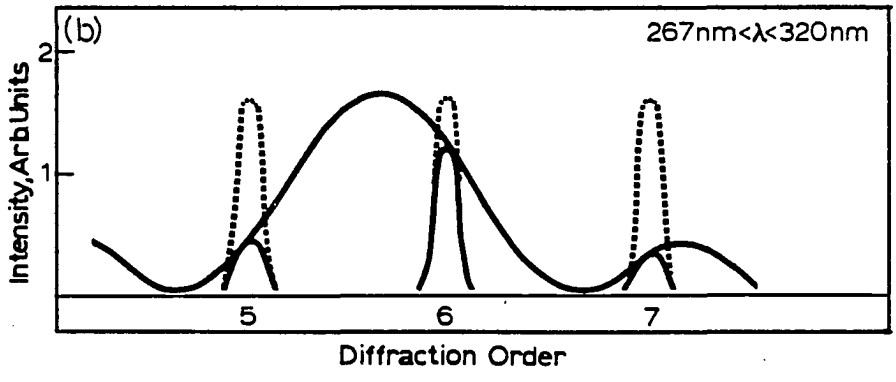
(b)
267nm<λ<320nm
Intensity,ArbUnits
2
1
5
6
7
Diffraction Order

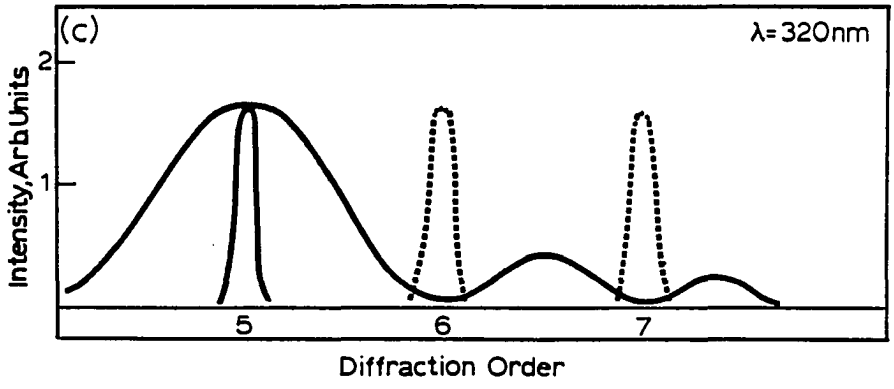
(c)
λ=320nm
Intensity,ArbUnits
2
1
5
6
7
Diffraction Order

tion efficiency at the expense of resolution. Linear dispersion was calculated to be 1.1 nm/mm for the new grating in a single monochromator. For the original gratings in a double monochromator, linear dispersion is reduced to 0.17 nm/mm. The closest aniline fluorescence peaks to be resolved are separated by ∿0.5 nm and have FWHM of roughly 0.2 nm. Using the new grating and slit settings of 75 microns, corresponding to a band pass of 0.0825 nm, these peaks were resolved. This configuration was used in all experiments.

Figure 2-12 illustrates the working principle of a grating sine drive (67). The lead screw is designed to vary the angle Θ to produce a linear relationship between the wavelength reading and sin Θ, according to

$$k\lambda = 2d \sin \Theta \cos \Phi, \tag{2.8}$$

where for our grating: d = 833.33 nm/groove, k = 1 (first order), and cos Φ = 0.9928.

Using a low pressure mercury pen lamp as a calibration source, the relationship between the Spex readout (λ_s) and the actual wavelength (λ_a) passing through the monochromator were shown to be nonlinear. The Spex dial reading was set to zero nm for 0th order specular reflection and slits were closed to 25 microns. Variation between λ_a and λ_s followed the relationship

$$\lambda_a = \frac{\lambda_s}{2} + c(\lambda_s) \tag{2.9}$$

where c is a function of wavelength varying from 5.8 nm at λ_s = 549 nm

Figure 2-12. Working principle of a grating sine drive. Rotation of the lead screw, either by hand or through the variable dc motor, provides a wavelength readout which varies linearly with sin θ

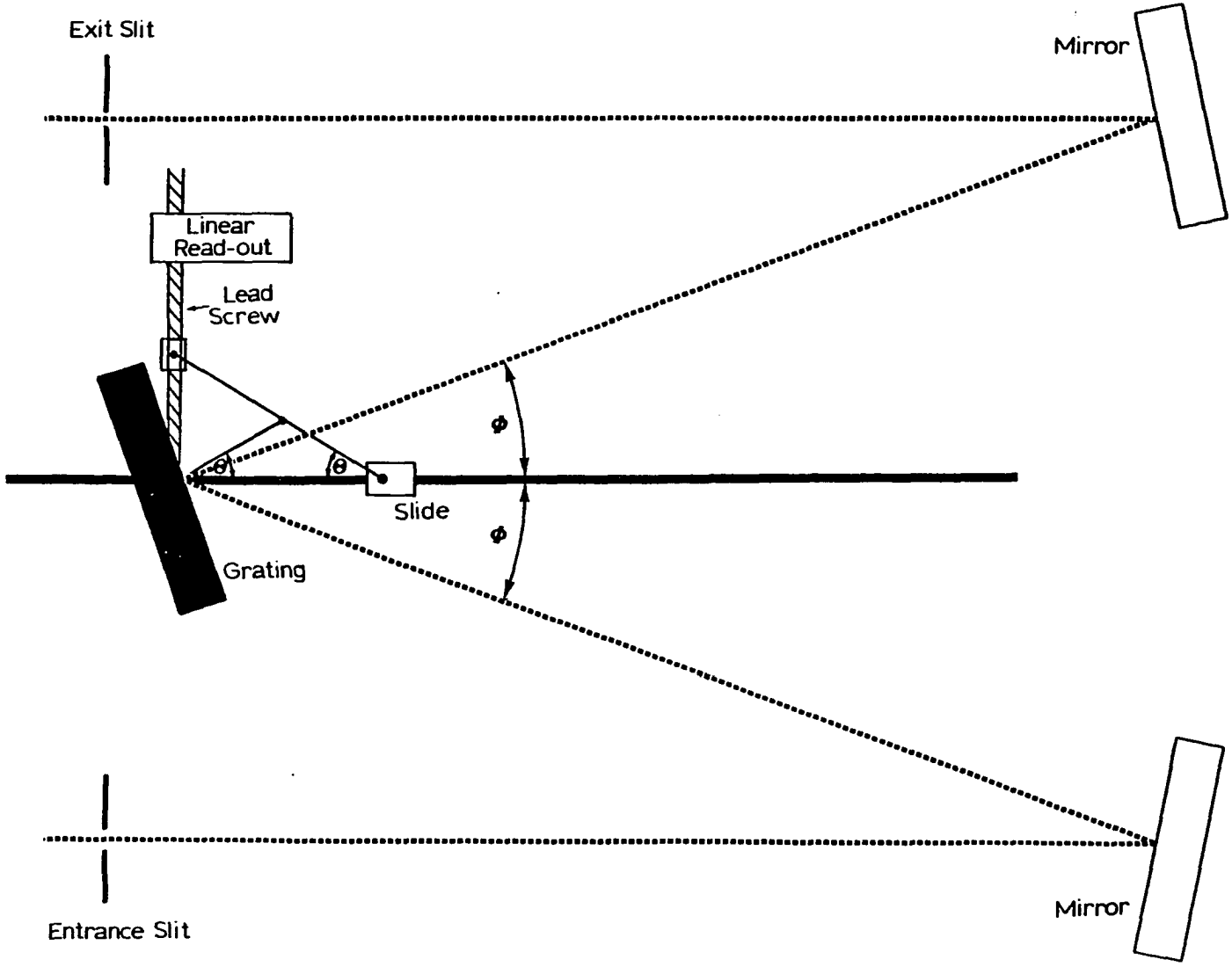
Exit Slit
Mirror
Linear
Read-out
Lead
Screw
Φ
θ
θ
Slide
Φ
Grating
Entrance Slit
Mirror

to 8.9 nm at λ_s = 714.8 nm.

After some time, it was observed that a plot of $\lambda_s/2$ *vs.* $c/(\lambda_s/2)$ produced a linear function. Using twelve mercury lines between 292 nm and 366 nm, a slope m and y-intercept b were obtained. Solving for c yields

$$c = (^{\lambda_s}/2)\ [\frac{(\lambda_s/2)-b}{m}]. \tag{2.10}$$

Inserting equation 2.10 into equation 2.9 yields

$$\lambda_a(\text{calc}) = (\frac{1}{4m})\ \lambda_s^2 + (\frac{1}{2} - \frac{b}{2m})\ \lambda_s, \tag{2.11}$$

where $b = 1.83 \times 10^2$ nm and $m = 2.18 \times 10^4$ nm.

The error between λ_a calculated from an input λ_s, and the real value of λ_a (λ_a(lit)), determined from a reference spectrum (68), is less than 0.03 nm for all lines in this region (Table 2-1). Comparison of λ_a(calc) to literature values (45) for aniline peaks has shown a similar correspondence.

A cursory inspection of the Spex drive mechanism provided no clues to the cause of the sine drive malfunction. Since correct peak assignments could still be made using equation 2.11, the monochromator was used in this unoptimized state. All aniline fluorescence bands were assigned literature values (32,45) upon positive identification of the corresponding transition.

An Amperex Type 56DUVP photomultiplier (PMT) was mounted at the exit slit of the monochromator and used for all work reported. It replaced an

Table 2-1. Monochromator calibration using a mercury line source. All values are in nm

λ_s	λ_a(lit)	c	λ_a(calc)	λ_a(calc)-λ_a(lit)
572.72	292.5410	6.18	292.52	-0.03
580.91	296.7280	6.27	296.75	0.03
591.37	302.1498	6.46	302.17	0.02
591.74	302.3475	6.48	302.36	0.01
592.11	302.5606	6.50	302.56	-0.01
592.47	302.7487	6.51	302.74	-0.01
611.45	312.5668	6.84	312.57	0.00
612.55	313.1549	6.88	313.14	-0.02
612.60	313.1839	6.89	313.17	-0.02
653.06	334.1477	7.62	334.15	0.01
712.46	365.0153	8.79	365.03	0.01
713.31	365.4836	8.83	365.47	-0.01

Amperex 56TVP PMT, which was to be used originally.

In most photomultipliers, the short wavelength cutoff is primarily a function of window material. The 56DUVP has a polished optical quartz window that gives it a sensitivity extending into the UV. The 56TVP, intended for work in the red and infrared, has a glass window. Although absorption by the glass causes spectral sensitivity to drop sharply below 300 nm, there is adequate signal at 290 nm to record spectra. Sample spectra from each tube are compared in Figure 2-13. Although it was expected that the gain would be higher for the 56DUVP, judged by performance specifications, experimentally they were observed to be comparable. At -1800V, the dark currents measured were 3nA and 40nA for the 56DUVP and 56TVP, respectively. The 56DUVP photomultiplier was selected because its signal to noise ratio was an order of magnitude improvement over that of the 56TVP.

The 56DUVP was run with the power supply (Model 1570, Power Designs Inc.) voltage set between -1500V and -1650V for most of our work. It is important to allow appropriate time for tube warmup before use. Normally, -1500V is supplied to the photomultiplier for one hour. This ensures that the gain on the tube has settled prior to recording spectra.

The output from the 56DUVP was transmitted to the signal input of a Princeton Applied Research Corp. (PARC) Model 122 lock-in amplifier. This signal was tied to a 150 Hz carrier frequency by amplitude modulation of the UV pump beam with a chopper. The beam chopper was built from a 30 Hz Globe motor and a five-blade chopping disk constructed in the

Figure 2-13. Comparison of aniline fluorescence spectra recorded using (a) 56TVP photomultiplier tube, and (b) 56DUVP photomultiplier tube

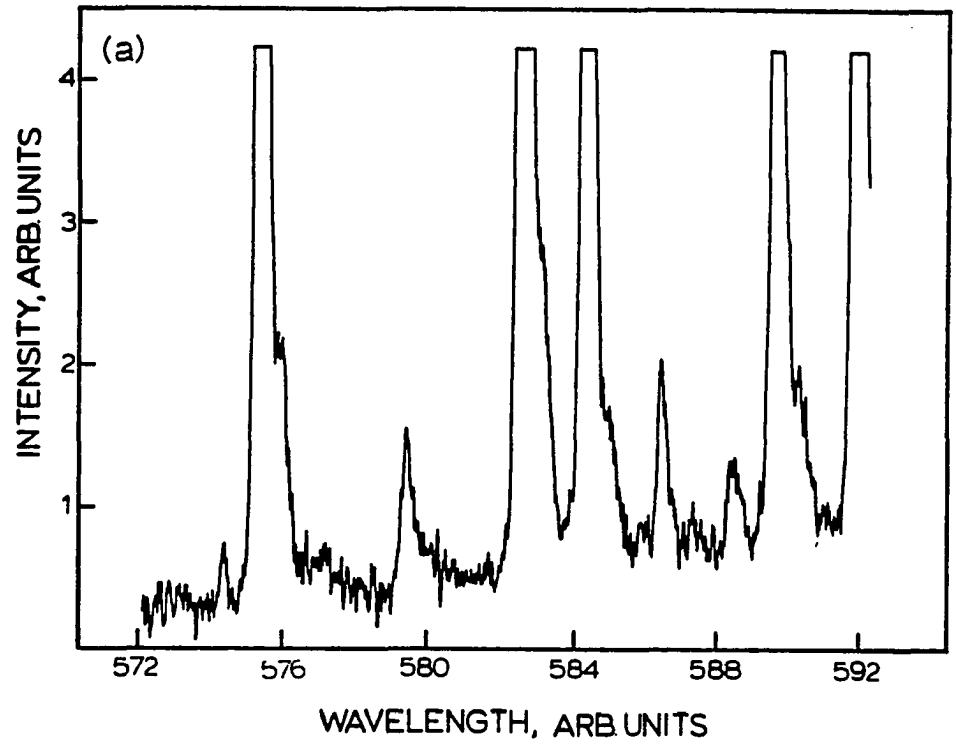
(a)
INTENSITY, ARB. UNITS
1
2
3
4
572
576
580
584
588
592
WAVELENGTH, ARB. UNITS

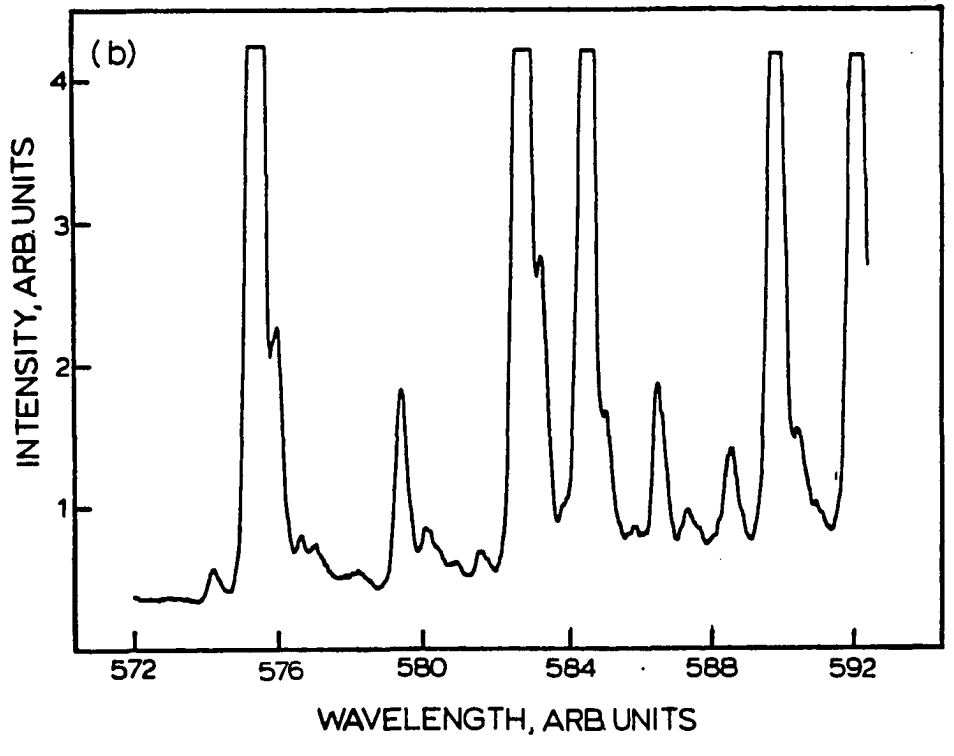
(b)
INTENSITY, ARB. UNITS
1
2
3
4
572
576
580
584
588
592
WAVELENGTH, ARB. UNITS

machine shop. A photodiode-LED pair, separated by the rotating chopper blades, generated a 150 Hz square wave used as a reference signal in the lock-in amplifier. Phase shifting was variable through external controls to achieve phase matching between signal and reference waves.

The photomultiplier gain was adjusted to keep all input signals to the lock-in amplifier below 20 mV. Normally, five or six scans were taken of each gas sample, at increasing lock-in sensitivities. Peak height ratios were not equivalent to the inverse ratios of full scale sensitivities for these plots, however. Corrected scale factors were calculated for each plot and were used to normalize all peak intensities to the least sensitive scan.

The range of the output signal at each sensitivity varied from 0 to -10 volts, full scale. A one-second RC time constant was chosen for the output filter of the lock-in amplifier as the best choice to balance system response time with noise suppression. The output was passed through a voltage follower, to buffer the lock-in, and then through an inverting amplifier with variable gain between 0.1 and 1.1. Typically, the inverting amplifier was adjusted to output a maximum signal of 5 volts, which went to the x-input of an Evans Associates ratio card.

The gain on the 1P28 photomultiplier was adjusted to give a dye laser SHG signal of approximately 0.7 μA. After passing through a current to voltage converter, the 3 volt signal went to the y-input of the ratio card. The x/y voltage output of the ratio card represented a fluorescence signal normalized to the SHG intensity.

Data were stored temporarily in a PARC Model 4101 scanning recorder. The PARC recorder had 1023 bytes of memory which were filled at a scanning rate of approximately 10 points/second. Input signals from the ratio card should be kept under 2 volts to prevent saturation of the peak in the recorder. An HP Model 120B oscilloscope simultaneously displayed a trace of the input data as the information was stored in the recorder. For permanent storage, the data were transferred to an IMSAI 8080 microcomputer, where a data file was created and stored on an 8-inch floppy disk. A Houston Instrument DMP-3 digital plotter, interfaced to the computer, provided a hard copy of the spectrum as it appeared on the oscilloscope trace.

Modifications of Apparatus for Photon Counting

The experimental conditions adopted to investigate the excitation transport theories of Gochanour, Andersen and Fayer (69) and Loring and Fayer (70) were different from the conditions used to study the vibrational relaxation pathways of aniline in the S_1 electronic state. Taking advantage of the pulsed output of the synchronously pumped dye laser and utilizing photon counting detection, time-resolved fluorescence decays of the dyes rhodamine 3B perchlorate (rh3B) and rhodamine 590 chloride (rh6G) were collected. The agreement between the fits of decays derived from the excitation transport theories to the observed fluorescence decays were used to infer the extent to which the transport theories were valid.

In the photon counting mode, the number of anode pulses produced by a phototube is proportional to the number of fluorescence photons impinging on the tube's photocathode. Each anode pulse is detected by the time-to-amplitude converter (TAC). The difference between the arrival time of an anode pulse and a reference signal is measured by the TAC, which generates a pulse whose amplitude is proportional to the temporal delay. The multichannel analyzer (MCA) associates a channel number with the pulse amplitude from the TAC, and the number of counts in that channel is incremented by one. After many excitation cycles, a histogram is accumulated in the MCA, representing a probability distribution for photon emission following an excitation pulse. Figure 2-14 provides a block diagram of the photon counting apparatus, and Figure 2-15 illustrates the photon counting method.

The preceding description is a simplistic representation of an actual photon counting system and serves only to introduce the fundamentals of the photon counting method. In the remainder of the chapter, photon counting will be discussed in greater detail. Emphasis will be placed on designing a system which maximizes the photon collection efficiency, improves the resolution, and alleviates distortions in the histograms. The requirements for a photon counting system will be discussed relative to the synchronously mode-locked laser system.

Although the greatest modifications occurred to the detection apparatus, some alterations of the SML lasers were also necessary. The Control argon ion pump laser was replaced by a Coherent Innova 90 argon ion laser

Figure 2-14. Block diagram of a photon counting apparatus in the conventional configuration. _____ optical signal; -------- electronic signal; the trigger signal can be derived from either an optical or electronic signal; the constant fraction discriminators supply standardized timing pulses; TAC, time-to-amplitude converter; MCA, multichannel analyzer

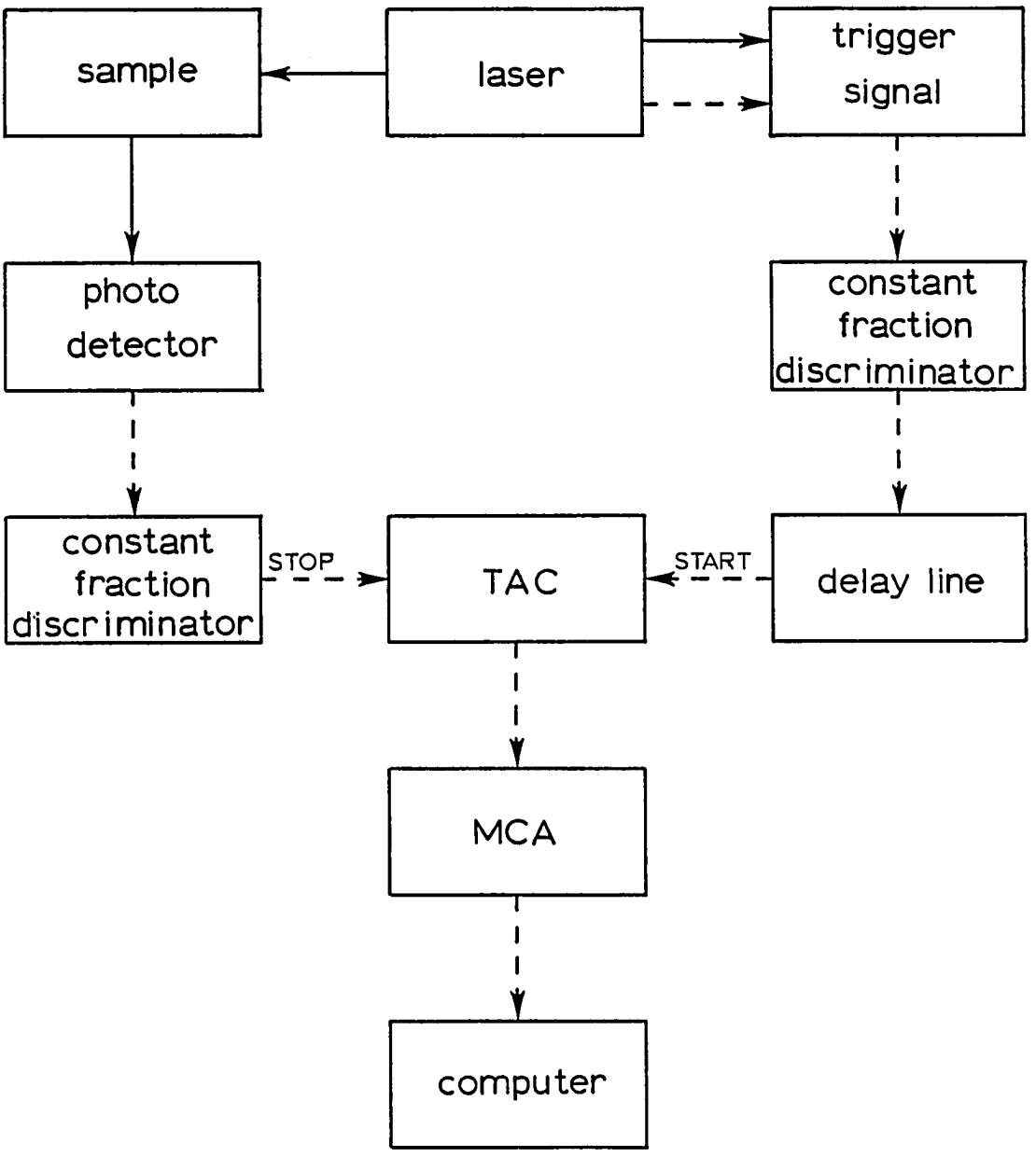
sample
laser
trigger signal
photo detector
constant fraction discriminator
constant fraction discriminator
STOP
TAC
START
delay line
MCA
computer

Figure 2-15. Illustration of the photon counting method (conventional configuration). The arrival of a trigger pulse initiates a voltage ramp in the TAC which is halted upon the arrival of a stop pulse from the photomultiplier tube (PMT). An amplitude pulse is generated whose height is proportional to the final voltage stored on the TAC timing capacitor. The amplitude pulse is converted by the analog-to-digital converter (ADC) into a memory address. The number stored in the appropriate memory address is then incremented by one. The TAC is reset if no stop pulse is received within 100 nsec

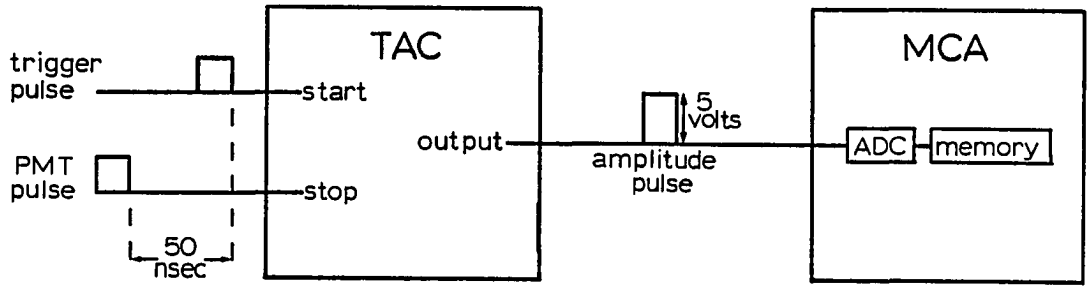
trigger
pulse
start
PMT
pulse
stop
50
nsec
TAC
output
5
volts
amplitude
pulse
MCA
ADC
memory

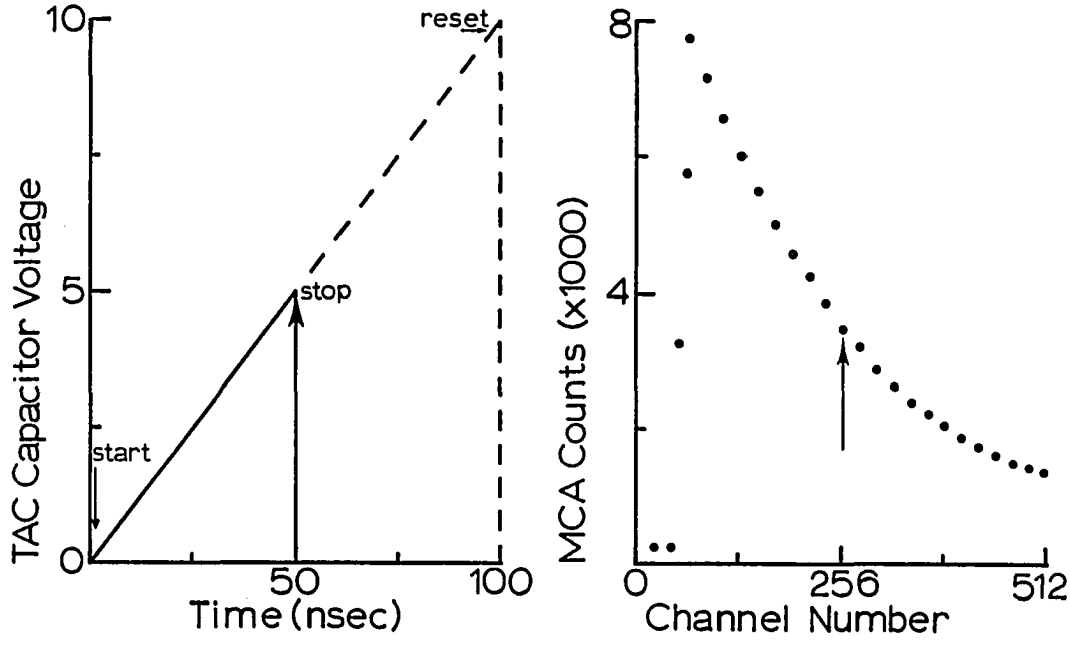
10
5
0
reset
stop
start
TAC Capacitor Voltage
50
100
Time (nsec)
8
4
MCA Counts (x1000)
0
256
512
Channel Number

with a 5 watt plasma tube. The Coherent laser mainframe, unlike the Control laser, permits cavities as short as 110 cm to be assembled. With this change, any of the three mode-locker acoustic resonances (at ca. 47.56, 47.96, or 48.36 MHz) can be used to mode-lock the argon ion laser. Once more, the extended cavity configuration was achieved by decoupling the mode-locker canister from the Invar resonator rods of the argon laser framework. The canister was mounted in an Aerotech Model AOM110-2, 0.14 arc-second resolution gimbal mount. The gimbal mount was attached to a Line Tool Model B XY translation stage (with 0.5 inch travel and 0.001 inch resolution) which, in turn, is attached directly to the optical table.

The frequency synthesis portion of the Harris Corp. modulator driver electronics failed prior to its use in experiments with the modified laser system. This section of the modulator driver was replaced by a 48.00 MHz crystal controlled oscillator from International Crystal Manufacturing. Instead of setting the drive frequency to match the resonance of the mode-locker crystal, the resonance frequency of the mode-locker had to be adjusted to match the 48.00 MHz output of the crystal controlled oscillator. Since the resonance frequency of the mode-locker crystal was temperature dependent, it could be matched to the output frequency of the crystal controlled oscillator by adjusting the temperature of the heating element in the mode-locker canister. The proper canister temperature was attained when the reflected voltage from the mode-locker crystal has been minimized. For the 48.00 MHz driving frequency, the required canister temperature was several degrees above

the ambient room temperature (∿68°F). Provided that the room temperature was maintained below the oven temperature, the mode-locking remained stable, as indicated by stability in the reflected voltage.

The 514.5 nm line from the argon ion laser pumped the dye laser. The laser tube current was kept at 26 amps, providing an average output power of ca. 350 mW. Since the vertically polarized pulses from the Coherent argon ion laser were optimal for pumping the Coherent dye laser directly, the 90° rotation plate was eliminated in the modified laser system.

As before, the synchronously mode-locked dye laser emitted a train of picosecond pulses separated by approximately 10.5 nsec. For photon counting applications, this repetition rate had to be reduced because the timing electronics cannot process signals at 96 MHz. An additional reason for reducing the dye laser repetition rate was that the fluorescence decays of the rh3B and rh6G samples were not complete after 10.5 nsec.

Cavity dumping of the SML dye laser provided a method for reducing the repetition rate of the dye laser output pulses. In the cavity-dumped configuration, all of the resonator mirrors have high reflectivity. Laser output is obtained by actively deflecting light from the cavity at a submultiple of the cavity round trip frequency.

The modifications required to convert the SML laser to a SML cavity-dumped system were relatively straightforward. A second fold was established within the cavity by replacing the 5% transmitting output coupler by two broad band high reflectivity mirrors with radii of curvature 7.5 cm (folding mirror, M3) and 15 cm (end mirror, M4). At the beam waist was positioned a Harris H-100 acousto-optic modulator (AOM) which

redirected the light through Bragg diffraction. As with mode-locking, the active element in the cavity-dumper consisted of a transducer transmitting acoustic pulses into a substrate of high quality fused quartz. During each round trip, the circulating light pulse passed through the AOM twice and was partially diffracted each time (71, 72). Light diffracted during the first pass was reflected by M4 and partially rediffracted into the cavity beam. Because of rediffraction, no more than 50% of the light within the laser cavity could be dumped at a given time.

The cavity-dumper is a home-built unit which incorporates the Harris modulator and driver into its design. As with the previous extended cavity configuration, the cavity-dumper optics were detached from the dye laser resonator rod. A Harris Model H-106 acousto-optic modulator mount was used to align the Bragg cell. The mount provided adjustment for two degrees of translation and one degree of rotation. Translation adjustments (along the y- and z-axes in Figure 2-16) permitted the Bragg cell to be positioned optimally with respect to the incident laser pulses. Translation in the z direction should position the cavity beam as close to the transducer as possible. Translation in the y direction continued until the laser pulse intersected the acoustic beam optimally (73), as determined by the intensity of the diffracted beam. The rotational degree of freedom (about the y-axis) provided the Bragg angle adjustment. The AOM could be rotated coarsely about the z-axis by loosing set screws and twisting the modulator within the mount, permitting the cavity beam incidence to be set at Brewster's angle.

Figure 2-16. Diagram of cavity-dumper. AOM, acousto-optic modulator; M3, folding mirror with 7.5 cm radius of curvature; M4, end mirror with 15 cm radius of curvature; prism, right-angle coupling prism. (a) is a side view of the cavity dumper; (b) is an overhead view

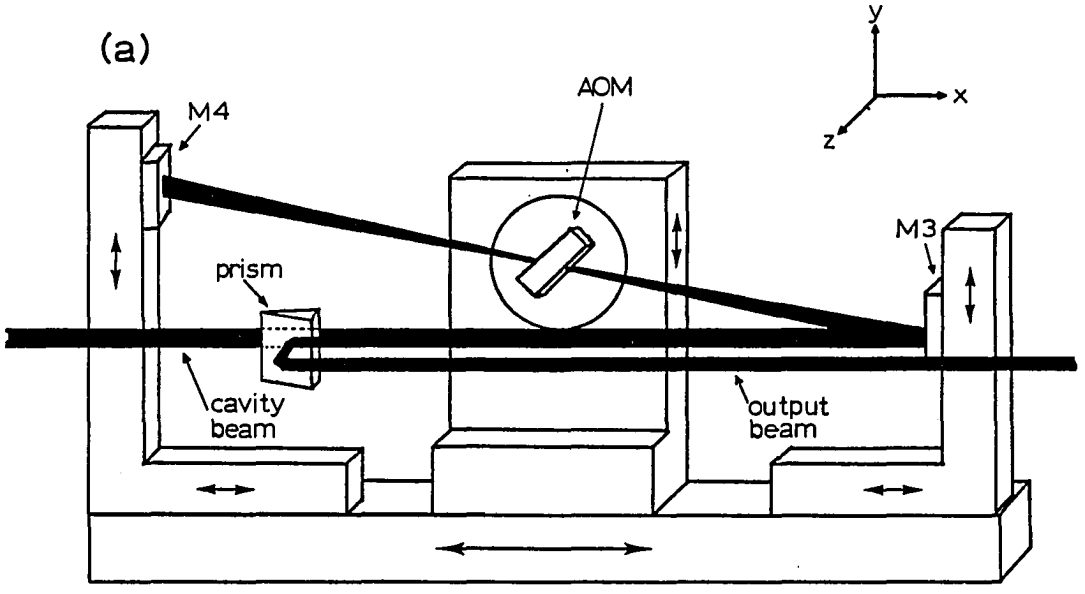
(a)
y
x
z
M4
AOM
M3
prism
cavity
beam
output
beam

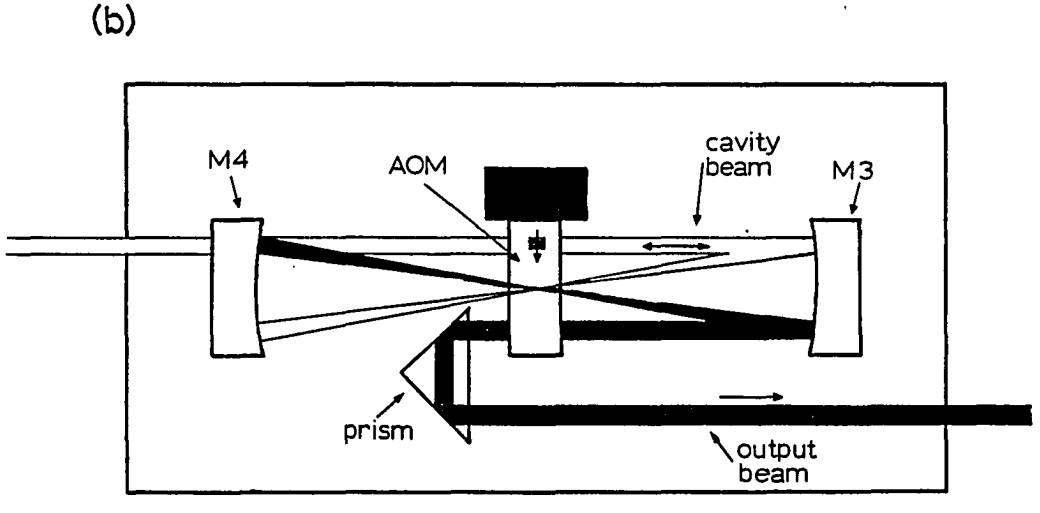
(b)
M4
AOM
cavity
beam
M3
prism
output
beam

Since the Harris mount did not provide translation in the x direction, mirrors M3 and M4 must be translated individually along the x-axis to intersect the cavity beam waist with the AOM Bragg cell. Translation and angle adjustments of mirrors M3 and M4 were afforded by Newport Research Corporation (NRC) Model MM-1 tiltables attached to Line Tool Model C micropositioners. Each micropositioner provided 0.5 inch translation along the x- and y- axes readable to 0.001 inch. The NRC tiltables, while being compact and relatively stable, had only coarse adjustment, which made fine tuning of the dye laser cavity difficult. Translation of M3 or M4 along the y-axis produced the same effect as rotation of the optics about the z-axis. Final adjustments on M3 and M4 were made by translating the optics along the y-axis with the Line Tool micropositioners. Freedom to translate the mirrors along the z-axis would facilitate cavity tuning further.

To synchronize the circulating dye laser pulse to the arrival of the argon laser pump pulse at the dye jet, the dye laser cavity must be matched to the argon laser cavity length. By translating M3, M4 and the AOM as a unit along the x-axis, the cavity length could be adjusted without affecting the optical alignment. The AOM mount and the two mirror mounts were attached an inch-thick aluminum stage translatable along the x-axis by a Line Tool Model M micropositioner with one inch translation.

The cavity-dumper driver contained the signal processing electronics required to phase-lock the dump drive signal with the light circulating within the cavity. The argon laser mode-locker driver provided a 48 MHz reference signal to the cavity-dumper driver. The cavity-dumper driver

Figure 2-17. Effect of cavity-dumper delay on dye laser output. In (a), the cavity-dumper delay is misadjusted, resulting in two output pulses for every dump command. In (b), the timing between the cavity-dumper pulse and the intracavity pulses is optimized resulting in a single output pulse

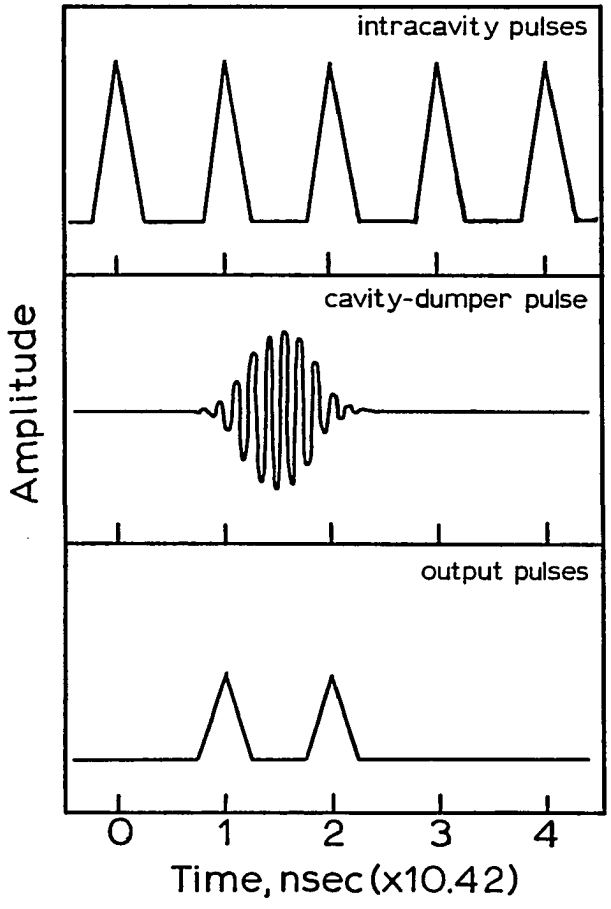
intracavity pulses
cavity-dumper pulse
output pulses
Amplitude
0
1
2
3
4
Time, nsec (x10.42)

(a)

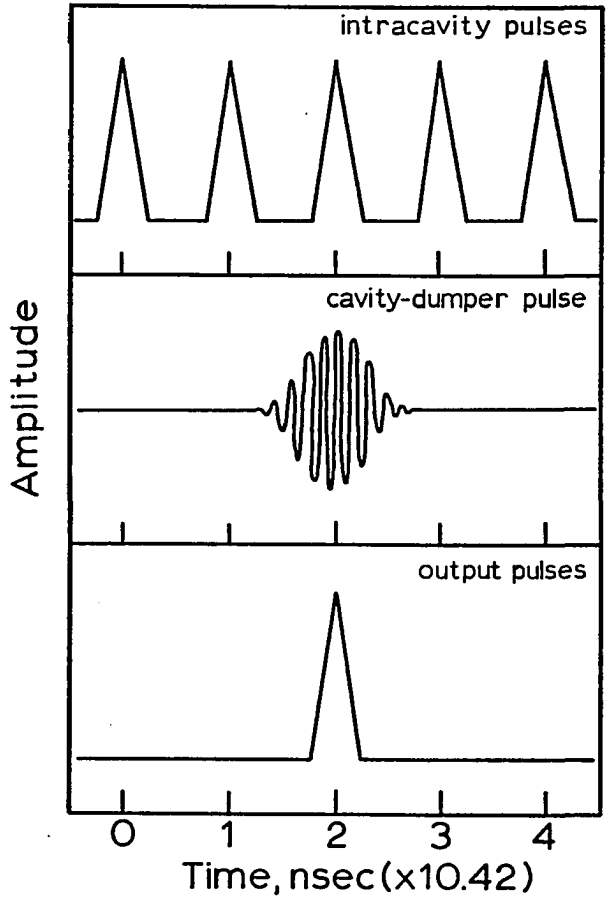
intracavity pulses
cavity-dumper pulse
output pulses
Amplitude
0
1
2
3
4
Time, nsec (x10.42)

(b)

contained a 384 MHz voltage controlled oscillator (VCO) with a tunable frequency range from 380 MHz to 388 MHz. The output of the VCO was divided by 8 and compared to the 48 MHz reference. A correction voltage was generated proportional to the deviation of the divided VCO output from the 48 MHz reference signal. This dc signal fed back into the VCO to force the deviation between the divided output of the VCO and the reference frequency to zero.

The VCO output also served as the input signal to a divider chain that determined the frequency at which pulses were dumped from the dye laser. Selection of the front panel pulse frequency switch determined which outputs of the divider chain were activated. The dumping command repetition rate, adjustable from single shot to 4.8 MHz, was left in the 4.8 MHz setting for all experiments.

The 4.8 MHz output signal from the cavity-dumper countdown circuit passed through a delay circuit (variable through the cavity-dumper front panel) to trigger a pulse generator. The pulse generator supplied a gated signal to the AOM containing a carrier frequency of 384 MHz within a pulse envelope of 10 nsec FWHM. The delay, variable to 16 nsec, was adjusted to synchronize the arrival of the cavity-dumper acoustic pulse with the cavity pulse of the dye laser in the Bragg cell. At a 4.8 MHz repetition rate, the cavity-dumper should extract one dye laser pulse out of every 20 pulses passing through the Bragg cell. However, as shown in Figure 2-18, all laser pulses passing through the Bragg cell were partially diffracted (to varying degrees) due to a low-amplitude, high frequency background signal transmitted by the cavity-dumper driver.

Figure 2-18. Effect of noise (transmitted by cavity-dumper) on dye laser output. The ideal condition (no noise) is shown in (a). Output pulse characteristics when noise is present on transmitted dump signal are shown in (b)

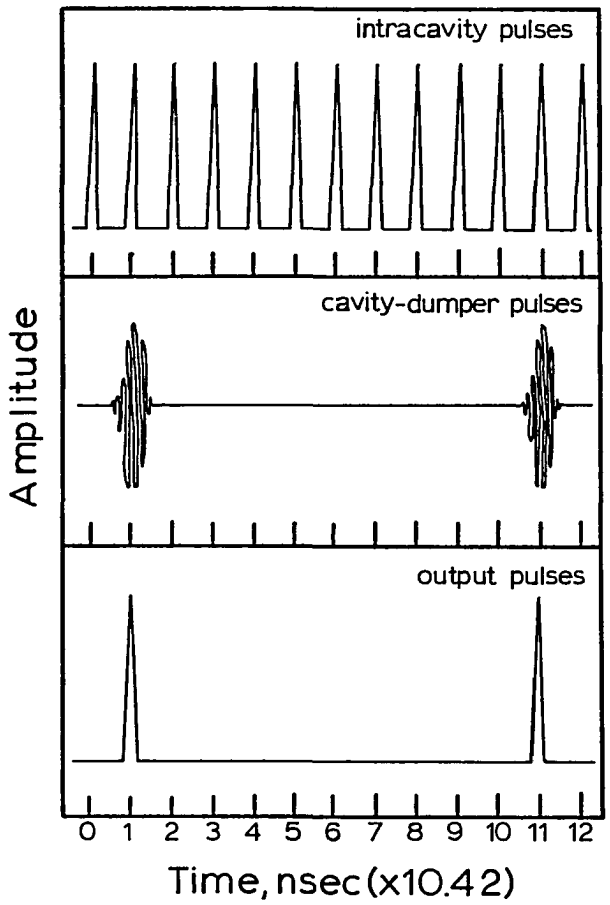
intracavity pulses
cavity-dumper pulses
output pulses
Amplitude
0 1 2 3 4 5 6 7 8 9 10 11 12
Time, nsec (x10.42)

(a)

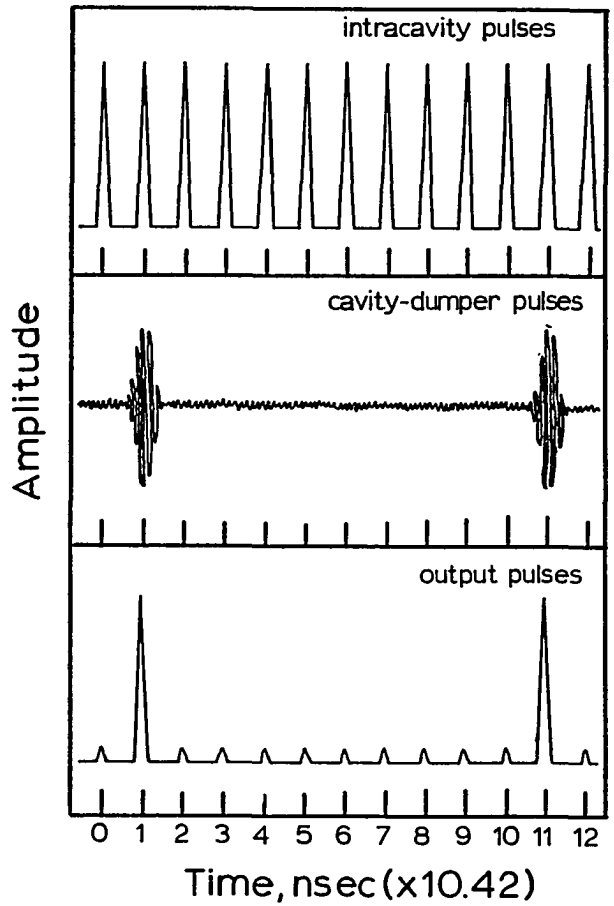
intracavity pulses
cavity-dumper pulses
output pulses
Amplitude
0 1 2 3 4 5 6 7 8 9 10 11 12
Time, nsec (x10.42)

(b)

Figure 2-19. Experimental arrangement for time-correlated single-photon counting. AOM, acousto-optic modulator; BS, beam splitter; PD, photodiode; CFD, constant fraction discriminator; MCP, microchannel plate; fl, fluorescence; TAC, time to amplitude converter; MCA, multichannel analyzer

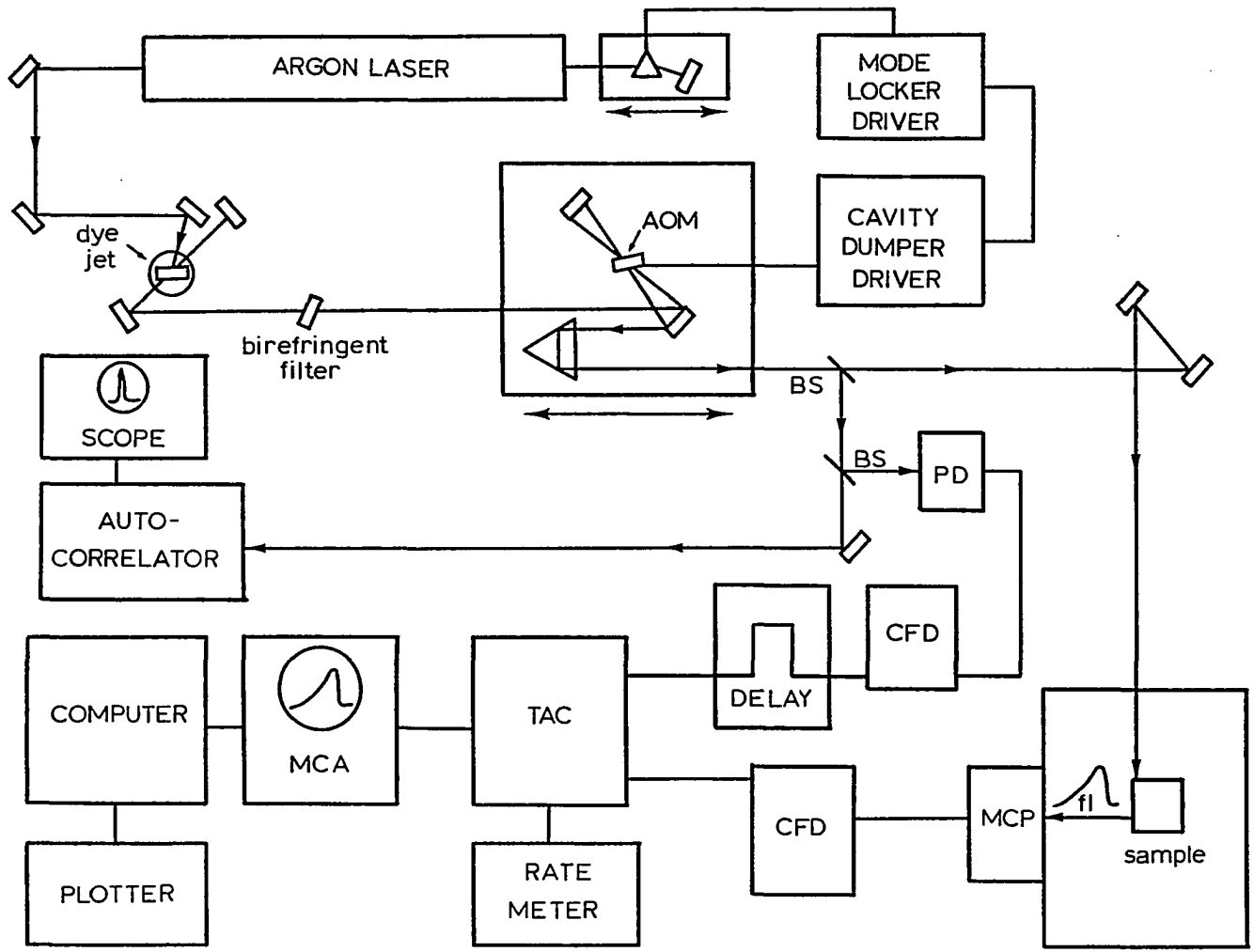
ARGON LASER
MODE LOCKER DRIVER
AOM
CAVITY DUMPER DRIVER
dye jet
birefringent filter
BS
BS
PD
SCOPE
AUTO-CORRELATOR
CFD
DELAY
COMPUTER
MCA
TAC
CFD
MCP
fl
sample
PLOTTER
RATE METER

Calibration test data from Harris Corporation indicate that the extinction ratio, defined as the ratio between the energy of the triggered pulse to that of the leakage pulse appearing 10.42 nsec later, should be 40 dB. Extinction ratios below 20 dB were measured here, using the standard Harris cavity-dumper driver and modulator. This value was improved by inserting a two-stage PIN diode suppressor element (74) between the RF amplifier of the dumper driver and the AOM. However, the extinction ratio quoted in the test data sheet was never attained.

The diffracted dye laser pulse (separated from the intracavity pulse by ∿3mm) was picked off by a right angle prism and redirected through the output port of the cavity-dumper. The ∿10 mW average power of the 575 nm output beam corresponded to a peak laser power of ∿200W. A beam splitter sampled 80% of the laser intensity which was input into a real-time, rotating-mirror autocorrelator (75). Autocorrelation pulse widths, viewed on a Tektronix Model 547 oscilloscope, were ∿10 psec FWHM. Pulse-to-pulse amplitude variations of the autocorrelation traces were less than 10%. Since the laser pulse profiles were monitored continuously, the condition of the excitation source could be monitored while the fluorescence decays were collected.

Pulses transmitted through the beam splitter were coupled into the sample compartment via two aluminum coated front surface mirrors. As shown in Figure 2-20, the vertically polarized dye laser pulses emerged with their polarization rotated by 90°.

As described previously, the photon probability distribution for fluorescence emission was built up by repetitive exposure of the sample

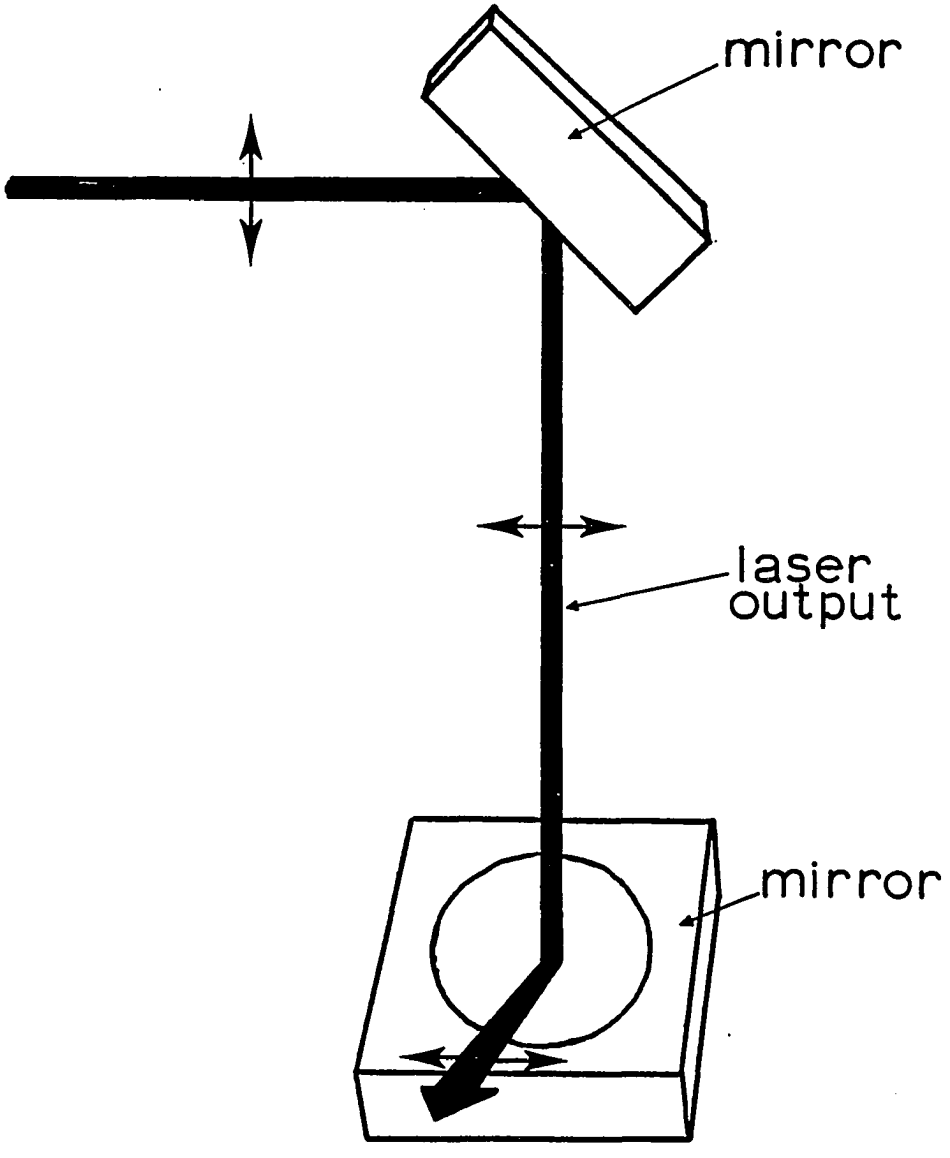

Figure 2-20. Transformation of dye laser polarization from vertical to horizontal following successive reflections off aluminum coated mirrors

to the laser pulses. Photon counting detection relies on accurately timing the arrival of a fluorescence photon at the photocathode relative to a reference signal. One source for the timing reference was the synchronous output port of the cavity-dumper driver. This port provided a trigger signal synchronized with the dump command to the AOM. Some jitter between the synchronous output pulse and the actual dumping of the dye laser pulse can exist due to mechanical drift in the laser cavity optic mounts or timing jitter in the cavity-dumper electronics (76). In another procedure, yielding less timing jitter, trigger pulses are derived from a photodiode viewing the laser pulses directly. Applying the latter method, ∿5% of the pulse intensity intended for the autocorrelator was sampled with a beam splitter and detected with an EG&G Model FOD-100 photodiode (risetime <1 nsec). Typical signals of ∿250 mV were derived and used for timing pulses.

A Hamamatsu Model 1564U microchannel plate photomultiplier (MCP) was used to derive the timing signal from the fluorescence photons. The MCP, with a bialkali photocathode, exhibited $\sim 6 \times 10^5$ gain at 3000V and 500nm incident wavelength; displayed an anode pulse risetime of 206 psec; and had a photoelectron transit time of ∿1 nsec (76). Other detectors considered for this application were Philips 56DUVP and Philips XP2020Q photomultiplier tubes (PMTs). The 56DUVP has a reported transit time of 43 nsec and anode risetime of 2 nsec (at 2200V); the XP2020Q a transit time of 28 nsec and anode risetime of 1.5 nsec (at 2200V) (76). The MCP was selected ultimately because it provided the best time resolution, judged by the FWHM of the instrument response function. The instrument

function (which is the response of the photon counting electronics to scattered laser pulses) is a convolution of the excitation pulse width and the jitter in the timing electronics and detector. By interchanging the photodetectors while retaining the same timing electronics and dye laser pulse widths, it was possible to make direct comparisons among photomultipliers. Measured instrument function FWHMs were ∿80 psec, ∿220 psec, and >500 psec for the MCP, XP2020Q, and 56DUVP, respectively.

It is worth noting that the instrument function widths are much narrower than the anode pulse widths. This is a consequence of the photon counting method, i.e., that the timing electronics only detect the arrival of a pulse. The transit time spread of photoelectrons for a single pulse is, therefore, irrelevant. What is important is the pulse-to-pulse statistical dispersion associated with the transit time spread (76).

Experimentally, one sees a correlation between the transit time spread and the dispersion associated with the spread (76). As the photoelectron transit times and corresponding transit time spreads become shorter, the transit time dispersion decreases, resulting in improved time resolution. PMTs for photon counting applications are developed to reduce the photoelectron transit times and anode pulse risetimes. Generally, the faster tubes sacrifice gain for improved resolution. The 56DUVP is a 14-dynode stage PMT with high gain (2×10^8 at 2200V). The XP2020Q, similar in design to the 56DUVP, has only a 12-stage dynode chain (gain 3×10^7 at 2200V). The improvement in the system's time resolution has been noted above (∿220 psec vs. >500 psec instrument function FWHM).

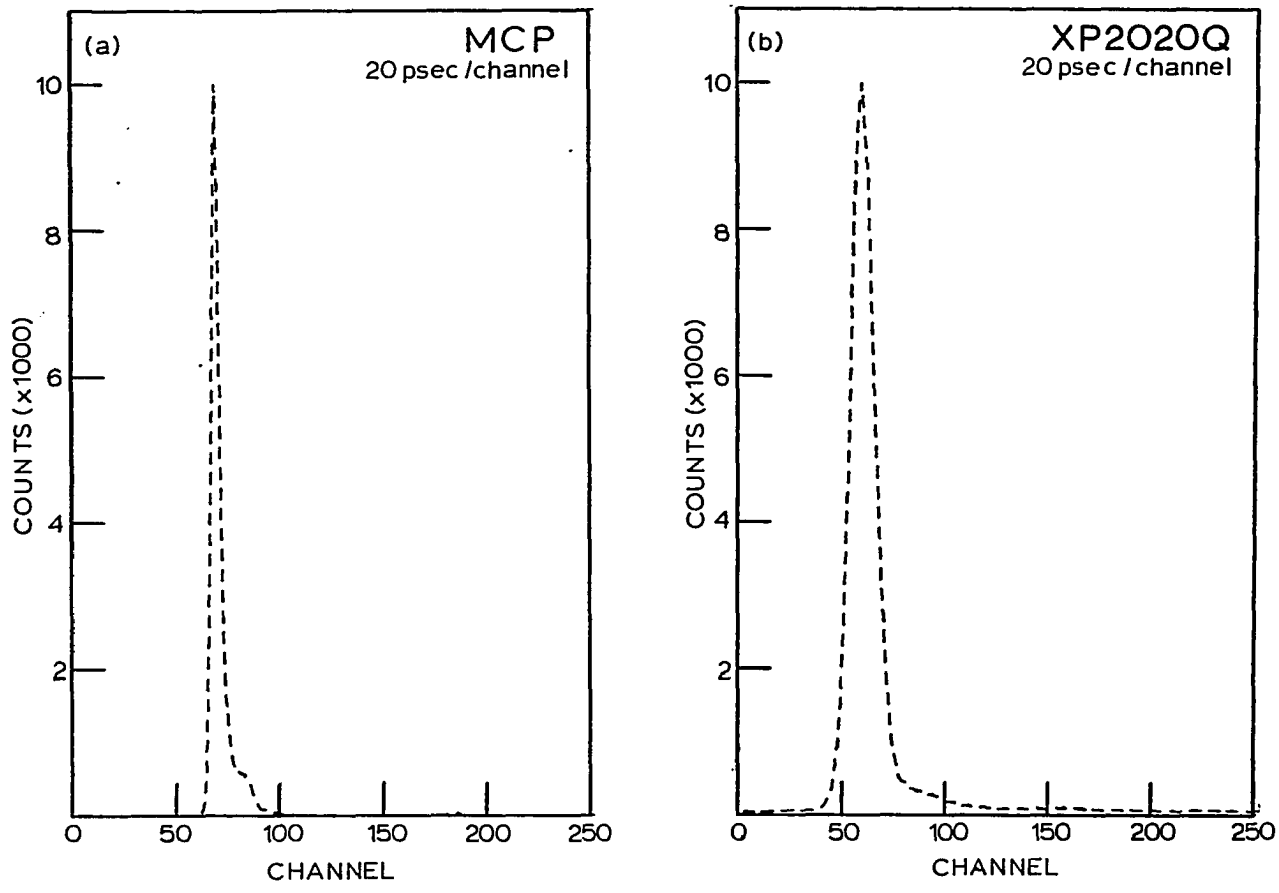

Figure 2-21. Instrument functions for MCP (a) and XP2020Q PMT (b)

The timing characteristics of detectors used for photon counting have been improved significantly with the development of microchannel plate photomultipliers. The MCP consists of an array of millions of glass capillaries (channels) less than 1 mm in length, with internal diameters 10 μm to 20 μm, fused together to form a thin disk (76). The inside walls are coated with a secondary emissive material. The short channel lengths and narrow bores serve to reduce the transit times to ∿1 nsec. Because the gain is $\sim 6 \times 10^5$ at 3000V, photocurrent pulses from the MCP are amplified and inverted by a B&H Electronics AC3011 MIC (3.15 GHz) 21-dB preamplifier and an EG&G IT100 inverting transformer.

As shown above, transit time dispersion reduces the system resolution. The inability of the timing electronics to determine the exact time when a pulse arrives also decreases the resolution. Inaccuracy in time derivation is due predominantly to two factors: jitter and walk (77). Jitter is the timing error introduced by noise on the anode pulses. Walk is the timing uncertainty caused by signal amplitude or rise-time variations. Owing to statistical fluctuations in the photoelectron multiplication process (78, 79), anode pulses generated by the MCP show large variations in pulse height. Unless compensated for, walk can be a major source of timing uncertainty in photon counting experiments.

To minimize the effects that noise and amplitude fluctuations have on the timing electronics, MCP and photodiode pulses are processed in discriminators before passing on to the TAC, as shown in Figure 2-14. Timing discrimination is generally attained using either a leading-edge discriminator or a constant-fraction discriminator (CFD). Leading edge

discrimination, the simpler of the two electronically, generates a timing signal when the input pulse amplitude rises through an adjusted threshold level. This form of discrimination works best when pulse rise times are very rapid and amplitude fluctuations are minimal. For constant fraction timing, a bipolar signal is generated by splitting the incoming photodetector signal, attenuating and inverting one pulse, delaying the other, and summing the two. A crossover pickoff of the composite signal initiates a timing signal to be relayed to the TAC. The result of this manipulation is that an input pulse is timed from a point on its leading edge that is a fixed fraction of the pulse height. For pulses with similar shapes, but varying amplitudes, this timing point is constant relative to a timing reference. The least walk is introduced into the timing when the zero crossing of the bipolar signal occurs with the greatest slope. The optimum choice of fraction (degree of attenuation on the split pulse) depends on the pulse shape and is usually determined experimentally. Likewise, the delay needed to internally generate the constant-fraction signal is variable and must be optimized.

A Tennelec Model TC455 constant fraction discriminator was used to derive timing signals from the MCP anode pulses. Input pulse rates greater than 200 MHz can be processed by the Tennelec CFD. For anode pulses with <1 nsec risetimes and 10:1 dynamic range in signal amplitudes, the walk in the CFD timing electronics was $\pm$10 psec, using a 0.2 fraction. The leading edge module with similar input signals ($\sim$1 nsec risetime and 10:1 dynamic range) contributed $< \pm$400 psec to the walk. A

Figure 2-22. Illustration of timing errors associated with leading edge discrimination. In (a), noise on the anode pulse causes the discriminator to trigger prematurely (jitter); in (b), different amplitude anode pulses, having the same origin, trigger the timing electronics at different times

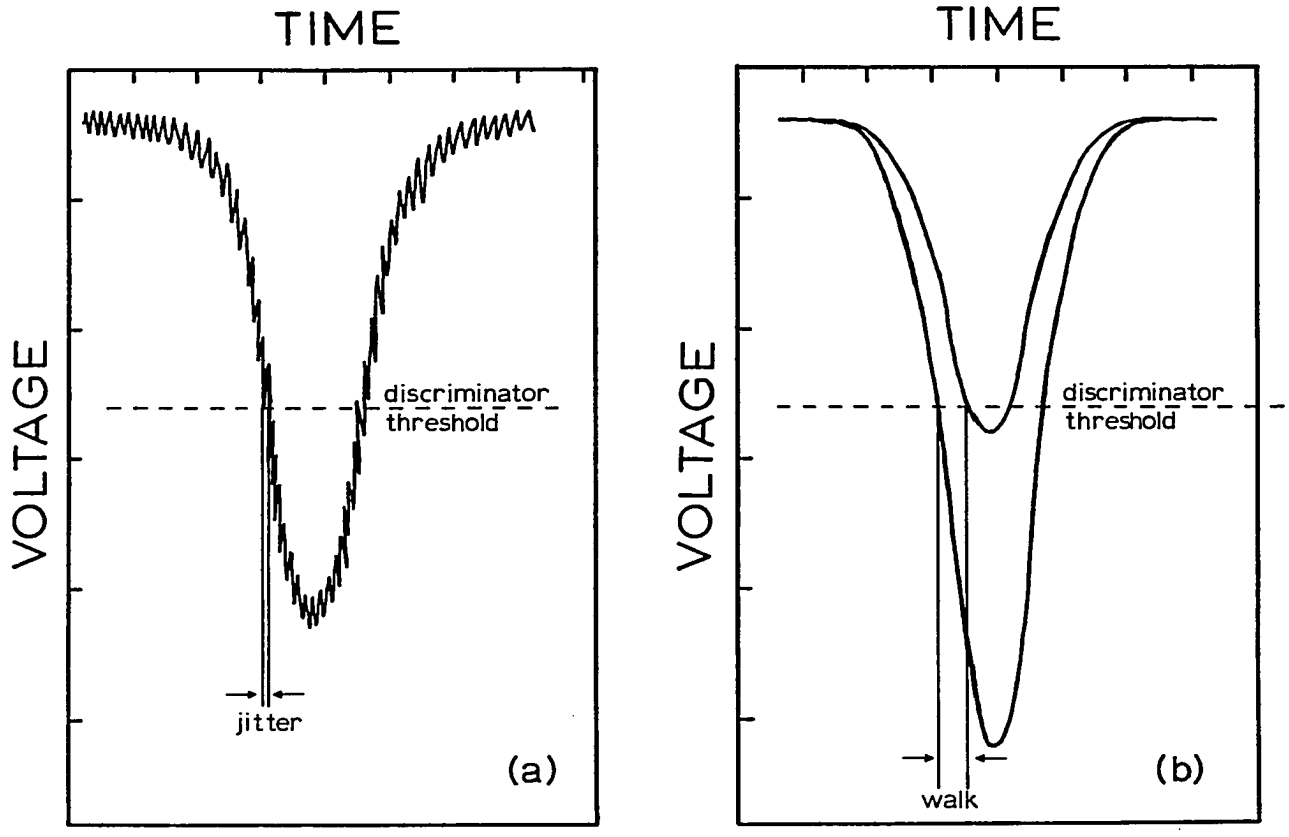
TIME
VOLTAGE
discriminator
threshold
jitter
(a)
TIME
VOLTAGE
discriminator
threshold
walk
(b)

0.2 fraction was used to derive the MCP timing pulses and the delay varied to achieve the narrowest instrument function pulse widths.

The Tennelec CFD consists of four independent constant fraction discriminators. Initial plans were to use one channel to process the anode pulses from the MCP and another channel to process the pulses from the photodiode. Apparently there was crosstalk between the channels in the CFD, however. This anomalous behavior was observed as a rippled output from the TAC when temporally random pulses were input into one channel of the CFD while a periodic reference signal was input into another channel on the same CFD. Under these conditions, the expected TAC output (viewed on the multichannel analyzer in the pulse height analysis mode) would be linear. To alleviate the distortion, pulses from the photodiode were rerouted into an EG&G Ortec Model 934 quad constant fraction discriminator. The Ortec CFD operates under the same principles as the Tennelec CFD. However, the walk for a specified amplitude dynamic range is higher for the Ortec CFD. For 200:1 dynamic range and <1 nsec pulse rise times, the Ortec CFD walk is $\leq\pm$150 psec, while the Tennelec CFD walk is $\leq\pm$30 psec. In addition, the Ortec CFD can process signals at a maximum rate of only 100 MHz.

In addition to reducing the walk in the timing pulses, CFDs are able to reduce the number of dark counts reaching the TAC, discriminating against these signals on the basis of their pulse height. The spurious output pulses from the MCP have a pulse height distribution dominated by low amplitude pulses (80, 81). Both the Ortec and Tennelec CFDs have variable threshold adjustments. The minimum setting for the Tennelec CFD

Figure 2-23. Illustration of constant fraction timing discrimination, using a 0.5 fraction. The upper frames of (a-d) illustrate timing for a large amplitude anode pulse; the lower frames show timing for a pulse with one half the amplitude. In (b), part of the input pulse has been delayed; in (c), the other half of the input pulse has been attenuated by 0.5 and inverted; in (d), the pulses from (c) and (d) have been summed to form a bipolar signal whose zero-crossing triggers a timing pulse. Contrary to the results using threshold discrimination, triggering of the timing pulse is independent of the anode pulse amplitude

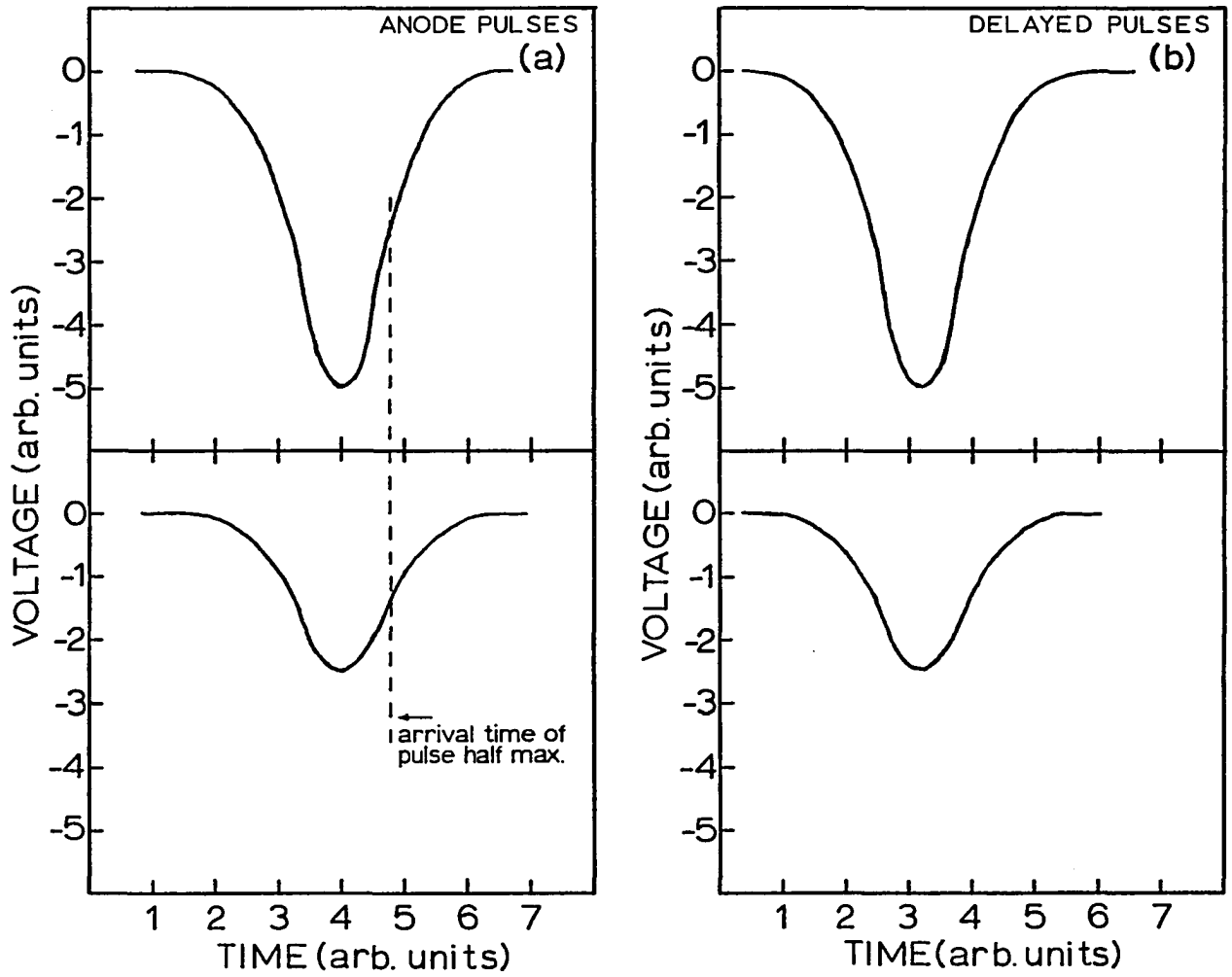
ANODE PULSES
(a)
DELAYED PULSES
(b)
VOLTAGE (arb. units)
0
-1
-2
-3
-4
-5
arrival time of
pulse half max.
1 2 3 4 5 6 7
TIME (arb. units)
TIME(arb. units)

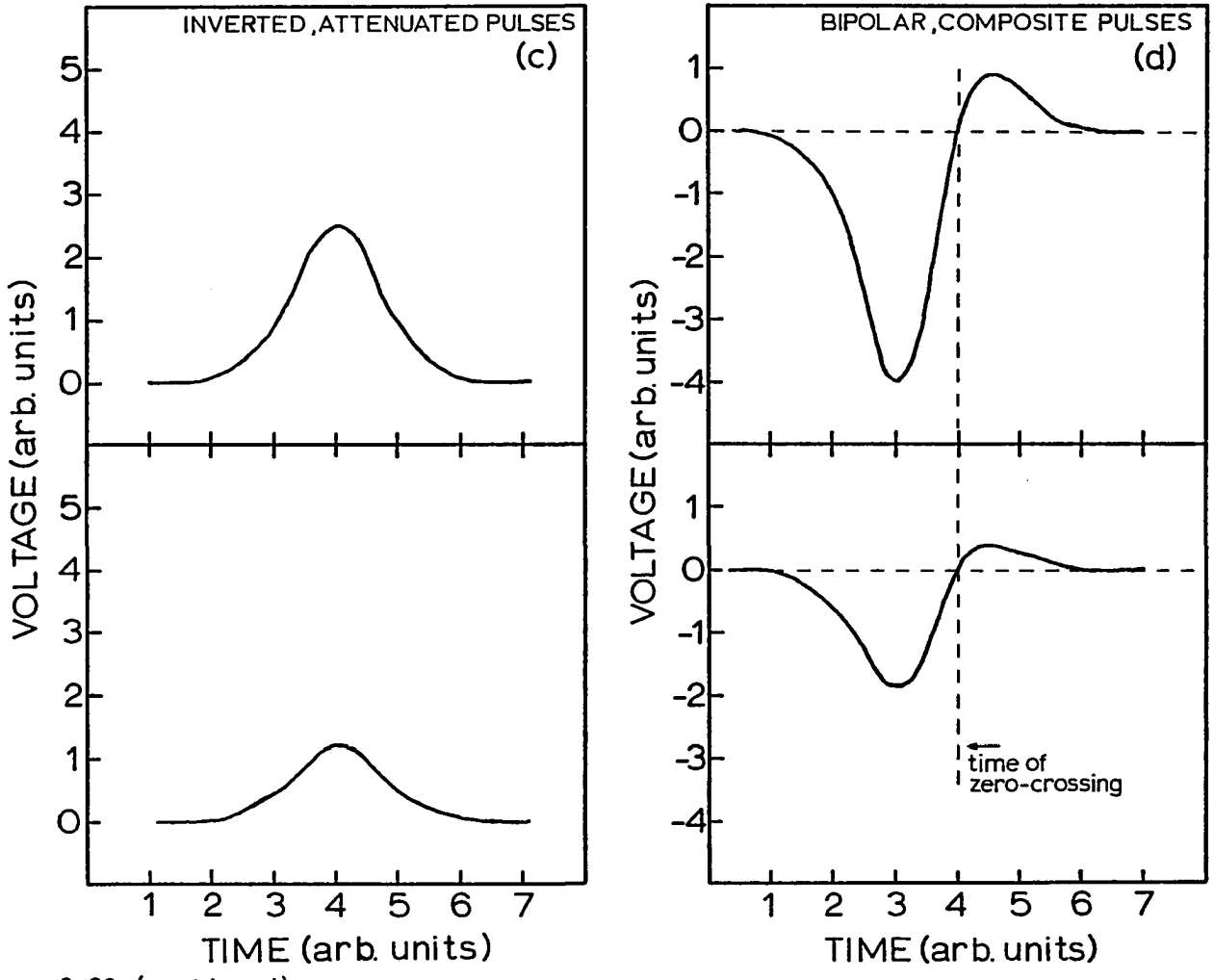

Figure 2-23 (continued)

is -5mV; the minimum Ortec CFD setting is -30mV. Pulses with amplitudes greater than the preset threshold are timed.

The threshold setting for trigger pulses from the photodiode is not critical, since the pulses are intense (~250mV) and have a relatively narrow amplitude distribution. The final setting was chosen by raising the threshold above the -30mV minimum and monitoring the discriminator output with a rate meter. When the dark counts have been discriminated against, a plateau in the output pulse rate vs. threshold setting will be encountered. A threshold setting approximately one-third of the way along this plateau is recommended (76).

More critical is the setting of the discriminator threshold for the MCP pulses. Since MCP pulses have a wide dynamic range of amplitudes, there is no clear dividing line between pulses associated with dark counts and pulses resulting from the detection of a photon. Raising the threshold improves the signal to noise level but reduces the rate at which valid pulses are accepted. The final choice of threshold is a compromise between the two.

As the CFD threshold level is raised, the FWHM of the instrument function can become narrower. This behavior should not necessarily be associated with improved time resolution. The observed narrowing of the instrument function can result from biasing the discriminator to pass pulses representing multiphoton events (two or more detected photons per excitation cycle). When single photon pulses overlap, they create a multiphoton pulse with an amplitude greater than either of the single pulses. The probability for overlap is greater at times close to the

maximum of the photon distribution (76). The distortion, different for the instrument function and the fluorescence decay, invalidates the convolution integral. Because it has such narrow anode pulse widths, the MCP should not exhibit this distortion as readily as a PMT would. However, it is advisable to attenuate the dye laser until the probability for multiphoton events is negligible. At this point, if raising the CFD threshold results in narrower instrument functions, it is probably a result of improved CFD performance due to the narrower dynamic range of input pulse amplitudes.

A more critical distortion related to the detection of multiphoton events concerns the Ortec Model 457 time to amplitude converter. The TAC, which measures the time interval between the pulses from the CFDs, has two signal inputs, two status outputs (TRUE START, BUSY) and a CONVERSION output. Upon receipt of a START signal and after a 12 nsec delay, the TAC timing capacitor is charged linearly from a source of constant current. The charging is discontinued upon acceptance of a STOP pulse, and a CONVERSION output pulse is generated with an amplitude proportional to the final charge on the capacitor (76, 82). If no STOP pulse is received within the TAC timing range (switch selectable from 50 nsec to 80 μsec), charging of the capacitor is automatically terminated with no CONVERSION pulse output. There is a ∿4 μsec delay before the timing capacitor can be reset and another START pulse accepted. The TRUE START output of the TAC gates on whenever a START pulse is accepted. The signal is routed to a Mechtronics rate counter which displays the number of TRUE STARTS per second. The BUSY output indicates the length of time

necessary to process each TRUE START. This processing time varies depending on the delay between the TRUE START and STOP pulses, but it is greater than 7 μsec.

The TAC dead time (on the order of μsec) creates the potential for distortion of the collected fluorescence decay profiles. Recall that the Tennelec CFD can process pulses at ∿200 MHz; this is much faster than the TAC processing rate of <143 KHz. The TAC, after receiving a START pulse (TRUE START), disables the START input to prevent subsequent START pulses from disrupting the signal processing. Because the TAC processing time is so long, only one event can be processed by the TAC per laser excitation cycle. When two MCP anode pulses, generated in the same excitation cycle, arrive at the TAC input, only the first will be processed. This biasing of the TAC output by multiphoton events is termed pile-up distortion (83-85).

The relationship between $N_A(i)$ (the number of MCP anode pulses created in time interval i) and N_i (the number of $N_A(i)$ pulses processed by the TAC) is (76)

$$N_A(i) = \frac{N_i}{1 - \frac{1}{N_E} \sum_{j=1}^{i-1} N_j}, \qquad (2.12)$$

where N_E is the number of excitation cycles. Since the number of detected pulses N_D is never less than $\sum_{j=1}^{i-1} N_j$, if N_D is much less than N_E

it follows that $N_A(i)$ approaches N_i. The choice of an acceptable ratio of N_D/N_E depends on the level of distortion which can be accepted. O'Connor and Phillips (76) report that detectable distortions exist in decay profiles when N_D/N_E is as low as 1/20. The ratio was reduced to ca. 1/500 for this work to eliminate distortions from multiphoton events.

The cost of eliminating pile-up distortions is that the collection time must be increased to achieve the same signal to noise ratio obtained with the higher collection rate. Two forms of electronic pile-up inspection allow some improvement in the collection efficiency over that described above. One is based on pulse discrimination, the other based on energy discrimination. In the former, the number of MCP generated pulses arriving at the TAC input during each excitation cycle is monitored (76). The arrival of a second START pulse within one cycle inhibits the CONVERSION output associated with the first input pulse and the TAC is reset. Energy discrimination assumes that a pulse height spectrum measured at the anode of the MCP has a well defined peak that corresponds to one-photon events. If the sum of all the pulse amplitudes from one excitation cycle exceeds the appropriate single photon pulse amplitude, the TAC CONVERSION output for that cycle is inhibited (76). Pile-up correction has been thoroughly investigated by Harris and Selinger (85), who concluded that avoidance of pulse pile-up distortions is best achieved by reducing the counting rate.

In the conventional TAC configuration, the photodiode sampling the laser output provides the START pulses, and the MCP provides the STOP pulses (as shown in Figures 2-14 and 2-15). As a result, events detected

immediately after sample excitation generate small amplitude CONVERSION outputs while those detected at later times generate large amplitude CONVERSION outputs. This layout for the counting electronics becomes highly inefficient as the ratio N_D/N_E approaches zero. Using this "conventional" configuration of the detection electronics and the cavity-dumped laser system described previously, START pulses enter the TAC input every 208 nsec. After accepting the first START input as a TRUE START, 35 or more of the ensuing START pulses will be rejected while the TAC is processing the first TRUE START. When N_D/N_E is 0.002, on the average less than one of every 500 TRUE START pulses will have a STOP pulse arrive within the 50 nsec timing range of the TAC (the setting used for all experiments). This represents an effective dead time for the TAC of greater than 99%. If instead the START and STOP inputs were reversed so pulses from the MCP provided the START signals, nearly every TRUE START accepted by the TAC would result in a STOP within the 50 nsec TAC range. Configured this way, events detected shortly after the sample is excited generate large amplitude CONVERSION outputs, while those detected later generate smaller CONVERSION outputs. This arrangement of the detection electronics (termed the inverted configuration) was used in the subsequent experiments which require photon counting detection. The Ortec CFD trigger pulse output passes through an Ortec 425A nanosecond delay line (variable in 1 nsec increments) to provide the proper timing delay between the STOP and START inputs to the TAC.

A region of interest within the full TAC timing range can be selected and expanded for a more critical definition of a portion of the decay

Figure 2-24. Variation of the TAC output using bias and amplifier adjustments. The TAC is set in the 50 nsec timing range. In (a), with no bias or amplification, the output pulse height is 10V for START and STOP pulses separated by 50 nsec. (b) shows the effect of bias on the TAC output. (c) shows the effect of the TAC amplifier on the TAC output

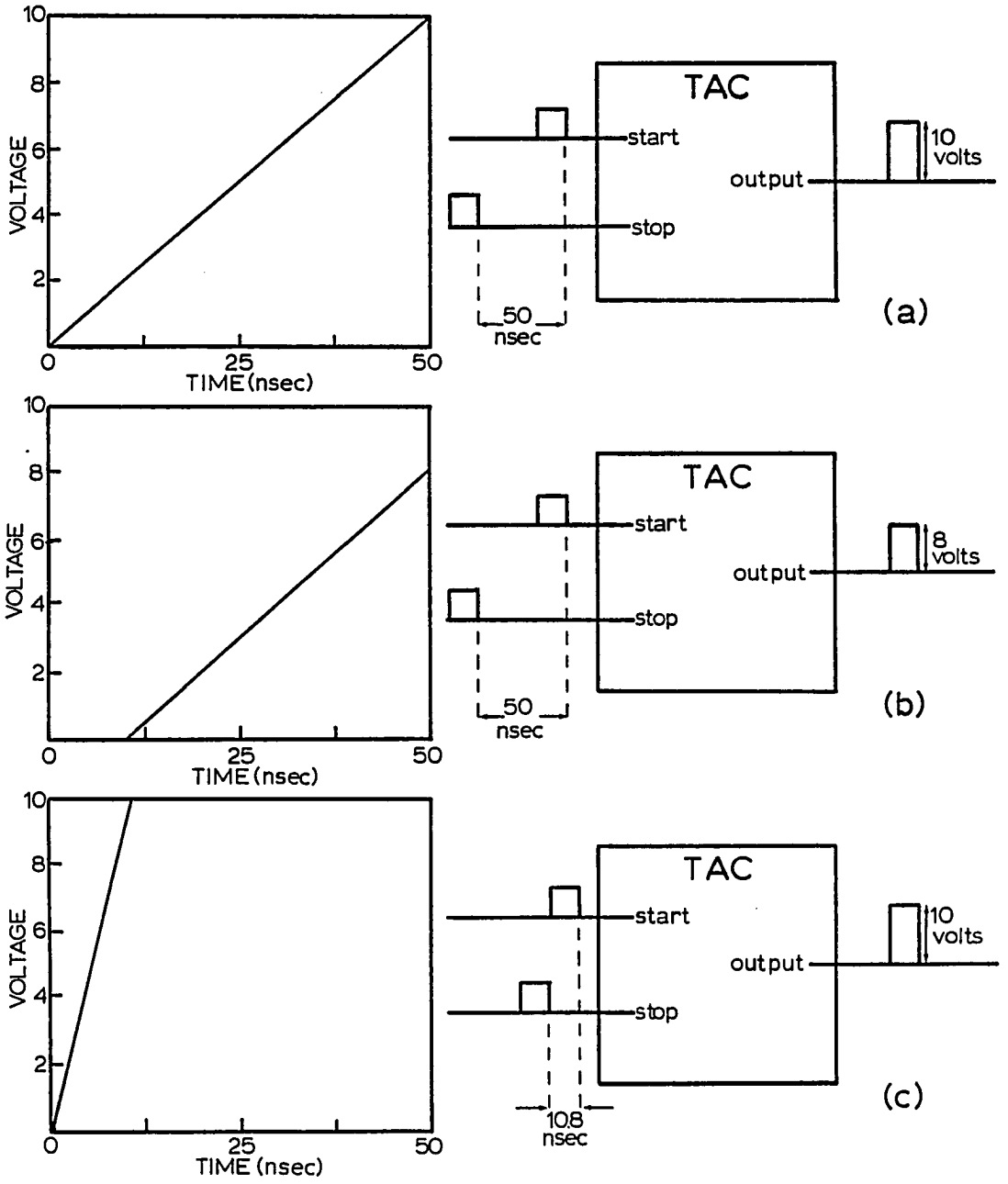
10
8
6
4
2
VOLTAGE
0
25
50
TIME (nsec)
TAC
start
stop
output
10
volts
50
nsec
(a)
8
volts
(b)
10.8
nsec
(c)

Figure 2-25. Operation of TAC in the "inverted" mode. (a) shows the timing relationship required between the START and STOP pulses to operate in the inverted configuration. Since the fluorescence decay in (a) indicates that only a 10 nsec window is needed, the TAC output is amplified to provide maximum resolution, as shown in (b) and (c). In this case, the selected 10 ns window is in a nonlinear region of the TAC timing range

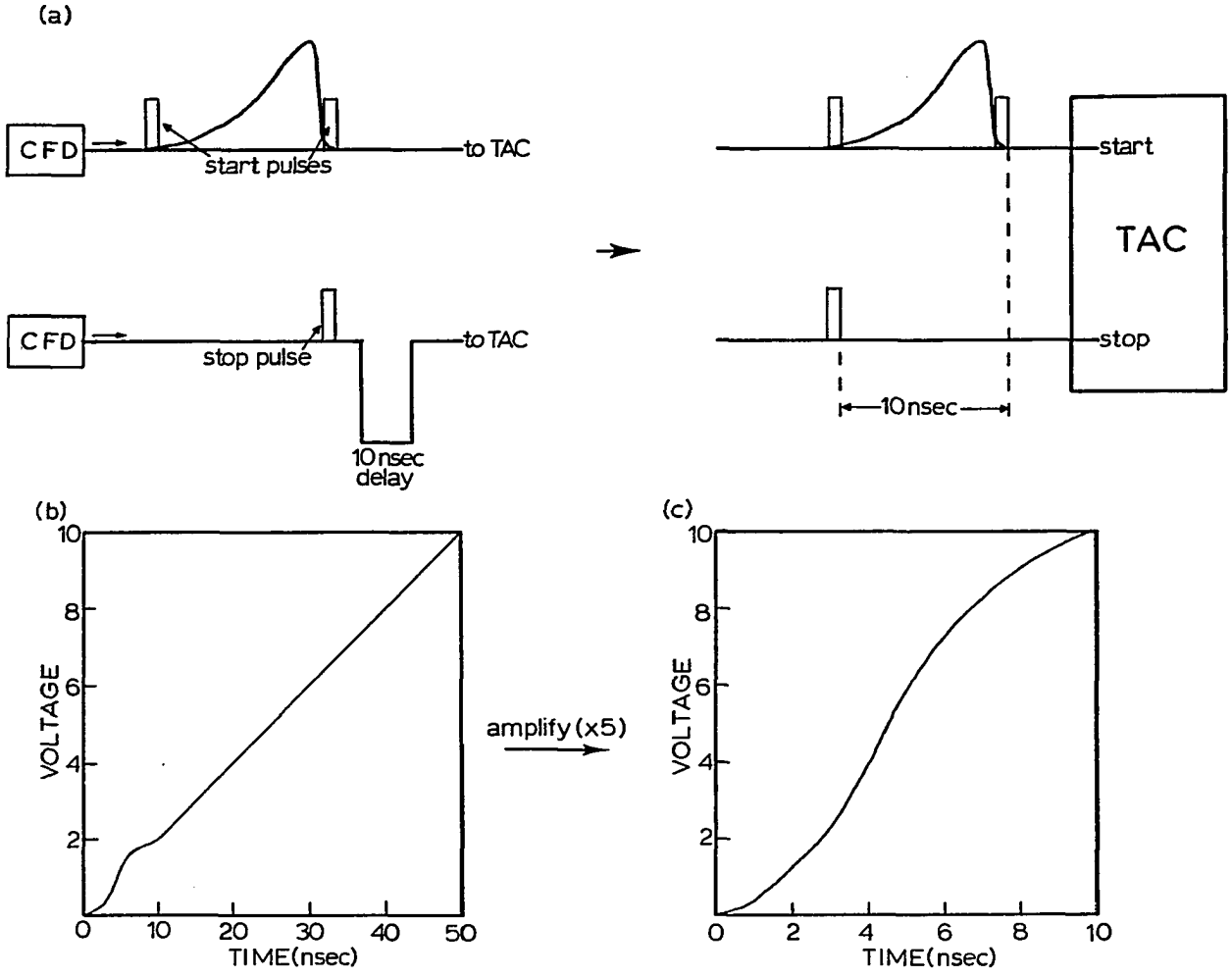
(a)
CFD
start pulses
to TAC
CFD
stop pulse
to TAC
10nsec
delay
start
TAC
stop
10nsec
(b)
VOLTAGE
TIME(nsec)
amplify (x5)
(c)
VOLTAGE
TIME(nsec)

Figure 2-26. Optimization of TAC window. To omit a nonlinear region of the TAC output from the timing window, a combination of delay, bias, and amplifier adjustments must be made. For the case where the first 10 ns are nonlinear, a 10 nsec delay must be added to the STOP pulse; the bias adjusted by 2V (c) and the output amplified (X5) for a 10 nsec window

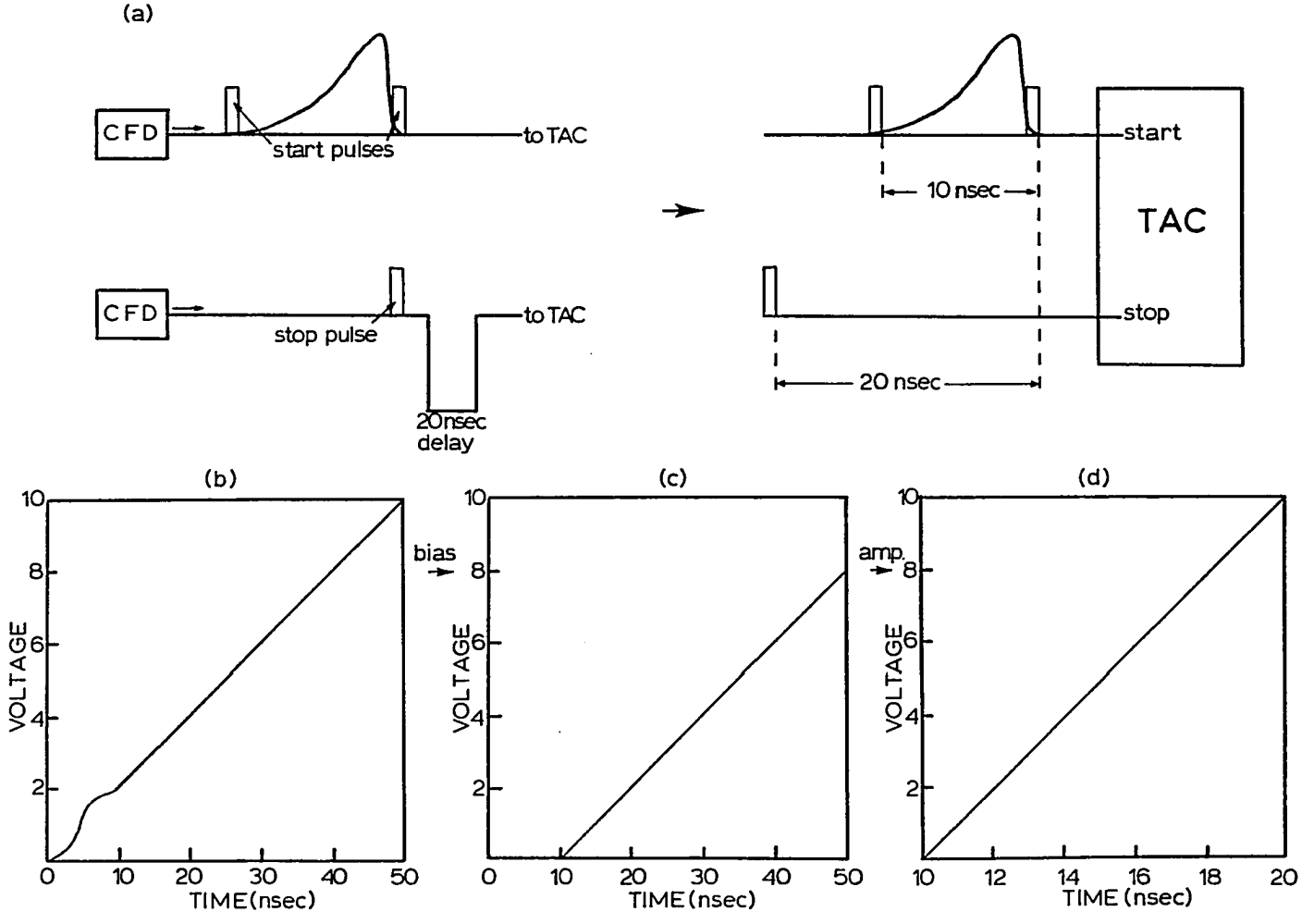
(a)
CFD
start pulses
to TAC
CFD
stop pulse
to TAC
20nsec
delay
start
10 nsec
TAC
stop
20 nsec
(b)
(c)
(d)
bias
amp.
VOLTAGE
TIME(nsec)
TIME (nsec)

curve. The fluorescence lifetimes of the dyes to be studied are ∿3 nsec. By adjusting the gain on the TAC amplifier, the 0-10 volt output range of the TAC was modified to yield information about a 12.80 nsec segment of the 50 nsec TAC timing range. The differential linearity of the TAC was tested using a flashlight excitation source (for random START pulses) and a signal generator (for periodic STOP pulses). By adjusting the TAC bias (0-10 volts d.c.) and choosing the proper delay for the STOP pulses, a linear 12.80 nsec window was attained.

CONVERSION outputs from the TAC were processed and stored in a Canberra Series 30 multichannel analyzer operating in the pulse height analysis (PHA) mode. In PHA operation, the MCA creates a histogram of the CONVERSION output pulse amplitudes. One factor affecting the pulse height histogram is the MCA resolution, the number of discrete voltage levels (or channels) into which the CONVERSION pulses will be sorted. Input pulse heights are processed by an analog-to-digital converter (ADC) and assigned to a channel of the MCA memory. The ADC will accept unipolar pulses from 0 to +10V, the amplitude range of the TAC CONVERSION output pulses. The MCA full scale input is +8 volts, with a 25% overrange for use with the MCA digital offset. The ADC offset is used to establish the relationship between memory channel Ø and the ADC channel numbers. For example, an ADC offset of 256 will shift channel x of memory to ADC channel (256 + x), where x is an integer between 0-1024. Pulses whose converted ADC channel values are less than 256 are not stored in memory.

The MCA memory contains 1024 data channels, each with a capacity to

store nearly 10^6 counts. The full memory can be switch selected so that 512 data channels correspond to the 8-volt range of the ADC; this allows two decays to be stored in the memory simultaneously. Choice of a time-scale was dictated in part by the presence of leakage pulses every 10.42 nsec after the main cavity-dumped pulse. By adjusting the 8-volt range of the TAC to correspond to slightly less than 10.42 nsec, the secondary pulses would not be stored in the MCA memory. The resulting histogram then represents a single fluorescence decay profile.

The secondary pulses are useful for calibration of the MCA time axis, since the TAC bias amplifier settings are only accurate to $\pm$5%. By adjusting the Ortec variable delay, the instrument function for the main cavity-dumped pulses was set to correspond to a CONVERSION output of several millivolts. When the resolution of the ADC was set to 20 psec/channel, the preceding leakage pulse had a CONVERSION output of $\sim$8.14 volts, or an ADC conversion address of channel 521. Since this is beyond the 512 channel range of the memory, the information was not stored. If, however, the ADC offset was set to 256 (from Ø) and another instrument function collected, the ADC conversion address (channel 521) would now be stored in memory address 265. The TAC amplifier was adjusted and the instrument functions collected until the proper number of channel spacings between the two pulses was obtained.

The dye laser pulse intensity was attenuated using neutral density filters until the number of TRUE START inputs into the TAC was less than 12,000 per second. Using the timing capability of the MCA, fluorescence decays were collected for 200 seconds. The number of counts in the peak

channel was typically between 5,000 and 15,000 counts. Instrument functions were collected until 10,000 counts were stored in the peak channel. Data accumulated in the MCA memory were transferred to a Digital Equipment Corporation MINC-23 computer and stored on a floppy disk.

The time-correlated photon counting system was used to measure the concentration depolarization for rh6G in glycerol excited by the dye laser. The rh6G, purchased from Exciton, was tested for impurities by thin-layer chromatography (TLC). Only one TLC spot was observed using Analtech silica gel G plates and three solvent systems (ethanol/acetone, ethanol/acetic acid, and 1-propanol/formic acid). The fluorescence cells were prepared by compressing a drop of the dye solution between two $\lambda/4$ fused quartz flats. This procedure produced cell thicknesses of $\sim$10 μm, based on measured optical densities from cells containing known rh6G concentrations. For the more dilute solutions, $\sim$100 μm cells were prepared using mylar as a spacer between the quartz flats.

The fluorescence collection optics and filters were mounted vertically within the sample chamber. Fluorescence was collected with a 5 cm focal length lens and focused by a 10 cm lens to a spot $\sim$3.75 cm from the face of the MCP. A variable rectangular aperture in the focal plane minimized the transmission of stray radiation to the MCP. Laser scatter and filter fluorescence were minimized by stacking two 3 mm Schott OG-590 filters on top of a 3 mm Schott RG610 filter. The excitation and analyzing polarizers were Promaster Spectrum 7 photographic polarizers. The analyzing polarizer was positioned between the sample cell and the collecting lens. A shutter, mounted between the focusing lens and the MCP,

permitted the sample chamber to be opened and the analyzing polarizer rotated without turning off the MCP high voltage, stabilizing the detection electronics. Differential detector sensitivity to photons polarized parallel and normal to the incident dye laser polarization was tested using an incandescent light source. The measured sensitivity is conservatively less than 2%.

A sample cell was mounted $\sim$5 cm below the collection lens; its surface was set parallel to the analyzing polarizer. The dye laser output was twice reflected (using front surface aluminum mirrors) to make the laser pulses incident on the cell at $\sim 75^{o}$ from the surface normal. Laser pulses were focused with a 10 cm focal length lens to $\sim$0.1 mm diameter and passed through the excitation polarizer prior to entering the sample.

Sample Preparation (Xanthene Dyes)

Samples were prepared by dissolving rh6G in glycerol to yield a solution concentration of $\sim 10^{-3}$ M. Dilutions were made by weighing aliquots of the stock solution to $\pm$0.1 mg, adding glycerol, and reweighing. Concentrations of the more dilute solutions were determined from optical density measurements taken on a Perkin Elmer Model 320 absorption spectrophotometer. The higher concentrations were calculated from these optical density measurements and the dilution factors. Solution concentrations ranged from $\sim 10^{-5}$ to $\sim 10^{-3}$ M.

For experiments measuring the fluorescence depolarization from rh3B adsorbed to fused silica, the layout of the optics, described above, was

Figure 2-27. Arrangement of optics inside of sample chamber. The dye laser output, polarized out of the plane of the paper, is twice reflected using aluminum coated mirrors, focused and directed onto the sample. The angle of incidence is $\sim 75^{o}$ from the surface normal. Fluorescence (fl) is passed through an analyzing polarizer and three colored glass filters. The fluorescence is collimated and focused through a variable aperture using a lens combination. The fluorescence is detected by the MCP

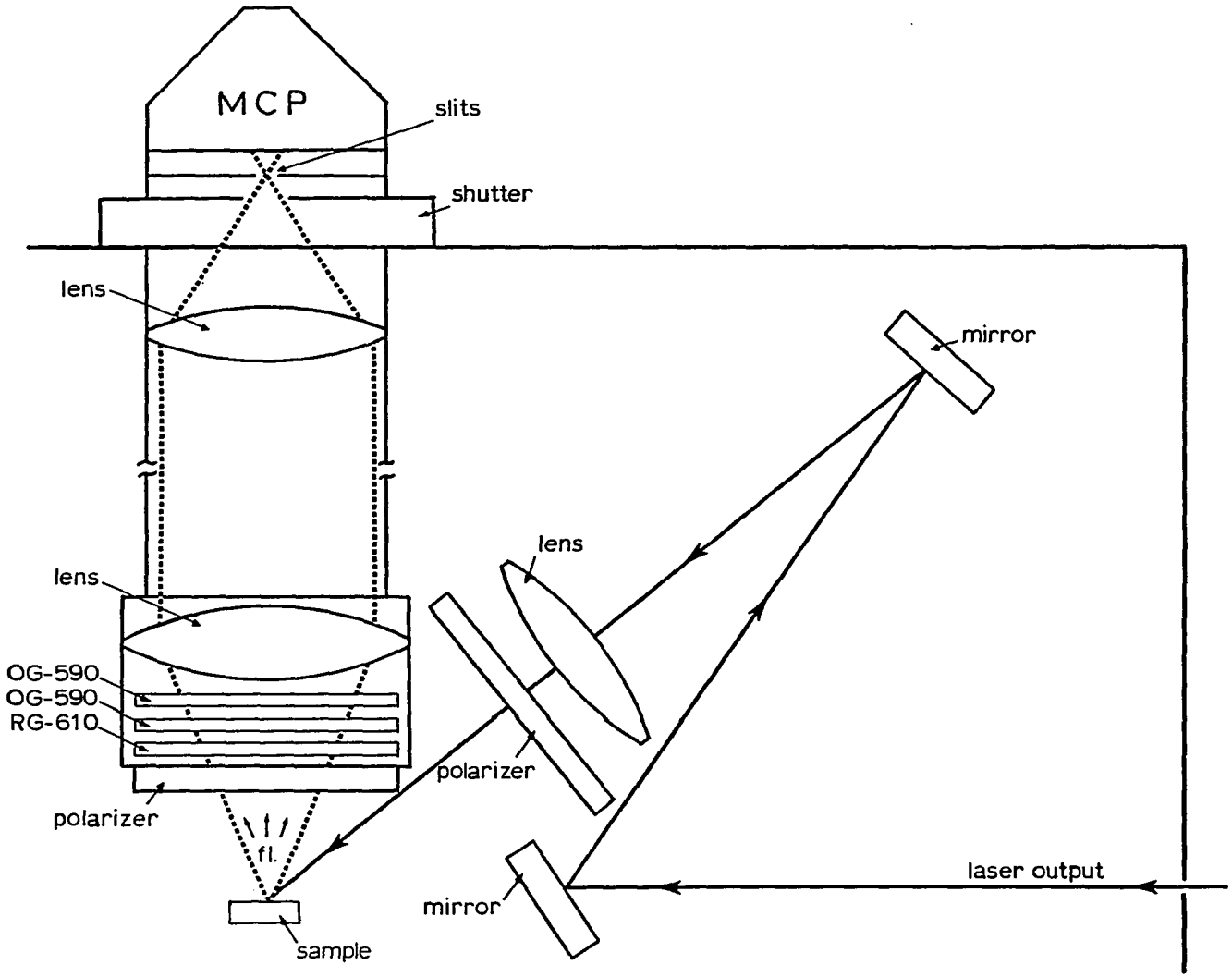
MCP
slits
shutter
lens
mirror
lens
lens
OG-590
OG-590
RG-610
polarizer
polarizer
fl.
laser output
mirror
sample

retained. rh3B, obtained from Eastman Kodak Laser Products, was used without further purification since TLC revealed no impurities. A 7.41×10^{-5} M solution of aqueous rh3B was prepared as a stock solution. The water was distilled, deionized, and filtered before use. rh3B solutions with varied concentration (3.7×10^{-9} to 7.4×10^{-7} M) were freshly prepared from the stock solution shortly before serving as baths for adsorbing rh3B onto $\lambda/4$ fused silica substrates.

All quartz substrates were cleaned in the following manner (86). First, the quartz flats were placed in hot chromosulfuric acid for $\sim$2 hours. After being removed and rinsed with distilled water, the flats were soaked in a dilute NaOH solution (pH 11) for $\sim$12 hours. Again, the slides were rinsed in distilled water and dried with hot air. All substrates were tested for the absence of fluorescing impurities prior to their use in experiments.

While a slide was immersed in the dye solution, a two-dimensional random distribution of rh3B molecules adsorbed to the surface was created. As the slide was raised, the solution clung to the hydrophilic quartz surfaces. The random distribution of dye molecules was altered by the solution layer. Potentially, a nonrandom distribution can be formed on the surfaces as the solvent evaporates. Past methods for removing the aqueous layer have included wicking it off with a tissue (87-89) and stripping it off by centrifugation (90). Neither method provided a satisfactory means of achieving random surface coverages. As the solvent front recedes in either case, dye was trapped within shrinking pools of solution from which it ultimately deposited on the surface. Surface

scans of the quartz faces revealed the poor quality of the surface coverages when these coating methods were used.

Surface scans were obtained by translating the laser output across the dye coated substrate and collecting the fluorescence as a function of position. Each sample, edge mounted to a plastic holder, was secured to a post held securely by a Newport Research Corporation Model VPT-4 translating post holder. The post holder, with a translation range of 0.5 inches, would not rotate the sample. The length adjustment ring of the post holder was coupled to a Superior Electric Type M061-FC08 slo-syn stepper motor via a belt drive. The step rate of the motor (controlled by an Imsai 8080 microcomputer) and gear ratios were selected to provide a 20 μm per second translation of the crystal. The photon counting detection electronics and optics were unchanged, except that the MCA was set in the multichannel scaling mode. In this mode, the MCA integrates counts in a memory channel for a preselected time. This dwell time was set at 0.5 seconds per channel. A single sweep of the MCA memory displayed the fluorescence intensity for a 5 mm section of the crystal.

A better method for preparing a two-dimensional random system of rh3B molecules required that the quartz surfaces be made hydrophobic. This was done by treating the clean slides with a solution of dichlorodimethylsilane in chloroform, rinsing them in methanol, and immersing them in distilled water. The slides, withdrawn from the water, emerged dry. Surface scans for the silane treated samples had macroscopically more uniform dye coverages than the untreated samples.

Figure 2-28. Surface scan of silane treated substrate coated with rh3B

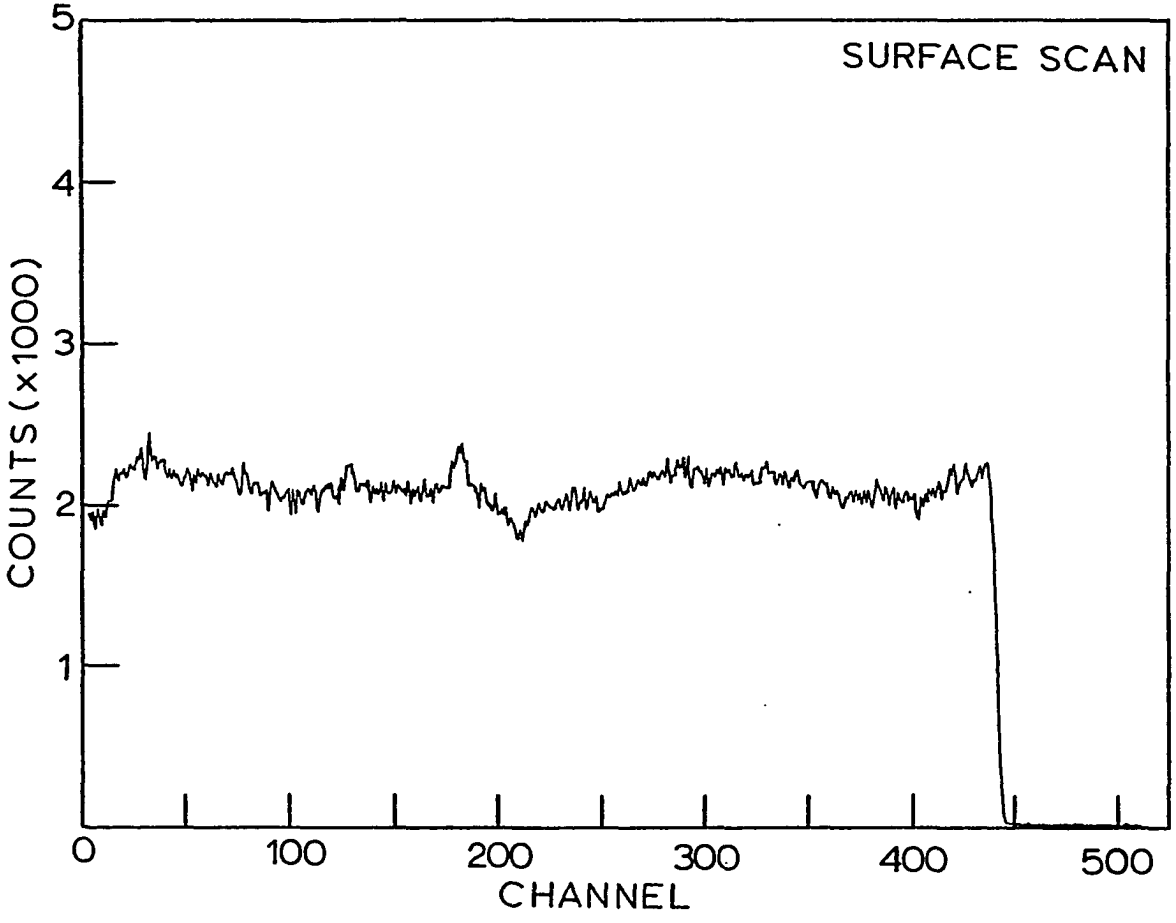
SURFACE SCAN
COUNTS (x1000)
5
4
3
2
1
0
100
200
300
400
500
CHANNEL

Silane treated slides were partially immersed in the rh3B solutions for 10 minutes. Further equilibration time did not change the surface coverage. Surface scans were collected for all samples to verify the uniformity of the surface coverages. Profile accumulations were limited to the uniformly coated areas of each sample.

The region of interest for this experimental study of the Fayer 2-D excitation transport theory ranged from reduced rh3B donor concentrations C_D of $\sim$0 (where there is essentially no energy hopping) to >1.0 (where energy hopping was rapid). C_D is a function of the rh3B surface number density. The rh3B surface coverages analyzed in Chapter VII were all too low to permit direct spectroscopic measurement of the rh3B surface number densities. The surface number densities can be approximated by measuring $I_{\parallel}$ and $I_{\perp}$, the intensity components of fluorescence polarized parallel and normal to the horizontally polarized excitation, respectively. When C_D is near zero, the ratio of $I_{\parallel}:I_{\perp}$ will be $\sim$3:1. As C_D increases beyond one, the ratio $I_{\parallel}:I_{\perp}$ approaches 1:1. Measured ratios ranged from 2.40:1, for flats coated from 7.41×10^{-9} M rh3B solutions, to 1.13:1, for flats coated from 7.41×10^{-7} M rh3B solutions. Intensities of the polarized fluorescence were measured using the photon counting collection optics, an XP2020Q photomultiplier tube, and an x-y recorder.

Measurements of $I_{\parallel}$ and $I_{\perp}$ for a flat coated from 7.4×10^{-7} M rh3B revealed a time dependence for the integrated fluorescence intensities. Over the initial three minutes of exposure, the fluorescence intensity decreased by $\sim$15%. This factor was reduced to under 7% over the next

Figure 2-29. Concentration dependent photo oxidation of rh3B adsorbed to fused quartz. In (a), substrate coated using 7.4×10^{-6} M rh3B; in (b), using 7.4×10^{-7} M rh3B; in (c), using 7.4×10^{-8} M rh3B; and in (d), using 7.4×10^{-9} M rh3B. BKG are the dark counts

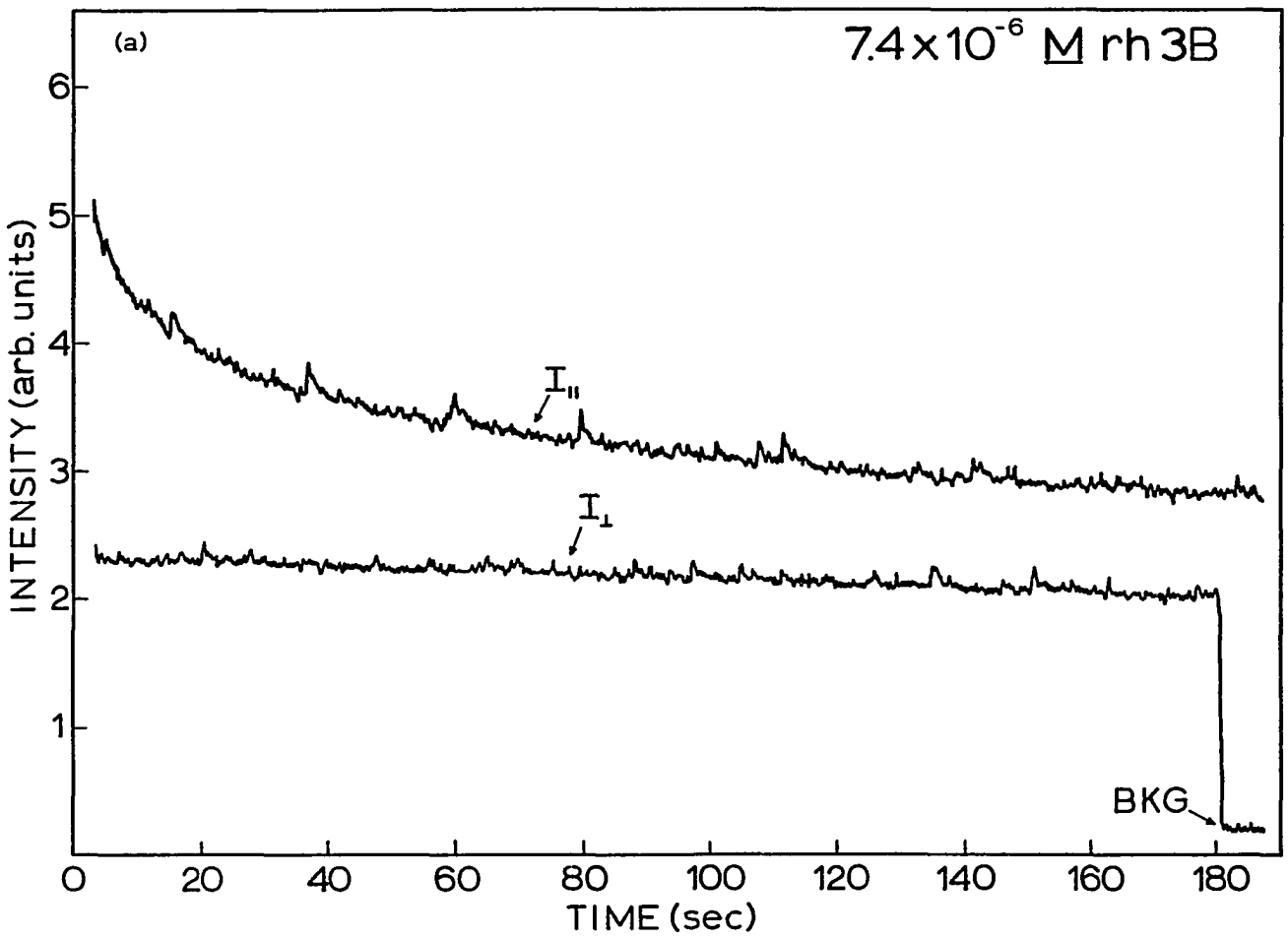
(a)
7.4x10⁻⁶ M rh 3B
INTENSITY (arb. units)
TIME (sec)
I∥
I⊥
BKG
0
20
40
60
80
100
120
140
160
180
1
2
3
4
5
6

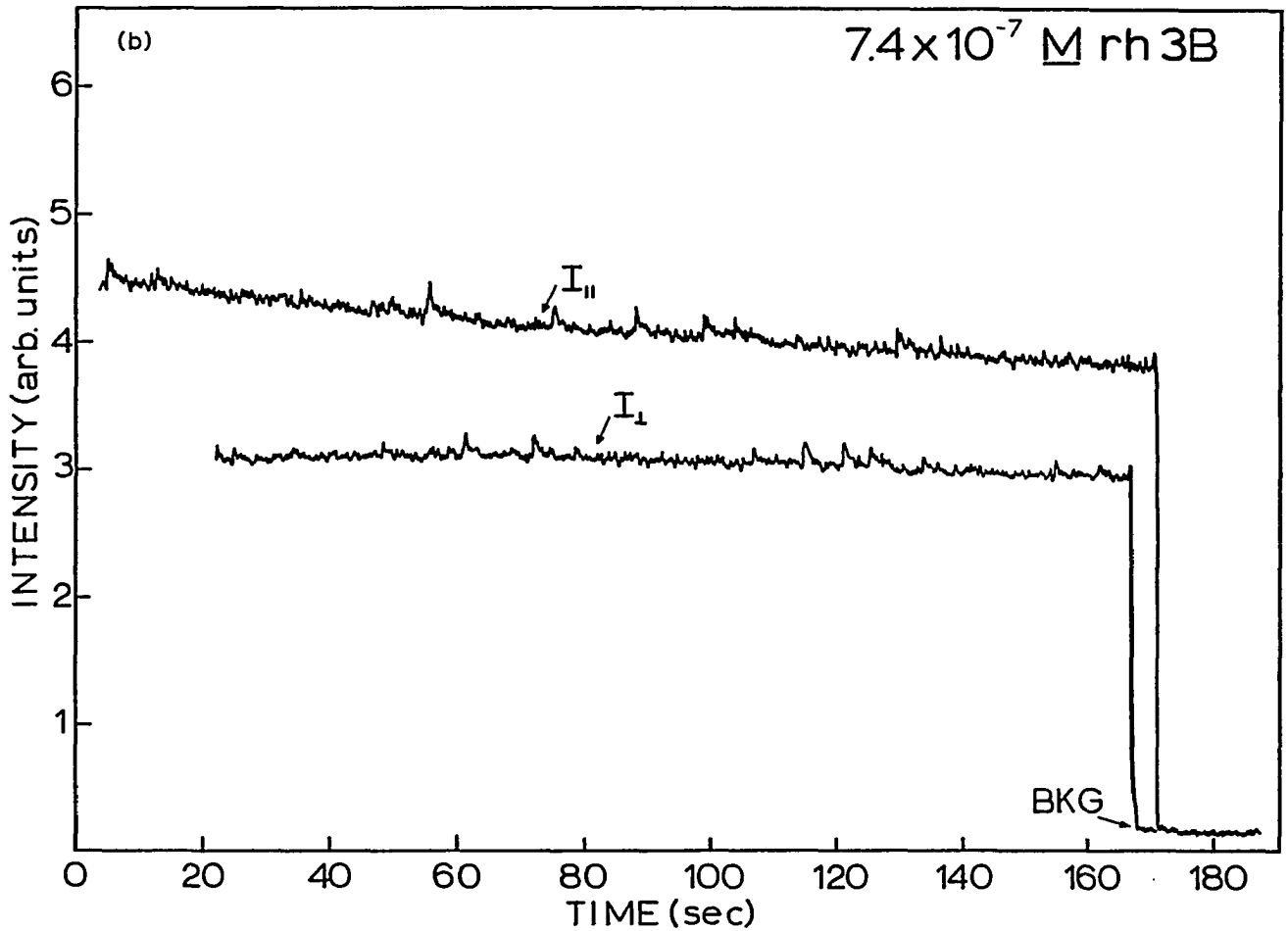

Figure 2-29 (continued)

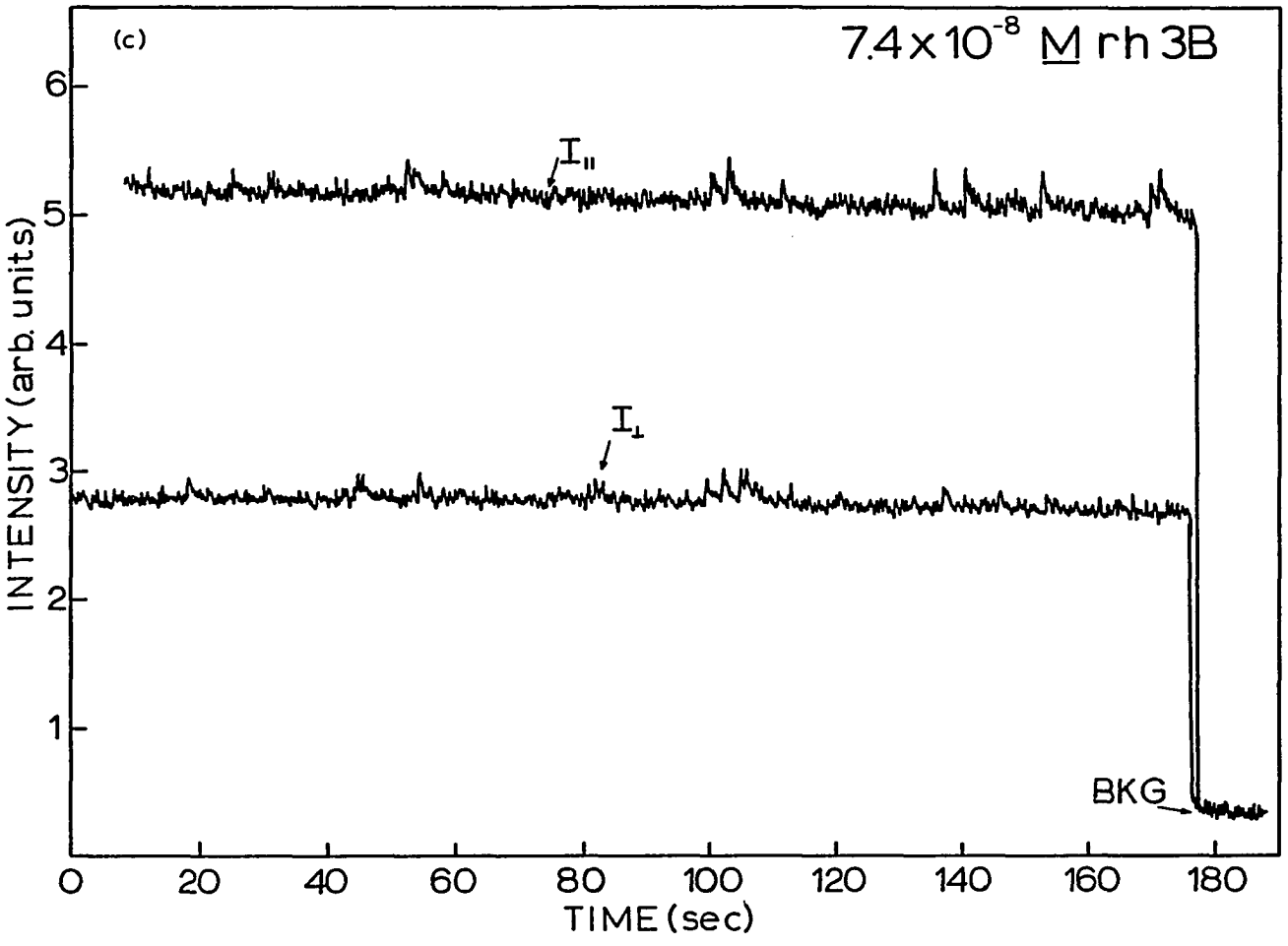

Figure 2-29 (continued)

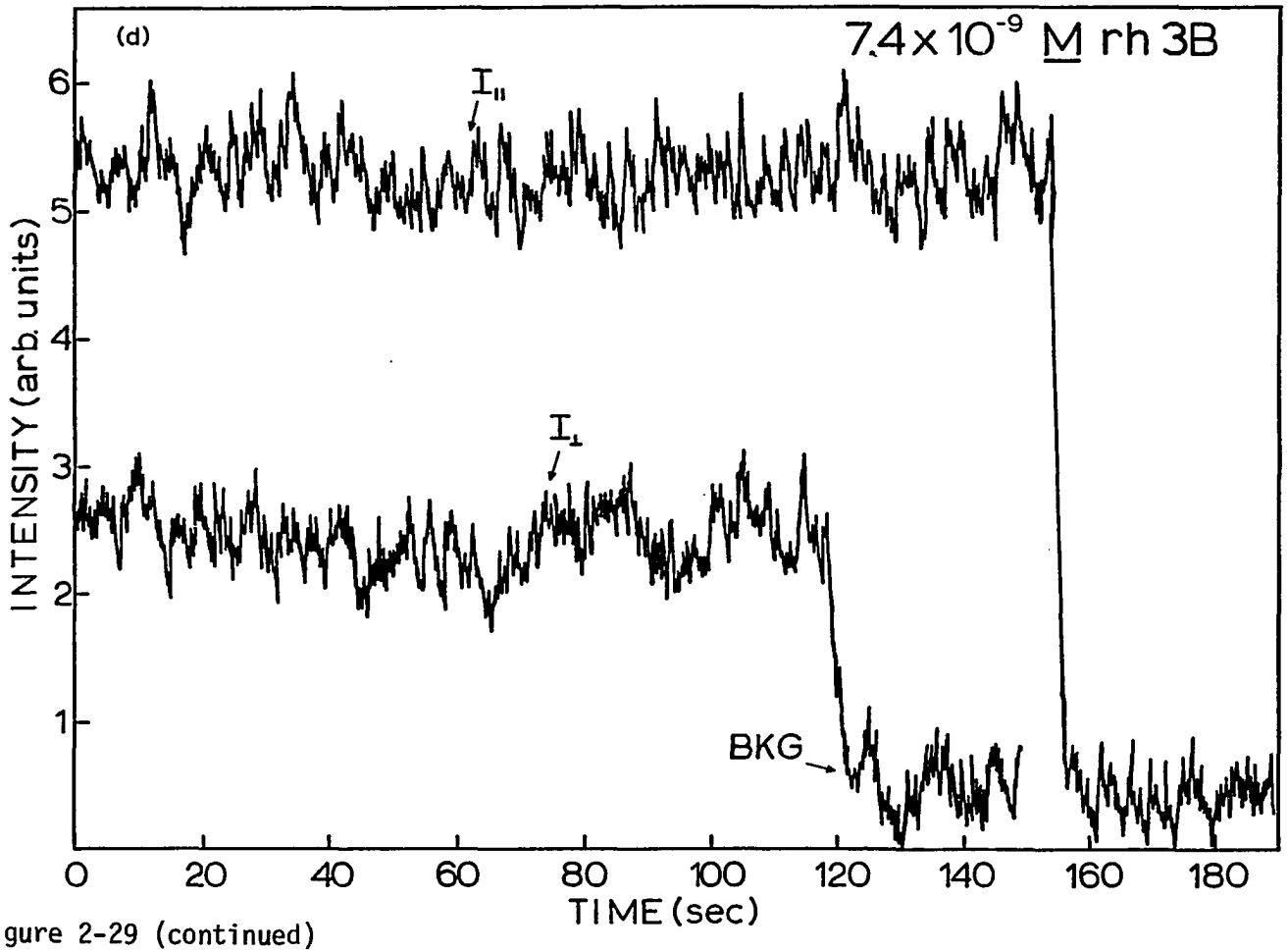

Figure 2-29 (continued)

three minutes. The laser intensity was approximately an order of magnitude greater than that used to measure fluorescence lifetimes.

A flat coated from 7.4×10^{-6} M rh3B was also tested for the time dependence of its fluorescence intensity. The initial decline in the intensity was $\sim$35% for the first minute of exposure, dropping to $\sim$5% decline per minute after three minutes. For samples coated from solution concentrations below 7.4×10^{-7} M, the time dependence of the fluorescence was less noticeable. The intensity decline, on a flat coated from 7.4×10^{-8} M rh3B, was $\sim$2% per minute of exposure. The decline was negligible for a flat coated from 7.4×10^{-9} M rh3B. The laser intensity, monitored over time ranges equivalent to those above, was stable. This coverage-dependent photochemistry precludes analysis of flats coated from rh3B concentrations greater than 7.4×10^{-7} M.

To minimize any effects due to photochemistry, the fluorescence decays were collected in the following order: an instrument function was collected and transferred to the computer; an $I_{\parallel}$ profile was collected in the first half of the MCA memory for 100 seconds; an $I_{\perp}$ profile was collected for 200 seconds in the second half of the MCA memory; another $I_{\parallel}$ profile was collected for 100 seconds and added to the $I_{\parallel}$ file stored in the first half of the MCA memory; the $I_{\parallel}$ and $I_{\perp}$ files were transferred to the computer and a magic angle profile (analyzing polarizer set at 45^{o} from $I_{\parallel}$) was collected for 200 seconds; and a second instrument function was collected to ensure that the laser pulse shape and detection electronics response had not deviated significantly from their earlier response.

The series of decays was collected a second time, while irradiating the same spot on the sample, to test whether photochemistry was affecting the fluorescence profiles. In addition, a second spot on each flat was irradiated and decays collected in order to test the macroscopic uniformity of the surface coverage.

CHAPTER III. DATA

Introduction

A primary goal of this energy transfer study is the measurement of rate constants $k_4(i)$ for populating individual vibronic levels i from the 0^0 level of aniline via single collisions with CO_2. Preliminary steps in the analysis entail recording aniline SVL fluorescence spectra under "collision-free" conditions and under "single-collision" conditions at several pressures of added gas.

Previous analyses of collision-induced energy transfer processes in S_1 polyatomic molecules have been effected through two related approaches (26,31). The kinetic models for energy transfer were identical in both approaches. The difference between the two schemes lay in the manner in which the raw data were plotted. Band intensities obtained from the spectra may be plotted in a form that varies linearly with either [M] or $[M]^{-1}$, where [M] is the collision gas pressure. Parmenter and Tang (26), studying benzene with several collision partners, plotted reciprocal relative intensities $(I-I_0)^{-1}$ vs. reciprocal pressures of added gas. Conversely, Chernoff and Rice (31) chose to plot L, a function of band intensity, vs. argon pressure for their aniline/argon system. Each of these approaches offers particular advantages and disadvantages as an analytical method for interpreting the aniline/CO_2 spectra.

Parmenter and Tang found an approximate value for the collision induced mode-to-mode energy transfer rate constant from the 6^1 vibronic

level as

$$k_4(i) = k_o^*/m, \tag{3.1}$$

where k_o^* is the decay rate constant of a growth level with no collision gas present, and m is the slope of the $(I-I_o)^{-1}$ vs. $[M]^{-1}$ plot. Rate constants attained using this method of analysis suffer from disproportionately large uncertainties caused by magnification of the error component in measurements of the relative band intensities when the added gas pressures are low.

Chernoff and Rice determined $k_4(i)$ values from plots of $I(1+K_S^*[M])$ vs. [M], where k_S^* is the Stern-Volmer quenching rate constant for the growth level under consideration, and I is the relevant band intensity uncorrected for emission resulting from processes other than aniline-argon collision induced energy transfer. The advantage of the technique is that the uncertainty in the slope is reduced from that in the previous method. This approach, however, requires knowledge of the overall collision induced decay rate constant k_4^* for depopulating a growth level via collisions with the added gas. Chernoff and Rice pumped each of the growth peaks directly and measured the decay as a function of added gas pressure using a single photon counting apparatus.

The Chernoff-Rice method is a superior technique for obtaining energy transfer rate constants. Its use in this work, however, is hindered by an inability to stimulate higher frequency transitions than the 0_0^0 vibronic transition, due to absorption of light by our $LiIO_3$ frequency doubling crystal. Conceivably, some of the growth levels could be populated

directly by pumping hot bands (Figure 3-1) or by switching to a KDP crystal for pumping frequencies higher than 34,040 cm^{-1}. Instead, an approximation is made which permits estimation of the collision induced decay rate k_4^* for growth levels without pumping them directly. This procedure will be discussed further in this chapter. All reported $k_4(i)$ values for the aniline/CO_2 system have been determined using this scheme.

In the ground electronic state, the NH_2 group on aniline is inclined from the ring plane by ∿42° (91). In the S_1 electronic state, the angle between the ring to nitrogen bond and the NH_2 plane is 30° ± 10° (92). Nonplanar aniline has only one element of point symmetry, a plane perpendicular to the ring plane, and so belongs to the point group C_s. Brand et al. (45) have shown that C_{2v} is the most practical point group classification when nonrigidity of the aniline molecule is accounted for. This classification acknowledges that inversion of the pyramidal structure produces prominent spectral features, but torsional splittings are not observed. Aniline has a $^1A_1$ ground and $^1B_2$ first excited singlet state, and the transition between these two electronic states is electric dipole-allowed. The transition dipole moment lies along the y-axis in the plane of the ring. Fluorescence bands from $'B_2 \rightarrow 'A_1$ electronic transitions have previously been assigned by Brand et al. (45). Table 3-1 lists approximate values for selected vibrational frequencies in the S_o and S_1 electronic states of aniline. These modes are depicted pictorially in Figure 3-2.

Figure 3-1. Aniline fluorescence excitation spectra using $LiIO_3$ crystal (a) and KDP crystal (b)

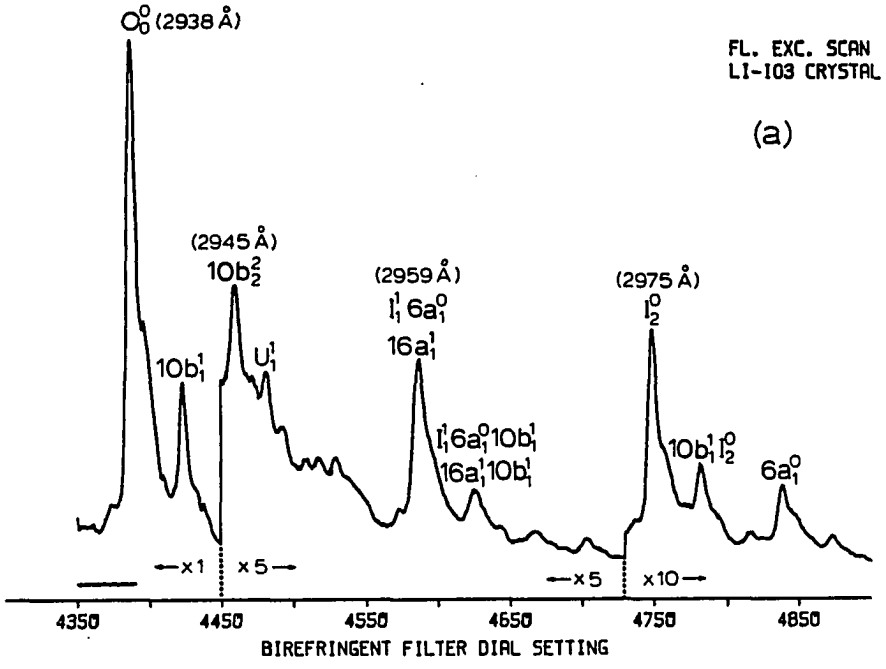
O_0^0 (2938 Å)
FL. EXC. SCAN
LI-103 CRYSTAL
(a)
(2945 Å)
$10b_2^2$
$10b_1^1$
U_1^1
(2959 Å)
$I_1^1 6a_1^0$
$16a_1^1$
$I_1^1 6a_1^0 10b_1^1$
$16a_1^1 10b_1^1$
(2975 Å)
I_2^0
$10b_1^1 I_2^0$
$6a_1^0$
←x1
x5→
←x5
x10→
4350
4450
4550
4650
4750
4850
BIREFRINGENT FILTER DIAL SETTING

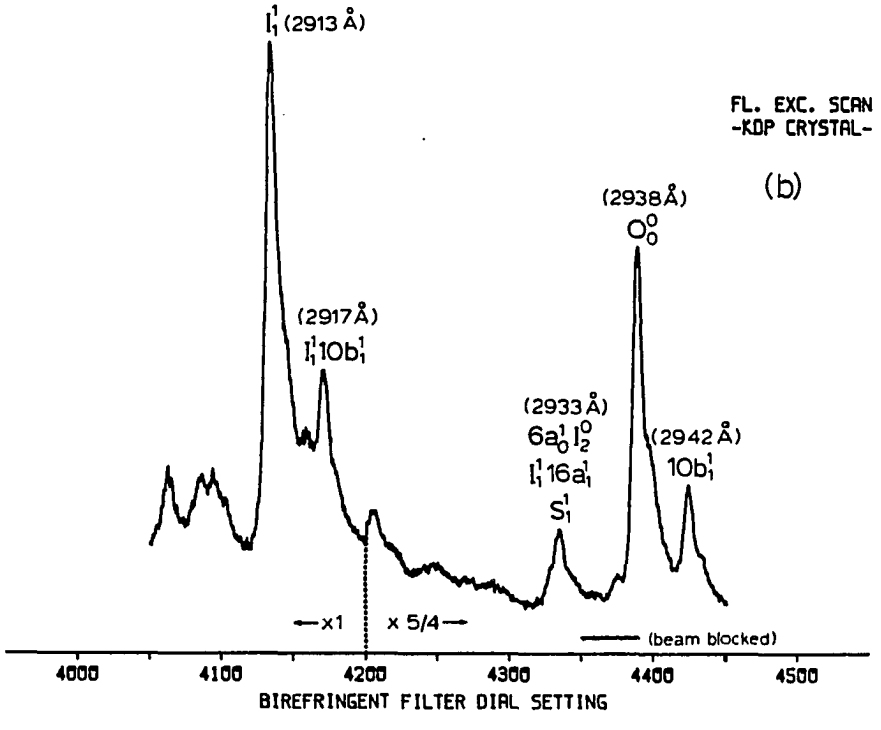
I_1^1 (2913 Å)
FL. EXC. SCAN
-KDP CRYSTAL-
(b)
(2938Å)
O_0^0
(2917Å)
$I_1^1 10b_1^1$
(2933 Å)
$6a_0^1 I_2^0$
$I_1^1 16a_1^1$
S_1^1
(2942 Å)
$10b_1^1$
←x1
x 5/4→
(beam blocked)
4000
4100
4200
4300
4400
4500
BIREFRINGENT FILTER DIAL SETTING

Table 3-1. Frequencies of selected vibrational modes[a]

Mode	Frequency, cm^{-1}	
	$^1A_1$[b]	$^1B_2$[c]
1	810	798
4	691	365[d]
6a	527	492
10b	233	193
15	390	350
16a	415	187[d]
16b	501	387[d]
I(v=1)	40.8[e]	337
I(v=2)	423[e]	760
I(v=3)	699[e]	1137

[a] 0_0^0 = 34,032 cm^{-1}.

[b] All values from Varsanyi (93), except where noted.

[c] All values from Brand et al. (45), except where noted.

[d] From Chernoff (32).

[e] From Larson et al. (91).

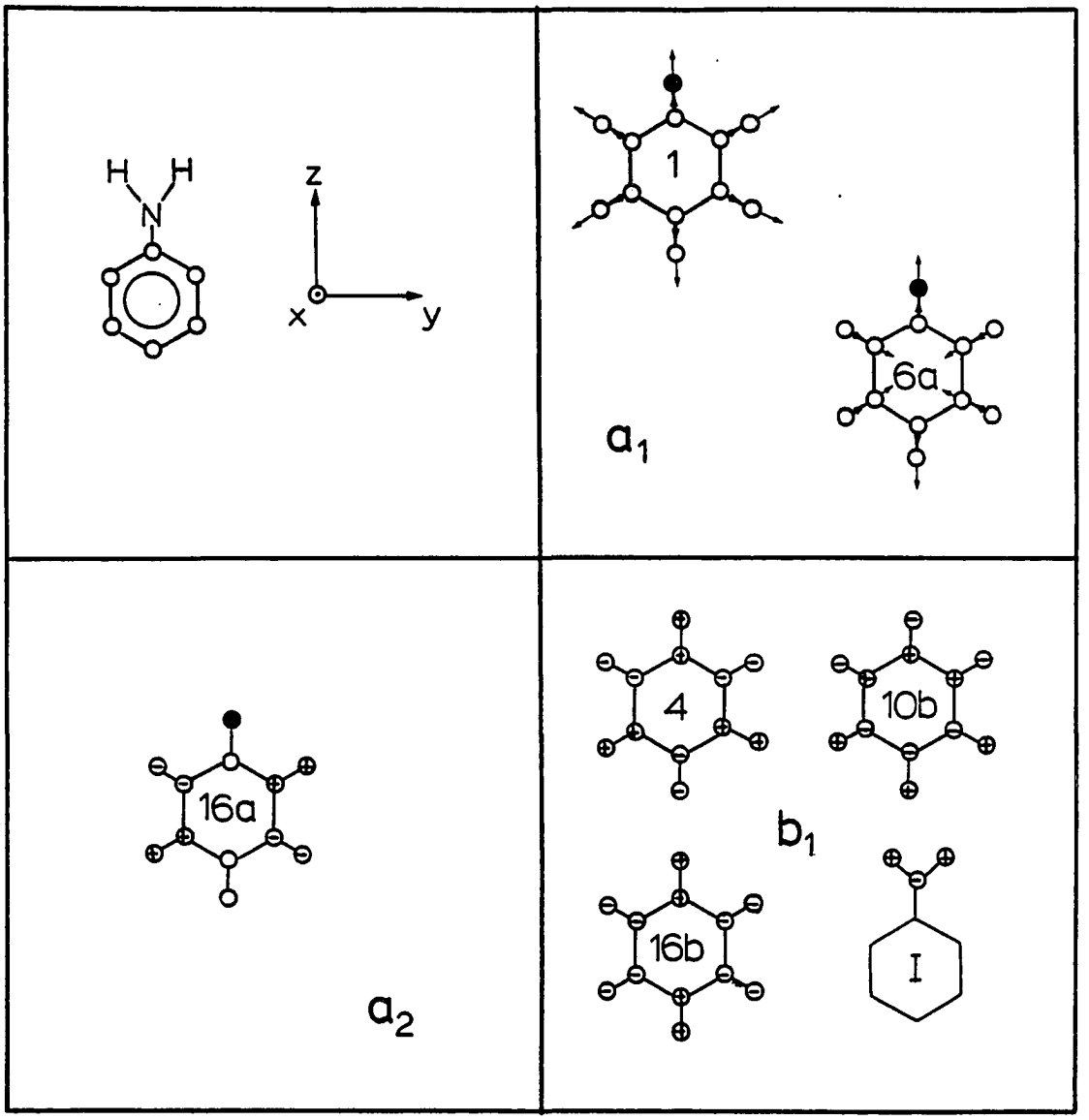

Figure 3-2. Selected vibrational modes of aniline

Kinetic Model for Collision Induced Energy Transfer

Parmenter and Tang presented a kinetic model to describe vibrational energy transfer in benzene (26). A similar kinetic scheme will be useful to describe the collision induced energy transfer process in aniline. Table 3-2 lists the notation used in the model.

Table 3-2. Symbols for the kinetic model

Symbol	Meaning
B	$^1A_1$ aniline in any vibrational level
B**	The directly excited 0^0 vibronic level in $^1B_2$ aniline
C	Aniline after nonradiative decay of the $^1B_2$ state
B*	$^1B_2$ aniline in any level other than the 0^0 level
B*(i)	A specific vibronic level of $^1B_2$ aniline other than the 0^0 level
B'	$^1B_2$ aniline in any level other than B*(i)
M	The added collision gas CO_2 in any state

Frequency doubled dye laser pulses are tuned to pump the 0^0_0 absorption band of aniline, producing B** via

$$B + h\nu \xrightarrow{I_a} B^{**}, \tag{3.2}$$

which may decay through fluorescence or via some unimolecular nonradiative pathway:

$$B^{**} \xrightarrow{k_1} B + h\nu, \tag{3.3}$$

$$B^{**} \xrightarrow{k_2} C. \tag{3.4}$$

Collisions with ground state aniline or added gas may deplete the initially pumped level through vibrational energy transfer. These processes are written as

$$B^{**} + B \xrightarrow{k_3} B^{*} + B, \tag{3.5}$$

$$B^{**} + M \xrightarrow{k_4} B^{*} + M. \tag{3.6}$$

A more explicit portrayal of the processes described by equations 3.5 and 3.6 may be given by

$$B^{**} + B \xrightarrow{k_3(i)} B^{*}(i) + B, \tag{3.7}$$

$$B^{**} + M \xrightarrow{k_4(i)} B^{*}(i) + M. \tag{3.8}$$

Decay of the new level $B^{*}(i)$ proceeds through channels analogous to those given for B^{**}, namely

$$B^{*}(i) \xrightarrow{k_1^{*}} B + h\nu, \tag{3.9}$$

$$B^{*}(i) \xrightarrow{k_2^{*}} C, \tag{3.10}$$

$$B^{*}(i) + B \xrightarrow{k_3^{*}} B' + B, \tag{3.11}$$

$$B^{*}(i) + M \xrightarrow{k_4^{*}} B' + M. \tag{3.12}$$

Aniline and CO_2 pressures are kept low enough that sequential processes such as

$$B^{**} + M \xrightarrow{k_4(j)} B^*(j) + M \xrightarrow{k_4^*(i)} B^*(i) + M \tag{3.13}$$

do not contribute significantly to the population of B*(i). The average time between B** - M collisions ranges from 3.04 to 18.3 nsec per hard sphere collision for added gas pressures of 30 and 5 torr, respectively. Since the lifetime of the S_1 state is ∿7 nsec (94), the assumption that on the average no more than one collision induced transition occurs during the lifetime of the excited state seems justified, provided that the overall collision induced decay rate k_4 expressed as a probability per hard sphere collision is less than ∿0.4.

From equations 3.7 - 3.12, the kinetic theory predicts

$$\frac{d[B^*(i)]}{dt} = k_3(i)[B][B^{**}] + k_4(i)[M][B^{**}] - k_1^*[B^*(i)] - k_2^*[B^*(i)]$$
$$- k_3^*[B][B^*(i)] + k_4^*[M][B^*(i)]. \tag{3.14}$$

In the steady state approximation, $\frac{d[B^*(i)]}{dt} = 0$ leads to

$$\frac{[B^*(i)]}{[B^{**}]} = \frac{k_3(i)[B] + k_4(i)[M]}{k_1^* + k_2^* + k_3^*[B] + k_4^*[M]}. \tag{3.15}$$

Fluorescence band intensities $I_f(i)$ can be used to determine level populations through the relation

$$I_f(i) = k_1(i)[B^*(i)], \tag{3.16}$$

where $k_1(i)$ is the radiative constant for the specific transition being

monitored. In this analysis, band heights will be used as a measure of band intensity due to uncertainty in measurements of band areas for overlapping peaks. The relationship between a growth peak height N and level population will, therefore, be written as

$$N = Q^*[B^*(i)], \tag{3.17}$$

where Q* is a factor relating the band height to level population. Similarly, for fluorescence emanating from the directly pumped level 0^o,

$$F_i = Q_i[B^{**}], \tag{3.18}$$

where F_i is the height of a reference band from the initial level, and Q_i is a factor related to the radiative rate constant for the transition. Let F be the summed height of three reference bands ($6a_1^o$, I_2^o, 1_1^o) emitted from the 0^o level. Similarly, Q is taken as the sum of Q_1, Q_2 and Q_3 -- factors relating the reference band heights to the population of B**. Equation 3.15 may be rewritten as

$$\frac{N}{F} = \frac{Q^*[B^*(i)]}{Q[B^{**}]} = \frac{k_3(i)[B] + k_4(i)[M]}{k_o^* + k_4^*[M]} \cdot \frac{Q^*}{Q}, \tag{3.19}$$

where $k_o^* \equiv k_1^* + k_2^* + k_3^*[B]$. k_o is defined similarly.

The height of the growth band N overestimates the level population of B*(i) resulting from collision induced processes. There are two other contributors to the fluorescence intensity measured for a growth band. The first is coincidental emission N_2 from the B** level, defined as

$$N_{2/F} = f. \tag{3.20}$$

The second is due to direct laser excitation of some population of the level B*(i). The Stern-Volmer relationship for decay of the level B*(i) and B** may be written as

$$\frac{N_3}{N_{30}} = \frac{k_o^*}{k_o^* + k_4^*[M]} = (1 + K_s^*[M])^{-1} \tag{3.21}$$

and

$$\frac{F}{F_o} = \frac{k_o}{k_o + k_4[M]} = (1 + K_s[M])^{-1} \tag{3.22}$$

respectively, where N_{30} and F_o are the emission intensities of the B*(i) and B** bands at zero added gas pressure. K_s and K_s^* are defined as $\frac{k_4}{k_o}$ and $\frac{k_4^*}{k_o^*}$, respectively. Combining equations 3.21 and 3.22 yields

$$\frac{N_3}{F} = \frac{1 + K_s[M]}{1 + K_s^*[M]} \cdot \frac{N_{30}}{F_o}, \tag{3.23}$$

the contribution to N/F from direct laser excitation of the level B*(i). Inclusion of the contributors presented in equations 3.20 and 3.23 to the right hand side of equation 3.19 leads to a relative band intensity

$$I = \frac{N}{F} = \frac{Q^*}{Q}\left[\frac{k_3(i)[B]+k_4(i)[M]}{k_o^*(1+K_s^*[M])}\right] + f + \frac{N_{30}}{F_o}\left(\frac{1+K_s[M]}{1+K_s^*[M]}\right). \tag{3.24}$$

Multiplying I through by $(1+K_s^*[M])$ forms a new function L, where

$$L = \frac{Q^*}{Q}\left(\frac{k_3(i)[B]+k_4(i)[M]}{k_o^*}\right) + f(1+K_s^*[M]) + \frac{N_{30}}{F_o}(1+K_s[M]). \tag{3.25}$$

Plotting L vs. [M] provides details of $k_4(i)$. Let m and b be the slope and intercept of this plot. Then

$$m = \frac{Q^*k_4(i)}{Qk_o^*} + fK_s^* + \frac{N_{30}K_s}{F_o} \tag{3.26}$$

and

$$b = \frac{Q^*k_3(i)[B]}{Qk_o^*} + f + \frac{N_{30}}{F_o} . \tag{3.27}$$

A value for the $\frac{Q^*k_4(i)}{Qk_o^*}$ term in equation 3.26 is necessary to calculate the rate constant for growth of the level B*(i) due to collision induced energy transfer. An approximation for this term is made by assuming

$$\frac{Q^*k_4(i)}{Qk_o^*} = m - bK_s^*. \tag{3.28}$$

The use of equation 3.28 does not lead to significant errors in the estimation of $k_4(i)$. The average time between B**-B collisions is 206 nsec per hard sphere collision. Thus, during the 7 nsec lifetime of the excited state, the energy transferred as a result of this process is considered negligible. Also assumed is that $K_s^* \approx K_s$, in accord with results obtained from the aniline/argon system (31). Thus, for data analysis $k_4(i)$ will be approximated as

$$k_4(i) = \frac{Qk_o^*}{Q^*}(m-bK_s^*). \tag{3.29}$$

Vibrational Energy Transfer from 0^0

The aniline single vibronic level fluorescence spectrum from 0° with no added CO_2 gas is shown in Figure 3-4(a). The same spectrum, shown in Figure 3-4(b) with higher sensitivity, points to the underlying growth bands present under nominally "collision-free" conditions.

Comparison of Figures 3-4(a) and 3-5(a) shows qualitatively the development of the growth bands in the aniline spectrum caused by collisions with CO_2. The sequence of plots in Figure 3-5 illustrates how quantitative values may be obtained for the growth level band intensities. The first scan (Figure 3-5(a)) is taken at a sensitivity which keeps the fluorescence from the directly pumped level on scale. Successive scans are taken at increased detection sensitivities to obtain more accurate values for fluorescence band intensities from growth levels B*(i). All band heights used for data analysis were obtained from plots where the relevant peak height is approximately full scale. These intensities are subsequently normalized to the heights of the fluorescence peaks emitted from 0^0 using an appropriate scale factor.

As was mentioned previously in equations 3.16 and 3.17, the Q factors are proportional to the radiative rate constants for a specific transition. For the allowed electronic transition $^1A_1 \rightarrow {}^1B_2$, application of the Born-Oppenheimer approximation and the Franck-Condon principle leads to an expression for Q as

$$Q \propto |M_e|^2 |\langle \phi_{v'} | \phi_{v''} \rangle|^2, \tag{3.30}$$

Figure 3-4. Aniline SVL fluorescence spectra with no collision gas. In (a), the fluorescence bands from the initially pumped level are kept on scale. The same spectrum recorded at higher sensitivity (b) shows growth levels populated by aniline-aniline collisions

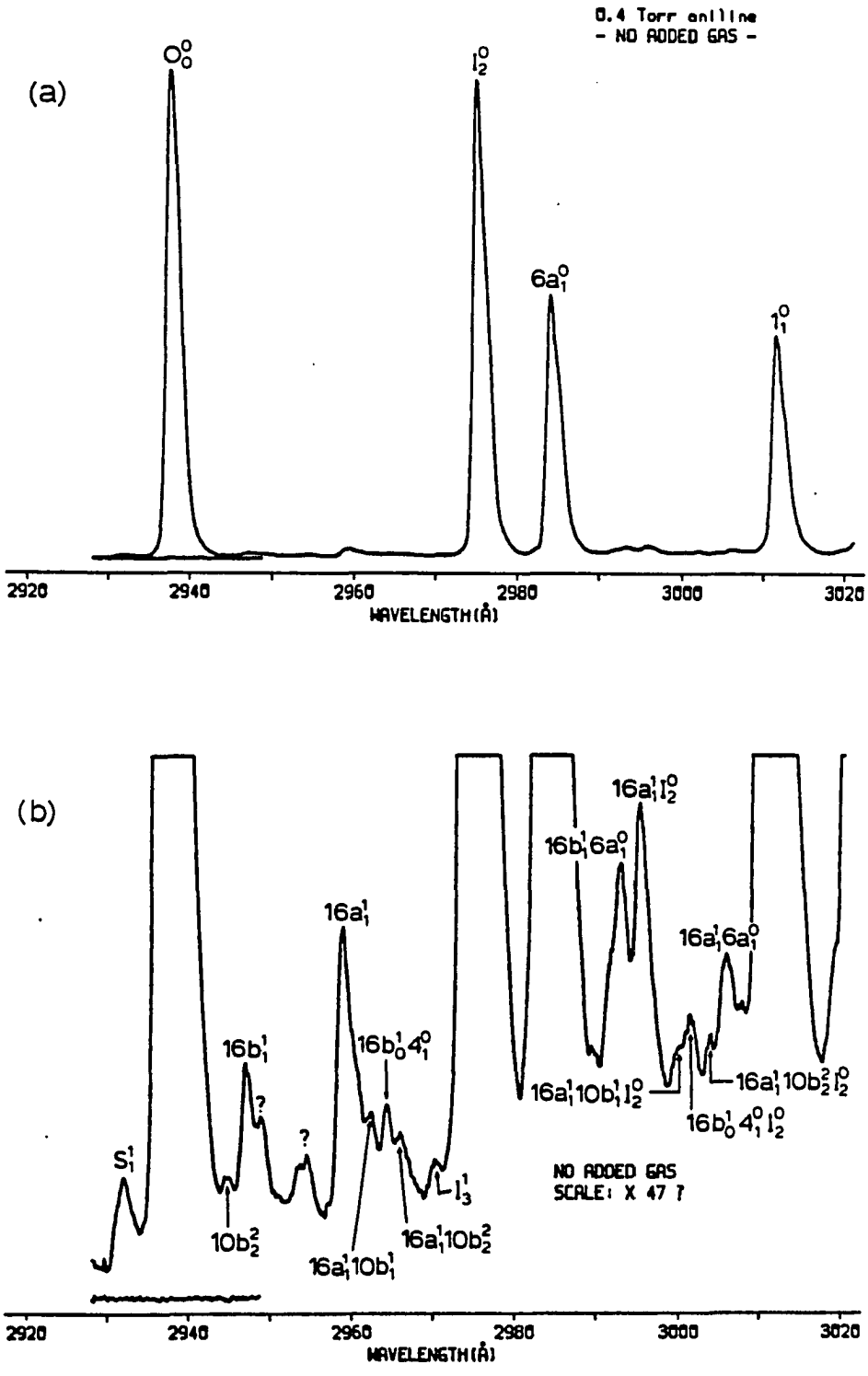
0.4 Torr aniline
- NO ADDED GAS -
(a)
0_0^0
1_2^0
$6a_1^0$
1_1^0
2920
2940
2960
2980
3000
3020
WAVELENGTH(Å)
(b)
$16a_1^1 1_2^0$
$16b_1^1 6a_1^0$
$16a_1^1$
$16a_1^1 6a_1^0$
$16b_1^1$
$16b_0^1 4_1^0$
$16a_1^1 10b_1^1 1_2^0$
$16a_1^1 10b_2^2 1_2^0$
$16b_0^1 4_1^0 1_2^0$
S_1^1
1_3^1
NO ADDED GAS
SCALE: X 47 ?
$10b_2^2$
$16a_1^1 10b_1^1$
$16a_1^1 10b_2^2$
2920
2940
2960
2980
3000
3020
WAVELENGTH(Å)

Figure 3-5. Aniline SVL fluorescence spectra with 20 torr CO_2 as the collision partner. In (a), at a scale x1, fluorescence originating from the pumped level 0° is on scale. The same spectrum recorded at scale factors of x3.4 and x7.5 for (b) and (c), respectively, shows fluorescence emanating from growth levels populated predominantly by aniline-CO_2 collisions. In (d), growth band fluorescence at frequencies higher than the 0_0^0 transition are shown at a scale factor x23

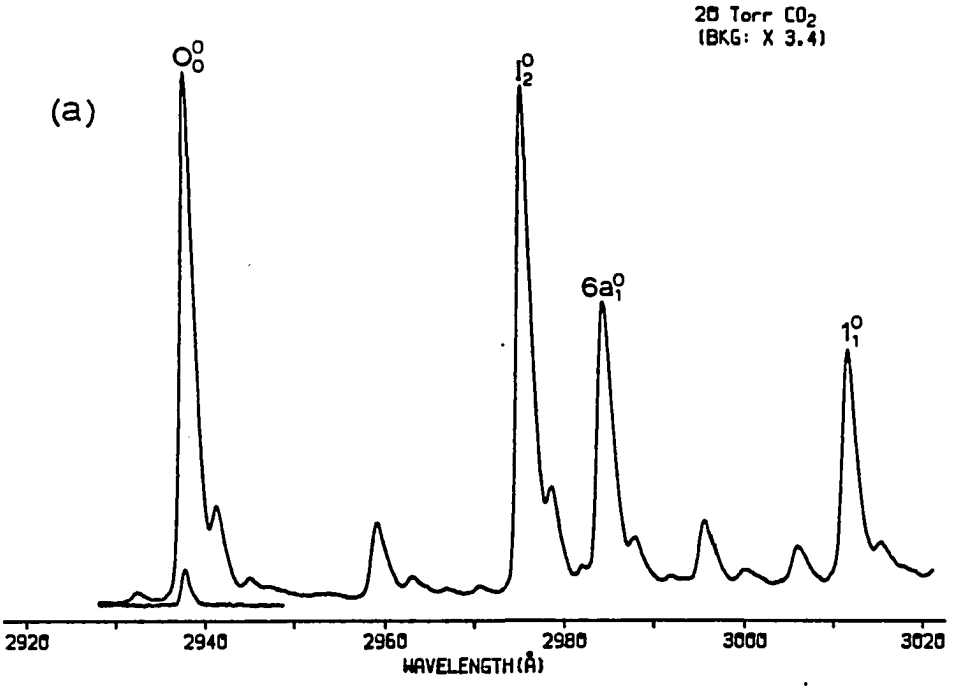
20 Torr CO_2
(BKG: X 3.4)
(a)
0_0^0
1_2^0
$6a_1^0$
1_1^0
2920
2940
2960
2980
3000
3020
WAVELENGTH(Å)

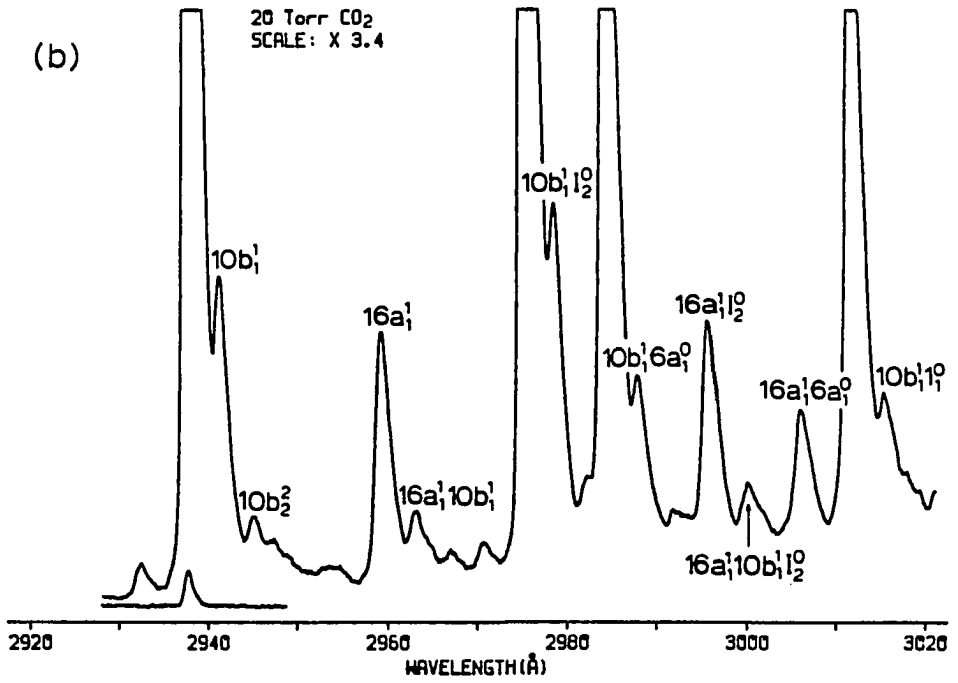
20 Torr CO_2
SCALE: X 3.4
(b)
$10b_1^1$
$10b_2^2$
$16a_1^1$
$16a_1^1 10b_1^1$
$10b_1^1 1_2^0$
$10b_1^1 6a_1^0$
$16a_1^1 1_2^0$
$16a_1^1 6a_1^0$
$10b_1^1 1_1^0$
$16a_1^1 10b_1^1 1_2^0$
2920
2940
2960
2980
3000
3020
WAVELENGTH(Å)

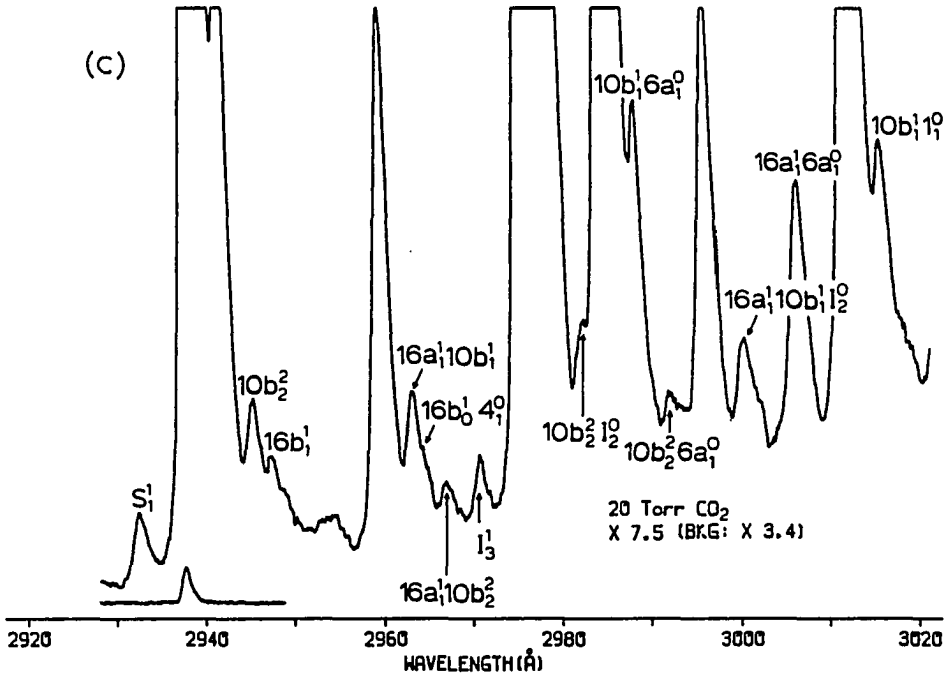

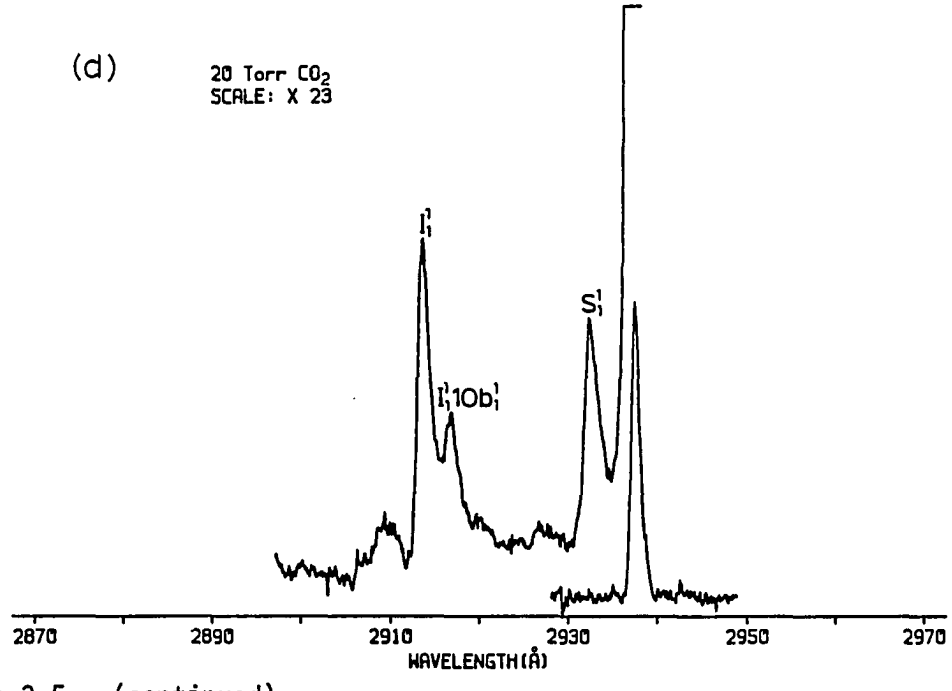

Figure 3-5. (continued)

Figure 3-6. Aniline fluorescence spectra showing intensity trends for transitions containing an inactive mode. Emission from the level 10b' is identical in appearance to emission from 0°, but shifted by 40 cm^{-1}

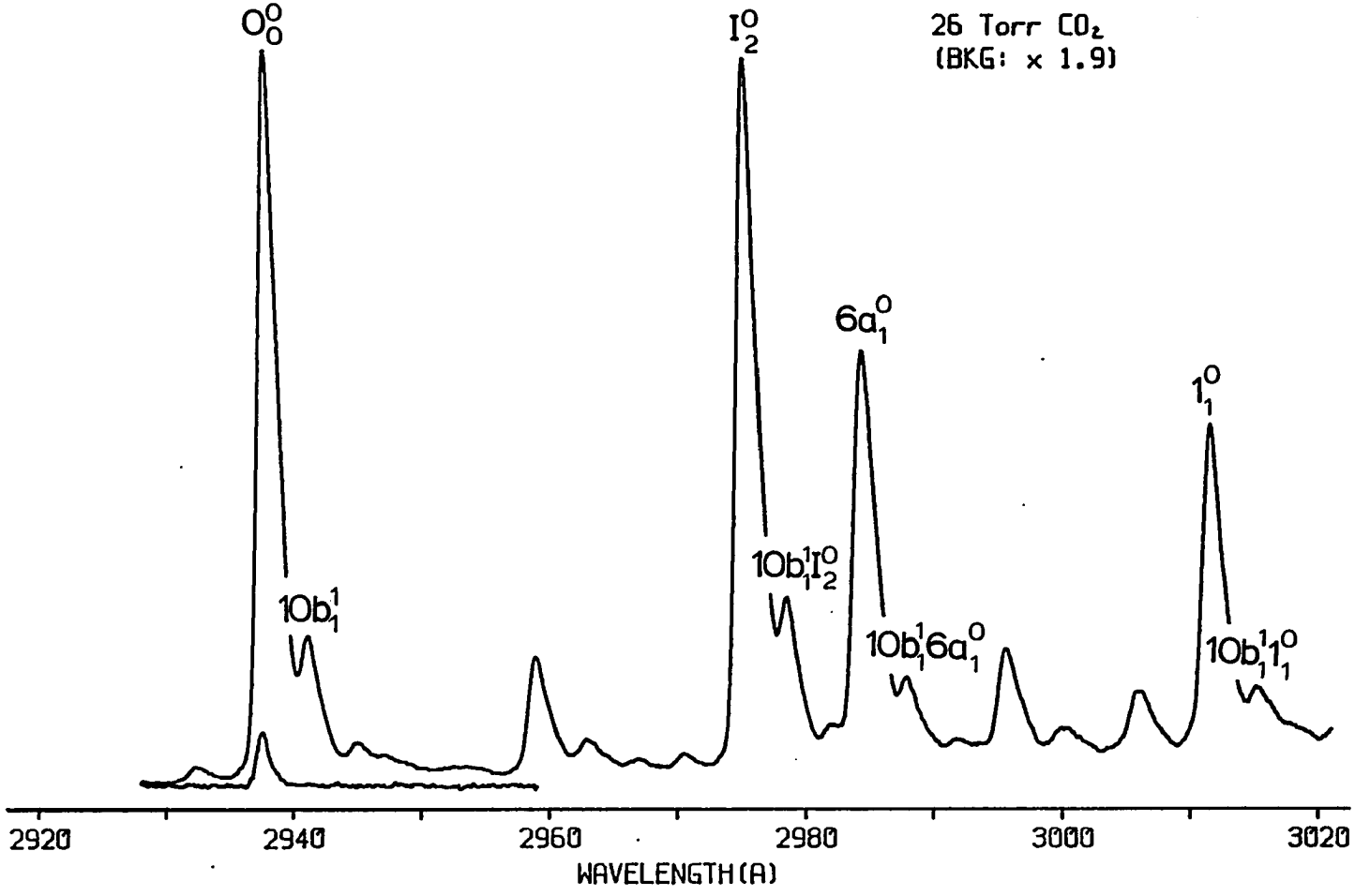
0_0^0
$10b_1^1$
1_2^0
$10b_1^1 1_2^0$
$6a_1^0$
$10b_1^1 6a_1^0$
1_1^0
$10b_1^1 1_1^0$
26 Torr CO_2
(BKG: x 1.9)
2920
2940
2960
2980
3000
3020
WAVELENGTH(A)

where M_e is the electronic dipole matrix element and $|\langle\phi_{v'}|\phi_{v''}\rangle|^2$ is the Franck-Condon factor. Q and Q* will always appear in the form of ratios. Therefore, only values for the Franck-Condon factors are needed to determine relative values for Q because the $S_1 \leftarrow S_0$ transition in aniline is strongly allowed and $|M_e|^2$ is constant. Based on equation 3.16, these factors can be evaluated from

$$\frac{I_f(i)}{I_f} = \frac{k_1(i)[B^{**}]}{k_1[B^{**}]} = |\langle\phi_{v'}|\phi_{v''}\rangle|^2, \tag{3.31}$$

where I_f is the summed intensity of all fluorescence originating from the directly pumped level B**. For this work, only the 0^0 level was directly pumped. Q* factors for combination levels containing inactive modes can still be determined, however, without directly exciting the emitting level. It was observed that these combination levels have emission spectra identical in appearance to the spectrum of the active fundamental but shifted in frequency (32). This effect is depicted in Figure 3-6 for aniline with 26 torr of added CO_2. Each fluorescence band emitted from $10b_1^1$ is shifted by 40 cm^{-1} from the related transition from 0^0. At 26 torr of CO_2, the ratios of intensities for $10b_1^1 I_2^0/I_2^0$, $10b_1^1 6a_1^0/6a_1^0$, and $10b_1^1 1_1^0/1_1^0$ are 0.26, 0.25 and 0.28, respectively. The overlap integral for $10b_1^1 I_2^0$ will be considered as

$$\langle 10b^1 I^0|10b_1 I_2\rangle = \langle 10b^1|10b_1\rangle \cdot \langle I^0|I_2\rangle = \langle I^0|I_2\rangle. \tag{3.32}$$

Thus, the relations of $Q^*(10b_1^1 I_2^0) = Q(I_2^0)$, $Q^*(10b_1^1 6a_1^0) = Q(6a_1^0)$ and

$Q^*(10b_1^1 1_1^0) = Q(1_1^0)$ are formed. Similar relationships are developed for all transitions containing inactive modes. All other conversion factors are accepted as the values obtained by Chernoff and Rice (31) scaled to the experimentally determined values from this work. These values are listed in Table 3-3.

Table 3-3. Population to band height conversion factors

Transition	Conversion factor (Q)[a]
I_2^0	100.0
0_0^0	80.9
$6a_1^0$	58.2
1_1^0	49.3
I_1^1	86.1[b]

[a]All conversion factors are scaled relative to $Q(I_2^0) = 100$.

[b]Calculated from Chernoff and Rice (31).

All Q factors are normalized to $Q(I_2^0) = 100$. The Q factor for the 0_0^0 transition is estimated from the intensity ratio $I_f(10b_1^1)/I_f(10b_1^1 I_2^0)$, since laser scatter will affect the measurement of $I_f(0_0^0)/I_f(I_2^0)$. The ratio $I_f(i)/I_f(I_2^0)$, where i represents a fluorescence band originating from 0^0, was measured at each CO_2 pressure. The average of these measurements was used to determine the Q factor for the transition. Similar fluctuations were observed for intensity ratios containing inactive modes,

such as $I_f(10b_1^1 I_2^0)/I_f(I_2^0)$ and $I_f(10b_1^1 6a_1^0)/I_f(6a_1^0)$. Based on the uncertainty in measured intensity ratios between various collision gas pressures, an error component of 15% is assigned to all Q factors.

Determination of $k_4(i)$ requires knowledge of the Stern-Volmer quenching rate constants K_s^* for the growth levels. Measurement of decay rates is not possible with this apparatus, warranting an indirect approach for estimating K_s^*. A first step in the approximation is the measurement of k_4 for the level 0^0. The Stern-Volmer relationship for decay of this directly pumped level yields

$$\frac{I_f^0(0^0)}{I_f(0^0)} = 1 + \frac{k_4}{k_o}[M], \tag{3.33}$$

where $I_f(0^0)$ and $I_f^0(0^0)$ are total emission intensities from the 0° level with and without added gas. This ratio of intensities may also be written as

$$\frac{I_f(0^0)}{I_f(0^0)} = \frac{Q'[B^{**}]^\circ}{Q'[B^{**}]} = \frac{[B^{**}]^\circ}{[B^{**}]}\ , \tag{3.34}$$

where $[B^{**}]^\circ$ is the 0^0 level population with no added gas, and Q' is the sum of all Q factors for emission from 0^0. Experimental conditions varied between the measurement of $I_f^0(0^0)$ and $I_f(0^0)$, prompting the assumption

$$[B^{**}]^\circ = [B^{**}] + \sum_i [B^*(i)]. \tag{3.35}$$

Using equation 3.17, level populations for B*(i) can be determined from

fluorescence intensities. Equation 3.34 may be rewritten

$$\frac{I_f^o(0^o)}{I_f(0^o)} = \frac{[B^{**}] + \sum_i [B^*(i)]}{[B^{**}]} = 1 + \frac{\sum_i (I_f(i)/Q^*(i))avg}{I_f(0^o)/Q'} \quad . \tag{3.36}$$

$(I_f(i)/Q^*(i))avg$ is defined as the sum of $I_f(i)/Q^*(i)$ for each band emitted from the level $B^*(i)$ divided by the number of bands originating from $B^*(i)$. $I_f^o(i)$, the growth peak fluorescence intensity with no added gas, is subtracted from $I_f(i)$ at each pressure in equation 3.36. The difference is plotted in Figure 3-7 as $I_f^o(0^o)/I_f(0^o)$ vs. $[CO_2]$. The resulting slope is 0.0177 $torr^{-1}$ - the ratio k_4/k_o. k_o has been determined to be 134 x 10^6 sec^{-1} (31), leading to a value for k_4 of 2.37 x 10^6 $torr^{-1}$ sec^{-1}.

An approximation proposed by Vandersall et al. (42) permits estimation of k_4^* for levels which decay rates as a function of added gas are not known. For CH_3F and H_2O as collision partners with aniline, values of k_4^* were determined experimentally for 3 and 2 emitting levels, respectively (Table 3-4). The ratios $k_4(CH_3F)/k_4(Ar)$ and $k_4(H_2O)/k_4(Ar)$ were each averaged over all measured emitting levels to determine appropriate factors for approximating $k_4(CH_3)$ and $k_4(H_2O)$ for emitting levels which were not measured directly. The factors determined were 5 and 10 for CH_3F and H_2O, respectively. Similarly for CO_2, values of $k_4(CO_2)$ will be estimated by multiplying the appropriate value of $k_4(Ar)$ by 2.15. The average uncertainty for k_4 values obtained through this method is 40%. Other rate constants prerequisite to the determination of K_s^* are the constants k_o^*. Previously determined literature values for k_o^* are used

Figure 3-7. Stern-Volmer plot for the decay of the 0° level as a function of added gas pressure. $I_f^o(0°)$ is obtained indirectly from measurements of level populations [B**] and [B*(i)]

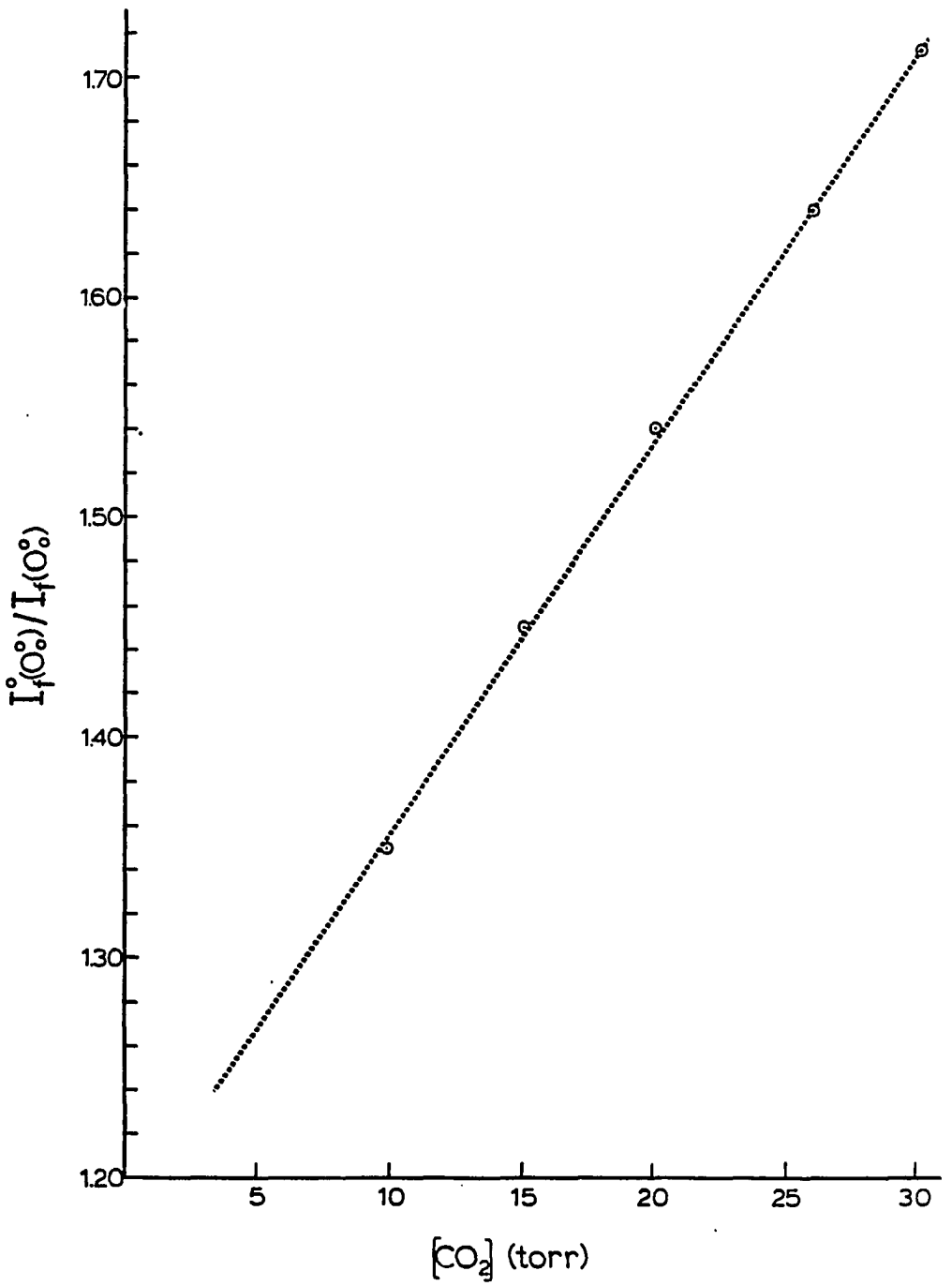
1.70
1.60
1.50
1.40
1.30
1.20
$I_f^\circ(0^\circ)/I_f(0^\circ)$
5
10
15
20
25
30
$[CO_2]$ (torr)

Table 3-4. Overall collision induced decay rate k_4 expressed in units of 10^6 $torr^{-1}sec^{-1}$

Emitting level	Ar[a]	CH_3F[b]	H_2O[b]	CO_2
0^a	1.1±0.1	6.1±0.2	13.8±1.0	2.4±0.3
10b'	4.1±0.5	16.2±1.1		
I'	2.6±0.1	19.0±0.7	23.4±0.5	

[a]From Chernoff and Rice (31).

[b]From Vandersall, Chernoff and Rice (42).

in this work (31). Calculated Stern-Volmer quenching rate constants are tabulated in Table 3-5 along with values for k_o^* and k_4^*.

Once K_s^* values have been determined, it is possible to evaluate $(m\text{-}bK_s^*)$ from equation 3.28. A plot of L vs. [M] is presented in Figure 3-8 for the growth band $16a_1^1$. There is a distinct upward curvature in the plot for CO_2 pressures greater than 15 torr. Similar observations were made for every growth band L vs. [M] plot. Probable causes for the observed behavior will be discussed in the next chapter. The effect of the deviations on $(m\text{-}bK_s^*)$ is presented in Table 3-6. Values of $(m\text{-}bK_s^*)$ using only those points lying along the linear portion of the L vs. [M] plots will lead to the most accurate measurement of the rate constants $k_4(i)$. All reported values of $k_4(i)$, unless noted otherwise, will be derived from data obtained at CO_2 pressures between 5 and 15 torr.

Table 3-5. Rate constants for overall decay of vibronic levels

Emitting level	k^*_o [a] ($10^6 sec^{-1}$)	k^*_4 ($10^6 torr^{-1} sec^{-1}$)	K^*_s ($torr^{-1}$)
0^{0} [b]	134 ± 1	2.4 ± 0.4	0.0176
$10b^1$	143 ± 3	9.0 ± 4.0	0.0616
$10b^2$	157 ± 2	10.0 ± 4.0	0.0630
$16a^1$	147 ± 2	5.5 ± 2.0	0.0380
$16b^1$	137 ± 4	4.5 ± 2.0	0.0314
I^1	122 ± 1	5.5 ± 2.0	0.0458
$I^1 10b^1$	131 ± 2	12.0 ± 5.0	0.0903
$16a^1 10b^1$	151 ± 4	8.0 ± 3.0	0.0527
$16a^1 10b^2$ [c]	151	8.0	0.0527

[a] From Chernoff and Rice (31).

[b] Values for 0^0 are defined as k_o, k_4 and K_s, respectively.

[c] Values for $16a^1 10b^2$ are assumed to equal the values determined for $16a^1 10b^1$.

Table 3-6. Effect of L vs. [M] data points[a] on ($m-bK_s^*$)

	$m-bK_s^*$, ($10^{-3}torr^{-1}$)			
Band	3 points	4 points	5 points	6 points
$10b_1^1$	6.98	7.47	7.63	7.84
$10b_1^1I_2^o$	8.05	8.83	9.34	9.88
$10b_1^16a_1^o$	4.83	5.16	5.49	5.92
$10b_1^1I_1^o$	4.14	4.62	5.25	5.47
$10b_2^2$	2.56	2.83	2.96	3.06
$10b_2^2I_2^o$	3.44	3.65	3.96	4.24
$10b_2^26a_1^o$	2.14	2.30	2.63	3.07
$16a_1^1$	5.04	5.36	5.54	5.62
$16a_1^1I_2^o$	5.34	5.44	5.61	5.77
$16a_1^16a_1^o$	3.70	3.87	4.06	4.39
$16b_1^1$	1.05	1.08	1.05	1.09
I_1^1	1.09	1.16	1.36	1.45
$I_1^110b_1^1$	0.95	1.05	1.20	1.26
$16a_1^110b_1^1$	2.14	2.45	2.74	2.82
$16a_1^110b_1^1I_2^o$	2.71	3.03	3.32	3.65
$16a_1^110b_2^2$	1.27	1.32	1.45	1.62

[a]Data points included are successive, beginning from 5 torr.

Figure 3-8. L vs. [M] plot used to derive mode-to-mode collision induced energy transfer rate constants. In (a), the linear regression includes all six data points. In (b), the linear regression includes only the three lowest pressure data points. The least squares fit in (b) is extrapolated to higher pressures to show the curvature in the data points in this region

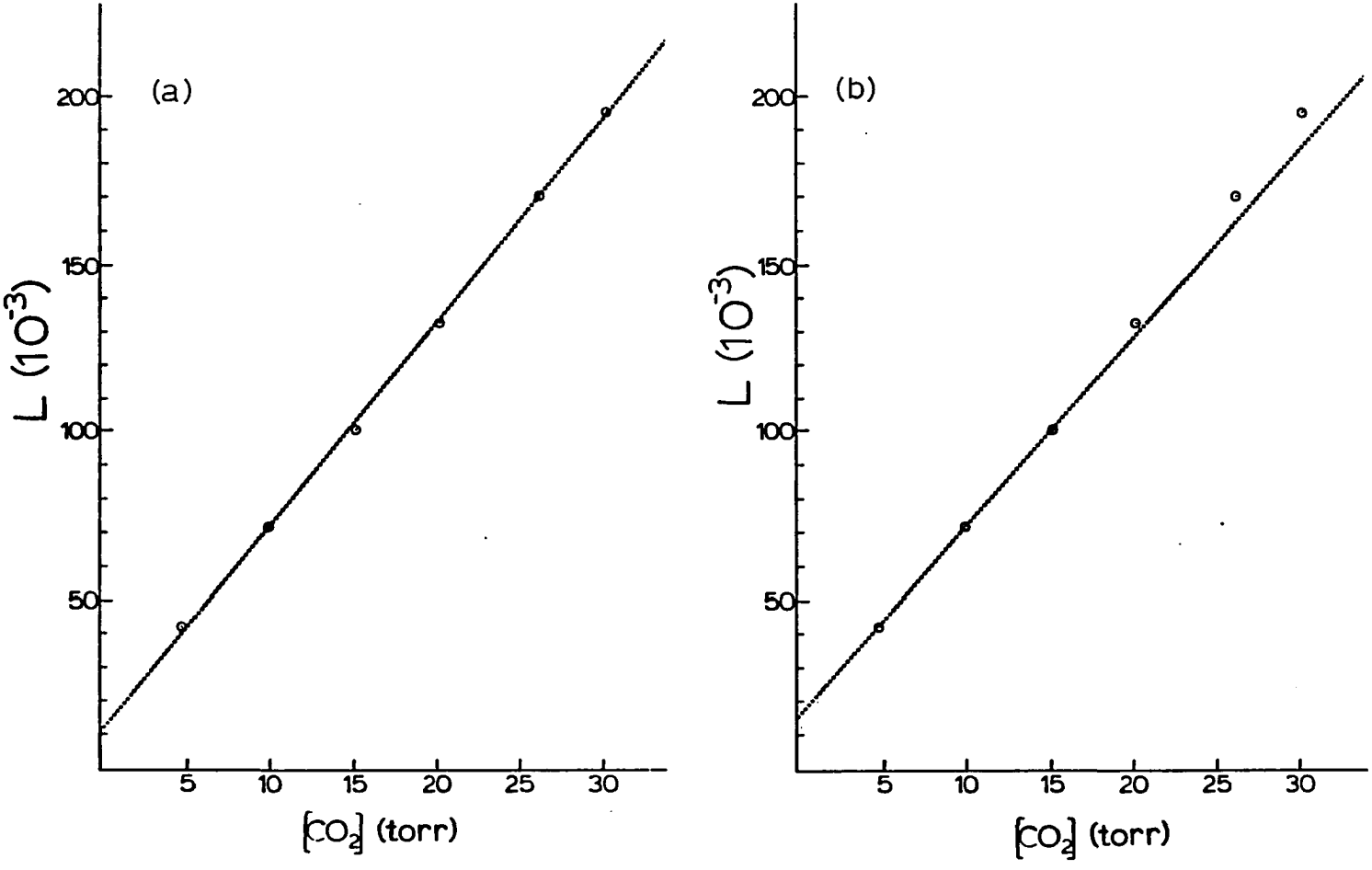
(a)
(b)
200
150
100
50
L (10^-3)
5
10
15
20
25
30
[CO2] (torr)

The uncertainty in $(m-bK_s^*)$ is evaluated by initially considering each component of the term separately. Uncertainty in the slope is expressed as (95)

$$\frac{\sigma_m}{m} = \frac{(6s^2/\Delta)^{\frac{1}{2}}}{m}, \tag{3.37}$$

where s^2 and Δ are defined as

$$s^2 = \frac{1}{4}\,(\Sigma L_i^2 + 6b^2 + m^2\Sigma M_i^2 - 2b\Sigma L_i - 2m\Sigma M_i L_i + 2mb\Sigma M_i)_1\,, \tag{3.38}$$

$$\Delta \equiv 6\Sigma M_i^2 - (\Sigma M_i)^2\,. \tag{3.39}$$

L_i is the value of L at a specific pressure of added gas $[M_i]$, and the summation Σ is an abbreviated form of $\sum_{i=i}^{6}$. Incertitude in the value of the intercept is written as (95)

$$\frac{\sigma_b}{b} = \frac{(\frac{s^2}{\Delta}\Sigma M_i^2)^{\frac{1}{2}}}{b}. \tag{3.40}$$

Uncertainty in K_s^* has been expressed previously as $\frac{\Delta K_s^*}{K_s^*} = 40\%$. The uncertainty in $(m-bK_s^*)$ is written

$$\frac{\Delta(m-bK_s^*)}{(m-bK_s^*)} = \frac{\{\sigma_m^2 + (K_s^*\sigma_b)^2 + (b\Delta K_s^*)^2\}^{\frac{1}{2}}}{(m-bK_s^*)}. \tag{3.41}$$

For the $16a_1^1$ transition

$$\Delta(m-bK_s^*) = \{(10^{-4}) + (10^{-5}) + (0.06)\}^{\frac{1}{2}}, \tag{3.42}$$

for an uncertainty of 5%. It should be noted that the 40% uncertainty in

K_s^* has a relatively small effect on the magnitude of $^{\Delta(m-bK_s^*)}/(m-bK_s^*)$. The error components of $(m-bK_s^*)$ for other growth bands are listed in Table 3-7.

Values for the mode-to-mode rate constants $k_4(i)$ calculated from equation 3.29 are presented in Table 3-8. Four error components are considered in an evaluation of the uncertainty in $k_4(i)$. The uncertainties in Q, k_o^*, and Q* are 9%, 2% and 15% for all growth levels. The uncertainty in $(m-bK_s^*)$ must be determined for each new level. Thus, for the transition, $16a_1^1$, where the uncertainty in $k_4(i)$ is expressed as

$$\frac{\Delta k_4(i)}{k_4(i)} = \{(\frac{\Delta(m-bK_s^*)}{(m-bK_s^*)})^2 + (\frac{\Delta Q}{Q})^2 + (\frac{\Delta k_o^*}{k_o^*})^2 + (\frac{\Delta Q^*}{Q^*})^2\}^{\frac{1}{2}} , \qquad (3.43)$$

an error component of 18% is estimated.

Table 3-7. Slopes, intercepts, and $(m-bK_s^*)$ values[a] for L vs. [M] plots, including individual error components

Band	Slope, m (10^{-3}torr^{-1})	Intercept, b (10^{-3})	$(m-bK_s^*)$ (10^{-3}torr^{-1})
$10b_1^1$	8.55 ± 0.04	25.57 ± 0.39	6.98 ± 0.63
$10b_1^1I_2^o$	10.21 ± 0.02	34.56 ± 0.24	8.05 ± 0.85
$10b_1^16a_1^o$	5.94 ± 0.01	18.03 ± 0.07	4.83 ± 0.44
$10b_1^1I_1^o$	5.30 ± 0.03	18.81 ± 0.32	4.14 ± 0.46
$10b_2^2$	2.63 ± 0.03	1.17 ± 0.37	2.56 ± 0.05
$10b_2^2I_2^o$	3.68 ± 0.06	3.79 ± 0.65	3.44 ± 0.12
$10b_2^26a_1^o$	2.55 ± 0.03	6.44 ± 0.37	2.14 ± 0.17
$16a_1^1$	5.63 ± 0.01	15.49 ± 0.08	5.04 ± 0.24
$16a_1^1I_2^o$	5.97 ± 0.02	16.74 ± 0.25	5.34 ± 0.26
$16a_1^16a_1^o$	4.09 ± 0.07	10.35 ± 0.71	3.70 ± 0.17
$16b_1^1$	1.21 ± 0.08	5.09 ± 0.82	1.05 ± 0.10
I_1^1	1.20 ± 0.07	2.32 ± 0.76	1.09 ± 0.09
$I_1^110b_1^1$	0.95 ± 0.04	-0.13 ± 0.76	0.95 ± 0.06
$16a_1^110b_1^1$	2.34 ± 0.15	3.57 ± 0.44	2.14 ± 0.18
$16a_1^110b_1^1I_2^o$	2.95 ± 0.02	4.62 ± 1.58	2.71 ± 0.10
$16a_1^110b_2^2$	1.38 ± 0.04	2.27 ± 0.44	1.27 ± 0.07

[a]Calculated using the three lowest CO_2 pressures.

Table 3-8. Observed rate constants $k_4(i)$ for mode-to-mode vibrational energy transfer in S_1 aniline for CO_2 as a collision partner

Level	Band	$k_4(i)$ ($10^6 torr^{-1} sec^{-1}$)	Uncertainty (%)	Avg. $k_4(i)$ ($10^6 torr^{-1} sec^{-1}$)
$10b^1$	$10b_1^1$	2.56	20	2.48
	$10b_1^1 I_2^o$	2.39	21	
	$10b_1^1 6a_1^o$	2.46	20	
	$10b_1^1 I_1^o$	2.49	21	
$10b^2$	$10b_2^2$	1.03	18	1.12
	$10b_2^2 I_2^o$	1.12	18	
	$10b_2^2 6a_1^o$	1.20	19	
$16b^1$	$16a_1^1$	1.90	18	1.82
	$16a_1^1 I_2^o$	1.63	18	
	$16a_1^1 6a_1^o$	1.94	18	
$16b^1$	$16b^1$	0.37	20	0.37
I^1	I_1^1	0.32	19	0.32
$I^1 10b^1$	$I_1^1 10b_1^1$	0.30	19	0.30
$16a^1 10b^1$	$16a_1^1 10b_1^1$	0.83	20	0.84
	$16a_1^1 10b_1^1 I_2^o$	0.85	18	
$16a^1 10b^2$	$16a_1^1 10b_2^2$	0.49	18	0.49

CHAPTER IV. DISCUSSION

Due to a systematic error not accounted for in the error analysis of Chapter III, the summation of individual calculated mode-to-mode energy transfer rate constants $k_4(i)$ exceeds the overall calculated collision induced decay rate k_4 by a factor of 3.27 for the aniline/CO_2 system. This result is not unexpected, however. When the 0^o level of aniline was pumped and argon used as the collision partner, Chernoff and Rice (31) found that the ratio $\Sigma k_4(i):k_4$ was 1.91:1. Similarly, for the aniline/H_2O and aniline/CH_3F systems (42), the sum of the mode specific collision induced rates outweighed the overall collision induced rate. The ratios for H_2O and CH_3F as the collision partner, respectively, were 1.37:1 and 2.16:1, when the 0^o level of aniline was initially pumped. Chernoff and Rice reported that the discrepancy between $\Sigma k_4(i)$ and k_4 for the aniline-argon system resulted from an underdetermined systematic error which their error analysis failed to identify (31). Vandersall et al. (42) did not comment on the disparity between $\Sigma k_4(i)$ and k_4 for their systems of aniline with H_2O or CH_3F as the collision gas.

As a preliminary study to the aniline/CO_2 analysis, the aniline/argon system was reanalyzed using the experimental arrangement shown in Figure 2-5. Values of $k_4(i)$ for collision induced decay of the 0^o level of aniline were obtained using both L vs. [M] and $(I-I_0)^{-1}$ vs. $[M]^{-1}$ plots. The rate constants so calculated agreed with one another, as well as with the results presented by Chernoff and Rice (31). The close agreement indicates that the undertermined errors in the rate constants $k_4(i)$

are probably due to a systematic error in measured fluorescence band intensities rather than an inherent error in the analytical method.

In the data analysis for the aniline/CO_2 system, individual rate constants $k_4(i)$ were corrected for fluorescence intensity resulting from coincidental emission at the growth band wavelength by the initially pumped level, and from direct laser excitation of some population of the growth level. Growth level population resulting from aniline-aniline collisions raises the intercept b of the L vs. [M] plots. Since the term bK_s^* amounts to about a 3 to 5 percent correction subtracted from the slope of the L vs. [M] plot, omission of aniline-aniline collisions as a contributor to growth band intensities results in $k_4(i)$ values which are systematically $\sim$1% too small. This small error should have no significant effect on the values of $k_4(i)$, considering the 20% uncertainty in the measurements.

Another possible source of error which could have a greater impact on the calculated rates concerns spectral congestion in the aniline fluorescence spectra. It was mentioned that growth band intensities are corrected for coincidental emission of light from the 0^0 level. However, no correction is made for growth bands which overlap each other. Since any two neighboring bands would grow as the pressure of the collision gas is increased, it is possible that a weak growth band on the shoulder of a strong growth peak will grow at a rate disproportionate to the actual growth rate of the level population.

The systematic error induced by spectral congestion is thus a

possible explanation for the disparity between the values of $\Sigma k_4(i)$ and k_4 reported for collision induced energy transfer rates in S_1 aniline. The magnitude of the error caused by growth band overlap has not been determined. It is possible that some other systematic error may be the major cause of the inequality between the rate constants $\Sigma k_4(i)$ and k_4.

The kinetic model proposed in Chapter II predicts that a plot of L vs. [M] should be linear. The upward curvature in the L vs. [M] plots for CO_2 as the collision gas may be ascribed to two probable causes. At CO_2 pressures above 15 torr, multiple hard-sphere collisions are expected during the 7 nsec lifetime of the aniline S_1 state. Each aniline molecule averages one hard-sphere collision with CO_2 every 2.3 nsec at 30 torr of CO_2 pressure. Even at this pressure, the probability for an aniline molecule to experience multiple stages of collision induced energy transfer is rather small. The ratio of the hard-sphere collision rate of k_{hs} to the overall collision induced decay rate k_4 from the 0^0 level of aniline is 4.61:1. Although sequential energy transfer processes should have a negligible effect on the calculated rate constants $k_4(i)$, they will nevertheless be considered as a possible source for the curvature in the L vs. [M] plots.

The second possible cause for the upward curvature in the L vs. [M] plots concerns the values of K_S^* used to determine L. From equations 3.24 and 3.25, it may be seen that when the calculated value of K_S^* is overestimated, the plot of L vs. [M] will curve upward. The curvature becomes more severe at higher pressures, where $K_S^*[M]$ begins to dominate in

the $(1+K_s^*[M])$ term. A similar downward curve is observed in an L vs. [M] plot when K_s^* is too low. Since K_s^* is obtained through a rather coarse approximation for the aniline/CO_2 system and its uncertainty is ~40%, it is likely a priori that overestimation of K_s^* is the cause for the upward curvature.

For argon as a collision partner, some pressures were used which allowed two hard-sphere collisions during the aniline excited state lifetime. However, twice as many hard-sphere collisions are required to induce energy transfer when argon is the collision partner in place of CO_2. Reported values for K_s^* are accurate within 10% and were measured for each growth level (31). Curvature in L vs. [M] plots should, therefore, be minimal for argon as the collision gas in the pressure region up to 25 torr.

For H_2O and CH_3F, the ratios k_{hs}/k_4 are 0.84 and 1.73, respectively. When the probability for energy transfer is near the hard sphere collision probability, it becomes important to reduce collision gas pressures to remain within the one hard-sphere collision region. Vandersall et al. (42) limited H_2O and CH_3F pressures to a maximum of only 5 torr, keeping the hard-sphere rate well within the one collision limit. Values of K_s^* for H_2O and CH_3F were determined in much the same manner as they were for CO_2. K_s^* was measured for two levels, and all others were approximated by multiplying the proper argon K_s^* value by an appropriate factor. Provided that gas pressures are kept at or below 5 torr for H_2O and CH_3F, any curvature in L vs. [M] plots for these gases should be negligible.

At CO_2 pressures of 15 torr or below, the effects of multiple hard-sphere collisions and errors in the estimation of K_s^* would appear to negligibly affect the linearity of L vs. [M] plots. For CO_2 pressures exceeding 15 torr, however, the plots begin to perceptibly curve upward. From the arguments presented above, it should be clear that the slopes calculated from points lying along the linear portion of the curves will lead to the most accurate values for $k_4(i)$.

The mode-specific collision induced decay rate constants $k_4(i)$ are frequently expressed as a value relative to the hard-sphere collision rate constant. The purpose for this normalization is to facilitate comparison between the relative magnitudes of the rate constants as the collision gases are varied. Comparisons among collision partners for aniline, however, are also obscured by the variation in the ratio $\Sigma k_4(i)/k_4$ for different gases. To aid in the comparison between rate constants, individual values for $k_4(i)$ are normalized by a factor $k_4/(k_{hs}\ k_4(i))$. Pathways and normalized rate constants for decay of the 0^o level of aniline with CO_2 as the collision gas are presented in Figure 4-1. It should be noted that the normalization factor is an approximate value intended only to provide a rough comparison between collision partners. In all likelihood, each $k_4(i)$ would have an individual normalization factor, if the cause for the disparity between $\Sigma k_4(i)$ and k_4 were positively known.

Collision induced energy transfer from the 0^o level of aniline for CO_2 as the collision gas seems to follow much the same flow pattern as

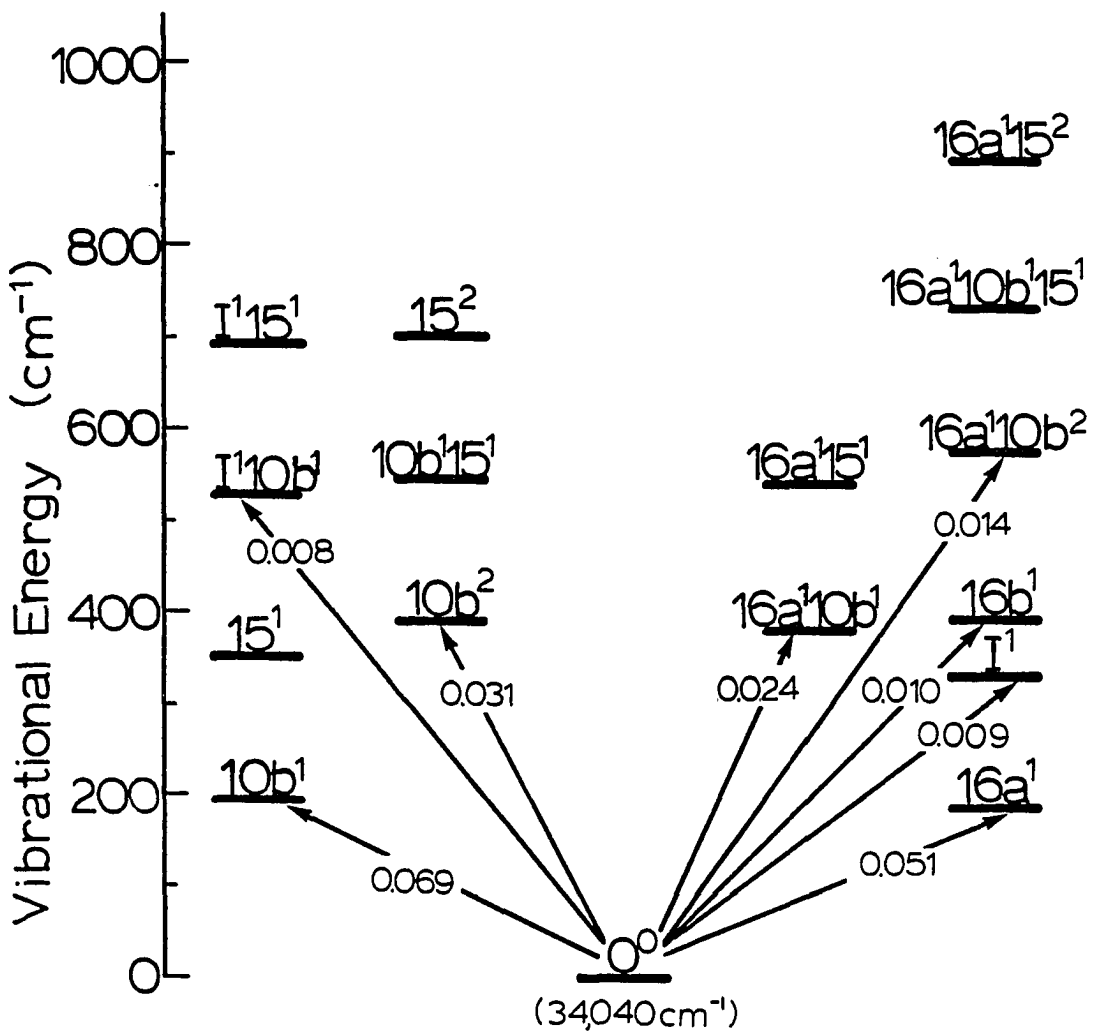

Figure 4-1. Pathways and normalized rate constants $k_4(i)$ for collision induced energy transfer from the 0^0 level of aniline. The rate constants $k_4(i)$, initially multiplied by a normalization factor $k_4/\Sigma k_4(i)$, are expressed in units of probability per hard-sphere collision

was found for Ar, H_2O, and CH_3F as collision partners. Normalized rate constants for mode specific collision induced decay of the 0^o level in S_1 aniline are listed in Table 4-1 for each of the collision partners. Mode selectivity does not vary substantially for different collision partners. In each case, energy transfer to levels $10b^1$ or $16b^1$ predominates. The magnitude of the normalized rate constants vary roughly in proportion to the overall collision induced decay rate constants of the 0^o level (see Table 3-4) for each growth level.

The quality of the aniline/CO_2 data is comparable to the data obtained for energy transfer in aniline with other collision partners (31, 42). Uncertainties near 20% are typical for the rate constants $k_4(i)$ in all reported aniline/collision gas systems. The signal to noise ratio in the fluorescence spectra recorded for collision induced energy transfer in aniline using CO_2 as a collision gas is higher than the signal to noise ratio obtained by Chernoff and Rice for their aniline/argon system (31). As a result, when the aniline/argon work was repeated here, two new growth bands were identified. The growth rate for these levels is presented in Table 4-1. The improved signal to noise ratio for our laser system is a result of the increased SHG power obtainable through the use of $LiIO_3$ rather than KDP as a frequency doubling crystal.

Continuation of the study of collisional energy transfer in S_1 aniline induced by CO_2 would include pumping higher aniline vibrational levels. Use of a KDP doubling crystal with properly chosen focusing

Table 4-1. Normalized rate constants for vibrational energy transfer from 0^0 aniline

Growth level	Collision partner			
	Ar[a]	CO_2	CH_3F[b]	H_2O[b]
$10b^1$	0.050	0.069	0.194	0.529
$10b^2$	0.013	0.031	0.088	0.161
$16a^1$	0.029	0.051	0.176	0.308
$16b^1$	0.016	0.010	0.028	0.070
I^1	0.002	0.009	0.040	0.073
$I^1 10b^1$	0.003[c]	0.008	0.031	
$16a^1 10b^1$	0.012[c]	0.024		
$I^1 16a^1$			0.024	0.056

[a]Normalized rate constants calculated from ref. (31), except where noted.

[b]Normalized rate constants calculated from ref. (42).

[c]Obtained from this work.

optics (Appendix) should lead to fluorescence spectra with sufficiently high signal to noise to yield quantitatively useful results. Spectral analysis would provide further details concerning the pathways of vibrational relaxation in S_1 aniline.

CHAPTER V. INTRODUCTION TO NONRADIATIVE EXCITATION TRANSPORT

Laser methods of fluorescence spectroscopy are increasingly being applied to systems beyond the realm of traditional chemical research (96, 97). The technique has proliferated, in part, because on the time scale of molecular fluorescence lifetimes, a wide range of molecular events can occur. The advent of ultrashort light pulses permits these events to be observed through variations in excited state lifetimes, emission polarizations or spectral characteristics of the fluorescence.

Detection of fluorescence anisotropy is one method which has proven to be useful for examining many biochemical and medical systems. The study of membrane dynamics (98, 99), segmental mobility of antibody molecules (97) and association reactions between antigens and antibodies (97) are instances in which important information has been garnered by monitoring the rotational diffusion of select fluorophores via fluorescence depolarization.

Nonradiative energy transport between molecules can also lead to the decay of fluorescence polarization similar to the effect observed due to rotational diffusion. Processes effectively probed include the initial light harvesting stages of photosynthesis (100-102), intra- and intermolecular polymer interactions (103-108) and relaxation pathways of dye molecules in solution (109, 110) and on a two-dimensional surface (111).

Either event, energy migration or rotational diffusion, probed through fluorescence depolarization measurements may provide insight into the molecular environments of the fluorophores in question. Analysis,

however, is dependent on accurate mathematical models to simulate the experimentally observed fluorescence profiles. Hence it is advantageous to establish conditions which will simplify analysis. If one is to use the rate of rotational diffusion to make assumptions about the structure and conformation of macromolecules, it is better to work at dilute concentrations in order to minimize the effects of nonradiative energy transport. Similarly, if excited state relaxation pathways are to be studied using fluorescence anisotropy measurements, solvent viscosities should be chosen which minimize rotational diffusion on the time scale of the molecular fluorescence lifetime.

Even in the absence of rotational diffusion, development of an accurate model to describe electronic excitation transport among a set of randomly distributed molecules has posed a challenging problem to theorists for many years (112-115, 69). Consideration must be given not only to the mechanism of energy transport--whether radiative, electron exchange, or multipole interactions are responsible for the energy transfer (116)--but also to the fact that in a random system there is no unique pathway through which energy can be transferred between two molecules. Rather, there is an infinite set of possible paths which involve all the molecules in the sample. Excitation transfer probabilities, in this case, are determined by solving the coupled master equations which assume the form (117)

$$\frac{dp_j}{dt} = \sum_{k=1}^{N} w_{jk}(p_k - p_j) - p_j/\tau_D \qquad (5.1)$$

when the system consists of N identical molecules with intramolecular excited state lifetime τ_D. Here p_j is the probability that the excitation resides on molecule j at time t and w_{jk} is the energy transfer rate between molecules j and k. In a system consisting of a one mm^3 volume containing 10^{-5} M solution, N in equation (5.1) would be of the order 10^{12}. A mathematical description of the excitation transfer process for any macroscopic system of particles such as this one would be inconceivable unless appropriate simplifying assumptions are made. A condition imposed by virtually every theory until recently has limited the studies to very low-concentration systems. In these dilute solutions, where the average intermolecular spacing is much greater than the molecular size, the excitation transfer rate w_{jk} in equation (5.1) can be attributed solely to the Förster dipole-dipole interaction (118). Setting molecule j at the origin of coordinates and molecule k at $\underline{R}$, the dipole-dipole transition rate is defined by (112)

$$w_{jk} = \frac{3}{2}\,[\underline{d}_j\cdot\underline{d}_k - 3(\underline{d}_j\cdot\underline{r}_{jk})(\underline{d}_k\cdot\underline{r}_{jk})]^2\,\frac{1}{\tau_D}\,(R_o/R)^6, \qquad (5.2)$$

where $\underline{d}_j$ and $\underline{d}_k$ are unit vectors along the transition moments of molecules j and k, respectively, $\underline{r}_{jk}$ is a unit vector directed along $\underline{R}$, and R_o is the intermolecular separation at which excitation transport and intramolecular decay are equally probable. When the system to be studied is a spatially random solution, it is often acceptable to use an orientation-averaged Förster rate equal to (119)

$$w_{jk} = \frac{1}{\tau_D} \quad (R_o/R)^6 \qquad (5.3)$$

which will simplify theoretical developments, although derived numerical coefficients will change slightly (109, 115).

When solution concentrations become sufficiently dilute, intermolecular energy transport becomes nearly negligible. At this point, an excited molecule is taken to interact with only one or two of its nearest neighbors. Early attempts by Vavilov (120) and Galanin (121) to approximate the master equation solutions in the low concentration limit assumed that, at most, one or two excitation hops occurred during the donor excited state lifetime. Subsequent theories relaxed the constraints limiting the number of hops and improved the agreement with experimental data (112, 122). For example, Förster (117) considered multiple hops within a set consisting of only two molecules. Thus, when a nearest neighbor B lies in close proximity to the photon excited donor A, there can be many hops between the pair during the fluorescence lifetime. Others considered the effect of the second nearest neighbor on the excitation transport process in the limit of multiple hops. Among those was Ore (123) who realized that, although molecule B is the nearest neighbor of the initial donor A, the reverse is not necessarily true. His addition to the theory provides that if B has a neighbor nearer than A, the excitation is lost from the subset (A,B)--this loss occurring with a certain probability each time the excitation visits B. This potential for the complete loss of excitation from the original subset constitutes a

rather severe correction term to account for the effect of a third molecule on excitation transport within a two molecule system.

Craver and Knox (122) reasoned that in a disordered system the excitation on the photon excited donor is likely to associate itself with a definite cluster of acceptors during its lifetime. The initial donor belongs to a cluster of the order n when that molecule and its n-1 nearest neighbors have no other neighbors closer than R_0, the Förster radius in equation (5.2). A cluster of order 3 is conceptually very similar to the situation considered by Ore (123). The difference lies in the fact that Craver and Knox account for the finite probability that the excitation may return from residence on the second nearest neighbor to repopulate the initially excited donor or nearest neighbor. Energy transport within a cluster of three molecules is the largest to be described analytically due to the increasing complexity of the mathematics with cluster size.

To ascertain whether any or all of the aforementioned theories accurately model the excited state dynamics in a three-dimensional random solution, one needs only to find a correlation between an experimental observable and the appropriate term from the theory. While excited state energy transfer between nonidentical molecules can be monitored through the process of sensitized luminescence (112, 124), for an ensemble of identical molecules the quantitative aspects of excitation transport are more difficult to observe and to interpret. Galanin (121) provided the link when he discovered that, for a solution pumped with polarized light, the overwhelming contribution to the fluorescence polarization was due to

emission from the initially excited molecules. Theoretically, the value of the polarization function for fluorescence emitted after one excitation hop is about 0.025, while that emanating from initially excited molecules is 0.5 (122). The fluorescence polarization, therefore, gives a direct indication of the probability that the emission emerged from the site of initial excitation.

In the preceding discussion, the polarization function had been considered inexplicitly. An introduction to the exact form of the function, along with an investigation into the origin of the emission polarization for a disordered system, will provide insight into the relationship between nonradiative energy transfer and fluorescence depolarization. For the moment, consideration will be restricted to steady state measurements of fluorescence intensities -- the conditions established for experimental verification of the excitation transport theories discussed previously.

When polarized light is incident upon a sample composed of randomly oriented chromophores, the probability of photon absorption by each molecule is proportional to $\cos^2\theta$, where θ is the angle the absorption dipole makes with the photon polarization vector (97). In addition, the fraction of molecules having absorption dipoles between θ and $\theta+d\theta$ is proportional to $\sin\theta d\theta$ in a randomly oriented sample. The distribution of molecules excited by polarized light, which is dependent on both of these factors will be given by

$$f(\theta)d\theta = \cos^2\theta\sin\theta d\theta. \tag{5.4}$$

Consider, for the purpose of illustration, a molecule whose absorption dipole is oriented with angle θ relative to the z-axis and angle ϕ from the y-axis. Light incident on this molecule travels in the x-direction and is polarized along the z-axis. Assuming conditions of parallel absorption and emission dipoles and immobility of the excited molecule, the intensities of the polarized light components radiated from the dipole along the y-axis (axis of observation) would be

$$I_{\parallel}(\theta,\phi) = \cos^2\theta \tag{5.5}$$

and

$$I_{\perp}(\theta,\phi) = \sin^2\theta\sin^2\phi, \tag{5.6}$$

where $I_{\parallel}$ indicates that the detected fluorescence is polarized parallel to the incident photon and $I_{\perp}$ signifies that the observed emission is polarized normal to both the observation axis and the polarization vector of the absorbed photon. In an isotropic solution, the total detected fluorescence intensity along these orthogonal planes results from a sum of the contributions from each fluorophore, so that

$$I_{\parallel} = \iint f(\theta)\ I_{\parallel}(\theta,\phi)d\theta d\phi \tag{5.5a}$$

and

$$I_{\perp} = \iint f(\theta)\ I_{\perp}(\theta,\phi)d\theta d\phi, \tag{5.6a}$$

where $f(\theta)$ is defined in equation (5.4). The imbalance of intensity between the parallel and perpendicular components is generally expressed

in terms of either the polarization or anisotropy. The polarization function p is defined as (112)

$$p = (I_{\parallel} - I_{\perp})/(I_{\parallel} + I_{\perp}) \tag{5.7}$$

and the anisotropy is expressed as

$$r = (I_{\parallel} - I_{\perp})/(I_{\parallel} + 2I_{\perp}). \tag{5.8}$$

While the polarization function is ideally suited to describe the ratio of polarized light intensity to the total collimated intensity emitted from a light source (97), use of the anisotropy function is more appropriate when describing excitation transport processes. The anisotropy is related to the polarization by

$$r(p) = (\frac{1}{p} - \frac{1}{3})^{-1} \tag{5.9}$$

and its importance in excitation transfer theories arises from its additive nature (125). Specifically, r(p) may be rewritten as (97)

$$r(p) = \sum_n f_n r(p_n) \tag{5.10}$$

where p_n is the polarization of the light emanated from a subset n of the emitters, assuming the subset could be isolated, and f_n is the fraction of the total fluorescence intensity emitted by the subset.

The manner in which subsets are defined can vary significantly for individual theories of excitation transport. For example, Vavilov (120, Galanin (121) and Weber (126) each grouped the system according to the

Figure 5-1. Fluorophore in a coordinate system. The black arrow represents an arbitrary dipole in solution. Exciting the dipole with vertically polarized light (polarized parallel to z-axis) creates fluorescence components $I_{\parallel}$ and $I_{\perp}$ (observed along y-axis) to have intensities proportional to $\cos^2\theta$ and $\sin^2\theta\sin^2\phi$, respectively

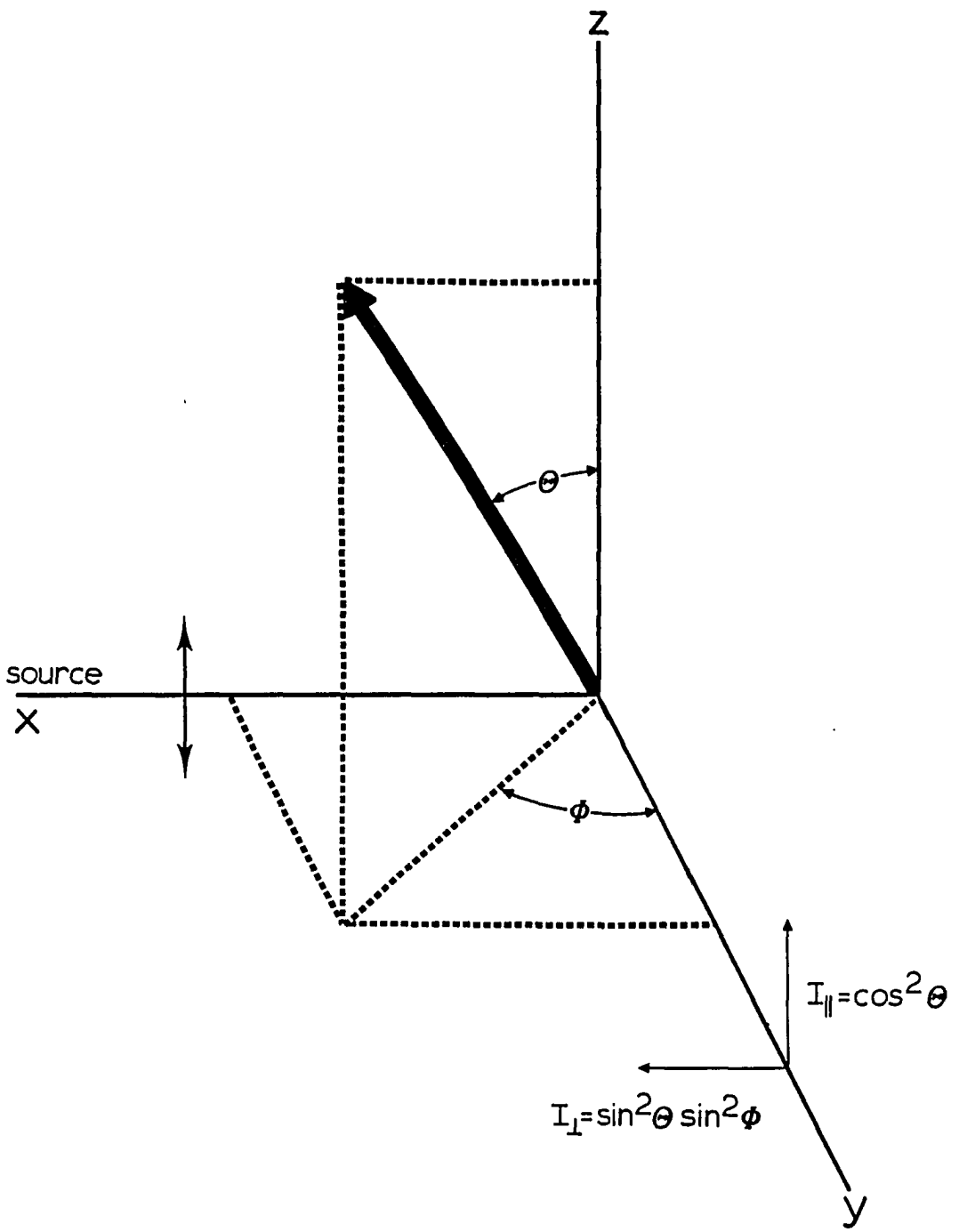
z
θ
source
x
φ
$I_{\parallel}=\cos^2\theta$
$I_{\perp}=\sin^2\theta\sin^2\phi$
y

number of excitation hops taking place during the excited state lifetime. Others, such as Förster (117) and Jablonski (127), divided the system into subsets containing n molecules (n=1,2,3...) within an "active sphere", while Craver and Knox (122) broke down the collection of disordered molecules into subsets defined by the size of the cluster that the excitation was contained within.

Provided that the summation in equation (5.10) includes all possible subsets, the manner in which the subsets are defined is immaterial. However, as noted above, obtaining a complete summation for any macroscopic, randomly oriented system is unrealistic. The fact that r(p) can be expressed as a series of terms related to the degree of excitation hopping permits the complete series to be approximated by summing over a few members of the progression. Once the complete series has been reduced to the sum over a few terms, however, the choice of subset definition assumes an increasingly important role. Förster (117), for example, by considering only the first term in his series expansion of r(p), confined the dipole-dipole interaction solely between the two nearest neighbors. Multiple hops between nearest neighbors are included in Förster's first term $r(p_1)$ in equation (5.10). Vavilov (120) also cut off r(p) after the first term. However, with his choice of subsets, contributions to the anisotropy function were restricted to excitations which undergo a single hop from the photon excited donor to its nearest neighbor. Clearly, Förster's anisotropy function will include all of the terms contained in Vavilov's approximation -- plus contributions from the higher order terms in Vavilov's theory.

One would expect that as more terms are included in the summation (in equation (5.10)), the calculated r(p) will more closely approximate the experimental r(p). On this basis, one would expect Förster's equation to more accurately model the observed fluorescence anisotropy than Vavilov's or Galanin's theories. Similarly, one would expect anisotropy functions from models, which include terms accounting for the possibility of hopping to next nearest neighbors, to more nearly approach the experimentally determined anisotropy than Förster's model. Because the mathematics becomes so unwieldy for these three-body and higher-order contributions, many theorists have incorporated simplifications into the models used to calculate these terms. One must not only question whether enough terms are included in the r(p) summation, but also whether the approximations applied in the theory are valid. For example, when Jablonski (127) considered energy transport between an excited donor and its two nearest neighbors, he made the assumption that all molecules within an active sphere are taken to interact equally with constant strength w_0 -- implying that the three molecules are equidistant from each other. Further, Jablonski assumed that $\tau_D w_0=1$, where τ_D is the excited state lifetime in equation (5.1).

Although the use of simplifying assumptions in the models does not allow a completely realistic picture of excitation transport to be presented, the true test of a model comes when theoretically determined anisotropies are compared to those obtained experimentally. An ideal model would include a minimum number of terms in the summation for r(p) and

afford a simplified, yet realistic portrayal of the molecular system, while providing an accurate fit to the experimental data.

As a rule, $r(p)/r(p_0)$ versus solution concentration is plotted whenever steady state anisotropy measurements are compared to theoretical values (112) -- $r(p_0)$ being the anisotropy in the limit of negligible energy transport. Experimental determination of the anisotropy as a function of concentration is difficult, however, because a separate sample is required for each point. Because measurements on a large number of concentrations spanning a wide range of concentrations are necessary to make a detailed comparison of theory and experiment, there has resulted a paucity of precise data from which to make a rigorous study (109). In many cases, theory has been compared with experimental results at a single concentration. Of the steady state models considered to this point, the cluster theory concept of Craver and Knox (122) has provided the best overall fit to the limited experimental data.

Hemenger and Pearlstein (114) demonstrated that time-resolved techniques could provide information on excitation transport commensurable to what was obtained from the steady state experiments of Craver and Knox (122). However, analysis of time-resolved fluorescence decay curves permit one to assess the validity of a model based on the data from a single sample (109). Hemenger and Pearlstein's model, like all of the steady state models of excitation transport, only yields a value for the probability that the excitation has remained on the initially excited molecule. Of course, in Hemenger and Pearlstein's case, this value is time dependent and defined in terms of an infinite summation (114)

$$A(T) = \sum_{l=0}^{\infty} \beta_l T^{l/2}, \tag{5.11}$$

where l corresponds to the number of molecules in an interaction volume about the photon excited donor, β_l is a numerical coefficient, and T is a function of time. Nevertheless, each of these models will, at best, provide information regarding the validity of assuming a dipole-dipole interaction among the molecules in the system and give an indication to the number of molecules partaking in the energy transfer process.

Haan and Zwanzig (115) effectuated a significant advancement in the theory with their Green's function solution to the master equation. The theory, which relies on time-resolved fluorescence decays for experimental verification, for the first time revealed details about the spatial transport of the excitation in a random, three-dimensional solution. While the theory is quite involved, it is worthwhile to highlight a few of its salient features.

As it was stated previously, there is effectively an infinite set of possible pathways through which the excitation may be transferred between two molecules. Conceivably, some of these paths would interlink every molecule in the sample, while other routes would couple only two molecules directly. Details regarding transport within a macroscopic system are obtained from the ensemble averaged density of excitations

$$P(r,t) = \langle \sum_j \delta(\underline{r}_j - \underline{r}) p_j(\underline{R},t) \rangle, \tag{5.12}$$

where $p_j(\underline{R},t)$ is the probability that an excitation is found on the j^{th} site, at time t, in configuration $\underline{R}$. $\underline{R}$ is specified by the positions of N molecules, $(\underline{r}_1, \underline{r}_2, \ldots \underline{r}_N)$. The angular brackets < > indicate that an average has been taken over all possible states of the system, e.g.,

$$<A(\underline{R})> = \frac{1}{\Omega^N} \int_{\Omega} d\underline{r}_1 \cdots \int_{\Omega} d\underline{r}_N \, A(\underline{R}), \tag{5.13}$$

with Ω being the system volume. Rewritten in terms of a Green's function, $P(\underline{r},t)$ becomes

$$P(\underline{r},t) = \int d\underline{r}' \, G(\underline{r},\underline{r}',t) \, P(\underline{r}',0). \tag{5.14}$$

The Green's function $G(\underline{r},\underline{r}',t)$ represents the ensemble averaged response to an impulse of excitation. Specifically, if there was unity probability that the excitation was located at $\underline{r}'$ at t=0, the Green's function would give the probability that, at a later time t, the excitation is at $\underline{r}$. In their theory, Haan and Zwanzig wrote this as

$$G(\underline{r},\underline{r}',t) = \frac{\Omega}{N} \sum_{j=1}^{N} \sum_{k=1}^{N} <\delta(\underline{r}_j - \underline{r}) \, [\exp(t\underline{W})]_{jk} \delta(\underline{r}_k - \underline{r}')> , \tag{5.15}$$

where $W_{jk} = (1-\delta_{jk})w_{jk} - \delta_{jk} \sum_{l \neq j} w_{jl}$, and w_{jk} as the Förster rate for excitation hopping between the j^{th} and k^{th} sites (see equation (5.3)). The Fourier-Laplace transform of the Green's function $\hat{G}(\underline{k},\varepsilon)$ was equated to a function containing a generalized diffusion coefficient $\hat{D}(k,\varepsilon)$ such that

$$\hat{G}(\underline{k},\varepsilon) = [\,\varepsilon + k^2\hat{D}(\underline{k},\varepsilon)]^{-1}. \qquad (5.15a)$$

By employing a scaling argument, density expansions of the Green's function and the generalized diffusion were constructed. In the thermodynamic limit ($N\to\infty$, $\Omega\to\infty$, with the density ρ held constant), the density expansion for the Green's function was written as

$$\hat{G}(\rho,\underline{k},\varepsilon) = \varepsilon^{-1} + \rho B_2(\underline{k},\varepsilon) + \rho^2 B_3(\underline{k},\varepsilon) + \ldots. \qquad (5.16)$$

The n^{th} order term in his expansion (containing ρ^n) is derived from excitation hopping along sets of n+1 molecules (69). Replacing the number density ρ by a dimensionless concentration C_D (which represents the average number of transfer sites within a sphere with radius R_0) by

$$C_D = (4/3)\pi\rho R_0^3 \qquad (5.17)$$

and using the scaling argument, the mean squared displacement $\langle r^2(t)\rangle$ was expanded as

$$\langle r^2(t)\rangle = R_0^2(t/\tau_D)^{1/3}[2.97514\ C_D(t/\tau_D)^{1/2} + 0.3268\ C_D^2(t/\tau_D) + \ldots]. \qquad (5.18)$$

Because only the first two terms were calculated in the expansion of $\langle r^2(t)\rangle$, the results of Haan and Zwanzig apply only to excitation transport within a dilute disordered solution in the short time limit. At low concentrations and early times, the mean squared displacement of the excitation increased as the $(5/6)^{th}$ power of time. Based on the variation

of the diffusion coefficient with time, Haan and Zwanzig infer that excitation transport may be diffusive in the long time limit for dilute solutions.

Gochanour, Andersen and Fayer (69, hereafter GAF) expanded on Haan and Zwanzig's model in an effort to accurately describe energy transport at along times or high concentrations as well as at short times and low concentrations. The formalism in the two theories is identical to the point where the ensemble averaged density of excitations $P(\underline{r},t)$ was written in terms of a Green's function (equation 5.14). The total Green's function was then expressed by GAF as the sum of two terms

$$G(\underline{r},\underline{r}',t) = G^s(\underline{r},\underline{r}',t) + G^m(\underline{r},\underline{r}',t). \tag{5.19}$$

$G^s(\underline{r},\underline{r}',t)$ is a measure of the probability that excitation on the photon excited donor at t=0 is on the same site at time t and $G^m(\underline{r},\underline{r}',t)$ is the probability that the excitation is found on a molecule a distance $\underline{r}-\underline{r}'$ from the site of initial excitation. These Green's functions are expressed in the theory as

$$G^s(\underline{r},\underline{r}',t) = \delta(\underline{r}-\underline{r}')\langle[\exp(t\underline{\underline{W}})]_{11}\rangle \tag{5.20}$$

and

$$G^m(\underline{r},\underline{r}',t) = (N-1)\langle\delta(\underline{r}_{12}-\underline{r}+\underline{r}')[\exp(t\underline{\underline{W}})]_{12}\rangle. \tag{5.21}$$

It should be noted that $G^s(\underline{r},\underline{r}',t)$ as defined above should provide the same information as A(T) in Hemenger and Pearlstein's theory (equation 5.11). $G^s(\underline{r},\underline{r}',t)$, an experimental observable, is a function of the

parallel and perpendicular components of the fluorescent emission, such that (109)

$$G^s(\underline{r},\underline{r}',t) = \frac{I_{\parallel}(t) - I_{\perp}(t)}{I_{\parallel}(t) + 2I_{\perp}(t)} . \tag{5.22}$$

The Fourier-Laplace transforms of G^s and G^m are given by (69)

$$\hat{G}^s(\varepsilon) = \langle[(\varepsilon-\underline{\underline{W}})^{-1}]_{11}\rangle \tag{5.23}$$

and

$$\hat{G}^m(\underline{k},\varepsilon) = (N-1)\langle\exp(i\underline{k}\cdot\underline{r}_{12})[(\varepsilon-\underline{\underline{W}})^{-1}]_{12}\rangle \tag{5.24}$$

respectively. The matrix $(\varepsilon-\underline{\underline{W}})^{-1}$, expanded in powers of ε and $\underline{\underline{W}}$, is written as

$$(\varepsilon-\underline{\underline{W}})^{-1} = \varepsilon^{-1} + \varepsilon^{-1}.\underline{\underline{W}}.\varepsilon^{-1} + \varepsilon^{-1}.\underline{\underline{W}}.\varepsilon^{-1}.\underline{\underline{W}}.\varepsilon^{-1} + ... \tag{5.25}$$

Substitution of this expansion into equation (5.23) leads to

$$\hat{G}^s(\varepsilon) = \varepsilon^{-1} + \sum_{n=1}^{\infty} (1/\varepsilon^{n+1})\langle(\underline{\underline{W}}^n)_{11}\rangle, \tag{5.26}$$

where the n^{th} order term in the infinite summation is given by

$$(1/\varepsilon^{n+1})\langle(\underline{\underline{W}}^n)_{11}\rangle = \sum_{i,j,\ldots k}^{N} (1/\varepsilon^{n+1})\langle W_{1i}W_{ij}\ldots W_{k1}\rangle. \tag{5.27}$$

Substituting the definition of W_{jk} (see equation (5.15) into equation (5.27) leads to a series of W_{jk} factors such that

$$(1/\varepsilon^{n+1})\langle W_{1i}W_{ij}\ldots W_{k1}\rangle = (1/\varepsilon^{n+1})\langle[w_{1i}+\delta_{1i}\sum_{q\neq i}(-w_{iq})]$$

$$\times[w_{ij}+\delta_{ij}\sum_{r\neq j}(-w_{jr})]\cdots[w_{k1}+\delta_{k1}\sum_{s\neq 1}(-w_{1s})]\rangle, \tag{5.28}$$

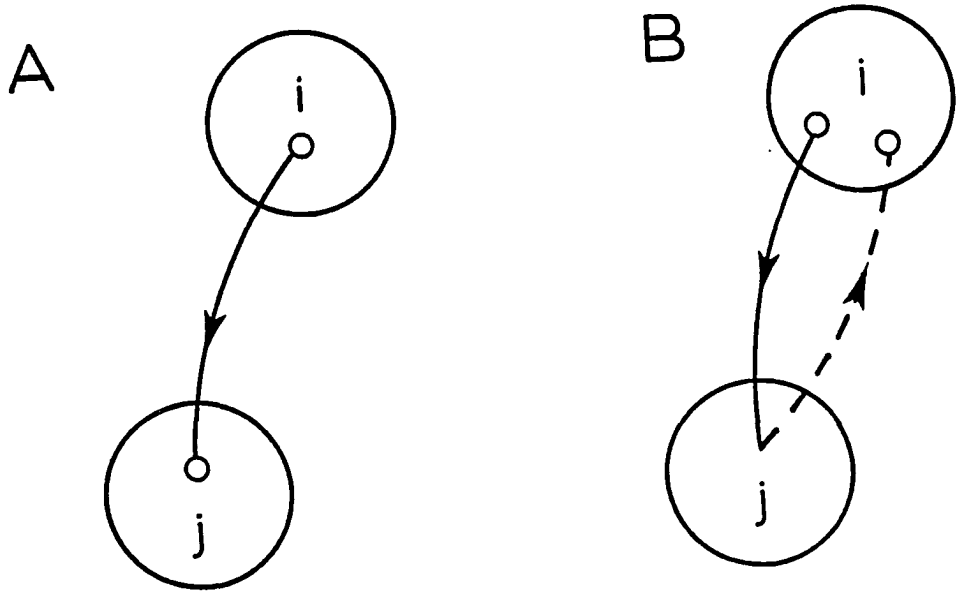

Figure 5-2. Diagrammatic structures for the factors w_{ij} and $-w_{ij}$ in the GAF model. Figure A is the structure for w_{ij}. Figure B is the structure for $-w_{ij}$

Figure 5-3. The diagrammatic expansion of $G^S(t)$. Each diagram contains a continuous path of solid and dashed arrows beginning and ending on circle 1. The diagrams shown represent all w_{ij} products in equation (5.26) for $n \leq 2$ (diagrams I-IV) and examples of diagrams for n=3 (diagrams V-VII). From (69)

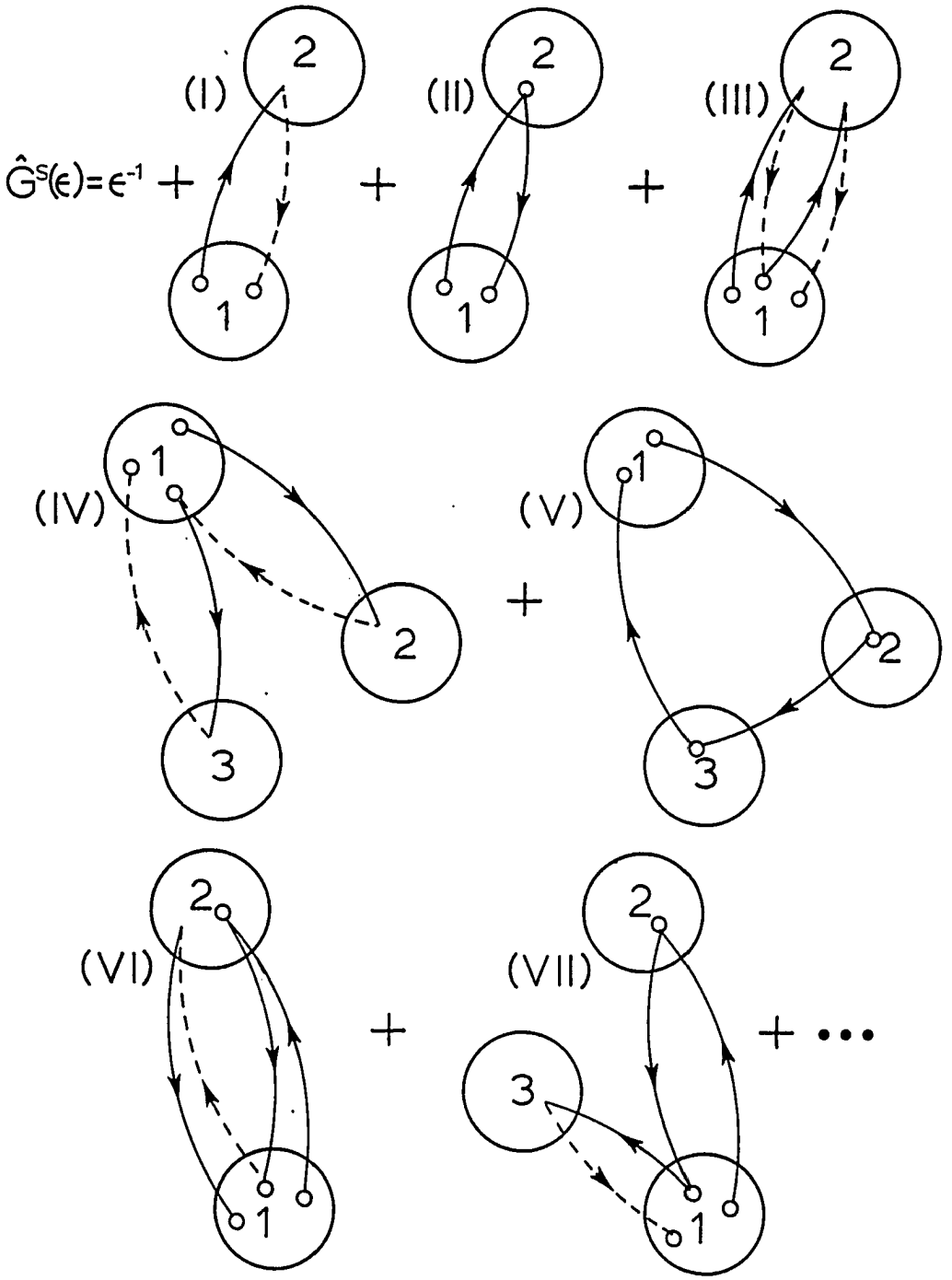
$\hat{G}^S(\epsilon)=\epsilon^{-1}$ +
(I)
(II)
(III)
(IV)
(V)
(VI)
(VII)
1
2
3
+ ...

which, when substituted into equation (5.26) for $<(\underline{\underline{W}}^n)_{11}>$, leads to an infinite series of products of w_{jk} factors. A similar procedure was employed to yield an infinite summation of product terms for $\hat{G}^m(\underline{k},\varepsilon)$. GAF generated two diagrammatic series corresponding to the functions $\hat{G}^s(\varepsilon)$ and $\hat{G}^m(\underline{k},\varepsilon)$. Each product term in the mathematical series for $\hat{G}^s(\varepsilon)$ and $\hat{G}^m(\underline{k},\varepsilon)$ is associated with a diagram. Diagrammatic structures for the factors w_{ij} and $-w_{ij}$ are presented in Figure 5-2. In the figure, small circles representing factors of ε^{-1}, solid arrows representing factors of w_{ij} and a dashed arrow symbolizing a negative sign, provide a device for determining the value of a product term in $\hat{G}^s(\varepsilon)$ or $\hat{G}^m(\underline{k},\varepsilon)$. Additionally, the diagrams allow for greater insight into the degree of excitation hopping associated with a particular product term. For example, one of the product germs in $\hat{G}^s(\varepsilon)$ with n equal to three would be $(1/\varepsilon^4)\ w_{12}w_{23}w_{31}$. The diagram representing this term would be constructed as shown in Figure 5-3 (V).

GAF reduced the complexity of the diagrammatic series for $\hat{G}^m(\underline{k},\varepsilon)$ through topological reduction. The first step in the simplification removed all loops from each diagram. A loop is defined as a succession of arrows that begins and ends on the same molecule. The result of removing all loops from the diagrammatic series is that a factor of $\hat{G}^s(\varepsilon)$ is associated with each small circle, rather than a factor of ε^{-1}. For clarity, a solid dot will be used to represent a factor of $\hat{G}^s(\varepsilon)$. The validity of this procedure was confirmed through analogous mathematical reduction of $\hat{G}^m(\underline{k},\varepsilon)$ (69). An example of a diagram with loops and its reduction to a diagram with no loops is illustrated in Figure 5-4.

Figure 5-4. Example of diagram with loops and its reduction to a diagram with no loops. In figure A a factor of ε^{-1} is associated with each small circle. Removing the loops between centers 1 and 3, and 2 and 4 results in the reduced diagram in figure B. The solid dots represent factors $\hat{G}^S(\varepsilon)$

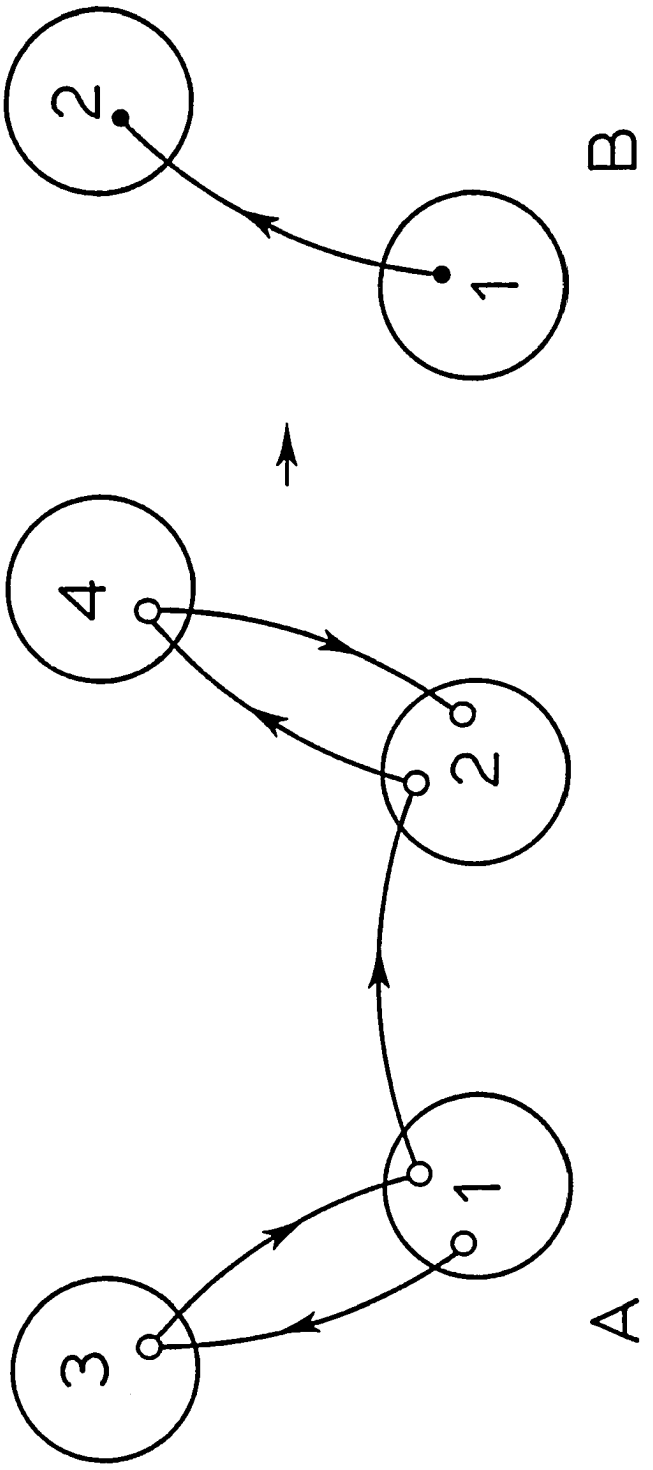
2
1
B
4
2
1
3
A

A second simplification in the diagrammatic series results from reducing diagrams with nodes into a set of diagrams with no nodes. This set can be used to construct the original diagram. Designating a root circle as the site excited initially (circle 1) or the site of photon emission (circle 2) and any other site as a field circle -- a node is defined as a vertex on a field circle which divides the circles in the diagram (except for the circle containing the node) into two uniquely defined sets. The first set contains sites visited before the excitation arrives at the node, while the second set contains all the sites visited by the excitation after the node. Figure 5-5 illustrates how a diagram with one node is divided into two diagrams with no nodes.

The process of topological reduction described above permits the initial $\hat{G}^m(\underline{k},\varepsilon)$ diagrammatic series to be expressed in terms of a smaller set of $\hat{G}^m(\underline{k},\varepsilon)$ diagrams from which the initial set can be generated. This reduced series of diagrams, terms $\tilde{\Sigma}(\underline{k}, \hat{G}^s(\varepsilon))$ by GAF, is both a function of $\hat{G}^s(\varepsilon)$ and used to generate $\hat{G}^s(\varepsilon)$. The sum of diagrams in $\tilde{\Sigma}(\underline{k}, \hat{G}^s(\varepsilon))$, which should include diagrams with an infinite number of circles (in the thermodynamic limit), has only been summed through diagrams containing three circles, due to the complexity of the GAF theory for a system with four or more circles (69). Summations of $\tilde{\Sigma}(\underline{k}, \hat{G}^s(\varepsilon))$ for diagrams with a maximum of two circles and three circles are designated as two-body and three-body contributions to the Green's function, respectively.

The second order density expansion of Haan and Zwanzig (115), although similar in appearance, is not equivalent to the three-body model

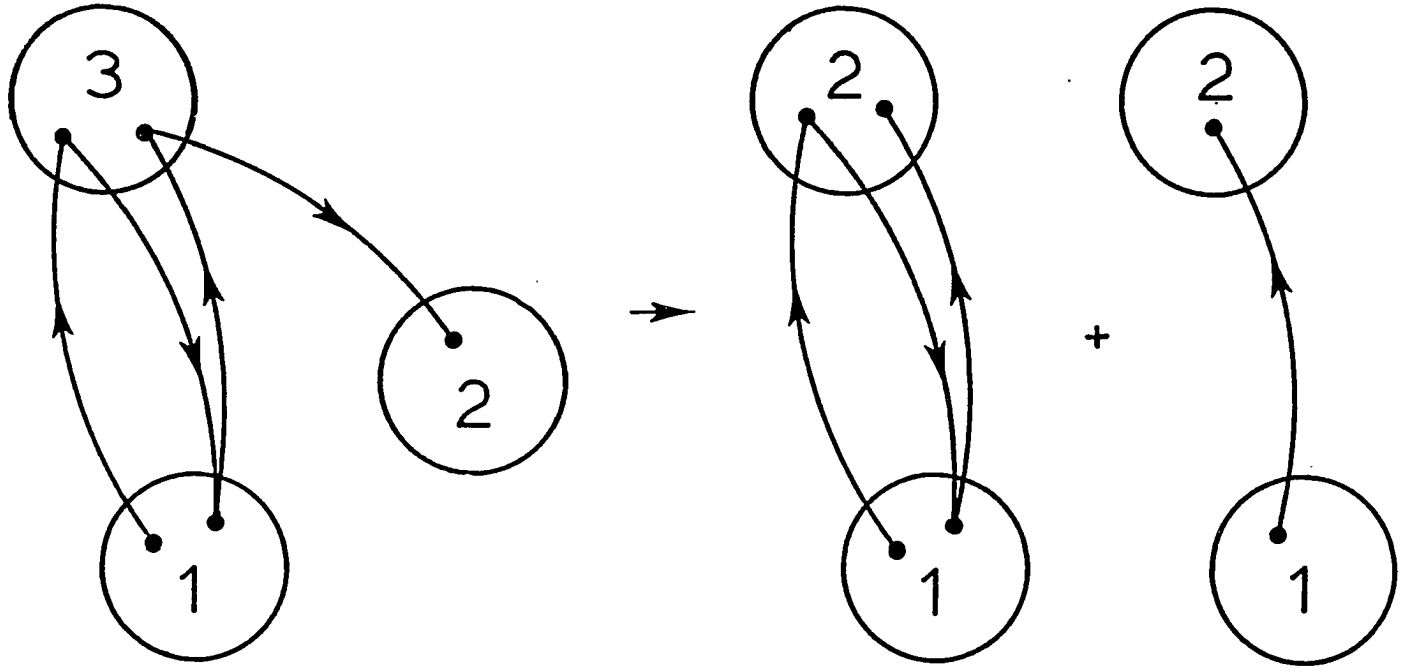

Figure 5-5. Division of a diagram with a node into two diagrams with no nodes

proposed by GAF (69). The three-body model includes all of those diagrams included in Haan and Zwanzig's second order result (see equation (5.16)) plus many higher order terms (69). These higher order terms are the result of the $\hat{G}^s(\varepsilon)$ factors associated with each vertex in GAF's model. The differences are accentuated by transforming one of Haan and Zwanzig's second order terms into diagrammatic form and comparing it with a similar three-body diagram. This comparison has been made in Figure 5-6.

Prior to the publication of GAF's work, Haan (128) developed an algebraic method to simplify the terms in the density expansion of Haan and Zwanzig (115). The technique paralleled the diagrammatic approach taken by GAF (69). However, in Haan's case, only the ε^{-1} factors associated with the nodal vertices were replaced by $\hat{G}^s(\varepsilon)$ factors (69). While Haan's model improves on Haan and Zwanzig's theory, it is a poorer approximation to the true hopping behavior than the GAF model since Haan does not replace all loops with $\hat{G}^s(\varepsilon)$ factors. A diagrammatic comparison of the two models is made in Figure 5-7 for a single term in the $\hat{G}^m(\underline{k},\varepsilon)$ series.

The intent in discussing the various theories, which depict excitation transport in disordered solutions, was ultimately to show that the GAF three-body theory comes closest to predicting the excitation dynamics for a wide range of solution concentrations. Haan and Zwanzig's second order approximation to the density expansion is indistinguishable from the GAF three-body theory in the low concentration, short time limit.

Figure 5.6. Diagrammatic comparison of terms from the Haan and Zwanzig theory and GAF theory. (A) represents the diagrammatic form of one of Haan and Zwanzig's second order terms. (B) represents a similar diagram from three-body GAF theory, where solid dots represent factors of $\hat{G}^S(\epsilon)$. If ϵ^{-1} and diagram (II) from Figure 5.3 are introduced for $\hat{G}^S(\epsilon)$, it is clear that GAF diagram recovers Haan and Zwanzig second order term plus many higher order terms. Figure C would be a 5^{th} order term in Haan and Zwanzig's density expansion

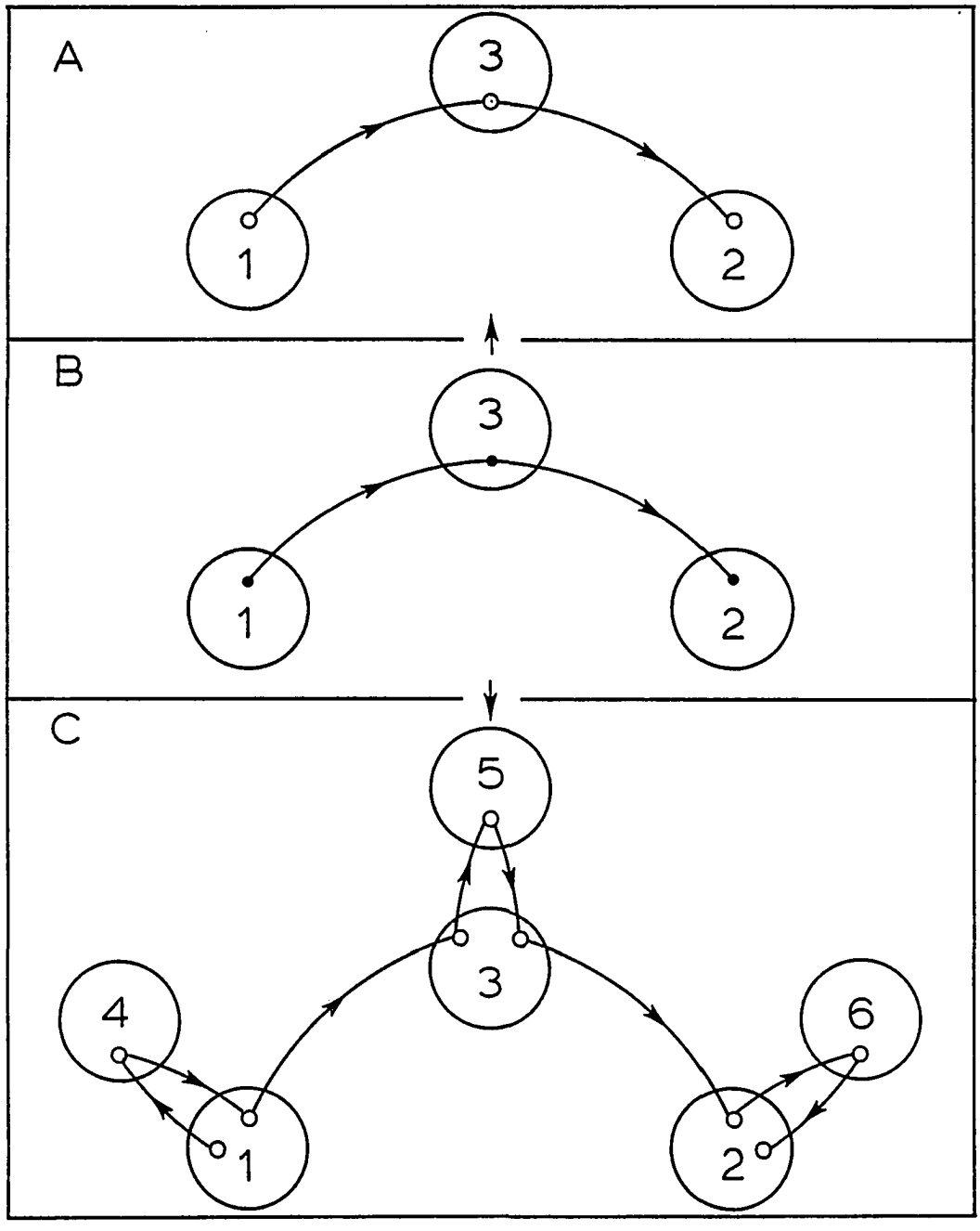
A
3
1
2
B
3
1
2
C
5
3
4
6
1
2

Figure 5-7. Diagrammatic expansion of terms included in GAF theory and Haan's modification of the Haan and Zwanzig theory. (A) A 2^{nd} order diagram from Haan and Zwanzig's density expansion. (B) Starting with same basis as (A), implicit $\hat{G}^S(\varepsilon)$ factors from Haan's (modification of Haan and Zwanzig) theory are replaced with structure (II) in Figure 5-3 to yield a 5^{th} order term in Haan and Zwanzig's theory. (C) Similar to (B), the factors $\hat{G}^S(\varepsilon)$ are replaced by structure (II) to show that more terms are included in GAF theory than in Haan's modification to Haan and Zwanzig's theory. Actually each of the structures in Figure 5-3 can be placed in $\hat{G}^S(\varepsilon)$ terms

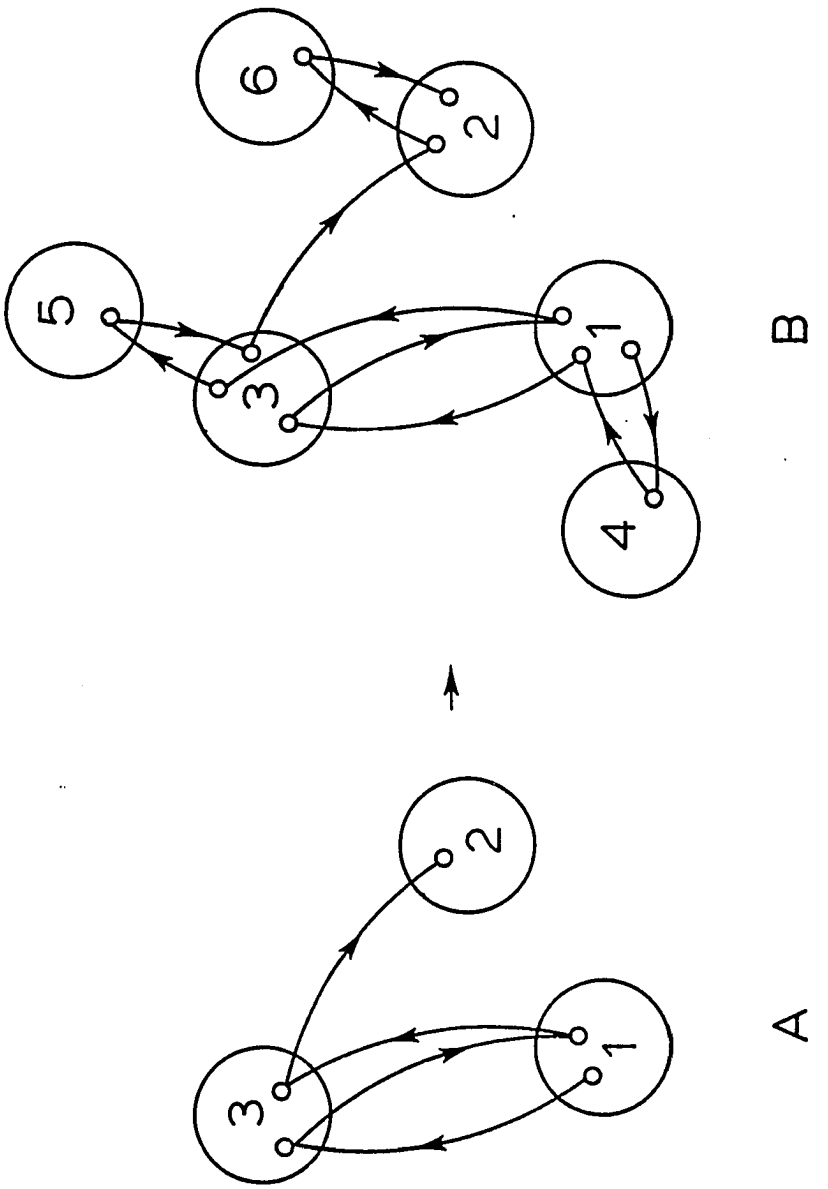
6
2
5
3
1
4
B
2
3
1
A

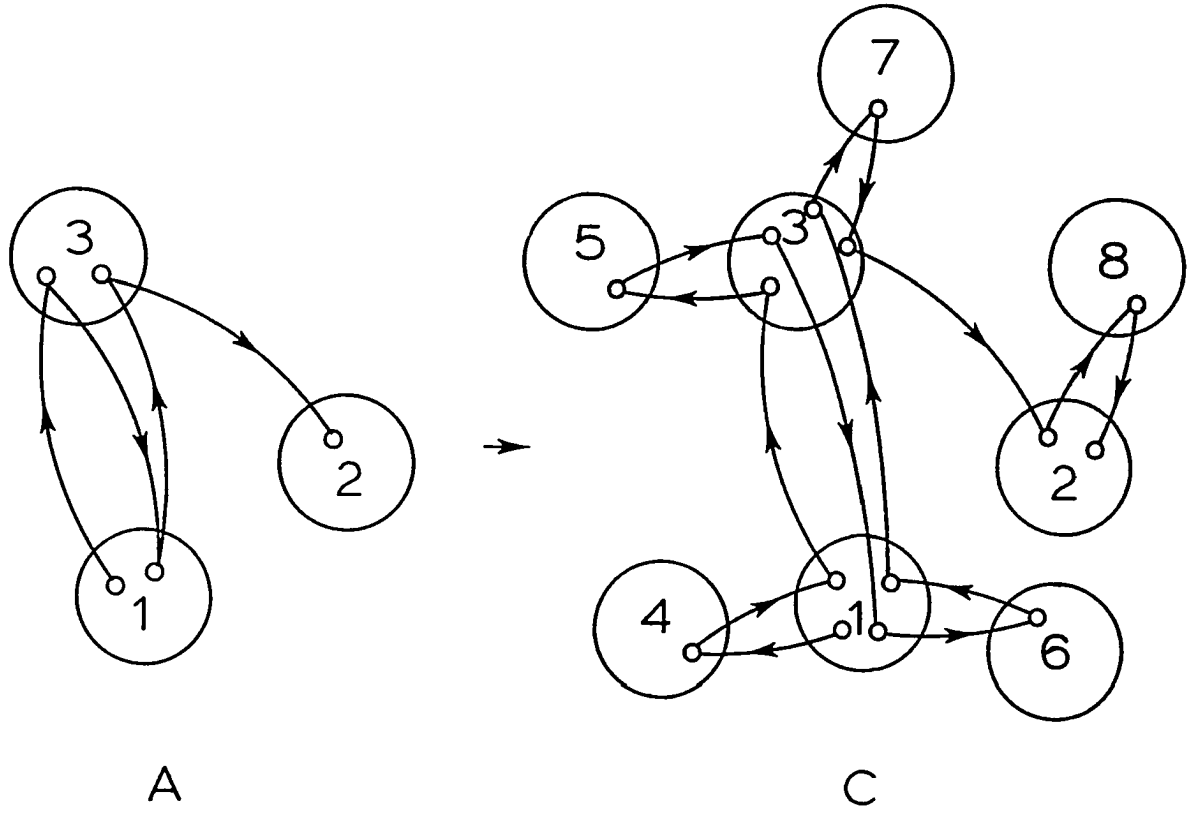

Figure 5-7 (continued)

However, as the solution concentration increases, the second order approximation to the density expansion fails, because higher order terms in the expansion become significant. Diagrammatically, the higher order terms are represented by figures that depict interactions among a larger number of sites than the first or second terms in the density expansion would include. While the figures that display Haan's modification to the theory include some of the higher than second order terms, an insufficient number are added to yield results accurate in the high density-long time regime (69). GAF's self-consistent three-body approximation, because it removes all loops in the diagrams composing the $\tilde{\Sigma}(\underline{k}, \hat{G}^s(\epsilon))$ series, provides an excellent model for describing the transport of excitation in solution. The three-body approximation includes many of the higher than second order diagrams from Haan and Zwanzig's theory, and the Green's function solution determined from the theory is well-behaved in the high-concentration, long time limit (69).

Values of the experimental observable, $\hat{G}^s(\epsilon)$, determined from time-resolved fluorescence anisotropy measurements by Gochanour and Fayer (109), were compared to the corresponding Green's function determined from GAF's three-body approximation. Their solutions consisted of rhodamine 6G(rh6G) in glycerol with solute concentrations ranging from $2.95\times10^{-5}\underline{M}(C_D=0.0)$ to $5\times10^{-3}\underline{M}(C_D=1.7)$. Excellent visual agreement, for both concentrated and dilute solutions, was obtained between the theoretically and experimentally derived values for times out to approximately 8ns ($\sim2.5\tau_D$).

One of Haan and Zwanzig's initial objectives was to determine if excitation transport is diffusive at long times (115). Although they could not demonstrate that transport was diffusive in this limit, they were able to establish that if excitation transport became diffusive in the long time limit, the diffusion coefficient would be proportional to $C_D^{4/3}$ (115). GAF, taking the limit as $t \to \infty$, found a limiting value for their generalized diffusion coefficient could be expressed as

$$0.483\ C_D^{4/3}\ R_0^2\ \tau_D^{-1}. \tag{5.29}$$

Thus, GAF's theory predicts that in the long time limit the diffusion coefficient is independent of time and has the proper dependence on C_D as required by Haan and Zwanzig's scaling argument (115).

The GAF theory was extended by Loring, Andersen and Fayer (129, hereafter LAF) to include the effects of trapping in a two-component, disordered, three-dimensional system. The system contains immobile donor and trap molecules placed randomly in a host medium which does not partake in the excitation transport process. Excitations can be transferred from donor to donor and from donor to trap, but the trapping step is considered to be an irreversible process. The LAF formalism parallels that developed in the GAF theory (69). Estimates of the Green's function derived from the LAF theory yield values for the generalized diffusion coefficient, the mean squared displacement of excitation and the time-dependent probabilities that the excitation is in the donor or trap ensembles. In the presence of traps and no donor or trap emission, the LAF

theory predicts that excitation transport in the donor ensemble is non-diffusive at all times (129). LAF stated that this result should be expected on physical grounds, since at long times, the excitation will become trapped and cease to move within the system. Hence, the mean squared displacement should attain some finite maximum value in the long time limit due to the presence of traps. A final statement made by LAF was that the functional form of donor population decay is nonexponential and not describable in terms of a trapping rate constant (129).

The influence of traps on the time development of donor fluorescence has been an active area of research for many years (70, 129-138). Traditional theories of excitation transport and trapping in a disordered system have yielded results which indicate that (neglecting fluorescence decay) depopulation of the donor ensemble progresses initially as $\exp(-at^{1/2})$ and as $\exp(-\overline{W}t)$ in the long time limit, where a and $\overline{W}$ are quenching rate constants (137). The short time behavior is believed to result from quasi-static quenching of the donor excitation by traps (139, 140). The functional form at early times is identical to the result obtained by Förster (141) describing excitation quenching in the limit of zero donor density. At later times, the excitation is quenched primarily as a result of its hopping within the donor ensemble until a trap is encountered (140). Excitation reaching these remote centers by way of their migration rather than direct transfer accelerate the decay process and make it exponential (140). Models conceived to describe the time development of the fluorescence in the presence of traps have largely been phenomenological (130, 131, 142). The general approach has required

the existence of a quenching sphere of radius R_W around each trap (134). An excitation, upon entering this region of strong interaction, is quenched. Two models of consequence have emerged from the foregoing premise: the first, a hopping model developed by Burshtein (131); the second, a diffusion model introduced by Yokota and Tanimoto (130). The hopping model is applicable when a migration step (defined as the average donor-donor separation for the system (134)) exceeds the radius of a quenching zone around the acceptor, while the diffusion model is relevant otherwise (134). An alternative criterion establishes that it is a hopping mechanism when $Z<<1$ and a diffusion mechanism when $Z>>1$ (140)

$$Z = (R_o^{DA} / R_o^{DD})^6 , \tag{5.30}$$

with R_o^{DA} and R_o^{DD} defined as the Förster radii (see equation (5.2)) for a donor-acceptor pair and a donor-donor pair, respectively. In both cases, the initial decay is nonexponential. The transition from this initial quasi-static part of the decay to the exponential one is determined approximately by the crossover time t_1. This crossover time is defined differently in the two theories (134). For the diffusion model, the crossover time is determined by the condition that $\exp(-(4/3)\pi c R_W^3)$, the number of excitations that do not fall initially into the quenching sphere, is equal to $\exp(-\overline{W}t)$. In other words, when

$$t_1 = (4/3)\pi c\ R_W^3/\overline{W}, \tag{5.31}$$

where c is the number of traps per cm^3 and $\overline{W}$ is the quenching rate constant, the donor decay transforms from its initial nonexponential character into an exponential form. The mean quenching rate constant increases with c and ρ (the number of donors per cm^3) when the migration-accelerated quenching has a hopping or diffusive character. In the hopping limit

$$\overline{W} = (\tfrac{2}{\pi})\Delta_D\Delta_T \tag{5.32}$$

where Δ_D and Δ_T are the reduced donor and reduced trap concentrations, respectively, and are defined by (140)

$$\Delta_D = (\tfrac{\sqrt{2}}{3})\pi^2\ \rho(R_0^{DD})^3 \tag{5.33}$$

and

$$\Delta_T = (\ \tfrac{2}{3})\pi^2\ c\ (R_0^{DA})^3. \tag{5.34}$$

In the diffusive limit, the quenching rate constant becomes (140)

$$\overline{W} = (\tfrac{2}{\pi})\Delta_D\Delta_T(2.3/(Z1/4)). \tag{5.35}$$

The reduced donor densities defined by Fedorenko and Burshtein Δ_D (140) and GAF C_D (69) (see equation (5.17)) vary slightly. They are related by

$$C_D = \frac{(2)^{3/2}}{\pi}\Delta_D. \tag{5.36}$$

The reduced trap densities are also defined differently. LAF (129) defined the reduced trap concentration C_T as

$$C_T = (4/3)\pi c(R_0^{DA})^3, \tag{5.37}$$

so that Δ_T and C_T are related by

$$C_T = (\frac{2}{\pi})\Delta_T. \tag{5.38}$$

It will be necessary to use both conventions in this work.

As was stated previously, LAF (129) discounted the notion that $G^D(t)$, the excited donor population (excluding relaxation via donor fluorescence), in the presence of traps, could be expressed in terms of a quenching rate constant $\overline{W}$. Their argument was founded on the shapes of theoretical curves of $G^D(t)$ for varied parameters. In the limit as $C_T \to 0$, finite C_D the GAF theory was recovered, while for $C_D \to 0$, finite C_T decay curves of $G^D(t)$ *vs* t approached the Förster results (129, 141). Fedorenko and Burshtein (140) countered that the hopping and diffusion models of fluorescence quenching are also supported by experimental data. They contended that the manner in which LAF obtained $G^D(t)$ obscures a direct comparison between the LAF model and the quenching sphere models. Specifically, the results derived from the LAF theory were actually $\hat{G}^D(\varepsilon)$, the Laplace transforms of $G^D(t)$. These transforms were inverted numerically by LAF and presented graphically to illustrate the predicted decays of the donor populations (129).

To facilitate comparison between the theories, Fedorenko and Burshtein (140) obtained analytical expressions for $G^D(t)$ using the theoretical model of LAF and performing the proper analytical inversions on $\hat{G}^D(\varepsilon)$. The resulting expressions for $G^D(t)$ were compared with their

counterparts from the quenching sphere theories under the proper limiting conditions. In the subsequent analysis, only the results from the LAF three-body model will be used for comparison with the quenching sphere models.

The general form of the analytical expression for $G^D(t)$ from the LAF theory was written as (140)

$$G^D(t) = \exp(-qt)g(t) \tag{5.39}$$

where

$$q = \frac{(\Delta_D+\Delta_T)^2}{4} - A(z) - B(z), \tag{5.40}$$

$$A(z) = (8/\pi^2)\{0.1887\ \Delta_D^2 + [0.3832-\alpha(z)]\Delta_D\Delta_T/\sqrt{2}\}, \tag{5.41}$$

$$B(z) = (4/\pi^2)\{0.3371\ \Delta_T^2 - [0.24604-\beta(z)]\sqrt{2}\Delta_D\Delta_T\} \tag{5.42}$$

and $\alpha(z)$, $\beta(z)$ are tabulated functions (129). Having defined the following terms (140)

$$a = \Delta_T/2 + (\Delta_D/2)[1-(4/\Delta_D^2)A(z)]^{1/2}, \tag{5.43}$$

and

$$b = \Delta_T/2 - (\Delta_D/2)[1-(4/\Delta_D^2)A(z)]^{1/2}, \tag{5.44}$$

an expansion for g(t) at short times was expressed as

$$g(t) = 1 - \frac{2}{\pi^{\frac{1}{2}}}\ \frac{a^2-b^2}{a-b}t^{1/2} + \frac{a^3-b^3}{a-b}t - \ldots \tag{5.45}$$

for $a^2t<<1$ and $b^2t<<1$ (in Fedorenko and Burshtein's notation, t is a normalized time equal to time/τ_D). Conversely, in the long time limit g(t) is representable as

$$g(t) = \frac{a+b}{2\pi^{\frac{1}{2}}a^2b^2}t^{-3/2} - \mathcal{O}(t^{-5/2}),\ b>0 \tag{5.46}$$

$$= \frac{1}{a\pi^{\frac{1}{2}}}t^{-1/2} - \mathcal{O}(t^{-3/2}),\ b=0 \tag{5.47}$$

$$= \frac{2|b|}{a-b}\exp(b^2t) + \mathcal{O}(t^{-3/2}),\ b<0. \tag{5.48}$$

Retaining only the first term in each of the expansions of g(t) in equation (5.39), Fedorenko and Burshtein (140) showed that for $t \to 0$

$$G^D(t) = \exp[-2\Delta_T(t/\pi)^{1/2}], \tag{5.49}$$

while for $t \to \infty$

$$G^D(t) = \frac{\Delta T}{2\pi^{\frac{1}{2}}a^2b^2}\frac{\exp(-qt)}{t^{-3/2}},\ b>0 \tag{5.50}$$

$$= \frac{1}{a\pi^{\frac{1}{2}}}\frac{\exp(-qt)}{t^{\frac{1}{2}}},\ b=0 \tag{5.51}$$

$$= \frac{2|b|}{a-b}\exp[-(q-b^2)t],\ b<0. \tag{5.52}$$

Based on equations (5.49 - 5.52), Fedorenko and Burshtein (140) argued that the LAF results, when expressed analytically, discounted the LAF assertion that the quenching process is "nonexponential and cannot be described in terms of a quenching rate constant" (129). The quenching process is actually nonexponential only when b>0, the quasi-static case corresponding to low donor and high trap concentrations. When b<0, however, the analytical form for $G^D(t)$ indicates that, given sufficient time, the donor decay should take on an exponential character with a mean quenching rate

$$\overline{W} = q\text{-}b^2 \qquad (5.53)$$

from equation (5.52). Fedorenko and Burshtein contend that the LAF approach, therefore, does not contradict but rather substantiates the conventional ideas on quenching kinetics in the limiting case where migration accelerated quenching occurs (b<0, equation (5.52)).

Fedorenko and Burshtein remarked that LAF came to a disparate conclusion regarding the presence of an exponential phase of donor excitation quenching solely because the points they chose for analysis (Δ_D,Δ_T,Z) forced the long time donor ensemble decay into the quasi-static decay regime (b>0, equations (5.50) and (5.51)). They later acknowledged (140) that in two instances (Figure 5-8, LAF (129)), where Δ_D/Δ_T = 7.2; 28.6; Z=1, the donor decay should obey the migration-accelerated quenching kinetics (b<0). If these two curves had been plotted using logarithmic coordinates, they continued, the exponential trend of $G^D(t)$ would have been evident for practically all times (140).

Given the coarse divisions associated with the ordinate and abscissa in Figure 5-8 of the LAF paper (129), it would be difficult to achieve an unambiguous conclusion regarding the nature of the decay profile. At best, one might state that the decay is nearly exponential over the time range plotted.

In addition to the theoretical results discussed above, there are experimental data which characterize the fluorescence decay of solutions with donor and trap concentrations in the region where one would expect migration-accelerated quenching kinetics to prevail (b<0). The study was

Figure 5-8. Schematic semi-log plot of $G^D(t)$ versus t, where $G^D(t)$ is the probability of finding the excitation in the donor ensemble (when fluorescence decay neglected). Curve (a): $G^D(t)$ in the absence of donor-donor transfer. Curve (b): $G^D(t)$ in the rapid transfer limit. Curve (c): $G^D(t)$ in the regime intermediate between the static and rapid transfer limits. All three curves have same initial slope; (a) is non-exponential at all times, (b) is exponential at all times, (c) becomes exponential as $t \to \infty$. From Huber (137)

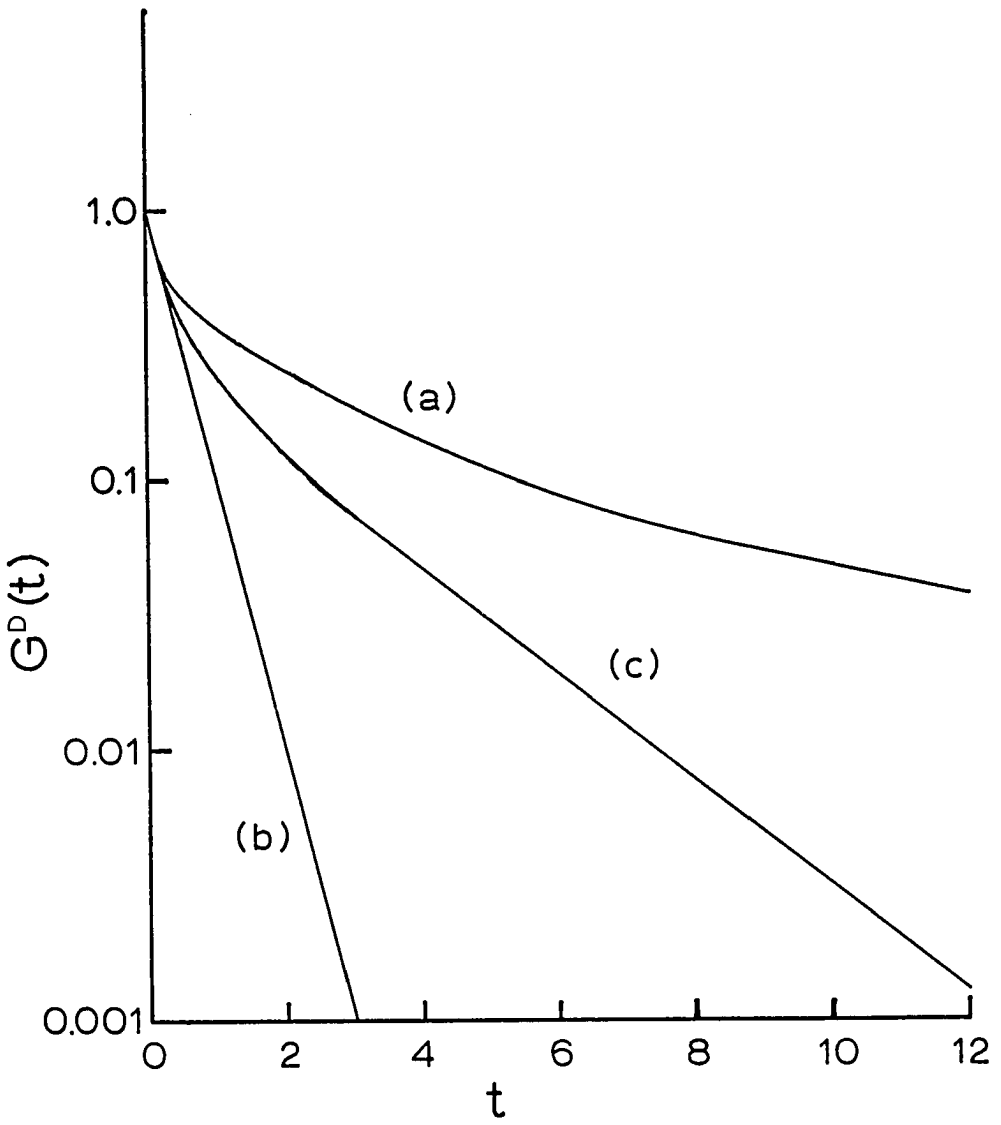
1.0
0.1
0.01
0.001
$G^D(t)$
(a)
(b)
(c)
0
2
4
6
8
10
12
t

performed by Lutz, Nelson, Gochanour and Fayer (143), who examined the trapping of excitation on rh6G monomers by rh6G dimers in glycerol solvent. rh6G concentrations ranged from 8.7×10^{-4} to 0.05 M. Although the actual rh6G monomer and dimer concentrations were not measured, it may be conservatively estimated that $\Delta_D > \Delta_T$ for the majority of the sample concentrations. Lutz et al. (143) report that, in general, the fluorescence decays for these solutions should be nonexponential, although the deviations from exponentiality should be slight. Only in the limit that $\Delta_T \to 0$ would one expect truly exponential behavior. The time-resolved decay of the excited donor population in a 1.74×10^{-2} M rh6G solution was chosen as a typical decay curve and plotted (Figure 5-4, Lutz et al. (143)) as the log of the detected signal versus time. The figure illustrates that the decay is quasi-exponential with minor systematic deviations being perceptible when the data were compared to a "best fit" exponential decay curve.

When LAF assert that the functional form of the donor population decay is nonexponential, they are aware that it should acquire more exponential character as $\Delta_T \to 0$ ($b<0$) (143). This trend, they feel, is supported by experimental data (143). On the contrary, Fedorenko and Burshtein (140) maintain that in the limit that $\Delta_D/\Delta_T > 1$ ($b<0$), the donor decay should be exponential, as predicted by the conventional models of hopping and diffusive quenching. Moreover, they claim that the LAF theory predicts the same exponential behavior (equation 5.52). The conflict between what LAF state (129) and what their theory predicts (140) (regarding the form of the donor decay for $b<0$) can be partially resolved

by reviewing how Fedorenko and Burshtein attained an analytical expression for LAF's $G^D(t)$. Taking only the first term in the expansion of g(t) (equation (5.52)) and substituting into equation (5.39), Fedorenko and Burshtein gained an exponential form for $G^D(t)$ (140). If they had included the second term in the expansion of g(t) in the substitution, however, the expression for $G^D(t)$ would no longer be exponetial. Thus, rather than supporting Fedorenko and Burshtein's contention (140), the analytical form of $G^D(t)$ is, in general, nonexponential (129).

When the trap concentration is much larger than the donor concentration and donor-donor interactions can be neglected (large $\Delta_T, \Delta_D \to 0$), the quenching kinetics can be described exactly. Förster showed that the decay of the donor population in this limit should proceed as (141)

$$G^D(t) = \exp[-2\Delta_T(t/\pi)^{1/2}] \tag{5.54}$$

for all t (normalized time), when the fluorescence decay is suppressed. The phenomenological quenching sphere models (134) reproduce exactly the Förster equation in the static quenching limit by virtue of a crossover time (which defines when the quenching converts from a Förster decay to an exponential decay) that goes to infinity as the Förster limit is approached.

Repeating a procedure they had applied in the limit of migration-accelerated quenching, Fedorenko and Burshtein (140) obtained an analytical form for LAF's $G^D(t)$ in the Förster limit. Again, the general form of the donor decay (neglecting fluorescence decay) fits

$$G^D(t) = \exp(-qt)f(t), \tag{5.55}$$

where

$$q = \Delta_T^2/4, \text{ in the two-body theory} \tag{5.56}$$

$$= \Delta_T^2/4 - A(z)-B(z), \text{ in the three-body theory} \tag{5.57}$$

with A(z), B(z) defined in equations (5.41) and (5.42), respectively. However, f(t), when expanded, gives (for $\Delta_T^2 t << 4$)

$$f(t) = 1 - ({}^2/_\pi 1/2)(\Delta_T^2 t)^{1/2} + (3/4)\Delta_T^2 t + \ldots \tag{5.58}$$

and (for $\Delta_T^2 t >> 4$)

$$f(t) = ({}^8/_\pi 1/2)(\Delta_T^2 t)^{-3/2} - ({}^{96}/_\pi 1/2)(\Delta_T^2 t)^{-5/2} + \ldots \tag{5.59}$$

which, when substituted into equation (5.55), yields

$$G^D(t) = \exp[-2\Delta_T({}^t/_\pi)^{1/2}], \text{ for } \Delta_T^2 t << 4 \tag{5.60}$$

$$= \exp[-qt]({}^8/_\pi 1/2)(\Delta_T^2 t)^{-3/2}, \text{ for } \Delta_T^2 t >> 4. \tag{5.61}$$

The short time behavior of LAF's $G^D(t)$ is identical to the derived result of Förster (141). At long times, however, the functional form of $G^D(t)$ deviates from Förster's result. To show the extent of deviation in the long time limit, Fedorenko and Burshtein prepared plots of the functions $\mathrm{Ln}(-\mathrm{Ln}(G^D(t)))$ versus $\mathrm{Ln}(\Delta_T^2 t)$ from the Förster equation and the two- and three-body analytical forms of LAF's $G^D(t)$. Those plots are reproduced here in Figure 5-9. Clearly, for large values of $\Delta_T^2 t$, both the two- and three-body approximations to the Förster equation are deficient. Neglect of higher order terms from the expansion of f(t) (equation (5.59)) in the

Figure 5-9. Excitation quenching kinetics in the static limit (Δ_D=0). Top curve is LAF two-body result; middle curve is LAF three-body result; bottom curve is Förster result. From Fedorenko and Burshtein (140)

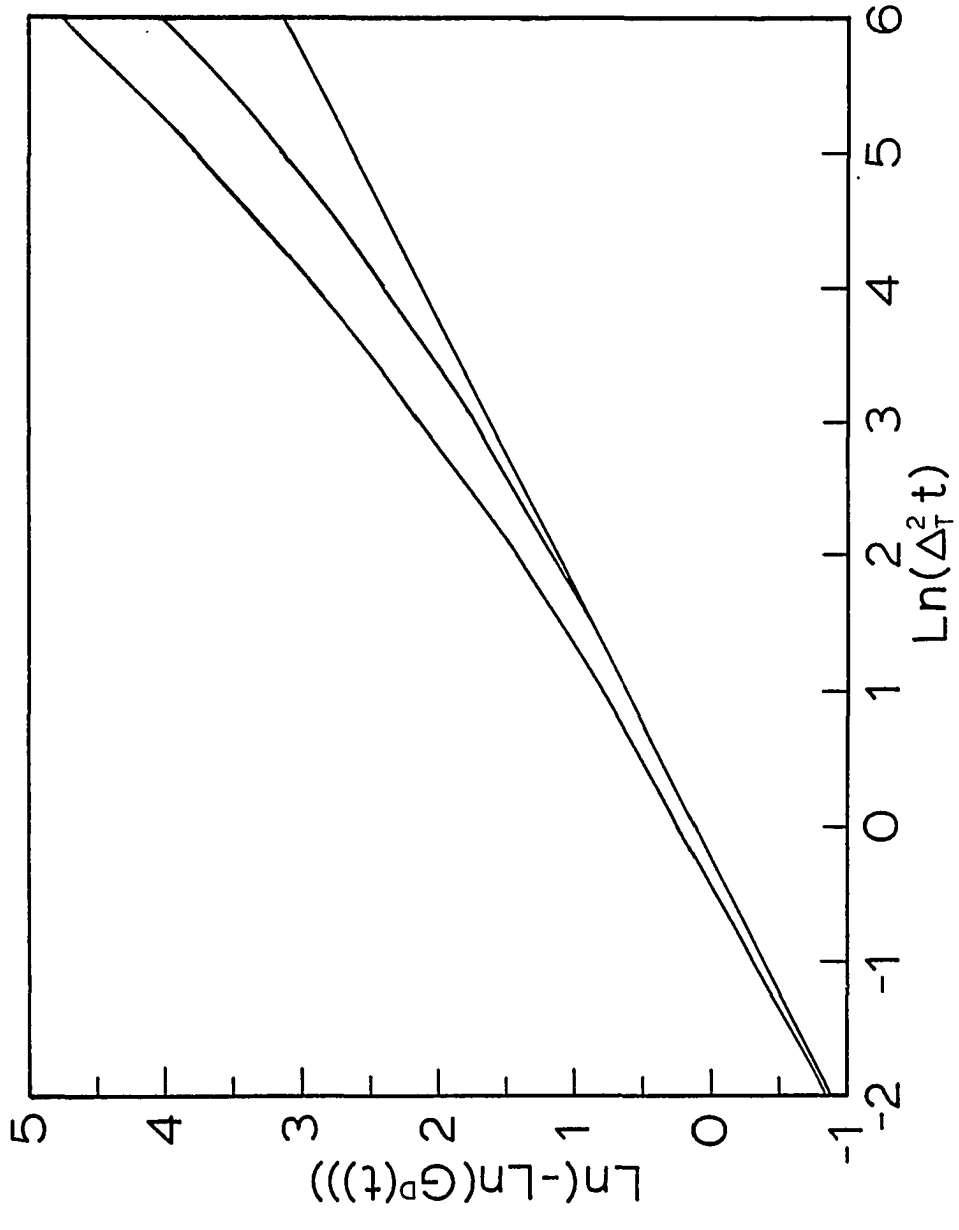
Ln(-Ln(G^D(t)))
Ln(Δ_T^2 t)
5
4
3
2
1
0
-1
-2
-1
0
1
2
3
4
5
6

expression for $G^D(t)$ (equation (5.55)) will not account for this deviation. Perhaps, as Fedorenko and Burshtein (140) speculated, the four-body and all higher order diagrams must be included in LAF's calculations to reduce the observed deviation to zero.

A more complete review of Figure 5-9 indicates that the LAF models provide better approximations to the Förster equation than they appeared to present during the previous cursory examination. For example, while the two-body model diverges from Förster's result at relatively short times, the three-body model does not begin to deviate until $Ln(\Delta T^2 t)$ is approximately two. For $\Delta T=1$, then, the LAF three-body model will reproduce the Förster result out to nearly seven lifetimes (τ_D). Similarly, where Fedorenko and Burshtein (140) show large deviations exist between the LAF approximations and the Förster equation ($Ln\Delta T^2 t \sim 6$), the form of the donor decay $G^D(t)$ has been followed out to over four hundred fluorescence lifetimes (for $\Delta T=1$). At this point the Förster equation predicts $G^D(t) \cong 10^{-10}$, while the LAF three-body theory estimates $G^D(t) \cong 10^{-22}$. Considering that the actual donor decay (including spontaneous emission) is (129)

$$N^D(t) = e^{-t} G^D(t) \tag{5.62}$$

(t is normalized time) -- when $t = 400\ \tau_D$, it is reasonable to assume that the Förster, LAF two-body and LAF three-body equations all predict the same result -- the probability that the excitation is in the donor ensemble is zero.

As Δ_T is increased, the divergence of LAF's models from the Förster result will occur at shorter times, due to the squared dependence of the abscissa in Figure 5-9 on Δ_T. Considering a Δ_T of 7.85 (C_T=5.0), for the LAF three-body model, the expected deviation should begin at a time of $\sim 0.05\tau_D$ (if the deviation begins at $Ln(\Delta_T^2 t) \tilde{=} 1.5$). Plotting the numerically derived $G^D(t)$ versus t (normalized) in Figure 5-10 (as LAF did in their Figure 7, 129)) gives another perspective on the deviation of LAF's models and the Förster result. On an expanded ordinate axis, LAF's numerically derived $G^D(t)$ (from the three-body theory) does not deviate visibly from the Forster result until $t \tilde{=} 0.05\tau_D$, in agreeent with Fedorenko and Burshtein's plot (Figure 5-9). Beyond $t \tilde{=} 0.05\tau_D$ in Figure 5-9, $G^D(t)$ has decayed to less than 10% of its initial value. Therefore, points at which there are relatively large errors in LAF's $G^D(t)$ correspond to times when the probabilities for excitation to be in the donor ensemble have neared zero.

Based on Figure 5-10, it is apparent that, for realistic times, the accuracy of the three-body approximation in the Förster limit supports the validity of the general trapping theory proposed by LAF. In this limit, four-body and higher order diagrams do not contribute significantly to $G^D(t)$ until times when the donor decay (excluding intramolecular decay) has decreased to less than one-tenth of its initial value.

The validity of the GAF model, which describes excitation migration in the absence of trapping, has also been questioned by Fedorenko and Burshtein (140). Their arguments are similar to those employed toward the LAF model. In this case, the kinetics of excitation migration from

Figure 5-10. Comparison of the two-body and three-body LAF approximations in the limit of zero donor concentration to Förster's exact solution of this limiting case. t is normalized time

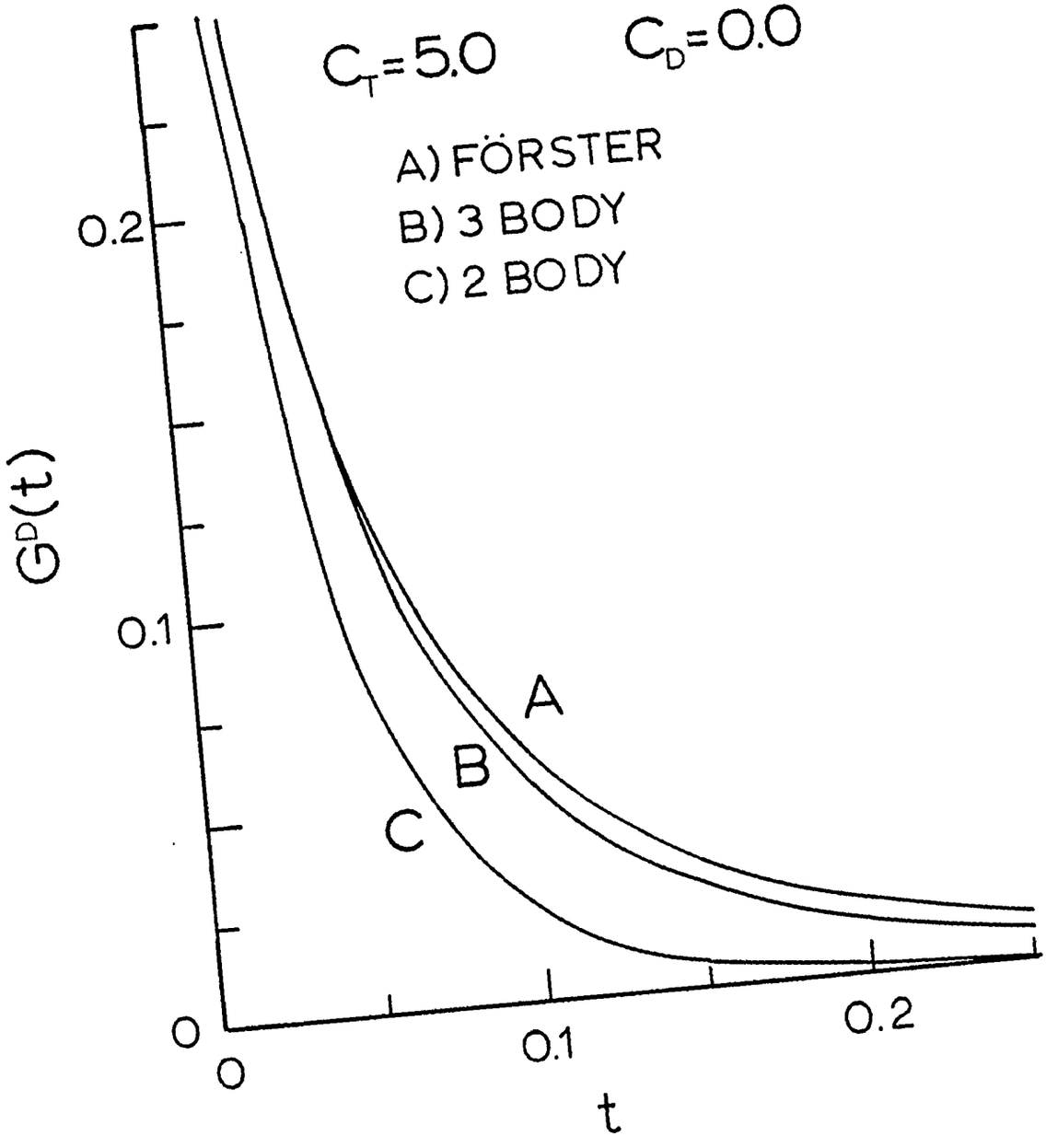
$C_T = 5.0$
$C_D = 0.0$
A) FÖRSTER
B) 3 BODY
C) 2 BODY
$G^D(t)$
0.2
0.1
0
A
B
C
0
0.1
0.2
t

the photon excited donor have been shown by Klafter and Silbey to obey (140, 144)

$$G^S(t) = \exp[-2\Delta_D(t/\pi)^{1/2}],\ (4\Delta_D^2/\pi)t<<9 \tag{5.63}$$

and

$$G^S(t) = (\pi/4\Delta_D^2 t)^{3/2},\ (4\Delta_D^2/\pi)t>>9 \tag{5.64}$$

where $G^S(t)$ is the probability that the excitation is on the photon-excited donor (excluding depopulation due to intramolecular decay) at time t (normalized). Δ_D is defined in equation (5.33). Alternatively, GAF's results (69), in the analytical form introduced by Fedorenko and Burshtein (140), were expressed as

$$G^S(t) = \exp[-2\Delta_D(t/\pi)^{1/2}],\ \Delta_D^2 t<<4 \tag{5.65}$$

and

$$G^S(t) = \exp(-qt)\ (8/\pi^{1/2})(\Delta_D^2 t)^{-3/2},\ \Delta_D^2 t>>4 \tag{5.66}$$

where q is defined in equations (5.56) and (5.57) for the two-body and three-body results, respectively. For short times, the results of Klafter and Silbey and GAF agree (140). In the long time limit, however, the GAF model associates with $G^S(t)$ an exponentially damped component not present in the Klafter and Silbey results (140).

Again, one may argue that, for Δ_D=1, neither the Klafter and Silbey (equation (5.64)) nor the GAF (equation 5.66)) results apply until times <u>much</u> greater than $\sim 6\tau_D$ are reached. By the time this asymptotic limit is attained, $G^S(t)$ is essentially zero. Although the asymptotic limit is

reached sooner as Δ_D is increased, the rate of decay of $G^S(t)$ also increases to yield similar conclusions.

As discussed above, Fedorenko and Burshtein have opposed the LAF and GAF theories on the basis that, when expressed analytically, neither model predicts the proper long time asymptotics of the excitation hopping processes they are presumed to model. The phenomenological quenching sphere models, which Fedorenko and Burshtein espouse, describe trapping as a static process at very short times and a process occurring via excitation migration at long times. The quenching sphere models have been shown to be accurate in these two limits (140). To be accurate for intervening times, the quenching sphere models should -- but do not -- describe the trapping as a convolution of static quenching and quenching resulting from excitation migration (134).

It has been shown (equation (5.62)) that the Green's function $G^D(t)$ and spontaneous emission act in conjunction to set an upper limit on the times when one would consider the excitation hopping and quenching processes to have physical significance. Discussion of migration and trapping beyond several fluorescence lifetimes becomes moot because there is essentially no excitation left in the donor ensemble at those times. The upper time limit set by $G^D(t)$ and spontaneous emission is, in general, reached before the asymptotic limits derived from the analytic limits derived from the analytic GAF and LAF expressions or the quenching sphere models (140). The regions of interest, when discussing migration and quenching, should therefore be the short and intermediate time ranges rather than the short and long time limits considered by Fedorenko and

Burshtein. Thus, the LAF and GAF models should not be dismissed solely because they do not obtain the proper asymptotic limits, especially when the long time limiting behavior will not be observed experimentally. In fact, for intermediate times, it is expected that the LAF and GAF theories will provide a much better approximation to the excitation migration and trapping processes than the conventional theories would provide.

To provide a comparison between the GAF three-body theory and experiment, Gochanour and Fayer (109) obtained decays for rhodamine 6G in glycerol using the following technique. Fluorescence profiles were acquired by KDP sum-frequency mixing of the rh6G fluorescence with variably delayed 1.06 μm pulses from a cw mode-locked Nd:YAG laser. The resulting 390 nm upconverted pulses were detected by a cooled photomultiplier and lock-in amplifier combination. In the following chapter, the GAF theory (69) will be reinvestigated using time-correlated photon counting to obtain the time-dependent fluorescence profiles for rhodamine 6G in glycerol. The superior data statistics afforded from this technique (145), together with autocorrelation functions of the residuals (146), provide a means for detecting systematic deviations between the data and three-body decay curves which are too small to be observed using sum-frequency mixing. Fluorescence decay profiles will be observed out to times of approximately 10 ns ($\sim 3\tau_D$). Numerical inversion (69, 147) of the theoretical results $\hat{G}^S(t)$ will enable direct comparisons to be made between the results derived from theory and experimental data over the time range considered. Agreement between the theory and experiments,

after the employment of this discriminating test, will substantiate the validity of the GAF three-body theory for times of practical interest. Disagreement between theory and experiment may signal the breakdown of the three-body model (due perhaps to the increasing importance of higher-body terms with increase in rh6G concentration).

The two-dimensional counterpart to the LAF three-dimensional transport and trapping theory has been developed by Loring and Fayer (70). In contrast to the three-dimensional LAF model (129) for two-dimensional systems, the three-body solutions to the master equation cannot be determined, because the three-body Green's function $G^s(t)$ fails to converge at long times (111). It was shown in the GAF three-dimensional results (69) that, in general, the three-body ($G^s(t)$ provides a much better approximation to the true Green's function than the two-body model. In two dimensions, it is expected that the two-body model will be even less reliable than in three dimensions because density expansions tend to converge less rapidly in systems of lower dimensionality (111). To date, no experimental measurements of the two-body $G^s(t)$ have been reported.

To provide a basis from which to analyze the Loring and Fayer two-body theory more thoroughly, the first experimental determination of the Green's function $G^s(t)$ will be performed for a two-dimensional disordered system. The random, two-dimensional systems were fashioned by adsorbing submonolayers of rhodamine 3B (rh3B) from solution onto optically flat fused quartz. rh3B was chosen as the donor species because it shows a reduced tendency to dimerize on the quartz substrate relative to many dyes (such as cresyl violet (148)), is free of acid-base equilibria which

complicated the fluorescence decay curves of rhodamine B (149, 150) and manifests a strong $S_1 \leftarrow S_0$ transition ($\varepsilon_{max} \sim 1.2 \times 10^5$ at 555 nm in ethanol) which can be pumped with a rh6G dye laser.

The Loring and Fayer theory (70), which includes the effects of excitation transport and trapping, has been reduced (to consider only donor-donor excitation transport) by setting C_T equal to zero in the Loring and Fayer equations. Thus the Loring and Fayer model, as presented here, renders itself as a two-dimensional analog to the GAF two-body theory (69).

The presence of trapping centers in a disordered system complicates the theory which describes the decay of the probability for excitation to remain on the photon-excited donor. The LAF model was shown to be an extension of the GAF theory (129) and the Loring and Fayer model, without traps, is a limiting case of the general Loring and Fayer theory (70). Hence, by experimentally investigating two- and three-dimensional systems without traps, one may gain a more thorough comprehension of the donor-to-donor excitation transport dynamics for realistic times and use these results as a basis for examining excitation transport and quenching in the more complex systems containing traps. Furthermore, experimental artifacts (such as dimer formation among donors, self-absorption, etc.) which can distort the data in systems with or without traps will be more easily discerned in the limit of zero trapping centers.

FLUORESCENCE DEPOLARIZATION OF RHODAMINE 6G IN GLYCEROL: A PHOTON-COUNTING TEST OF 3-DIMENSIONAL EXCITATION TRANSPORT THEORY

by

John F. Hedstrom, David E. Hart, Philip A. Anfinrud, and Walter S. Struve

Department of Chemistry and Ames Laboratory - USDOE
Iowa State University, Ames, IA 50011

CHAPTER VI. FLUORESCENCE DEPOLARIZATION OF RHODAMINE 6G IN GLYCEROL: A PHOTON-COUNTING TEST OF 3-DIMENSIONAL EXCITATION TRANSPORT THEORY

Introduction

It has long been recognized that accurate modeling of fluorescence concentration depolarization in solution is a formidable theoretical problem. Early attempts to describe the influence of Förster dipole-dipole excitation transport (1) on fluorescence depolarization frequently assumed that transfer was limited to one or two excitation hops from the initially excited molecule (2, 3), or that excitation was exchanged only between nearest and next-nearest neighbor molecules in solution (4-6). To our knowledge, the first realistic calculations of the probability $G^S(t)$ that excitation is found on the initially excited molecule at time t were provided by Gochanour, Andersen, and Fayer (7), who worked out diagrammatic Green's function expansions of solutions to the excitation transport master equation (8) and obtained successive self-consistent approximations to $G^S(t)$. The latter Green's function is related to the fluorescence depolarization in solution by (9)

$$G^S(t) = 2.5,\frac{I_{\parallel}(t) - I_{\perp}(t)}{I_{\parallel}(t) + 2I_{\perp}(t)} \qquad (6.1)$$

where $I_{\parallel}(t)$ and $I_{\perp}(t)$ are the fluorescence intensity components polarized parallel and normal to the excitation polarization. (This equation holds if the solvent is viscous enough to inhibit rotational depolarization

during the fluorescence lifetime, if the molecular absorption and emission transition moments coincide, and if the excitation pulse energy is small enough so that the orientational distribution of unexcited molecules is random.) Gochanour and Fayer (9, hereafter GF) tested their second-lowest (three-body) self-consistent approximation to $G^s(t)$ by measuring the experimental time-dependent fluorescence components

$$I_{\parallel}(t) = Ae^{-t/\tau}[1 + 0.8\ G^s(t)]$$
$$I_{\perp}(t) = Ae^{-t/\tau}[1 - 0.4\ G^s(t)] \qquad (6.2)$$

for rhodamine 6G (rh6G) in glycerol. By computing the three-body Green's function $G^s(t)$, which depends on the known rh6G concentration and on the isotropic dye lifetime τ (which they measured at sufficiently high dilution so that $G^s(t) \to 1$ for all t), they were able to check experimental fluorescence intensities against convolutions of their Gaussian experimental response function with theoretical profiles generated from equation (6.2). Excellent visual agreement was obtained, with divergences of $\lesssim$5% for times up to $\sim$2.5 τ ($\sim$8 ns).

GF obtained their fluorescence profiles by KDP sum-frequency mixing of rh6G fluorescence with variably delayed 1.06 μm pulses from a cw mode-locked Nd: YAG laser, and the resulting 390 nm up-converted pulses were detected by a cooled photomultiplier and lock-in amplifier. In this paper, we use time-correlated photon counting to obtain time-dependent fluorescences for rh6G in glycerol. This technique (10) offers far superior data statistics, and autocorrelation functions of the residuals (11) can elicit systematic deviations between data and theoretical profiles

which are too small to observe using sum-frequency mixing. Our data analysis in the next section provides a check on whether the polarized fluorescence components actually exhibit the form of equation (6.2), or whether the single-exponential factors are distorted, e.g., by excitation trapping at rh6G dimers, which accelerates fluorescence decay and renders it nonexponential in highly concentrated solutions. Our analysis also avoids parameter correlation (covariance) between the rh6G concentration (which influences $G^S(t)$) and τ in equation (6.2), so that it is unnecessary to rely on independent low-concentration measurements to obtain the isotropic dye lifetime τ. This advantage is important, because τ varies significantly with rh6G concentration even in 10 μm path-length fluorescence cells due to self-absorption (12) and (at higher concentrations) excitation trapping. It develops that because the absorption and fluorescence spectra of rh6G overlap so much near 540 nm (12), self-absorption cannot be even approximately suppressed in such thick cells at the millimolar concentrations over which excitation transport competes efficiently with intramolecular decay. At the lowest rh6G concentrations, our fluorescence decay profiles prove to be <u>indistinguishable</u> from theoretical profiles calculated using the three-body Green's function $G^S(t)$ in equation (6.2) when the autocorrelations of residuals are examined. Nonstatistical autocorrelations are obtained at the higher rh6G concentrations, but these differences are shown to arise largely from nonexponentiality in the isotropic decay function (i.e., excitation trapping by rh6G dimers) and from self-absorption, rather than from inaccuracies in the three-body Green's function.

Experimental Section

An acousto-optically mode-locked argon ion laser (Coherent Innova 90 with 5 W plasma tube operated at 26A) pumped a cavity-dumped rh 590 dye laser (Coherent CR-599-01 tuned with three-plate birefringent filter) to produce tunable picosecond pulses which exhibited zero-background autocorrelations with ∿8 ps fwhm. The mode-locker was a Harris Corporation H-401 unit driven at 48 MHz. The 4.8 MHz cavity dumper included a Harris Corporation H-100 acousto-optic modulator and H-102 driver, with folding reflectors mounted on Newport Research Corporation beam directors and Line Tool Co. translators. Laser performance was monitored and optimized with a rotating-mirror real-time autocorrelator (13).

Commercial rhodamine 590 chloride (rh6G) was obtained from Exciton; the unpurified dye showed only one TLC spot using Analtech silica G plates and three different solvent systems (ethanol/acetone, ethanol/acetic acid, and n-propanol/formic acid). Fluorescence cells were formed from $\lambda/4$ fused quartz flats (treated with dichlorodimethylsilane) by compressing a drop of solution between two flats. Optical density measurements on rh6G solutions of known concentration in such cells showed that this procedure typically yielded solutions with ∿10 μm path length. Thinner cells (∿2 to 4 μm) could be obtained by etching the Al coating from a ∿4 mm diameter circular area of an optically flat front-surface reflector, and then bounding the sample between a surface so treated and a fused quartz flat.

Horizontally polarized dye laser pulses were incident on the horizontal rh6G cell surface at $\sim 75^{o}$ from normal. Fluorescence was collected vertically with a 5 cm f.l. quartz lens and was focused by a 10 cm f.l. lens through a variable rectangular aperture prior to detection by a Hamamatsu 1564U microchannel plate phototube (MCP) with bialkali photocathode and borosilicate glass window. The MCP exhibited $\sim 6 \times 10^{5}$ gain at 3000V, 500 nm and a transit time spread of 76 ps at 3200 V. Laser scatter and filter fluorescence were minimized by two 3 mm Schott RG-590 filters and a 3 mm Schott RH-610 filter. Excitation pulses were focused with a 10 cm f.l. quartz lens to ~ 0.1 mm diameter at the cell surface. The excitation and analyzer polarizers were Promaster Spectrum 7 photographic polarizers; the analyzer was placed between the cell and the collecting lens. The differential detector sensitivity to fluorescence photons polarized parallel and normal to the excitation polarization was conservatively less than 2%.

MCP photocurrent pulses were amplified and inverted using a B&H Electronics AC3011 MIC (3.15 GHz) 21 dB preamplifier and an EG&G IT100 inverting transformer. Amplified pulses were passed through a Tennelec TC455 quad constant-fraction discriminator (CFD) and served as START pulses in an Ortec 457 time-to-amplitude converter (TAC). An EG&G FOD-100 photodiode operating in the photoconduction mode sampled dye laser pulses; its signal was processed through an Ortec 934 quad CFD to provide STOP pulses. TAC output was stored in a Canberra Series 30 MCA operated in the PHA mode to yield 5.0, 10.0, or 20.0 ps channel resolution. Instrument functions for deconvolution of raw data were obtained

by scattering 575 nm laser pulses from a clean quartz substrate, and typically exhibited ~80 ps fwhm. After a transfer to a Digital Equipment Corporation MINC-23 system with dual floppy disk drive operating in an RT-11 environment with FB monitor, fluorescence profiles were analyzed with a Marquardt nonlinear regression (14) program.

Data Analysis

For a given fluorescence decay law N(t), the convolute-and-compare analysis forms the convolution C_n in the n^{th} channel of N(t) with the instrument function x(t),

$$C_n = \sum_{i=1}^{N} x(i - s)N(n - i), \tag{6.3}$$

where s is a variable, integral shift parameter. For the trial function N(t), we use $I_{\parallel}(t)$ or $I_{\perp}(t)$ in equation (6.2), with the three-body approximation (9) to the Green's function given by the numerical inverse Laplace transform (15) of

$$\hat{G}^s(\varepsilon) = \tau\{(\pi^2\gamma^2C^2/4)\,[1 - [1+(32/\pi^2\gamma^2C^2)^2](\varepsilon\tau-0.1887\gamma^2C^2)]^{1/2}] + 4(\varepsilon\tau - 0.1887\gamma^2C^2)\} / [4(\varepsilon\tau - 0.1887\gamma^2C^2)^2]. \tag{6.4}$$

Here $\gamma = 0.846$ is a constant which arises from the dipole-dipole orientational dependence of the excitation transfer probability (9), and the reduced concentration

$$C = \frac{4}{3}\pi R_0^3 \rho \tag{6.5}$$

depends on the dye molecule density ρ and on the Förster parameter R_0 which characterizes the excitation hopping rate w_{jk} between molecules with transition moments oriented along d_j and d_k separated by distance R_{jk},

$$w_{jk} = \frac{2}{3\tau}\left(\frac{R_0}{R_{jk}}\right)^6 K_{jk}^2 \tag{6.6}$$

$$K_{jk} = \hat{d}_j \cdot \hat{d}_k - 3(\hat{d}_j \cdot \hat{R}_{jk})(\hat{d}_k \cdot \hat{R}_{jk}).$$

Since $G^S(t)$ depends on the reduced concentration C and on the isotropic lifetime τ, convolutions of the model functions in equation (6.2) with the instrument function contain four adjustable parameters: A, τ, C, and s. (Cavity-dumping at 4.8 MHz made it unnecessary to include the baseline as an adjustable parameter, or to build the mode-locked laser pulse periodicity into the modeling function as was done in earlier work (16).) These four parameters can be simultaneously optimized in the nonlinear regression program to minimize

$$\chi^2 = \sum_{i=M}^{N} (C_i - Y_i)^2/Y_i, \tag{6.7}$$

where Y_i is the number of fluorescence counts accumulated in channel i and (M, N) is the channel range used in the analysis. Our 80 ps fwhm

instrument function was not wide compared to the 20 ps channel spacing. Since the convolute-and-compare analysis was restricted to integral shift parameters s, choosing M=1 produced disproportionate contributions to χ^2 from the rising-edge portion of the fluorescence profiles. Channel M was instead typically placed ~10 channels before the peak channel, and the continuous curves representing optimized fits to our data profiles (Results and Discussion) begin with channel M.

Covariance can compromise the uniqueness of fits based on simultaneous variation of C and τ, because increases in C can be compensated by increases in τ to yield a Green's function which is nearly unchanged over the analyzed channel range. The isotropic lifetime τ was, therefore, extracted from single-exponential fits to magic-angle fluorescence profiles, which were accumulated at all rh6G concentrations with an analyzing polarizer aligned at 54.7^{o} from the excitation polarization to yield profiles proportional to $I_{\parallel}(t) + 2I_{\perp}(t)$. The results of such single-exponential fits to magic-angle profiles are summarized in Table 6.1 for five rh6G concentrations between 1.43×10^{-5} M and 4.12×10^{-3} M. The cell thickness in all cases was 10 μm. The visual quality of the fits is shown for four of the samples in Figure 6-1. Reduced χ^2 values tend to increase with concentration, and they range from ~1.1 to 3.8. The relative inaccuracy of the single-exponential fit in the latter case arises from nonexponential decay behavior introduced by excitation trapping (17) by rh6G dimers, which are more numerous at the higher concentrations. The autocorrelations of residuals (13)

$$A_n = \frac{2N'}{(N-M)} \frac{\sum_{i=1}^{(N-M)/2} Y_i^{\frac{1}{2}} (C_i - Y_i) Y_{i+n}^{\frac{1}{2}} (C_{i+n} - Y_{i+n})}{\sum_{i=1}^{N'} Y_i (C_i - Y_i)^2}, \qquad (6.8)$$

with N' equal to the number of channels comprising the fluorescence profile, provide a more discriminating test for quality of fit. The nearly statistical autocorrelation which is shown for the lowest concentration in Figure 6-1 shows that that magic-angle profile is nearly indistinguishable from single-exponential decay under present counting statistics.

Table 6-1. Magic angle fits of rhodamine 6G fluorescence profiles

Sample	Concentration, M	τ, ns	χ_r^2
1	1.43×10^{-5}	3.40	1.180
2	6.29×10^{-4}	3.56	1.944
3	1.62×10^{-3}	3.72	2.306
4	2.45×10^{-3}	3.78	3.237
5	4.12×10^{-3}	3.32	3.782

Of particular interest in Table 6-1 is the marked variation of the optimized lifetime τ with rh6G concentration. Though all of the magic-angle profiles in this table were obtained with 10 μm fluorescence cells, self-absorption (which dilates the fluorescence lifetime without sensibly

Figure 6-1. Magic-angle fluorescence profiles for samples 1, 3, 4, and 5 in Table 6-1. Continuous curves are optimized convolutions of single-exponential decay functions with the instrument function. Inset plots show autocorrelations of residuals. Time calibration is 20 ps per channel. Cell thickness was 10 μm in each case

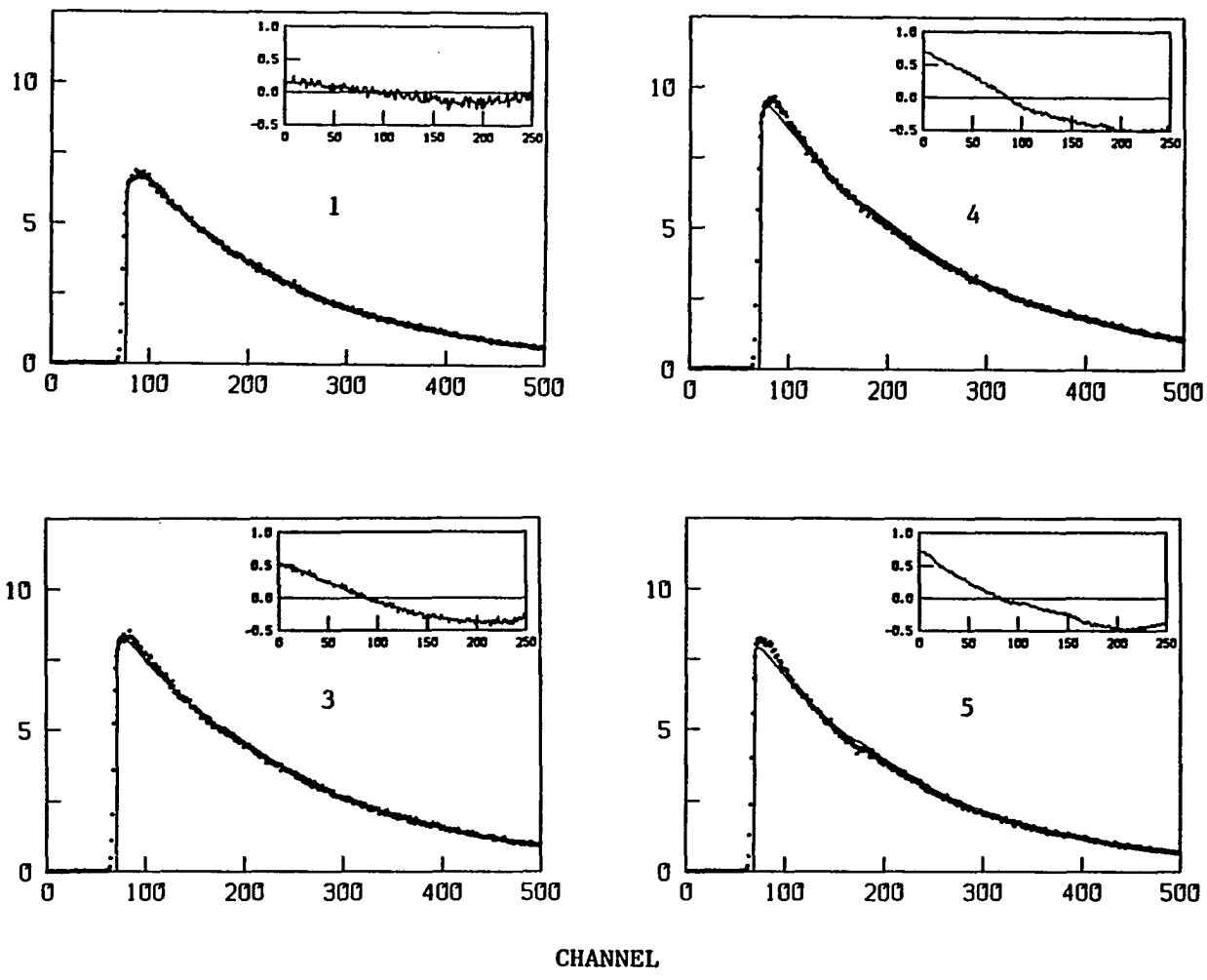

10^3 COUNTS

CHANNEL

affecting its exponentiality (12) increases τ from 3.40 to 3.78 ns in samples 1 through 4; excitation trapping reduces τ to 3.32 ns at the highest concentration (sample 5). Much larger τ variation with rh6G concentration (up to 4.83 ns at 2.45×10^{-3} M) was observed in a 100 μm cell. Following Hammond (12), the isotropic lifetimes τ may be converted into lifetimes τ_c corrected for self-absorption via

$$\tau_c = \tau(1 - aQ_0) \tag{6.9}$$

with

$$aQ_0 = 2.65\ cl \int_0^\infty \varepsilon_F\ E(\lambda)(0.039 - \log A_F)d\lambda. \tag{6.10}$$

$E(\lambda)$ is the rh6G emission spectrum normalized to the fluorescence quantum yield Q_0, ε_F is the rh6G absorption coefficient at the fluorescence wavelength, A_F is the sample absorbance at the fluorescence wavelength, c is the solution concentration, and l is the cell length. Using values of ε_F, $E(\lambda)$, and Q_0 for rh6G in ethanol (12), one obtains the lifetimes τ_c corrected for self-absorption in Table 6-2. For the four lowest concentrations, τ_c is between 3.37 and 3.39 ns; this mutual consistency strongly suggests that self-absorption is the primary origin of lifetime dilation in samples 1-4, and that a 10 μm cell is not thin enough to completely remove this artifact at any of these concentrations. The correction is almost negligible ($\lesssim$0.3%) in sample 1, but amounts to $\sim$12% in sample 4. For sample 5, τ_c is $\sim$500 ps shorter than those found at lower concentrations, indicating that trapping is rapid at 4.12×10^{-3} M.

Table 6-2. Lifetime corrections for self-absorption

Sample	Path length (μm)	a	τ, ns	τ_C, ns
1	10	0.003	3.40	3.39
2	10	0.058	3.56	3.37
3	10	0.106	3.72	3.35
4	10	0.131	3.78	3.32
5	10	0.160	3.32	2.82

The magic-angle profile analyses provide initial τ values for deconvolution of the $I_{\parallel}(t)$ and $I_{\perp}(t)$ profiles using equations (6.2) and (6.4) as model functions. Both of these profiles are deconvoluted simultaneously, with minimization of their combined χ^2. This procedure effectively eliminates parameter correlation, because the effects of changing C (or τ) have opposite sign in $I_{\parallel}(t)$ and $I_{\perp}(t)$ according to equation (6.2). This was demonstrated in trial deconvolutions of simulated profiles, computed by convoluting a 100 ps fwhm Gaussian instrument function with $I_{\parallel}$ and $I_{\perp}$ decay laws calculated with equations (6.2) and (6.4) with C = 0.5 and τ = 4.0 ns. Independent deconvolution of these simulated $I_{\parallel}$ and $I_{\perp}$ profiles yielded optimized lifetimes of 4.016 and 4.008 ns, and optimized reduced concentrations of 0.535 and 0.468, respectively (Table

6-3). In the linked deconvolution, the common values of τ and C converged to 3.996 ns and 0.5008 instead. Table 6-3 also shows that considerably larger fractional differences in C are obtained between independent and linked deconvolutions when C = 0.1 instead of C = 0.5 is used to simulate the data profiles; this occurs because $G^S(t)$ is less sensitive to C when the latter is small. In each of these tests, Gaussian noise was added to the simulated profiles.

Table 6-3. Deconvolutions of simulated $I_{\parallel}$ and $I_{\perp}$ profiles

	τ = 4.000 ns		C = 0.5000	
	Independent		Linked	
	$I_{\parallel}$	$I_{\perp}$	$I_{\parallel}$	$I_{\perp}$
A	0.1129	0.3049	0.1122	0.3025
τ, ns	4.0156	4.0077	3.9961	3.9961
C	0.5349	0.4684	0.5008	0.5008
χ^2_r	1.024	1.022	1.032	1.032

	τ = 4.000 ns		C = 0.1000	
	Independent		Linked	
	$I_{\parallel}$	$I_{\perp}$	$I_{\parallel}$	$I_{\perp}$
A	0.1092	0.3206	0.1085	0.3188
τ, ns	4.0305	4.0257	3.9960	3.9960
C	0.1311	0.0797	0.0998	0.0998
χ^2_r	1.024	1.023	1.032	1.032

Covariance can thus be ruled out as a source of artifacts in our data analysis. The magic-angle analyses we have described show that excitation trapping by dimers considerably distorts the isotropic decay behavior at the highest concentration, and that lifetime dilation by self-absorption is difficult to suppress in rh6G solutions. These phenomena affect the fluorescence anisotropy (and the measured Green's function $G^S(t)$) in ways which are difficult to correct for rigorously. Excitation trapping reduces the fluorescence depolarization and the apparent value of C, because excitation transport is interrupted at a lifetime shorter than the intramolecular lifetime τ_D. Self-absorption leads to inflated values of the measured reduced concentration, because absorption and reemission of fluorescence in solution contributes an additional mechanism for depolarization. A realistic assessment of these effects is important in a careful experimental test of excitation transport theory.

Results and Discussion

The polarized fluorescence profiles are displayed with the optimized convolutions of equation (6.2) with the instrument function for samples 1, 3, 4 and 5 in Figure 6-2. These profiles exhibit the expected trend from slight to strong fluorescence depolarization over the rh6G concentration range (1.43×10^{-5} to 4.12×10^{-3} M) within the displayed time period of $\sim$10 ns. In Table 6.4, we list the final fitting parameters for these $I_{\parallel}(t)$ and $I_{\perp}(t)$ profiles. The visual fits, the reduced χ^2 values in Table 6-4, and the autocorrelations of residuals shown in Figure 6-2

Figure 6-2. Fluorescence profiles $I_{\parallel}(t)$ and $I_{\perp}(t)$ for samples 1, 3, 4, and 5 in Table 6-1. Continuous curves are optimized convolutions of model functions computed from equations (6.2) and (6.4) with the instrument function. Upper and lower inset plots show autocorrelations of residuals for $I_{\parallel}(t)$ and $I_{\perp}(t)$, respectively. Time calibration is 20 ps per channel; cell thickness was 10 μm in each case

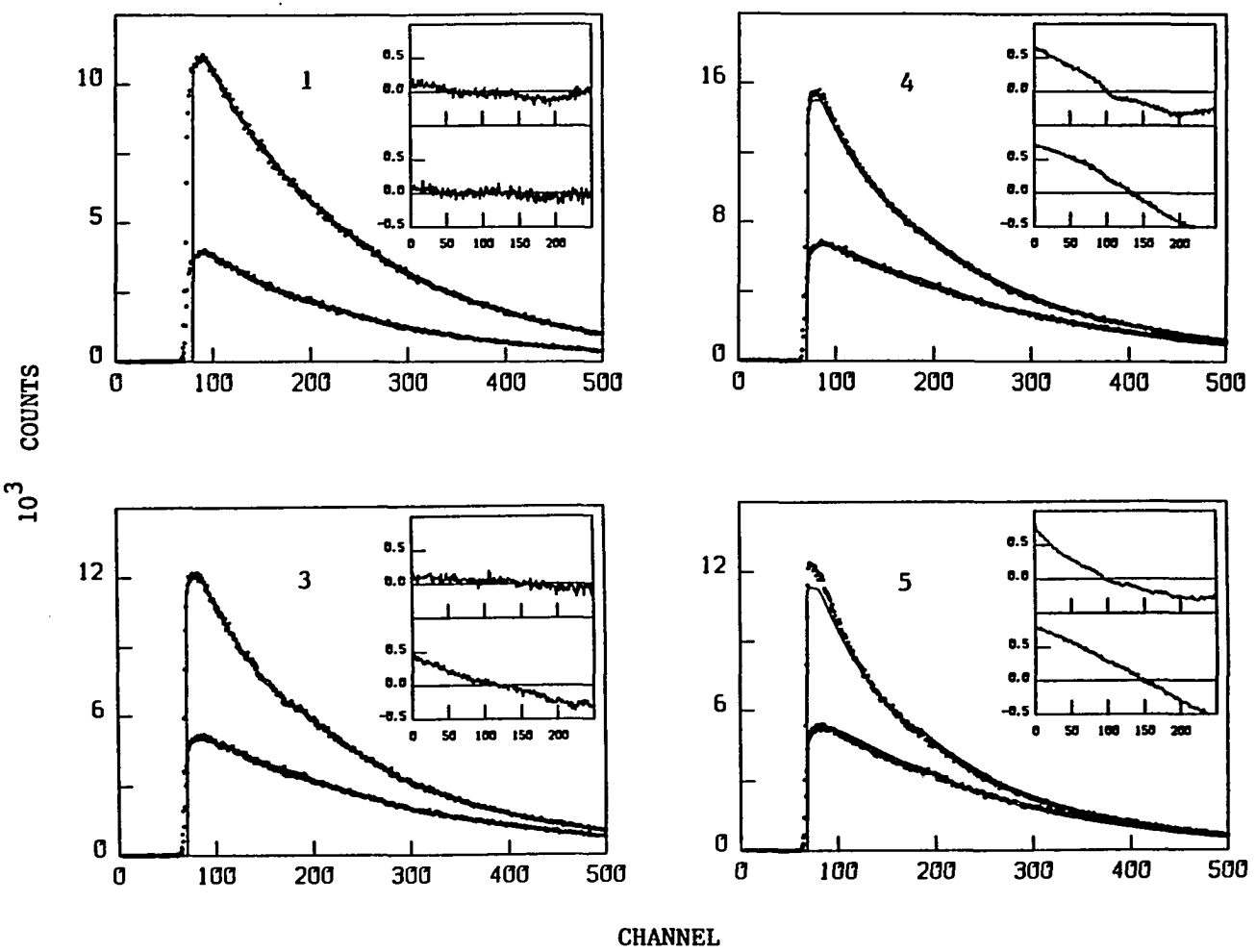
1
4
3
5
10^3 COUNTS
CHANNEL

Table 6-4. Fitting parameters for anistropic fluorescence profiles

$I_{\parallel}(t) = Ae^{-t/\tau}[1 + 0.8G^s(t)]$

$I_{\perp}(t) = Ae^{-t/\tau}[1 - 0.4G^s(t)]$

Sample		τ, ns	C	χ_r^2
1	$\parallel$	3.41	0.0675	1.141
	$\perp$			1.172
2	$\parallel$	3.68	0.368	1.318
	$\perp$			1.926
3	$\parallel$	3.77	0.927	1.270
	$\perp$			2.153
4	$\parallel$	3.69	1.22	3.006
	$\perp$			4.501
5	$\parallel$	3.22	1.26	6.170
	$\perp$			5.268

all tend to worsen at the highest rh6G concentrations. The origin of part of these discrepancies is clearly the fact that the magic-angle profiles are not precisely single exponential (Figure 6-1), especially at the highest concentrations, so that the single-exponential isotropic factors in equation (6.2) cannot represent the true decay behavior. The least-squares program attempts to compensate for this nonexponentiality by adjustment of the parameters in $G^s(t)$ when fitting $I_{\parallel}(t)$ and $I_{\perp}(t)$, with the result that the autocorrelations in some cases (samples 2 and 3) are markedly better for the $I_{\parallel}(t)$ profile than for the magic-angle profile. The trend in optimized reduced concentrations C versus rh6G molarity M is summarized in Figure 6-3 for samples 1-5, with additional

Figure 6-3. Optimized reduced concentrations C of rh6G solutions, from nonlinear least-squares fits to $I_{\parallel}(t)$ and $I_{\perp}(t)$ profiles of model functions calculated from three-body Green's function $G^{S}(t)$. Data points are included for solutions in 10 μm cell (●) and 100 μm cell (○). Straight lines give actual reduced concentration versus rh6G solution molarity for dyes with Förster parameters R_0 = 50, 60, and 70Å

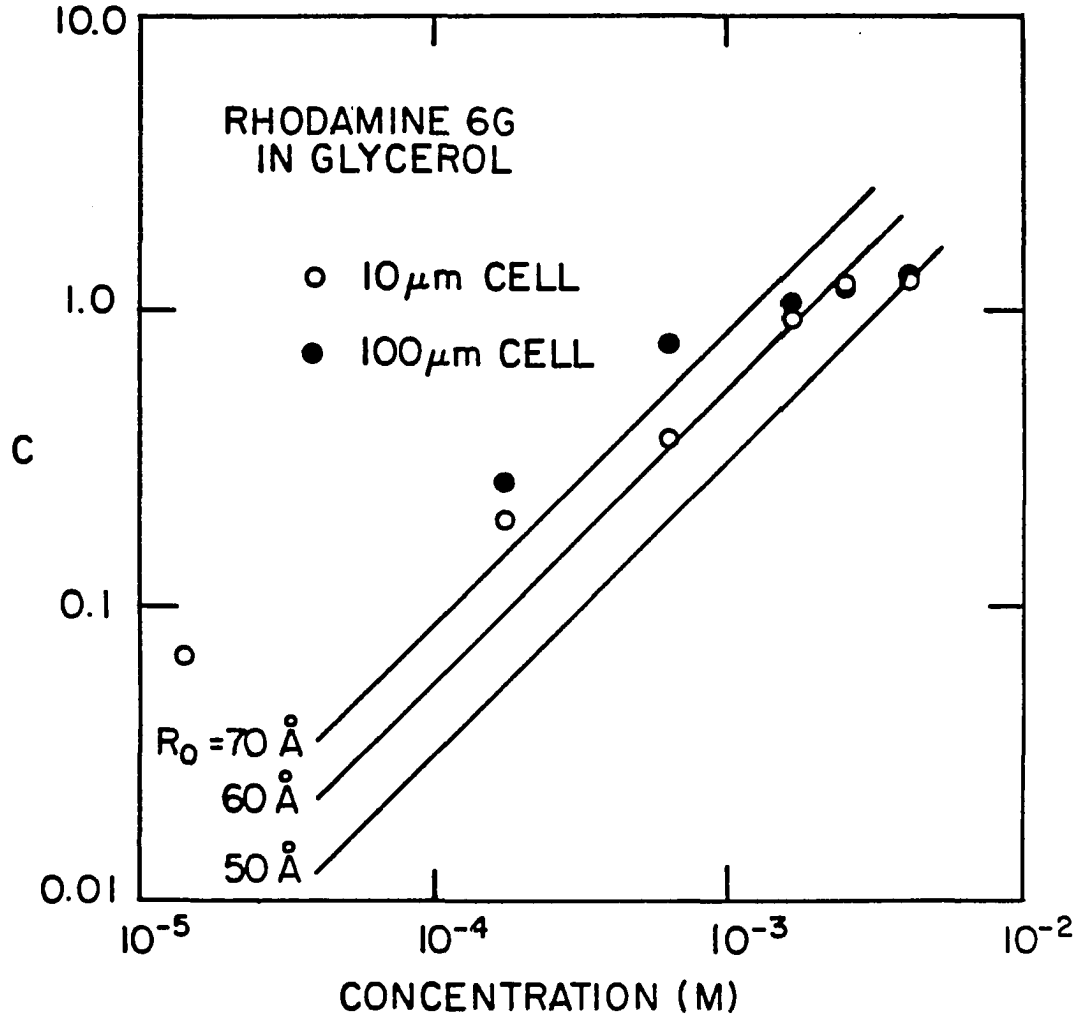
10.0
1.0
0.1
0.01
C
RHODAMINE 6G
IN GLYCEROL
o 10μm CELL
● 100μm CELL
R0 =70 Å
60 Å
50 Å
10-5
10-4
10-3
10-2
CONCENTRATION (M)

data points added for a sample with M = 1.76 x 10^{-4} M. Solutions with cell thicknesses of both 10 μm and 100 μm (whose profiles and fitting parameters are not shown) are included in this plot. C should in principle be proportional to M through equation (6.5); this is approximately obeyed only by the 10 μm samples over the limited concentration range (6 x 10^{-4} to 2.4 x 10^{-3} M), where the proportionality factor corresponds to $R_0 \sim 60\text{Å}$. At higher concentrations, C values obtained in both 10 μm and 100 μm cells level off due to excitation trapping, which artificially depreciates the apparent reduced concentration. The separations between the 10 μm and 100 μm data points at the other concentrations are a consequence of greater self-absorption in the thicker samples, and they show that this effect can materially influence the measured fluorescence anisotropy as well as the isotropic lifetimes in our samples (Table 6-2).

Our method of data analysis formally differs from that of GF in that these authors varied C to most closely match their profiles with convolutions of equation (6.2) at one concentration (2.6 x 10^{-3}M, comparable to that of our sample 4). This optimized value of C (0.83) was used to infer that $R_0 = 50\text{Å}$, and this Förster parameter was used to calculate theoretical decay profiles for comparison with their data obtained at other concentrations, yielding visually excellent results. If they were so handled, our data would have yielded similar results, but with a somewhat larger empirical value of R_0 between 50 and 60Å (Figure 6-3). What our present analysis shows is that the apparently small differences between the calculated and experimental profiles arise primarily from

self-absorption and excitation trapping artifacts, rather than from discrepancies between the three-body and true Green's functions $G^S(t)$. Avoiding such artifacts would require better sample design: thinner sample cells and more effective inhibition of rh6G aggregation. GF employed cells ranging from 300 to 5 μm in thickness, and we used 10 μm cells at all of our concentrations. Figure 6-3 and Table 6-2 together suggest that cells thinner than ∿2 μm should be used, at least at the highest concentrations. We constructed such cells by etching 4 mm diameter areas of Al coating from λ/4 glass substrates using HF solution, only to find that the substrate material itself fluoresced in the red under 575 nm laser excitation. Experiments with a well-constructed ∿1 μm thick cell are planned in our laboratory. Excitation trapping is clearly a more persistent problem, particularly in the dynamically interesting high-concentration regime in which breakdowns in any self-consistent approximation to $G^S(t)$ will first become apparent. Self-absorption can be minimized in well-designed transient-grating experiments (18) to test the excitation transport theory. Such experiments do not offer data with the statistical quality available in photon counting, and their results are similarly influenced by excitation trapping if the latter is not properly taken into account.

Our data points for the two lowest concentrations in Figure 6-3 lie significantly higher than would be expected for physically reasonable Förster parameters R_0. Self-absorption is not likely to contribute significantly at such concentrations; the large divergences are in part a

consequence of the relative insensitivity of $G^S(t)$ to C for $t \lesssim 2\tau$ when $C \lesssim 0.1$.

In summary, a rigorous least-squares analysis of polarized photon-counting fluorescence profiles from rh6G in glycerol shows that differences between the theoretical and experimental decay curves are dominated by trapping and self-absorption. These differences are not particularly large (especially when viewed on a linear scale as in Figure 6-2), and in this sense the three-body Green's function does provide a very good approximation to the true Green's function in the present three-dimensional disordered systems. An original motivation of this work was to determine whether systematic errors could be detected in the three-body Green's function, thereby identifying areas for further improvement in the theory. Our technology and data analysis are sufficiently well developed to achieve this in samples in which excitation trapping can be suppressed during the excited state lifetime, and work is in progress to develop such samples.

Acknowledgments

The Ames Laboratory is operated for the U. S. Department of Energy by Iowa State University under Contract No. W-7405-Eng-82. This work was supported by the Office of Basic Energy Sciences. We thank Professor Michael Fayer for valuable discussions, and are indebted to Robert Crackel for his help with the corrections for self-absorption.

References Cited

1. Förster, T. Disc. Far. Soc. 1959, 27, 7.
2. Galanin, M. D. Tr. Fiz. Inst. 1950 5, 339.
3. Vavilov, S. I. Zh. Eksp. Teor. Fiz. 1943, 13, 13.
4. Craver, F. W.; Knox, R. S. Mol. Phys. 1971, 22, 385.
5. Craver, F. W. Mol. Phys. 1971, 22, 403.
6. Ore, A. J. Chem. Phys. 1959, 31, 442.
7. Gochanour, C. R.; Andersen, H. C.; Fayer, M. D. J. Chem. Phys. 1979, 70, 4254.
8. Förster, T. Ann. Phys. 1948, 6, 55.
9. Gochanour, C. R.; Fayer, M. D. J. Phys. Chem. 1981, 85, 1989.
10. O'Connor, D. V.; Phillips, D. "Time-correlated Single Photon Counting"; Academic Press: New York, 1984.
11. Grinvald, A.; Steinberg, I. Z. Anal. Biochem. 1974, 59, 583.
12. Hammond, P. R. J. Chem. Phys. 1979, 70, 3884.
13. Yasa, Z. A.; Amer, N. M. Opt. Commun, 1981, 36, 406.
14. Marquardt, D. W. J. Soc. Ind. Appl. Math. 1963, 11, 431.
15. Stehfest, H. Commun. ACM 1970, 13, 47.
16. Anfinrud, P.; Crackel, R. L.; Struve, W. S. J. Phys. Chem. 1984, 88, 5873.
17. Loring, R. F.; Andersen, H. D.; Fayer, M. D. J. Chem. Phys. 1982, 76, 2015.
18. Miller, R. J. D.; Pierre, M.; Fayer, M. D. J. Chem. Phys. 1983, 78, 5138.

EXCITATION TRANSPORT AND FLUORESCENCE ANISOTROPY OF RHODAMINE 3B ON AMORPHOUS QUARTZ

by

John F. Hedstrom, David E. Hart, Philip A. Anfinrud, and Walter S. Struve

Department of Chemistry and Ames Laboratory - USDOE
Iowa State University, Ames, Iowa 50011

CHAPTER VII. EXCITATION TRANSPORT AND FLUORESCENCE ANISTROPY OF RHODAMINE 3B ON AMORPHOUS QUARTZ

Introduction

Electronic excitation transport and trapping in disordered systems have provided challenging problems to theorists interested in predicting time-dependent observables such as excited state populations, fluorescence depolarization, and the transient grating effect (1). Such properties may be extracted from solutions to the coupled master equations which govern the set of probabilities p_j that electronic excitation resides on molecule j at time t. In the absence of excitation trapping, these master equations assume the form (2)

$$\frac{dp_j}{dt} = \sum_k^N w_{jk} (p_k - p_j) - p_j/\tau_D \qquad (7.1)$$

for a system of N identical donor molecules with intramolecular excited state lifetime τ_D. The coefficients w_{jk} are Förster dipole-dipole transition rates (3)

$$w_{jk} = \frac{3}{2\tau_D}\left(\frac{R_o}{r_{jk}}\right)^6 [\hat{d}_j\cdot\hat{d}_k - 3(\hat{d}_j\cdot\hat{r}_{jk})(\hat{d}_k\cdot\hat{r}_{jk})]^2, \qquad (7.2)$$

where $\hat{r}_{jk}$ is the position of molecule j relative to that of molecule k, $\hat{d}_j$ and $\hat{d}_k$ are unit vectors along the respective transition moments, and R_o is the intermolecular separation at which excitation transport and

intramolecular decay have equal probability. Since excitation can migrate from molecule to molecule in sequences with unlimited length and topology, exact solutions to the master equations have not been achieved for arbitrary donor molecule number densities in systems of any dimensionality. Early attempts to approximate the master equation solutions tended to assume either that one or two excitation migrations occurred at most during the donor excited state lifetime (4, 5), or that excitation sharing was limited to nearest (6) or nearest and next-nearest neighbors (7).

Beginning in 1979, Andersen, Fayer and their coworkers developed Green's function expansions of the master equation solutions (8-11) to yield successive self-consistent approximations to $G^S(t)$, the time-dependent probability that electronic excitation will be found on the photon-excited donor molecule. $G^S(t)$ is experimentally observable using the transient-grating effect (12), and is also related to the time-dependent fluorescence depolarization (13) by

$$G^S(t) = 2.5 \frac{I_{\parallel}(t) - I_{\perp}(t)}{I_{\parallel}(t) + 2I_{\perp}(t)} \qquad (7.3)$$

in three-dimensional systems, where $I_{\parallel}(t)$ and $I_{\perp}(t)$ are the fluorescence intensity components polarized parallel and normal to the linearly polarized excitation. It has been verified (13) that the next-lowest (three-body) self-consistent approximation to $G^S(t)$ in three dimensions (8) yields calculated fluorescence polarization components in excellent agreement with those observed in concentrated dye solutions, and the

master equation has been considered essentially solved for three-dimensional disordered systems.

For two-dimensional systems (e.g., molecules adsorbed onto a flat surface, comparable master equation solutions are not available because in two dimensions the three-body Green's function $G^s(t)$ fails to converge at long times (14). The lowest-order, two-body approximation (11) is expected to be less reliable in two than in three dimensions because density expansions tend to converge less rapidly in systems with lower dimensionality. No experimental measurements of two-dimensional $G^s(t)$ have been reported to our knowledge. In this work, we have measured fluorescence anisotropies for rhodamine 3B (R3B) adsorbed onto optically flat fused quartz. Our experimental fluorescence components $I_{\parallel}(t)$ and $I_{\perp}(t)$ are deconvoluted with model decay functions which incorporate the two-dimensional, two-body Green's function $G^s(t)$ for donor molecules randomly distributed on a flat surface. At very low coverages, we find that essentially no fluorescence depolarization occurs within several donor lifetimes (or equivalently that $G^s(t) \rightarrow 1$ for all t); this implies that dye reorientation contributes negligibly to the observed fluorescence depolarization, which then arises exclusively from excitation transport among motionless, adsorbed donors. R3B was chosen for the donor species because it dimerizes much less in our surface coating procedure than many dyes (including cresyl violet (15)), is free of acid-base equilibria which complicate the fluorescence profiles of rhodamine B (16, 17), and exhibits an $S_1 \leftarrow S_0$ absorption band ($\varepsilon_{max} \sim 1.2 \times 10^5$ at 555 nm in ethanol) which can be pumped by a rhodamine 590 synchronously-pumped dye laser.

The relationship between $G^S(t)$ and the fluorescence components I (t) and I (t) depends on the angular distribution of fixed donor transition moments on the surface (18), so a knowledge of this distribution is important to the data analysis. It is possible to priori that R3B molecules adsorbed on $\lambda/4$ fused quartz can experience microscopic surface roughness with a mean periodicity small enough to produce transition moments which are nearly randomly oriented in three dimensions. Second-harmonic anisotropy measurements on "optically flat fused quartz" substrates coated with less than one monolayer of xanthene dyes (rhodamine 6G, rhodamine B, and acidic fluorescein (19, 20) have implied that the transition moments in these systems form characteristic fixed angles θ^* from the macroscopic surface normal (Figure 7-1), with random distributions in the azimuthal adsorption angle ϕ. The derived adsorption angles (e.g., $\theta^* = 52 \pm 4^o$ and 55 ± 4^o for the long-axis polarized $S_1 \leftarrow S_0$ transitions in rhodamine 6G and rhodamine B, respectively) support the hypothesis that adsorption occurs through bonding of the -COOH or -COOR groups to the fused silica substrate. Since these substrates are not absolutely flat on a molecular scale, our transition moment distributions cannot actually be restricted to single, sharp cones of half-angles θ^*. This is demonstrated in Figure 7-2(a), which compares fluorescence profiles (obtained by techniques described in the Experimental Section) for R3B on $\lambda/4$ quartz excited by horizontally and by vertically polarized laser pulses. The fluorescence was collected along the vertical surface normal in both cases without an analyzing polarizer. The two profiles should

Figure 7-1. Experimental geometry. The surface lies in the xy plane. Laser pulses are y-polarized in most of this work, and fluorescence is observed along the z-axis. For analysis, dye transition moments are assumed to be randomly distributed on a cone of half-angle θ^* from surface normal

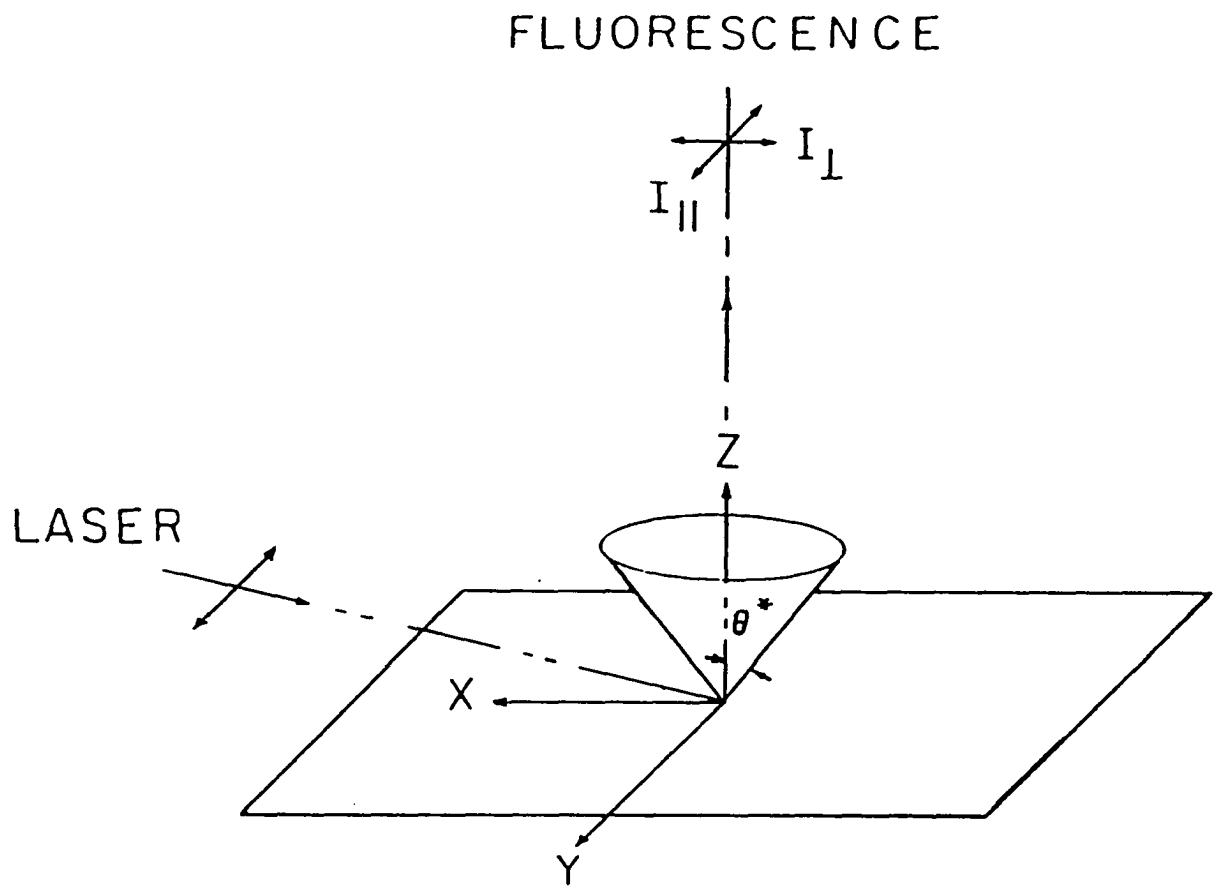
FLUORESCENCE
$I_{\perp}$
$I_{\parallel}$
Z
LASER
θ^*
X
Y

Figure 7-2. Fluorescence profiles from R3B on optically flat quartz, viewed along surface normal (a) without analyzing polarizer for out-of-plane (upper) and in-plane (lower) laser polarizations; (b) for in-plane laser excitation with a perpendicular analyzing polarizer (upper) and with no analyzing polarizer (lower). Counting times were adjusted to yield 10^4 peak counts in each profile. R3B coverage is similar to that of sample 3 in Table 7-1. Time calibration is 20 ps/channel

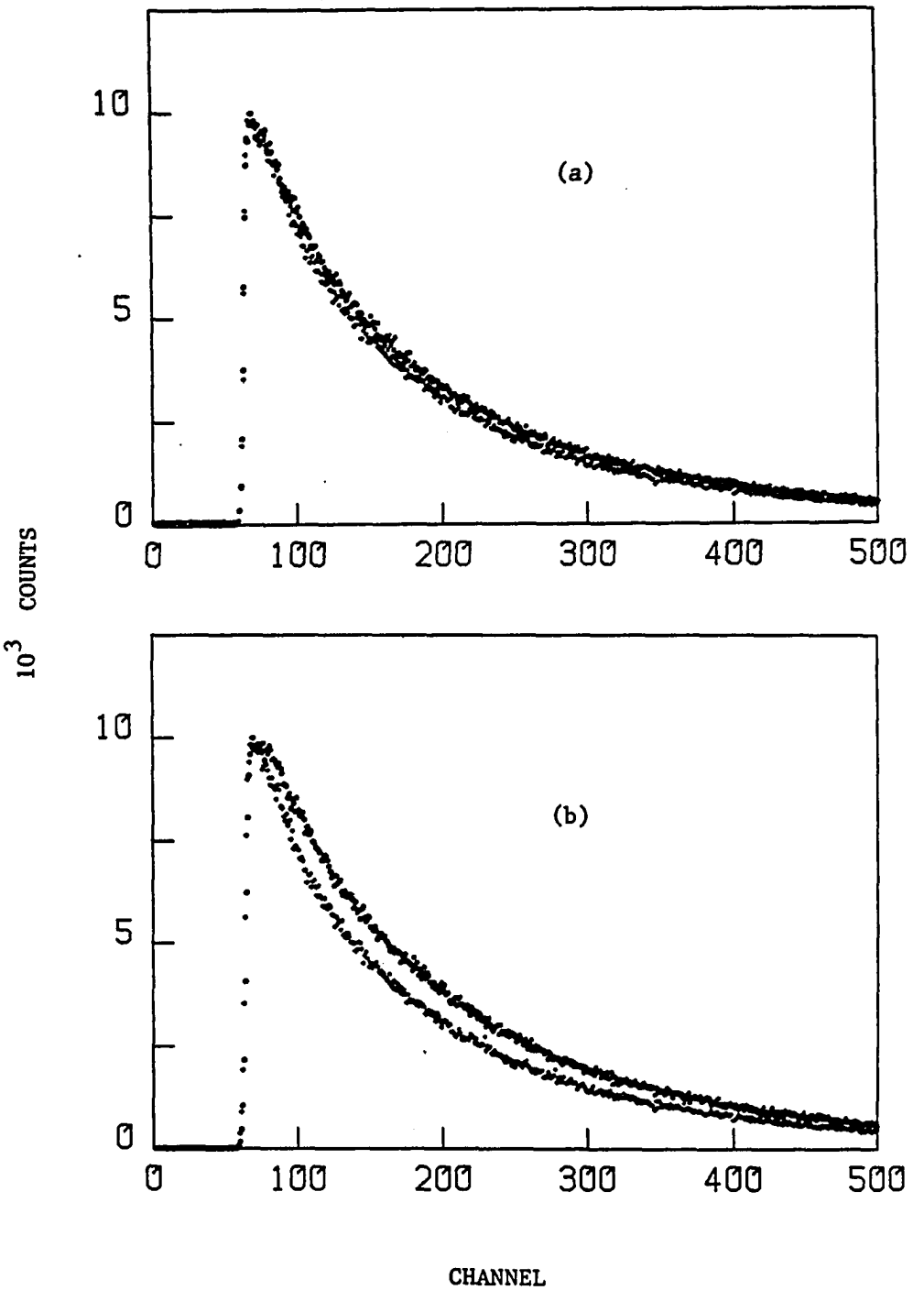
10
5
0
(a)
0
100
200
300
400
500
10
5
0
(b)
0
100
200
300
400
500
10^3 COUNTS
CHANNEL

exhibit identical time dependence if the transition moments are restricted to a single cone with its symmetry axis parallel to the surface normal. They would differ materially if the transition moments were randomly oriented in three dimensions, and would correspond to $I_{\parallel}(t) + I_{\perp}(t)$ and $2I_{\perp}(t)$ in the three-dimensional notation of equation (7.3). In Figure 7-2(b), we contrast horizontally excited fluorescence profiles collected from the same R3B/quartz sample (i) with an analyzing polarizer oriented perpendicular to the excitation polarization and (ii) with no analyzing polarizer. Since the difference between the pair of profiles in Figure 7-2(b) is much larger than that in Figure 7-2(a), fluorescence depolarization in our R3B/quartz systems is dominated by changes in the azimuthal adsorption angle ϕ attending excitation transport, rather than by ensemble variations in the orientation of the cone axis. As a first approximation, it will therefore be assumed that the R3B transition moments are restricted to lie on the surface of a single cone of half-angle θ^* (whose value does not enter in the relationship between $G^S(t)$ and the time-dependent fluorescence polarization components) aligned parallel to the macroscopic surface normal.

In the next section, we derive expressions for $I_{\parallel}(t)$ and $I_{\perp}(t)$ in terms of $G^S(t)$ for our experimental geometry, and obtain the two-dimensional, two-body Green's function $G^S(t)$ using Forster dipole-dipole transition rates w_{jk} with the correct orientation dependence (12). The Experimental Section contains the experimental procedure. In the Data Analysis section, we describe the data treatment, a nonlinear least-squares convolute-and-compare analysis which uses model decay functions

derived from the two-body Green's function and which fits the isotropic and anisotropic parts of $I_{||}(t)$ and $I_{\perp}(t)$ independently in order to avoid covariance between the isotropic lifetime parameters and the parameters in $G^S(t)$. In the section presenting Results and Discussion, several factors which specifically influence the interpretation of surface fluorescence anisotropy measurements are considered. These include surface flatness, positional randomness of fluorescing donors on the surface, effects of excitation trapping on fluorescence anisotropy, and effects of site inhomogeneity on the observed isotropic decay behavior.

Calculation of Fluorescence Components and the Two-Body Green's Function $G^S(t)$

The long-axis polarized $S_1 \leftarrow S_0$ absorption and fluorescence transitions in R3B are assumed to have parallel transition moments which are aligned at a fixed angle θ^* from the surface normal the z-axis, but are randomly distributed in ϕ. The excitation polarization lies in the surface plane (the xy-plane) and is parallel to the y-axis; the pumping pulses propagate in the xz plane. The orientational probability distribution for excited state transition moments at time t after laser pulse excitation at t=0 is (21)

$$W(\theta\phi t) = \int_0^{2\pi} d\phi \int_0^{\pi} d\theta\, G(\theta_0\phi_0|\theta\phi t)\, W(\theta_0\phi_0), \qquad (7.4)$$

where $G(\theta_0\phi_0|\theta\phi t)$ is a Green's function propagator and $W(\theta_0\phi_0)$ is the initial probability distribution created by electric-dipole absorption at $t = 0$. Since θ is fixed at the adsorption angle θ^*, this becomes

$$W(\phi t) = \int_0^{2\pi} d\phi \; G(\phi_0|\phi t) \; W(\phi_0) \tag{7.5}$$

with

$$W(\phi_0) = \frac{1}{\pi} \sin^2\theta^* \cos^2\phi_0. \tag{7.6}$$

The angles ϕ and ϕ_0 are measured from the y-axis. The propagator can be expanded in terms of $\Phi_m(\phi) = (2\pi)^{-1/2} \exp(im\phi)$,

$$G(\phi_0|\phi t) = \sum_{m=-\infty}^{\infty} c_m(t) \, \Phi_m^*(\phi_0) \, \Phi_m(\phi) \tag{7.7}$$

and obeys the boundary conditions

$$G(\phi_0|\phi 0) = \delta(\phi - \phi_0) \equiv \sum_{m=-\infty}^{\infty} \Phi_m^*(\phi_0) \, \Phi_m(\phi) \tag{7.8}$$

$$\int_0^{2\pi} d\phi \; G(\phi_0|\phi t) = 1.$$

This requires that $c_0(t) = 1$ and $c_m(0) = 1$. Combining equations (7.5) - (7.8) then implies that the orientational probability distribution must evolve as

$$W(\phi t) = \frac{\sin^2\theta_0^*}{2\pi} (1 + c_2(t) \cos 2\phi). \tag{7.9}$$

The fluorescence components $I_{\parallel}(t)$ and $I_{\perp}(t)$ observed along the z-axis are

$$I_{\parallel}(t) = P(t) \int_0^{2\pi} d\phi \, W(\phi t) \sin^2\theta^* \cos^2\phi$$

$$= P(t) \sin^4\theta^* (1 + \tfrac{1}{2} c_2(t))/2 \qquad (7.10a)$$

$$I_{\perp}(t) = P(t) \int_0^{2\pi} d\phi W(\phi t) \sin^2 \theta^* \sin^2\phi$$

$$= P(t) \sin^4 \theta^* (1 - \tfrac{1}{2} c_2(t))/2, \qquad (7.10b)$$

where $P(t)$ is the isotropic decay law. It may be shown that if all of the fluorescence depolarization proceeds via electronic excitation hopping between stationary dye molecules on the surface, $c_2(t)$ can be identified with $G^s(t)$, the exact probability that the excitation is found on the laser-excited dye molecule at time t. Craver (18) has shown that for the present transition moment adsorption geometry and excitation polarization

$$G^s(t) = 2 \frac{I_{\parallel}(t) - I_{\perp}(t)}{I_{\parallel}(t) + I_{\perp}(t)} \quad , \qquad (7.11)$$

which is consistent with equation (7.10). This equation supersedes equation (7.3), which describes fluorescence depolarization in a three-dimensionally random distribution of transition moments. No knowledge of the adsorption angle θ^* is required to extract $G^s(t)$ from the fluorescence components using equation (7.11), provided fluorescence is observed

along the surface normal. If the surface were inclined by an angle λ about the y-axis, equation (7.11) would be replaced by

$$G^s(t) = 2 \frac{I_{\parallel} \cos^2\lambda \ (1 + 2 \tan^2\lambda \cot^2\theta^*) - I_{\perp}}{I_{\parallel} \cos^2\lambda + I_{\perp}} \tag{7.12}$$

Loring and Fayer (11) derived a self-consistency equation for the Laplace transform of the two-body Green's function $G^s(t)$ in two dimensions in the absence of excitation trapping,

$$\hat{G}^s(\varepsilon) = (\varepsilon + \rho \int d\vec{r}_{12} \frac{w_{12}}{(1 + 2 \hat{G}^s(\varepsilon) w_{12})})^{-1} . \tag{7.13}$$

Here ρ is the surface number density of donor molecules. For simplicity the transfer rate w_{12} was set equal to the orientationally averaged Förster rate $(R_0/r_{12})^6/\tau_D$, leading to

$$\hat{G}^s(\varepsilon) = (\varepsilon + \frac{\pi C}{\tau_D} (\frac{4}{27})^{1/2} (\frac{2\hat{G}^s(\varepsilon)}{\tau_D})^{-2/3})^{-1} . \tag{7.14}$$

$C \equiv \pi R_0^2 \rho$ is the (dimensionless) reduced donor coverage, and equals the mean number of donor molecules occupying a circle of radius R_0. Using the correct orientational dependence in w_{12} yields instead the self-consistency equation

$$\hat{G}^s(\varepsilon) = (\varepsilon + \frac{\pi C}{\tau_D} (\frac{4}{27})^{1/2} (\frac{2\hat{G}^s(\varepsilon)}{\tau_D})^{-2/3} a^{1/3} \, d\Omega_1 d\Omega_2 |K_{12}|^{2/3})^{-1} , \tag{7.15}$$

where

$$K_{12} = \hat{d}_1 \cdot \hat{d}_2 - 3\,(\hat{d}_1 \cdot \hat{r}_{12})\,(\hat{d}_2 \cdot \hat{r}_{12})$$

and

$$a = (\cos^4\theta^* + \tfrac{5}{4}\sin^4\theta^*)^{-1}.$$

The integral in equation (7.15) is carried out over all orientations Ω_1 and Ω_2 of transition moment pairs randomly distributed on the θ^* cone. Consideration of the anisotropy in w_{12} therefore replaces the reduced coverage C in the two-body Green's function with γC, where

$$\gamma = a^{1/3} \int d\Omega_1 d\Omega_2 |K_{12}|^{2/3} \qquad (7.16)$$

is a constant which depends on the cone angle θ^*. A similar result is obtained when the anisotropy in w_{12} is incorporated into calculating the two-body, three-dimensional Green's function (13); in that case, the reduced concentration of donor species becomes multiplied by

$$\gamma = (\tfrac{3}{2})^{1/2} \int d\Omega_1 d\Omega_2 |K_{12}| = 0.846. \qquad (7.17)$$

This correction brings theoretical fluorescence profiles into excellent agreement with experimental fluorescence components emitted by rhodamine 6G solutions in glycerol (13). Our reduced dye coverages are far less precisely known than then reduced dye concentrations used in solution work, since our submonolayer R3B coatings generally exhibit optical densities <0.002 at their absorption maximum. We therefore approach comparisons of our experimental profiles with theory by determining to what

extent agreement is possible for optimized reduced coverages C in non-linear least-squares analyses using the two-body, two-dimensional form of $G^s(t)$.

Experimental Section

A Coherent Innova 90 argon ion laser with 5W plasma tube operated at 26A was acousto-optically mode-locked by a Harris Corporation H-401 unit driven at 48 MHz. It pumped a cavity-dumped rh 590 dye laser (Coherent CR-599-01 with three-place birefringent filter), which produced tunable picosecond pulses with ~8ps fwhm. The cavity dumper combined a Harris Corporation H-100 AOM crystal, an H-102 driver synchronized with the mode-locker driver to provide a 4.8 MHz repetition rate, and optics mounted on Newport Research Corporation beam directors and Line Tool Co. translators. A real-time rotating-mirror zero-background autocorrelator (22) provided monitoring and optimization of laser performance.

Rhodamine 3B perchlorate (R3B) was obtained from Eastman Kodak Laser Products and was used without further purification. TLC of R3B on Analtech Silica Gel G plates revealed only one spot with ethanol/acetone, ethanol/acetic acid and n-propanol/formic acid solvents. The surface substrates were $\lambda/4$ fused quartz. In most experiments, substrates were treated with dichlorodimethylsilane prior to dipping in aqueous R3B solutions with varied concentration (3.7×10^{-9} M to 7.4×10^{-7} M), yielding hydrophobic surfaces with macroscopically uniform dye coatings of less

than one monolayer. To test for possible effects of adsorption site inhomogeneity on fluorescence properties, some substrates were untreated, or treated with monochlorotrimethylsilane before dye coating. Untreated substrates yielded visibly less uniform coverage (observed by total fluorescence count rate monitoring during computer-controlled translational surface scanning), but the time-dependent fluorescence profiles were not markedly sensitive to surface pretreatment. Such surface scans identified fluorescence "hot spots" arising from surface scratches or other imperfections, and profile accumulations were limited to uniformly coated areas.

Horizontally polarized dye laser pulses at 575 nm were focused to $\sim$0.1 mm diameter at $\sim 75^{o}$ incidence on horizontal quartz substrates coated with R3B. Fluorescence was collected vertically with a 5 cm f.l. quartz lens and condensed by a 10 cm f.l. lens through a variable rectangular aperture onto a Hamamatsu 1564U microchannel plate phototube (MCP) with bialkali photocathode and borosilicate glass window. The MCP exhibited $\sim 6 \times 10^{5}$ gain at 3000V, 500 nm and a transit time spread of 76 ps at 3200V. 3 mm Schott filters (two RG-590 and one RG-610) screened 575 nm laser scatter and filter fluorescence from the MCP. The dye laser polarization was purified with a Promaster Spectrum 7 polarizer; an identical polarizer was used as analyzer between the substrate and collecting lens. The differential sensitivity to parallel- and perpendicular-polarized light was less than 2%.

Photocurrent pulses were amplified and inverted with a B&H Electronics AC3011 MIC (3.15 GHz) 21 dB preamplifier and an EG&G IT100 inverting transformer. The amplified pulses were processed in a Tennelec TC455 quad constant-fraction discriminator (CFD) and were used as START pulses in an Ortec 457 time-to-amplitude converter (TAC). The signal from dye laser pulses sampled by an EG&G FOD-100 photodiode in the photoconduction mode was passed through an Ortec 934 quad CFD to provide STOP pulses. TAC output was accumulated in a Canberra Series 30 MCA in the PHA mode, yielding 5.0, 10.0, or 20.0 ps channel resolution. Laser pulses scattered from a clean quartz substrate were used for generating instrument functions ($\sim$80 ps fwhm) for deconvolution of raw data.

Fluorescence profiles were transferred to a Digital Equipment Corporation MINC-23 system with dual floppy disk drive operating in an RT-11 environment and analyzed with a Marquardt nonlinear regression (23) program.

Data Analysis

Given a trial decay law N(t), the convolute-and-compare analysis computes the convolution C_n in the $\underline{n}$th channel of N(t) with the instrument function x(t),

$$C_n = \sum_{i=1}^{n} x\,(i-s)\,N(n-i) \qquad (7.18)$$

The variable shift parameter s allows for delay variations between profiles evaluated under changing experimental conditions. Following equation (7.10) and the subsequent discussion, we use as trial functions for $I_{\parallel}(t)$ and $I_{\perp}(t)$

$$I_{\parallel}(t) = AP(t)\ (1 + G^{s}(t)/2),$$
$$I_{\perp}(t) = AP(t)\ (1 - G^{s}(t)/2), \tag{7.19}$$

where $G^{s}(t)$, the two-body two-dimensional Green's function, is the inverse Laplace transform of

$$G^{s}(\varepsilon) = \{(\frac{1}{2\varepsilon} + (\frac{1}{4\varepsilon^{2}} + \frac{0.01637\alpha}{\varepsilon^{3}})1/2)1/3 + (\frac{1}{2\varepsilon} - (\frac{1}{4\varepsilon^{2}} + \frac{0.01637\alpha}{\varepsilon^{3}})1/2)1/3\}3. \tag{7.20}$$

At this level of approximation, $G^{s}(t)$ depends on the single parameter

$$\alpha = C^{3}/\tau_{D}. \tag{7.21}$$

Equation (7.19) implies that the analyzing polarizer's magic angle, at which the detected fluorescence profiles will behave as P(t) for our assumed adsorption geometry, is 45° (vs. 54.7° for fluorescence emitted from solutions). Three fluorescence profiles were typically accumulated from each sample: $I_{\parallel}(t)$, $I_{\perp}(t)$, and a magic angle profile. Ideally, P(t) should be a single-exponential decay function, and we have in fact obtained excellent single-exponential fits to magic-angle profiles from rhodamine 6G in glycerol in all but the most concentrated solutions, in

which excitation trapping by dye dimers distorts the isotropic decay function P(t) (23). For R3B on quartz, however, single-exponential fits to magic-angle profiles consistently yielded large values of

$$\chi^2 = \sum_{i=M}^{N} (C_i - Y_i)^2/Y_i, \qquad (7.22)$$

where Y_i is the experimental number of counts in channel i and (M, N) is the channel range used in the analysis. Even at the lowest R3B coverages, excellent fits (reduced χ^2 between 0.901 and 1.068) resulted from using a triexponential model function to analyze magic angle profiles obtained from most of our R3B/quartz samples (Table 7-1). This departure of the isotropic decay function P(t) from single-exponentiality can arise from adsorption site inhomogeneity, from dye inhomogeneity, or from excitation trapping by adsorbed dye aggregates. The first two causes are unlikely because (i) we obtained results similar to those in Table 7-1 for R3B coated onto untreated quartz substrates as well as substrates treated with dichlorodimethylsilane or monochlorotrimethylsilane; (ii) the R3B dye purity was verified by TLC (previous section), and its $-CO_2Et$ functional group cannot produce the carboxylic acid-base equilibrium exhibited by dyes like rhodamine B (16); and (iii) the nonexponential character of P(t) increases markedly with surface coverage in Table 7-1. In samples 1-3, the magic-angle profiles were dominated by a long component with lifetime $\tau_3 = 4.05 \pm 0.1$ ns; in the two samples with higher coverage, τ_3 decreases to 3.63 and 2.67 ns and the shorter lifetime components gain more importance. Excitation trapping by aggregates is

therefore a major origin of nonexponentiality in P(t) at our higher coverages. This concentration behavior parallels that observed in solution (13, 23) but is more pronounced because dyes form aggregates more readily on surfaces than in alcoholic solution (15).

Table 7-1. Triexponential fitting parameters for magic-angle profiles

$$N(t) = A_1\exp(-t/\tau_1) + A_2\exp(-t/\tau_2) + A_3\exp(-t/\tau_3)$$

Sample	R3B concn. in aqueous coating solution, M	A_1	τ_1, ns	A_2	τ_2, ns	A_3	τ_3, ns	χ_r^2
1	3.7×10^{-9}	1.0	3.59	19.10	1.86	54.1	4.07	1.068
2	7.4×10^{-9}	1.0	0.194	5.71	2.23	17.0	4.13	0.901
3	3.7×10^{-8}	1.0	0.976	6.27	2.36	17.8	3.95	0.948
4	7.4×10^{-8}	1.0	0.327	4.85	1.65	12.5	3.63	1.031
5	7.4×10^{-7}	1.0	0.186	2.12	1.08	2.88	2.67	1.070

The experimental $I_{\parallel}$ and $I_{\perp}$ profiles are then deconvoluted using equations (7.19) and (7.20) with the isotropic lifetime parameters in P(t) fixed as determined in the analyses of the magic-angle profiles. Parameter correlation between P(t) and $G^s(t)$ is thus avoided. $G^s(t)$ itself contains only α (defined in equation (7.21)) as an adjustable parameter in the two-body approximation, so $G^s(t)$ contributes very little functional flexibility to $I_{\parallel}(t)$ and $I_{\perp}(t)$. Both of the latter profiles

are deconvoluted simultaneously, and their combined χ^2 is minimized using a common, optimized α value. The inverse Laplace transform of equation (7.20) is evaluated numerically (24) in order to compute $G^s(t)$ during deconvolution. Our 80 ps fwhm instrument function is not wide compared to the 20 ps channel spacing used in most of this work. The convolute-and-compare algorithm is restricted to integral shift parameters s (equation (7.18)), so that choosing M=1 as the initial channel for computing χ^2 (equation (7.22)) produces disproportionate contributions to χ^2 from the sharply rising portions of the fluorescence profiles. Channel M is therefore typically placed $\sim$10 channels before the peak channel, and the continuous curves which represent convolutions of the optimized model functions with the instrument function in the figures accompanying the Results and Discussion section all begin with channel M.

The quality of data fits using the model functions in equation (7.19) can be estimated by evaluating the autocorrelations of residuals (25),

$$A_n = \frac{2N}{(N-M)} \frac{\sum_{i=1}^{(N-M)/2} Y_i^{1/2} (C_i - Y_i) Y_{i+n}^{1/2} (C_{i+n} - Y_{i+n})}{\sum_{i=1}^{N} Y_i (C_i - Y_i)^2}, \qquad (7.23)$$

where N is the number of channels comprising the fluorescence profile. The autocorrelation A_0 in channel 0 is unity. For model functions which are indistinguishable from the true decay functions, the autocorrelations A_n in other channels consist of random statistical fluctuations about $A_n = 0$. Such statistical autocorrelations were obtained for all of the

triexponential fits to the magic-angle profiles summarized in Table 7-1, meaning that the triexponential decay model is sufficiently flexible to replicate the observed isotropic decays P(t) to within photon counting fluctuations. These triexponential fits serve only as phenomenological descriptions of P(t) for deconvolution of the $I_{\parallel}$ and $I_{\perp}$ profiles using variable $G^s(t)$ in equation (7.19), and physical interpretations of the preexponential and lifetime parameters in Table 7-1 do not enter in the data analysis. Strictly speaking, excitation trapping by aggregates influences the fluorescence anisotropy as well as P(t) and the relation between the fluorescence components $I_{\parallel}(t)$ and $I_{\perp}(t)$ and the Green's function $G^s(t)$ in equation (7.19) is applicable only in the limit where the donor-donor excitation hopping rate greatly exceeds the rate of excitation trapping. This approximation is more nearly obeyed in samples 1-3 (in which the isotropic decay behavior varies slowly with donor coverage) than in samples 4 and 5, where the long-component lifetime τ_3 in Table 7-1 begins to decrease rapidly with increased coverage. Gochanour and Fayer (13) observed isotropic lifetime shortening from 3.1 to $\sim$2.85 ns in their most highly concentrated rhodamine 6G/glycerol solutions, and corrected for this effect by using reduced lifetimes in the isotropic decay portion of their three-dimensional analogs to equation (7.19). Such corrections are inherent in our procedure of using the least-squares triexponential parameters from Table 7-1 in P(t) while varying α in $G^s(t)$ to fit the observed fluorescence anisotropy.

Results and Discussion

The experimental $I_{\parallel}(t)$ and $I_{\perp}(t)$ profiles are plotted for samples 2-5 in Figure 7-3; the same spots were irradiated on these surfaces to obtain both these profiles and the magic-angle profiles described in Table 7-1. The continuous curves are convolutions of the model functions in equation (7.19) with the instrument function, optimized with respect to α and the shift parameters s in equation (7.18). The upper and lower inset plots in each part of Figure 7-3 show the autocorrelations of residuals (equation (7.23)) for $I_{\parallel}(t)$ and $I_{\perp}(t)$, respectively. The time scale in Figure 7-3 spans ca. 10 ns, or more than $2\tau_D$ for R3B on quartz. At the lowest coverage shown in Figure 7-3 (sample 2), the fluorescence depolarization is relatively small because $I_{\parallel}/I_{\perp}$ changes comparatively little between t=0 and $2\tau_D$; much larger depolarizations are evident in samples 3-5.

In Table 7-2, we list the final least-squares fitting parameter α, the reduced χ^2, and the reduced coverage computed from $C=(\alpha\tau_D)^{1/3}$ using τ_D=4.05 ns, for samples 1-5. The optimized reduced coverage C generally increases with the concentration of R3B coating solution used; a notable exception is the fact that C turns out to be larger for the irradiated point on sample 3 than for that on sample 4. At the highest coverage studied (C=0.651 for sample 5 in Table 7-2), the mean separation between nearest-neighbor donor molecules is still larger than $R_0 \sim 51$ Å for R3B on quartz (26). At and above such coverages, the fluorescence count rate decayed noticeably during a typical counting period of ~5 min. Stable

Figure 7-3. Fluorescence profiles $I_{\parallel}(t)$ and $I_{\perp}(t)$ for samples 2-5 in Table 7-1. Continuous curves are optimized convolutions of the model functions in equation (7.19) with the instrument function. Upper and lower inset plots show autocorrelations of residuals for $I_{\parallel}(t)$ and $I_{\perp}(t)$, respectively. Time calibration is 20 ps/channel; all fluorescences were excited with in-plane laser polarization

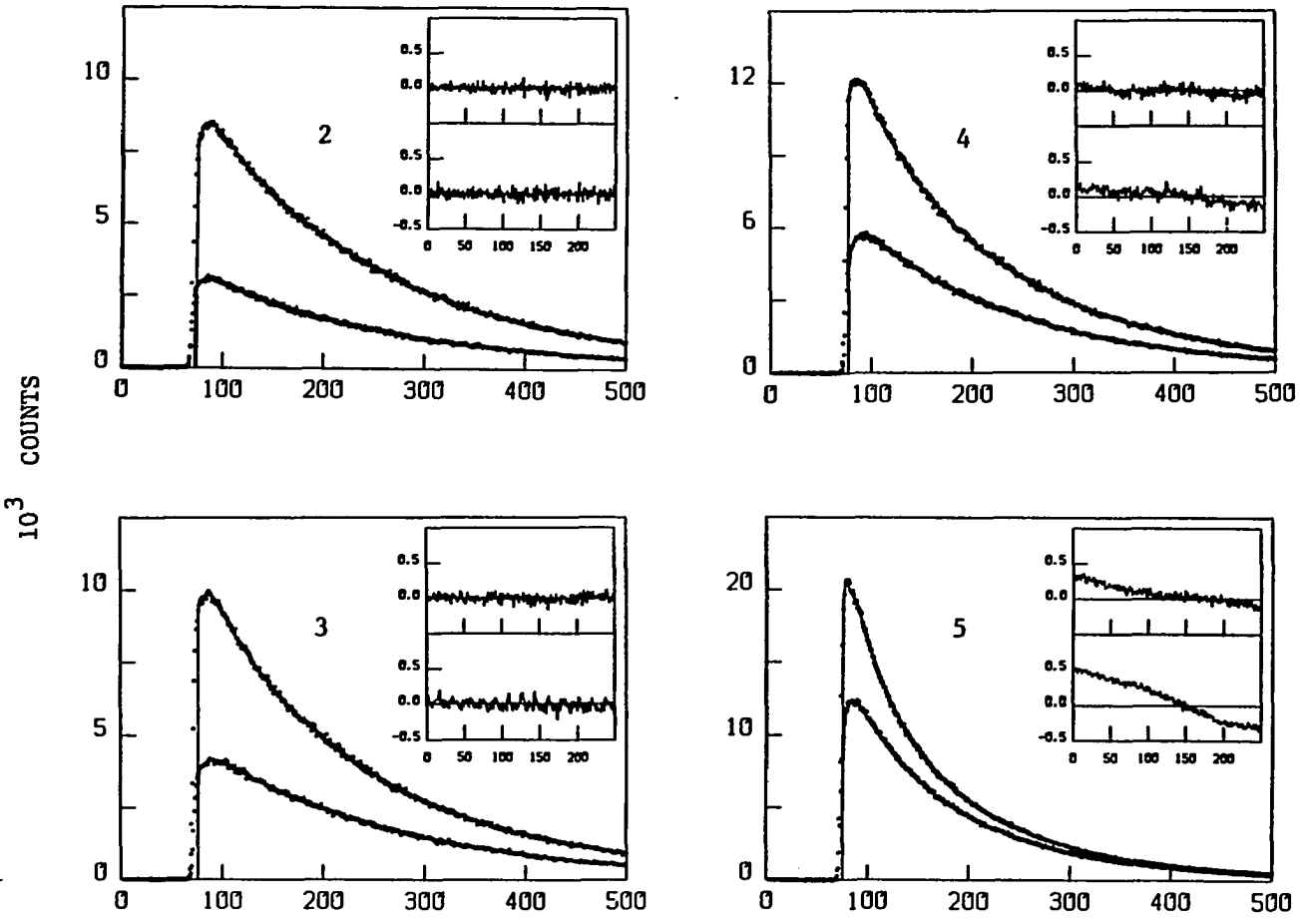
2
4
3
5
10^3 COUNTS
CHANNEL

count rates were obtained at lower coverages, implying that coverage-dependent photochemistry depleted the surface density of R3B monomers at sufficiently high densities. This photochemistry precluded studying coverages higher than that in sample 5; in the latter case, excitation trapping visibly accelerates the decay in the profiles of Figure 7-2(5) in comparison to the decay observed in samples 2-4 (Figure 7-3(2-4)).

Table 7-2. Fitting parameters for anisotropic fluorescence profiles[a]

$$I_{\parallel}(t) = P(t)\ (1 + \tfrac{1}{2}\ G^{s}(t))$$
$$I_{\perp}(t) = P(t)\ (1 - \tfrac{1}{2}\ G^{s}(t))$$

Sample		α, ns^{-1}	C[b]	χ_r^2
1	$\parallel$	1.29×10^{-4}	0.0805	1.004
	$\perp$			1.119
2	$\parallel$	2.75×10^{-4}	0.104	1.104
	$\perp$			1.055
3	$\parallel$	2.16×10^{-2}	0.444	1.009
	$\perp$			1.046
4	$\parallel$	1.75×10^{-2}	0.414	1.288
	$\perp$			1.229
5	$\parallel$	6.80×10^{-2}	0.651	1.676
	$\perp$			2.155

[a]Triexponential parameters in P(t) fixed at values listed in Table 7-1.

[b]Computed assuming $_D$ = 4.05 ns.

In Figure 7-4, we plot optimized reduced coverages versus concentration of aqueous R3B coating solution for triads of profiles obtained by (i) pumping of a given spot, (ii) consecutive pumping of the same spot, and (iii) pumping of a new spot. Photochemistry tends to produce spreads in C values which are largest at the highest coverage, although considerable scatter is also observed at the lowest coverage because in this regime $G^S(t)$ is a weak function of α ($G^S(t) \to 1$ for all t when $\alpha \to 0$). These reduced coverages are not linear in the coating solution concentration, but their locus resembles a Langmuir isotherm in that C levels off at the higher concentrations (27). The continuous curves are plots of the Langmuir type I isotherm function

$$C = \frac{\alpha M}{1 + \beta M} \tag{7.24}$$

for several values of the ratio α/β, which equals the limiting coverage at large coating solution molarities M. Near-Langmuir adsorption behavior has been reported for rhodamine B solution-coated onto SnO_2 and glass (28), and the implications of Figure 7-4 for the interpretation of our data will be discussed below.

The visual agreement between the optimized convolutions and the fluorescence profiles in Figure 7-3 is so close that the autocorrelation functions are useful for determining how well equation (7.19) models the decay behavior. The autocorrelations are statistical for the $I_{\parallel}(t)$ and $I_{\perp}(t)$ profiles from samples 1 (not shown), 2, and 3; systematically nonstatistical autocorrelations appear in samples 4 and 5. The

Figure 7-4. Optimized reduced coverages C for nonlinear least-squares fits to $I_{\parallel}(t)$ and $I_{\perp}(t)$ profiles for samples 1-5, plotted versus concentration M of R3B coating solution for (O) irradiation of an initial spot, (Δ) consecutive irradiation of the same spot, and ($\square$) irradiation of a new spot on R3B - coated quartz. Continuous curves are Langmuir adsorption functions $C = \alpha M/(1 + \beta M)$ for limiting reduced coverages α/β = 0.5, 1.0, 5.0, and 10.0 (bottom through top), adjusted to pass through C = 0.1 at 5.0×10^{-9} M. The numerical value of γ = 1.10, computed using equation (7.16) with $\theta^* = 52^{o}$ (19), was used to adjust the optimized reduced coverages for this figure

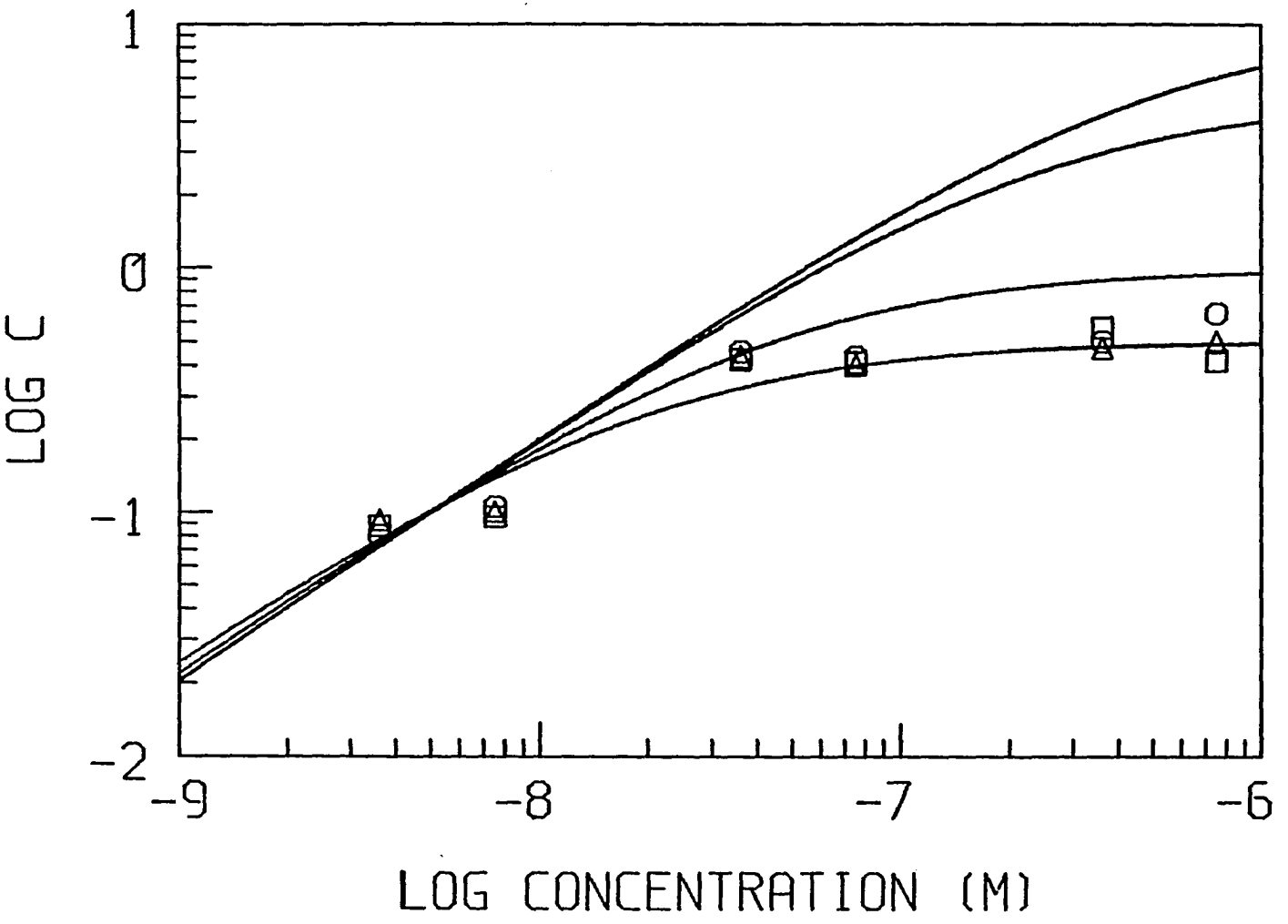
1
0
-1
-2
LOG C
-9
-8
-7
-6
LOG CONCENTRATION (M)

latter deviations are not a consequence of modeling artifacts in the isotropic decay functions P(t), since our triexponential fits to the magic-angle profiles (Table 7-1) yielded statistical autocorrelations similar to those in Figure 7-3(2) in all five samples. Close inspection of the unreduced plots for Figure 7-3(5) reveals that the deviations in $I_{\parallel}$ and $I_{\perp}$ anticorrelate, and so they arise from disagreement between the optimized two-body Green's function $G^s(t)$ and the observed anisotropy function $C_2(t)$, which enters with opposite sign in the parallel and perpendicular components of equation (7.10). The two-body Green's function contributes appreciably to the observed decay in $I_{\parallel}(t)$ and $I_{\perp}(t)$ even for C = 0.08 (sample 1), since $G^s(t)$ in this approximation decays from 1.0 to 0.916 by $t = 2\tau_D$ for this value of C. The nonexponential character in $G^s(t)$ evolves rapidly as C is increased from 0.1 to 1.0 (Figure 7-5), and it appears remarkable that statistical autocorrelations are obtainable for C as large as 0.444 (sample 3). The quality of any self-consistent approximation to $G^s(t)$ declines as the reduced coverage or concentration is increased (8, 15), and in this context the nonstatistical autocorrelations obtained at the highest coverages in Figure 7-3 are not surprising.

However, a likelier cause for the larger deviation at higher coverage is excitation trapping. The R3B coverages which are spanned in Figure 7-4 are all too low for direct spectroscopic measurement of the actual R3B surface number density $\rho (= C/\pi R_0^2)$. The optical density of a quartz surface coated with 7.4×10^{-5} M aqueous R3B was determined to be $0.002 \pm .00025$ using a Perkin-Elmer 320 UV-visible spectrophotometer, corresponding to a reduced coverage of $C \sim 9.0$. This fixes a minimum value for

Figure 7-5. Two-body approximation to the two-dimensional Green's function $G^S(t)$, plotted versus (t/τ_D) for reduced coverages C = 1.0, 0.8, 0.6, 0.4, 0.2, and 0.1 (bottom through top, respectively)

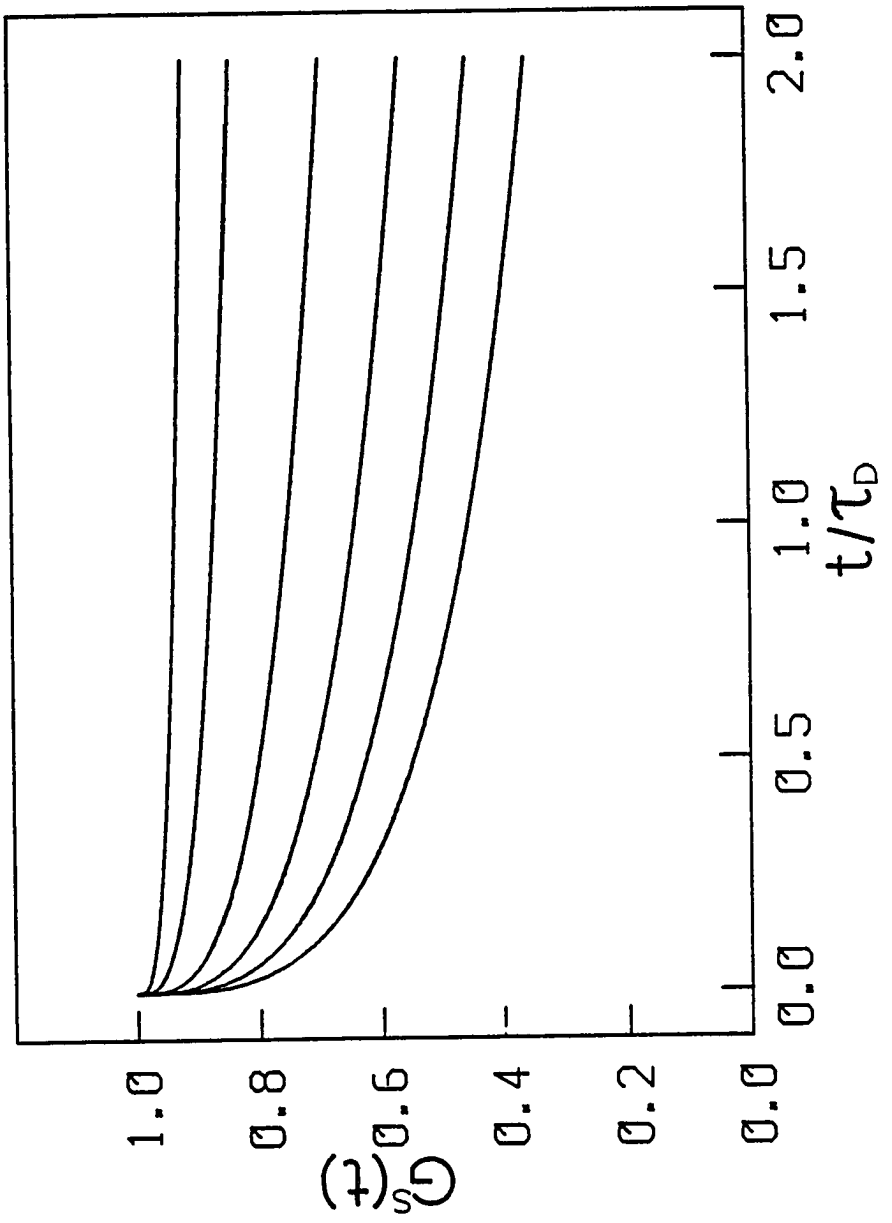
1.0
0.8
0.6
0.4
0.2
0.0
$G^S(t)$
0.0
0.5
1.0
1.5
2.0
t/τ_D

$\alpha/\beta \sim 9.0$ in the isotherms of Figure 7-4 (all of which are adjusted to pass between the sets of points representing samples 1 and 2), if Langmuir adsorption behavior is indeed followed. The isotherms for C = 5.0 and C = 10.0 pass near the points for samples 1-3, but at the higher coverages (samples 4 and 5) the optimized coverages from least-squares fitting of the fluorescence profiles lie far below the isotherms. These shortfalls arise physically from the fact that lifetime shortening by excitation trapping interrupts the depolarization process, so that the apparent value of the dynamical parameter C becomes smaller than the actual reduced coverage of donors. It appears certain that the true isotherm in the neighborhood of coating solution concentrations 10^{-7} to 10^{-6} M resembles the plotted isotherm for C = 10.0 more than it resembles the locus of optimized reduced coverages from the fluorescence data, since C must be on the order of 9.0 at 4.7×10^{-5}M. At the highest coverage, then, the optimized reduced coverage is about an order of magnitude too low.

In summary, the model functions which use the two-body Green's function $G^s(t)$ in equation (7.19) yield optimized convolutions which are statistically indistinguishable from the experimental profiles from the three samples with lowest coverage (1-3). Figure 7-4 shows that large distortions in the optimized reduced coverage are caused by excitation trapping in the other samples, and poorer autocorrelations are found in those samples. These disagreements do not arise primarily from inaccuracy in the two-body Green's function at these higher coverages; an effective test of the theory for C larger than $\sim$0.4 requires samples in which

aggregation and excitation trapping are more completely suppressed than was possible in our systems. Other desiderata for two-dimensional excitation transport systems are improved surface flatness and/or uniformity of adsorption geometry (as evidenced by the profiles in Figure 7-2), and a knowledge of the spatial donor distribution on the surface. In the present systems, aggregation of R3B on quartz shows that the donor distribution is not truly random, so that strictly speaking the surface density ρ cannot be factored out of the integral over $\vec{r}_{12}$ in equation (7.13). These drawbacks may be avoided by studying fluorescence depolarization in dye-dodecanoic acid layers at N_2 - water interfaces (29), where better surface flatness, more uniform transition moment distributions, and true spatial randomness may yield a more controlled test of two-dimensional excitation transport theory.

Acknowledgments

The Ames Laboratory is operated for the U.S. Department of Energy by Iowa State University under Contract No. W-7405-Eng-82. This work was supported by the Office of Basic Energy Sciences. We thank Professor Michael Fayer for helpful discussions.

References

1. Fayer, M. D. Ann. Rev. Phys. Chem. 1982, 33, 63.
2. Förster, T. Annalen Physik 1948, 6, 55.
3. Förster, T. Disc. Far. Soc. 1959, 27, 7.

4. Galanin, M. D. Trudy Fiz. Inst. 1950, 27, 7.

5. Vavilov, S. I. J.E.T.P. 1943, 13, 13.

6. Ore, A. J. Chem. Phys. 1959, 31, 442.

7. Craver, F. W.; Knox, R. S. Mol. Phys. 1971, 22, 385.

8. Gochanour, C. R.; Andersen, H. C.; Fayer, M. D. J. Chem. Phys. 1979, 70, 4254.

9. Loring, R. F.; Andersen, H. C.; Fayer, M. D. J. Chem. Phys. 1982, 76, 2015.

10. Loring, R. F,; Andersen, H. C.; Fayer, M. D. Chem. Phys. 1984, 85, 149.

11. Loring, R. F.; Fayer, M. D. Chem. Phys. 1982, 70, 139.

12. Miller, R. J. D.; Pierre, M.; Fayer, M. D. J. Chem. Phys. 1983, 78, 5137.

13. Gochanour, C. R.; Fayer, M. D. J. Phys. Chem. 1981, 85, 1989.

14. Fayer, M. D., private communication.

15. Anfinrud, P.; Crackel, R. L.; Struve, W. S. J. Phys. Chem. 1984, 88, 5873.

16. Sadkowski, P. J.; Fleming, G. R. Chem. Phys. Lett. 1978, 57, 526.

17. Faraggi, M.; Peretz, P.; Rosenthal, I.; Weinraub, D. Chem. Phys. Lett. 1984, 103, 310.

18. Craver, F. W. Mol. Phys. 1971, 22, 403.

19. DiLazzaro, P.; Mataloni, P.; DeMartin, F. Chem. Phys. Lett. 1985, 114, 103.

20. Heinz, T. F.; Shen, C. K.; Richard, D.; Shen, Y. R. Phys. Rev. Lett. 1982, 48, 478.

21. Tao, T. Biopolymers 1969, 8, 609.

22. Yasa, Z. A.; Amer, N. M. Opt. Commun. 1981, 36, 406

23. Anfinrud, P.; Hart, D. E.; Hedstrom, J. F.; Struve, W. S. To be published.

24. Stehfest, H. Commun. ACM 1970, 13, 47.

25. Grinvald, I.; Steinberg, I. Z. Anal. Biochem. 1974, 59, 583.

26. This value for R_0 was evaluated for R3B with Equation (4) of Reference 3, using measured absorption and fluorescence spectra for R3B adsorbed on quartz.

27. Langmuir, I. J. Am. Chem. Soc. 1916, 38, 2267.

28. Itoh, K.; Chiyokawa, Y.; Nakao, M.; Honda, K. J. Phys. Chem. 1984, 106, 1620.

29. Subramanian, R.; Patterson, L. K. J. Phys. Chem. 1985, 89, 0000.

CHAPTER VIII. SUMMARY

The experiment investigating energy transfer in aniline induced by collisions with carbon dioxide was the first in a series of experiments designed to study the effect of molecular rotation on energy transfer rates. These later experiments (158) have shown that the Moore correlation (44) of up-pumping probabilities with partner rotational parameters yields no evidence of V-R processes in aniline-partner collisions. This is contrary to previous experience with vibrational relaxation governed by close-range repulsion in small molecules in their electronic ground states.

The propensity rules for mode-to-mode energy transfer in aniline-partner collisions appear to be determined primarily by intramolecular anharmonic or Coriolis coupling within aniline. This observed behavior is contrary to the assumptions which underlie the modified SSH theories (14, 15).

Recently, Freed (159) has formulated a theory for efficient collision-induced mode-to-mode energy transfer in large molecules which accounts for many of our observed results. His theory postulates a purely intramolecular coupling mechanism for collision-induced vibrational energy transfer. It is applicable to large molecules in which the high density of vibrational states leads to mixing of levels whose energies lie within a few hundred wave numbers of each other.

An important property successfully explained by the Freed theory is the fact that energy transfer rates in S_1 state aniline and other large

polyatomics are so large, amounting to appreciable fractions of the hard-sphere collision rates. There has been speculation (24) that the electronic excitation endows the polyatomic species with enhanced energy transfer rates as a consequence of presumably larger van der Waals force constants between the excited state molecule and collision partners. However, the long-range potential dominance of mode-to-mode transfer and large cross sections both arise naturally as consequences of intramolecular anharmonic coupling in the Freed large-molecule theory. Experiments by Lawrance and Knight (37) provide support to this hypothesis. Their work shows that large collisional energy transfer rates also occur in ground state p-difluorobenzene. The predominance of the long-range potential in aniline-perturber collisions is also suggested by our lack of evidence for V-R processes, which depend large on the short range potential anisotropy in collisions between small molecules.

The first experiment investigating the GAF three-body theory's ability to describe excitation transport in a three-dimensional system was performed by Gochanour and Fayer (109). Gochanour and Fayer obtained their fluorescence profiles by KDP sum-frequency mixing of rh6G fluorescence with the variably delayed fundamental output from a CW mode-locked Nd:YAG laser, and the resulting 390 nm upconverted pulses were detected by a photomultiplier and lock-in amplifier. The noise present on Gochanour and Fayer's decay curves using this arrangement, however, prevented precise comparisons between theoretical curves and experimental data.

Our goal was to reinvestigate the GAF three-dimensional, three-body theory using picosecond laser excitation and time-correlated photon counting. This system facilitated collecting data with a high signal-to-noise ratio and, therefore, the data obtained provided a more stringent test of the GAF excitation theory in three dimensions.

In performing the experiments, it was found that excitation trapping by rh6G dimers considerably distorts the isotropic decay behavior in the higher concentration solutions. Additionally, lifetime dilation due to self-absorption is difficult to suppress in these solutions, due to the small Stoke's shift for rh6G. These phenomena affect the fluorescence anisotropy in ways which are difficult to correct for rigorously. Gochanour and Fayer's data were affected similarly by these experimental artifacts.

Due to the presence of artifacts, no statement can be made regarding the accuracy of the GAF three-body theory. Subsequent work in testing the three-body theory at high reduced donor concentrations will require reducing the effects of trapping. This can be accomplished by using a donor molecule such as DODCI, which has a large R_0. Self-absorption can be minimized by using thinner sample cells.

Fluorescence profiles collected from rh3B adsorbed to fused silica provided the first data from which the GAF two-dimensional, two-body theory could be analyzed. Fluorescence profiles agreed well with the theory for reduced surface coverages up to 0.4. At higher coverages, excitation trapping by rh3B dimers truncates the depolarization process,

yielding apparent reduced coverages which are appreciably lower than the true coverages.

The motivation behind the two-dimensional excitation transport experiment was to determine whether systematic errors in the Green's function calculated from the two-body theory could be identified. Several experimental difficulties prevented us from making an absolute statement regarding the accuracy of the Loring and Fayer (70) two-body theory. The difficulties included photodecomposition and trapping at higher surface coverages, lack of single exponential magic-angle decays, unknown rh3B surface number densities and dye molecule transition dipole adsorption geometries which did not form a well defined cone on the fused silica surface.

An improved system for studying the two-dimensional, two-body theory could be constructed by preparing in a Langmuir-Blodgett trough a monolayer film of dye (such as octadecyl rhodamine B) interspersed in a fatty acid. This would provide improved surface flatness and permit dye surface number densities to be determined. By choosing a proper fatty acid spacer, aggregation among dye molecules may be eliminated.

LITERATURE CITED

1. Kaplan, H.; Levine, R. D.; Manz, J. Chem. Phys. 1976, 12, 447.
2. Knudtson, T. J.; Eyring, E. M. Ann. Rev. Phys. Chem. 1974, 25, 255.
3. Letokhov, V. S. Ann. Rev. Phys. Chem. 1977, 28, 133.
4. Moore, C. B.; Smith, I. W. M. Faraday Discuss. Chem. Soc. 1979, 67, 146.
5. Earl, B. L.; Gamss, L. A.; Ronn, A. M. Accts. Chem. Research 1978, 11, 183.
6. Jortner, J.; Levine, R. D. In "Advances in Chemical Physics"; Jortner, J.; Levine, R. C.; Rice, S. A., Eds.; Wiley: New York, 1981; Vol. 46.
7. Weitz, E.; Flynn, G. In "Advances in Chemical Physics"; Jortner, J.; Levine, R. C.; Rice, S. A., Eds.; Wiley: New York, 1981; Vol. 47.
8. Moore, C. B. In "Advances in Chemical Physics"; Prigogine, I.; Rice, S. A., Eds.; Wiley: New York, 1973; Vol. 23.
9. McDonald, J. D. Ann. Rev. Phys. Chem. 1979, 30, 29.
10. Sheorey, R. L.; Flynn, G. J. Chem. Phys. 1980, 72, 1175.
11. Earl, B. L.; Isolani, P. C.; Ronn, A. M. Chem. Phys. Lett. 1976, 39, 95.
12. Yardley, J. T. "Introduction to Molecular Energy Transfer"; Academic: New York, 1980.
13. Schwartz, R. N.; Slawsky, Z. I.; Herzfeld, K. F. J. Chem. Phys. 1952, 20, 1591.
14. Tanczos, F. I. J. Chem. Phys. 1956, 25, 439.
15. Stretton, J. L. Trans. Faraday Soc. 1965, 61, 1053.
16. Parmenter, C. S. J. Phys. Chem. 1982, 86, 1735.
17. Miklavc, A.; Fischer, S. Chem. Phys. Lett. 1976, 44, 209.
18. Miklavc, A.; Fischer, S. J. Chem. Phys. 1978, 69, 281.

19. Fink, E. H.; Comes, F. J. Chem. Phys. Lett. 1974, 25, 190.

20. Fink, E. H.; Akins, D. L.; Moore, C. B. J. Chem. Phys. 1972, 56, 900.

21. Lengel, R. K.; Crosley, D. R. J. Chem. Phys. 1978, 68, 5309.

22. Ennen, G.; Ottinger, C. Chem. Phys. 1974, 3, 404.

23. Marcoux, P. J.; Piper, L. G.; Setzer, D. W. J. Chem. Phys. 1977, 66, 351.

24. Rice, S. A. In "Advances in Chemical Physics"; Jortner, J.; Levine, R. D.; Rice, S. A., Eds.; Wiley: New York, 1981; Vol. 47.

25. Lin, H. M.; Seaver, M.; Tang, K. Y.; Knight, A. E. W.; Parmenter, C. S. J. Chem. Phys. 1979, 70, 5442.

26. Parmenter, C. S.; Tang, K. Y. Chem. Phys. 1978, 27, 127.

27. Atkinson, G. H.; Parmenter, C. S.; Tang, K. Y. J. Chem. Phys. 1979, 71, 68.

28. Yardley, J. T.; Moore, C. B. J. Chem. Phys. 1968, 49, 1111.

29. Yuan, R. C. L.; Flynn, G. W. J. Chem. Phys. 1973, 58, 649.

30. Grabner, F. R.; Flynn, G. W. J. Chem. Phys. 1974, 60, 398.

31. Chernoff, D. A.; Rice, S. A. J. Chem. Phys. 1979, 70, 2521.

32. Chernoff, D. A. Ph.D. Dissertation, University of Chicago, Chicago, Ill., 1978.

33. McDonald, D. B.; Rice, S. A. J. Chem. Phys. 1981, 74, 4907.

34. Knight, A. E.; Parmenter, C. S. J. Phys. Chem. 1983, 87, 417.

35. McDonald, D. B.; Rice, S. A. J. Chem. Phys. 1981, 74, 4918.

36. Lawrance, W. D.; Knight, A. E. W. J. Chem. Phys. 1982, 76, 5637.

37. Lawrance, W. D.; Knight, A. E. W. J. Chem. Phys. 1982, 77, 570.

38. Rettschnick, R. P. H.; Ten Brink, H. M.; Langelaar, J. J. Mol. Struct. 1978, 47, 261.

39. Ten Brink, H. M.; Langelaar, J.; Rettschnick, R. P. H. Chem. Phys. Lett. 1979, 62, 263.

40. Leeuw, G.; Langelaar, J.; Rettschnick, R. P. H. J. Mol. Struct. 1980, 61, 101.

41. Tang, K. Y.; Parmenter, C. S. J. Chem. Phys. 1983, 78, 3922.

42. Vandersall, M.; Chernoff, D. A.; Rice, S. A. J. Chem. Phys. 1981, 74, 4888.

43. Cottrell, T. L.; Matheson, A. J. Trans. Faraday Soc. 1962, 58, 2336.

44. Moore, C. B. J. Chem. Phys. 1965, 43, 2979.

45. Brand, J. C. D.; Williams, D. R.; Cook, T. J. J. Mol. Spectrosc. 1966, 20, 359.

46. Millar, D. P.; Zewail, A. H. Chem. Phys. 1982, 72, 381.

47. Preuss, D. R.; Gole, J. L. Appl. Opt. 1980, 19, 702.

48. Crowell, M. H. IEEE J. Quantum Electron. 1965, QE-1, 12.

49. DiDomenico, M. J. Appl. Phys. 1964, 35, 2870.

50. Sapriel, J. "Acousto-Optics"; Wiley: New York, 1979.

51. O'Shea, D.; Callen, W. R.; Rhodes, W. "Introduction to Lasers and Their Applications"; Addison-Wesley: Reading, 1977.

52. Kaminow, I. P. "An Introduction to Electrooptic Devices"; Academic: New York, 1974.

53. Kogelnik, H. W.; Ippen, E. P.; Dienes, A.; Shank, C. V. IEEE J. Quantum Electron. 1972, QE-8, 373.

54. Siegman, A. E.; Phillion, D. W.; Kuizenga, D. J. Appl. Phys. Lett. 1972, 21, 345.

55. Fowles, G. R. "Introduction to Modern Optics", 2nd ed.; Holt, Rinehart and Winston: New York, 1975.

56. Chan, C. K. "Synchronously Pumped Dye Lasers". Spectra-Physics Laser Techn. Bull. No. 8, February 1978.

57. McDonald, D. B.; Waldeck, D.; Fleming, G. R. Opt. Commun. 1980, 34, 127.

58. Shapiro, S. L.; Cavanagh, R. R.; Stephenson, J. C. Opt. Lett. 1981, 6, 470.

59. Kim, D. M.; Kuhl, J.; Lambrich, R.; von der Linde, D. Opt. Commun. 1978, 27, 123.

60. Kleinman, D. A. Phys. Rev. 1962, 128, 1761.

61. Midwinter, J. E.; Warner, J. Br. J. Appl. Phys. 1965, 15, 1135.

62. Akhmanov, S. A.; Kovrygin, A. I.; Sikhorukov, A. P. In "Quantum Electronics"; Rabin, H.; Tang, C. L., Eds.; D. Van Nostrand: New York, 1974; Vol. I, Chapter 8.

63. Lasermetrics Technical Memorandum TM-751, Lasermetrics, Teaneck, N. J., 1975.

64. Gutherie, A. "Vacuum Technology"; Wiley: New York, 1963.

65. Lipson, S. G.; Lipson, H. "Optical Phyica", 2nd ed.; Cambridge University Press: Cambridge, 1981.

66. Hayatt, G. S.; Pieuchard, G. "Handbook of Diffraction Gratings Ruled and Holographic"; Jobin-Yvon: Metuchen, N. H., ca. 1975.

67. Willard, H. H.; Merritt, Jr., L. L.; Dean, J. A. "Instrumental Methods of Analysis", 5th ed.; D. Van Nostrand: New York, 1974.

68. "Atomic Energy Levls". Natl. Bur. Stand. (U.S.) Circ. 467, Vol. III.

69. Gochanour, C. R.; Andersen, H. C.; Fayer, M. D. J. Chem. Phys. 1979, 70, 4254.

70. Loring, R. F.; Fayer, M. D. Chem. Phys. 1982, 70, 139.

71. Maydan, D. J. Appl. Phys. 1970, 41, 1552.

72. Johnson, R. H. IEEE J. Quantum Electron. 1973, QE-8, 255.

73. Maydan, D. IEEE J. Quantum Electron. 1970, QE-6, 15.

74. Pascal, D.; Laval, S. J. Phys. E : Sci. Instrum. 1984, 17, 384.

75. Yasa, Z. A.; Amer, N. M. Opt. Commun. 1981, 36, 406.

76. O'Connor, D. V.; Phillips, D. "Time-correlated Single Photon Counting"; Academic: New York, 1984.

77. "Radiation Spectroscopy and Analysis Instruments for Research and Industry"; Ortec Inc. Oak Ridge, Tenn. 1976, Catalog 1004.

78. Candy, B. H. Rev. Sci. Instrum. 1985, 56, 183.

79. Knight, A. E.; Selinger, B. K. Austr. J. Chem. 1973, 26, 1.

80. Meade, M. L. J. Phys. E : Sci. Instrum. 1981, 14, 909.

81. Morton, G. A. Appl. Opt. 1968, 7, 1.

82. Haugen, G. R.; Wallin, B. W.; Lyttle, F. E. Rev. Sci. Instrum. 1979, 50, 64.

83. Coates, P. B. J. Phys. E : Sci. Instrum. 1968, 1, 878.

84. Davis, C. C.; King, T. A. J. Phys. A : Gen. Phys. 1970, 3, 101.

85. Harris, C. M.; Selinger, B. K. Austr. J. Chem. 1979, 32, 2111.

86. Mobius, D.; Bucher, H. In "Physical Methods of Chemistry"; Weissberger; Rossiter, Eds.; Wiley: New York, 1972; Part IIIB.

87. Willig, F.; Blumen, A.; Zumoten, G. Chem. Phys. Lett. 1984, 108, 222.

88. Liang, Y.; Moy, P. F.; Poole, J. A.; Ponte Goncalves, A. M. J Phys. Chem. 1984, 88, 2451.

89. Liang, Y.; Ponte Goncalves, A. M.; Negus, D. K. J. Phys. Chem. 1983, 87, 1.

90. Wokaun, A.; Lutz, H. P.; King, A. P.; Wil, V. P.; Ernst, R. R. J. Chem. Phys. 1983, 79, 509.

91. Larson, N. W.; Hansen, E. L.; Nicolaisen, F. M. Chem. Phys. Lett. 1976, 43, 584.

92. Christoffersen, J.; Hollas, J. M.; Kirby, G. H. Mol. Phys. 1969, 16, 441.

93. Varsanyi, G. "Assignments for Vibrational Spectra of Seven Hundred Benzene Derivatives"; Wiley: New York, 1974; Vol. I.

94. Ware, W. F.; Garcia, A. M. J. Chem. Phys. 1974, 61, 187.

95. Bevington, P. R. "Data Reduction and Error Analysis for the Physical Sciences"; McGraw-Hill: New York, 1969.

96. Hochstrasser, R. M.; Johnson, C. K. Laser Focus 1985, 21, 100.

97. Lakowicz, J. R. "Principles of Fluorescence Spectroscopy"; Plenum: New York, 1983.

98. Prendergast, F. G.; Haugland, R. P.; Callahan, P. J. Biochemistry 1981, 20, 7333.

99. Engel, L. W.; Prendergast, F. G. Biochemistry 1981, 20, 7339.

100. Schneider, S.; Hefferle, P.; Geiselhart, P.; Mindl, T.; Door, F.; John, W.; Scheer, H. In "Ultrafast Phenomena IV"; Auston, D. H.; Eisenthal, K. B., Eds.; Springer-Verlag: New York, 1984.

101. Campillo, A. J.; Shapiro, S. L. In "Ultrashort Light Pulses"; Shapiro, S. L., Ed.; Springer-Verlag: New York, 1977.

102. Bolt, J. D.; Sauer, K. Biochimica et Biophysica Acta 1981, 637, 342.

103. Ediger, M. D.; Fayer, M. D. Macromolecules 1983, 16, 1839.

104. Fredrickson, G. H.; Andersen, H. C.; Frank, C. W. Macromolecules 1984, 17, 1496.

105. Fredrickson, G. H.; Andersen, H. C.; Frank, C. W. Macromolecules 1984, 17, 54.

106. Fredrickson, G. H.; Andersen, H. C.; Frank, C. W. J. Chem. Phys. 1983, 79, 3572.

107. Fredrickson, G. H.; Andersen, H. C.; Frank, C. W. Macromolecules 1983, 16, 1456.

108. Fredrickson, G. H.; Frank, C. W. Macromolecules 1983, 16, 1198.

109. Gochanour, C. R.; Fayer, M. D. J. Phys. Chem. 1981, 85, 1989.

110. Anfinrud, P. A.; Hart, D. E.; Hedstrom, J. F.; Struve, W. S. J. Phys. Chem. 1986, 90, 0000.

111. Anfinrud, P. A.; Hart, D. E.; Hedstrom, J. F.; Struve, W. S. J. Phys. Chem. 1986, 90, 2374.

112. Knox, R. S. Physica 1968, 39, 361.

113. Craver, F. W. Molecular Physics 1971, 22, 403.

114. Hemenger, R. P.; Pearlstein, R. M. J. Chem. Phys. 1973, 59, 4064.

115. Haan, S. W.; Zwanzig, R. J. Chem. Phys. 1978, 68, 1879.

116. Förster, T. Disc. Far. Soc. 1959, 27, 7.

117. Förster, T. Annalen Physik 1948, 6, 55.

118. Lamola, A. A. In "Technique of Organic Chemistry"; Leermakers, P. A.; Weissberger, A., Eds.; Interscience: New York, 1969; Vol. 14.

119. Knox, R. S. In "Bioenergetics of Photosynthesis"; Govindjee, R., Ed.; Academic: New York, 1975.

120. Vavilov, S. I. J.E.T.P. 1943, 13, 13.

121. Galanin, M. D. Trudy Fiz. Inst. 1950, 5, 339.

122. Craver, F. W.; Knox, R. S. Molecular Physics 1971, 22, 385.

123. Ore, A. J. Chem. Phys. 1959, 31, 442.

124. Dexter, D. L. J. Chem. Phys. 1953, 21, 836.

125. Weber, G. Biochem. J. 1952, 51, 145.

126. Weber, G. Trans. Faraday Soc. 1954, 50, 552.

127. Jablonski, A. Acta Phys. 1955, 14, 295.

128. Haan, S. W. Ph.D. Dissertation, University of Maryland, College Park, MD, 1977.

129. Loring, R. F.; Andersen, H. C.; Fayer, M. D. J. Chem. Phys. 1982, 76, 2015.

130. Yokota, M.; Tanimoto, O. J. Phys. Soc. Jpn. 1967, 22, 779.

131. Burshtein, A. I. Sov. Phys.-JETP 1972, 35, 882.

132. Miller, R. J. D.; Pierre, M.; Fayer, M. D. J. Chem. Phys. 1983, 78, 5138.

133. Doktorov, A. B.; Burshtein, A. I. Sov. Phys.-JETP 1976, 41, 671.

134. Artamonova, M. V.; Briskina, C. M.; Burshtein, A. I.; Zusman, L. D.; Skleznev, A. G. Sov. Phys.-JETP 1972, 35, 457.

135. Blumen, A.; Silbey, R. J. Chem. Phys. 1979, 70, 3707.

136. Godzik, K.; Jortner, J. J. Chem. Phys. 1980, 72, 4471.

137. Huber, D. L. Phys. Rev. B 1979, 20, 2307.

138. Zusman, L. D. Sov. Phys.-JETP 1977, 46, 347.

139. Burshtein, A. I. J. Lumin. 1985, 34 167.

140. Fedorenko, S. G.; Burshtein, A. I. Chem. Phys. 1985, 98, 341.

141. Forster, R. Z. Naturforsch. 1949, 4A, 321.

142. Huber, D. L. In "Laser Spectroscopy of Solids"; Yen, W. M.; Selzer, P. M., Eds.; Springer-Verlag: New York, 1981.

143. Lutz, D. R.; Nelson, K. A.; Gochanour, C. R.; Fayer, M. D. Chem. Phys. 1981, 58, 325.

144. Klafter, J.; Silbey, R. J. Chem. Phys. 1980, 72, 843.

145. O'Connor, D. V.; Phillips, D. "Time-correlated Single Photon Counting"; Academic: New York, 1984.

146. Stehfest, H. Commun. ACM 1970, 13, 47.

147. Grinvald, A.; Steinberg, I. Z. Anal. Biochem. 1974, 59 583.

148. Anfinrud, P.; Crackel, R. L.; Struve, W. S. J. Phys. Chem. 1984, 88, 5873.

149. Sadkowski, P. J.; Fleming, G. R. Chem. Phys. Lett. 1978, 57, 526.

150. Faraggi, M.; Peretz, P.; Rosenthal, I.; Weinraub, D. Chem. Phys. Lett. 1984, 103, 310.

151. Zernike, F.; Midwinter, J. E. "Applied Nonlinear Optis"; Wiley: New York, 1973.

152. Kurtz, S. K. In "Laser Handbook"; Arecchi, F. T.; Schulz-Dubois, E. O., Eds.; North-Holland: Amsterdam, 1972; Vol. I, Chapter D1.

153. Boyd, G. D.; Ashkin, A.; Dziedzic; Kleinman, D. A. Phys. Rev. 1965, 137, A1305.

154. Boyd, G. D.; Kleinman, D. A. J. Appl. Phys. 1968, 39, 3597.

155. Kleinman, D. A. In "Laser Handbook"; Arecchi, F. T.; Schulz-Dubois, E. O., Eds.: North-Holland: Amsterdam, 1972; Vol. II, Chapter E4.

156. Nath, G.; Haussuhl, S. Appl. Phys. Lett. 1969, 14, 154.

157. Sliker, T. R.; Burlage, S. R. J. Appl. Phys. 1963, 34, 1837.

158. Pineault, R. L.; Crackel, R. L.; Hedstrom, J. F.; Struve, W. D. J. Chem. Phys. 1984, 80, 5545.

159. Freed, K. F. Chem. Phys. Lett. 1984, 106, 1.

ACKNOWLEDGMENTS

There are many people deserving of special recognition for their input into the research contained in this dissertation. However, none deserve more credit than my research advisor -- Professor Walter Struve. The mere "thank you" that I provide here cannot come close to repaying him for his guidance, patience, and the many ideas he has contributed to these projects. Additionally, I would like to thank Dr. Struve, his wife Helen, and Taco for sacrificing their house on occasion so that the group could view slides of Europe and partake in enjoyable evenings of conversation (and good food).

I would like to thank Richard Pineault and Robert Crackel for their input into the collision induced energy transport research, while David Hart and Philip Anfinrud deserve special recognition (and thanks) for their contributions to the excitation transport studies in disordered systems.

I would like to thank Dave for being a good friend, roommate and cook. Along with Dave, I should mention Cristiano Morgante and Michael McGlade as good friends who have influenced my life in many ways.

I would like to thank the other members of the Struve group -- Timothy Causgrove, Baihao Chen, Sandra Bellefeuille and Shumei Yang -- for their friendship and support.

Sandra Calvert deserves special recognition for ably typing the manuscript and wading through the equations.

Once again, thanks to all of my relatives and friends whose support has meant so much to me over the years.

APPENDIX: OPTIMIZATION OF FREQUENCY DOUBLING CONDITIONS

Both $LiIO_3$ and KDP crystals were considered for frequency doubling the dye laser output. Obviously, the crystal which could produce the highest SHG conversion efficiency at the frequency of the aniline 0_0^0 transition would be the preferred choice for this work. The SHG power obtainable from a frequency doubling crystal depends not only on the crystal thickness and orientation but also on conditions such as focusing of the laser fundamental and absorption of light by the crystal. The purpose of this appendix is to determine the optimum conditions for generating second harmonic light from the dye laser fundamental with each crystal. A final comparison between the two crystals under these conditions will determine which is to be used in experiments.

Certain parameters which affect the conversion efficiency will be fixed and not considered as variables for increasing the SHG output. Among these, the crystal lengths $l(LiIO_3)$ and l(KDP) are fixed at 2 mm and 12.5 mm, respectively. The dye laser output fundamental will be tuned to 600 nm. Initially, the dye laser output will be focused into each doubling crystal with a 7.0 cm focal length lens. The focused beam radius a_w will be approximately 13 μm. It follows that the confocal parameter (62)

$$b = k_1 a_w^2, \tag{A.1}$$

a measure of the length of the focal region, is equal to 1.7 mm. k_1 is

equal to $\frac{2\pi}{6.00\times10^{-8}}$ mm^{-1}. It is convenient to define a focusing parameter

$$\xi = {}^{1}/b, \tag{A.2}$$

which for $LiIO_3$ and KDP is 1.18 and 7.37, respectively.

The ordinary and extraordinary indices of refraction for $LiIO_3$ and KDP are listed in Table A-1 for 300 nm and 600 nm wavelengths.

Table A-1. Indices of refraction for $LiIO_3$ and KDP at 300 nm and 600 nm

Wavelength (nm)	Refractive index[a]			
	$n_o(LiIO_3)$[b]	$n_e(LiIO_3)$[c]	n_o(KDP)	n_e(KDP)
300	2.063	1.847	1.563	1.512
600	1.887	1.739	1.524	1.478

[a]Refractive indices for KDP are from ref (151). Refractive indices for $LiIO_3$ are calculated from the Sellmeier dispersion formula in ref (152).

[b]n_o is the ordinary index of refraction.

[c]n_e is the extraordinary index of refraction.

Symbols for the indices of refraction may be written as n_i^j, where i is equal to 1 or 2, and j is equal to o or e, or as n_k, where k is either 1, 2, o, or e. The latter notation will be used when one of the parameters in the refractive index is inferred. The symbols 1 and 2 designate refractive indices for 600 nm and 300 nm light, respectively. When the crystal is rotated to the phase matching angle

$$\theta_m = \arcsin\left[\left(\frac{n_2^e}{n_1^o}\right)^2 \frac{[(n_2^o)^2 - (n_1^o)^2]}{[(n_2^o)^2 - (n_2^e)^2]}\right]^{\frac{1}{2}} , \tag{A.3}$$

the refractive index (74)

$$n(\theta_m) = \frac{n_o n_e}{(n_o^2 \sin^2\theta_m + n_e^2 \cos^2\theta_m)^{\frac{1}{2}}} \tag{A.4}$$

for $LiIO_3$ and KDP, respectively, is 1.887 and 1.524. Under phase matching conditions, the Poynting vector and phase propagation direction of the SHG deviate by (153)

$$\rho = \arctan\left[\tfrac{1}{2}(n_1^o)^2\{(n_2^e)^{-2} - (n_2^o)^{-2}\} \sin 2\theta_m\right] . \tag{A.5}$$

For $LiIO_3$ and KDP, ρ is 84 mrad and 27 mrad, respectively. The absorption coefficients of the laser fundamental and SHG are symbolized by α_1 and α_2, respectively. Several additional formulas which will be useful are

$$\alpha = \alpha_1 - \tfrac{1}{2}\alpha_2, \tag{A.6}$$

$$\alpha' = \alpha_1 + \tfrac{1}{2}\alpha_2, \tag{A.7}$$

$$B = \rho(lk_1)^{\frac{1}{2}}/2, \tag{A.8}$$

$$\delta_o = 2a_w/b, \tag{A.9}$$

$$\beta = \rho/\delta_o, \tag{A.10}$$

$$\kappa = \alpha b/2, \tag{A.11}$$

$$\mu = (1-2f)/l, \tag{A.12}$$

where f is the distance traveled through the crystal to reach the laser focal point, and

$$\sigma = b\Delta k/2, \tag{A.13}$$

where Δk equals $(2\omega_1/c)(n_1-n_2(\theta))$ with ω_1 and c being the frequency of the laser fundamental and the speed of light, respectively. Some of the terms presented above are illustrated in Figure A-1.

SHG power may be expressed as (154)

$$P_2 = KP_1^2 l k_1 e^{-\alpha' l}\, h(\sigma,\beta,\kappa,\xi,\mu), \tag{A.14}$$

where P_1 is the input laser power, K is a function defined as

$$K = \frac{128\pi^2\omega_1^2 d^2}{c^3 n_1^2 n_2(\theta_m)}, \tag{A.15}$$

and h is a function containing all of the optimizable parameters. The effective nonlinear coefficient d in equation A.15 is equal to 1.0 for KDP and 11.9 for $LiIO_3$. Since only relative SHG powers for each crystal are required for this analysis, it is convenient to redefine K as K_{eff}, where

$$K_{eff} = \frac{d^2}{n_1^2 n_2(\theta_m)}. \tag{A.16}$$

For $LiIO_3$, K_{eff} is equal to 21.5, and for KDP it equals 0.3. Similarly, the SHG power P_2 may be redefined as P_2^{eff}, where

$$P_2^{eff} = K_{eff}\, l\, e^{-\alpha' l}\, h(\sigma,\beta,\kappa,\xi,\mu). \tag{A.17}$$

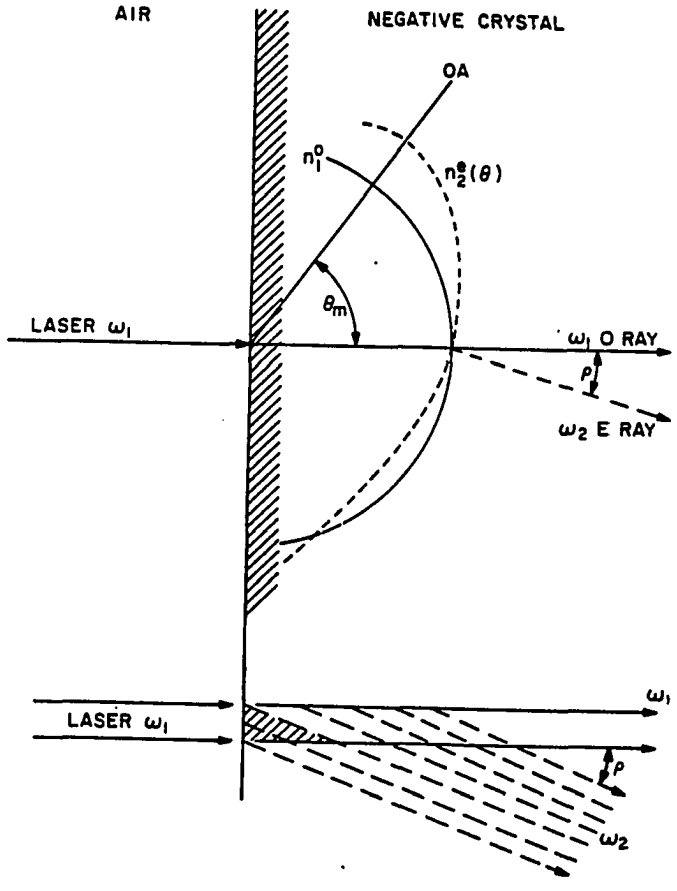

Figure A-1. Phase matching conditions for a negative uniaxial crystal. The symbol OA represents the optic axis of the crystal whose orientation, relative to the point where n_1^o equals $n_2^e(\theta)$, establishes the phase matching angle θ_m. Also illustrated is the walk-off angle ρ between the dye laser fundamental ω_1 and the SHG ω_2. From ref (155)

To determine the effect of focusing on SHG power, initial conditions are set where all absorption of light by the crystal is assumed to be negligible (α=0), and the focus is set at the center of the crystal ($f=^{l}/2$). This leads to

$$\kappa(KDP) = \kappa(LiIO_3) = \mu(KDP) = \mu(LiIO_3) = 0 \qquad (A.18)$$

in equations A.11 and A.12. The function h in equation A.17 will, therefore, be dependent on only three parameters, σ, β and ξ. From equations A.2, A.8 and A.10, it is clear that β may be expressed as

$$\beta = B\xi^{-\frac{1}{2}} , \qquad (A.19)$$

leading to an expression for h in terms of σ, β and ξ. Since l is not considered here as an optimizable parameter, the value of B is consequently not variable. ξ can be varied by changing the focusing lens preceding the SHG crystal. Experimentally, the phase matching parameter σ is optimized for each B and ξ by fine adjustment of the crystal orientation to maximize the second harmonic power. The function $h(\sigma,\beta,\xi)$ is expressed as $h_m(B,\xi)$, whenever σ is assumed to be optimized. For $LiIO_3$, with a 7.0 cm lens focusing the 600 nm laser fundamental, values of B, ξ and h_m are 6.08, 1.18 and $\sim$0.15, respectively. For KDP, under identical conditions, B, ξ, and h_m are 4.88, 7.37 and $\sim$0.1, respectively. From Figure A-2a, it is clear that $\xi(LiIO_3)$ is very close to the optimum value for obtaining high SHG conversion efficiency. Approximately 50% more SHG power could be obtained from the KDP crystal, however, if ξ(KDP) were reduced to $\sim$1.8. This could be accomplished by replacing the 7.0 cm

focal length lens with a 15.0 cm focal length lens.

If μ is reconsidered as an optimizable parameter, results similar to those depicted in Figure A-2b are obtained for all values of B and ξ. Thus, assuming no absorption by the crystal, the focus of the laser fundamental should always be at f = $^1/_2$. Under the optimum conditions presented thus far for each crystal, a ratio for the SHG power obtained from the two crystals $P_2^{eff}(LiIO_3)$: $P_2^{eff}(KDP)$, is approximately 10:1.

The $LiIO_3$ absorption coefficients at 600 nm and 300 nm are 0.128 mm^{-1} and 0.715 mm^{-1}, respectively (156). For KDP, the absorption coefficients at 600 nm and 300 nm are both equal to 0.031 mm^{-1}(157). When crystal absorption is included as a factor affecting SHG conversion efficiencies, the effective SHG powers can be obtained by multiplying the previously calculated values of P_2^{eff} by $\exp(\mu\alpha l - \alpha' l)$. For clarity, a new term $P_2^{eff'}$ is used for the effective SHG power when absorption effects are included. Thus, $P_2^{eff'}$ is defined as

$$P_2^{eff'} = P_2^{eff} \exp(\mu\alpha l - \alpha' l). \qquad (A.20)$$

The ratio $P_s^{eff'}(LiIO_3)$: $P_2^{eff'}(KDP)$ is still approximately 10:1, after absorption of light by the crystal is accounted for. Values for $P_2^{eff'}$ are a maximum for $LiIO_3$ when μ is equal to -1 and for KDP when μ is equal to 1. This corresponds to a laser fundamental beam focus near the rear and front surfaces of the crystals, respectively.

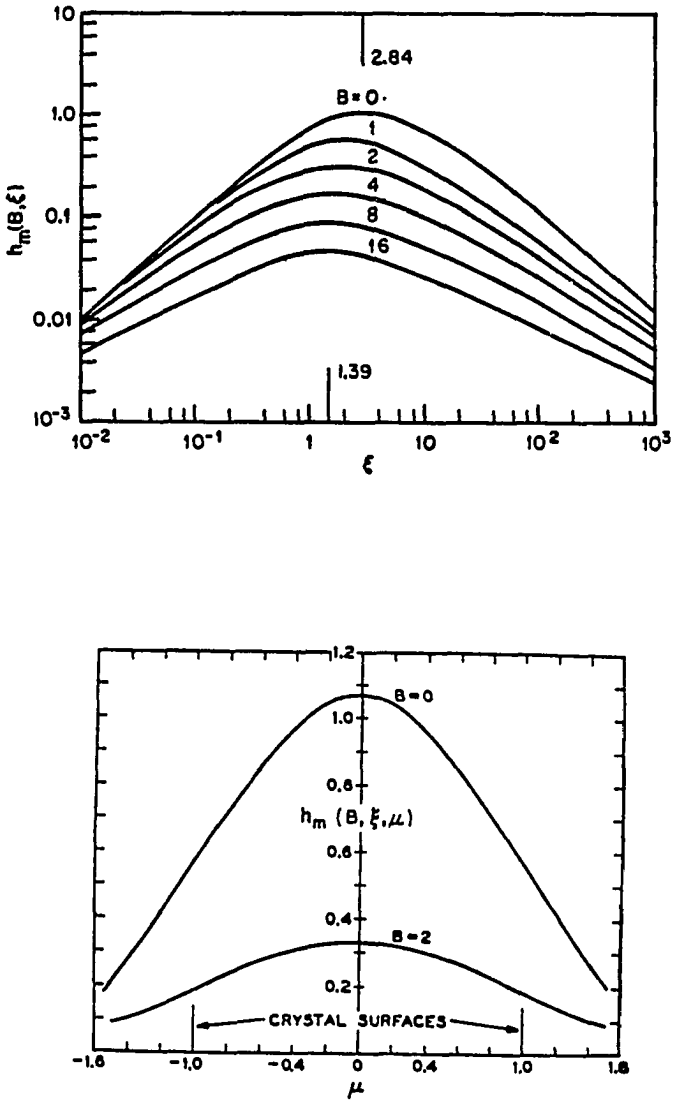

Figure A-2. Influence of focusing parameters on SHG power. In (a), the effect of variations in ξ on h_m for several values of B is illustrated. In (b), the effect of a third parameter μ on h_m is presented for cases where B=0, ξ=2.8 and B=2, ξ=1.7. From ref (155)